

Spinodal nanodecomposition in magnetically doped semiconductors

T. Dietl,^{1,2,3} K. Sato,^{4,*} T. Fukushima,⁵ A. Bonanni,^{6,†} M. Jamet,⁷ A. Barski,⁷ S. Kuroda,⁸ M. Tanaka,⁹ Pham Nam Hai,¹⁰ and H. Katayama-Yoshida⁵

¹*Institute of Physics, Polish Academy of Sciences, PL-02-668 Warszawa, Poland*

²*Institute of Theoretical Physics, Faculty of Physics, University of Warsaw, PL-02-093 Warszawa, Poland*

³*WPI-Advanced Institute for Materials Research (WPI-AIMR), Tohoku University, Sendai 980-8577, Japan*

⁴*Graduate School of Engineering, Osaka University, Suita, Osaka 565-0871, Japan*

⁵*Graduate School of Engineering Science, Osaka University, Toyonaka, Osaka 560-8531, Japan*

⁶*Institut für Halbleiter-und-Festkörperphysik, Johannes Kepler University, A-4040 Linz, Austria*

⁷*Commissariat à l'Energie Atomique, INAC/SP2M-UJF, F-38054 Grenoble, France*

⁸*Institute of Materials Science, University of Tsukuba, Tsukuba, Ibaraki 305-8573, Japan*

⁹*Department of Electrical Engineering and Information Systems, The University of Tokyo, Tokyo 113-8656, Japan*

¹⁰*Department of Physical Electronics, Tokyo Institute of Technology, Tokyo 152-8552, Japan*

(Dated: March 4, 2020)

This review presents the recent progress in computational materials design, experimental realization, and control methods of spinodal nanodecomposition under three- and two-dimensional crystal-growth conditions in spintronic materials, such as magnetically doped semiconductors. The computational description of nanodecomposition, performed by combining first-principles calculations with kinetic Monte Carlo simulations, is discussed together with extensive electron microscopy, synchrotron radiation, scanning probe, and ion beam methods that have been employed to visualize binodal and spinodal nanodecomposition (chemical phase separation) as well as nanoprecipitation (crystallographic phase separation) in a range of semiconductor compounds with a concentration of transition metal (TM) impurities beyond the solubility limit. The role of growth conditions, co-doping by shallow impurities, kinetic barriers, and surface reactions in controlling the aggregation of magnetic cations is highlighted. According to theoretical simulations and experimental results the TM-rich regions appear either in the form of nanodots (the *dairiseki* phase) or nanocolumns (the *konbu* phase) buried in the host semiconductor. Particular attention is paid to Mn-doped group III arsenides and antimonides, TM-doped group III nitrides, Mn- and Fe-doped Ge, and Cr-doped group II chalcogenides, in which ferromagnetic features persisting up to above room temperature correlate with the presence of nanodecomposition and account for the application-relevant magneto-optical and magnetotransport properties of these compounds. Finally, it is pointed out that spinodal nanodecomposition can be viewed as a new class of bottom-up approach to nanofabrication.

Contents

I. Introduction	2	IV. Spinodal nanodecomposition in (Ga,Mn)N	21
II. Theory of spinodal nanodecomposition	5	A. A controversial system	21
A. <i>Ab initio</i> materials design	5	B. Experimental evidences for spinodal nanodecomposition in (Ga,Mn)N	21
B. Pairing energy	5	C. Co-doping with shallow impurities and δ -doping in (Ga,Mn)N	23
C. Monte Carlo simulation of nanodecomposition	8	V. Spinodal nanodecomposition in (Ga,Fe)N	25
1. Dairiseki phase	9	A. Diluted Ga,Fe)N: current status	25
2. Konbu phase	10	B. Fabrication and properties of spinodally decomposed (Ga,Fe)N	25
D. Super-paramagnetic blocking phenomena	10	C. Fe distribution from nanoscale characterization	26
E. Mixing energy; nucleation and spinodal regions	11	D. Phase diagram of the spinodal decomposition in (Ga,Fe)N	28
F. Cahn-Hilliard theory of spinodal decomposition	13	E. Co-doping with shallow impurities in (Ga,Fe)N	29
III. Spinodal nanodecomposition in (Ga,Mn)As	15	F. Magnetic properties of (Ga,Fe)N	30
A. Fabrication methods and nanocomposite structure	15	VI. Spinodal nanodecomposition in (Ge,Mn)	32
B. Magnetic properties	17	A. Mn dilution in germanium	32
C. Magneto-optical phenomena	18	B. From Mn dilution to phase separation	33
D. Magnetoresistance	19	1. Review of experimental results	33
1. Films	19	C. Growth and structure of thin (Ge,Mn) films with spinodal decomposition	34
2. Spin-valve structures	20	1. Sample preparation	34
E. Spinodal nanodecomposition in other magnetic III-V compounds	20	2. Morphology of (Ge,Mn) films	35
		3. Lateral and vertical control of nanocolumns	36
		4. Two-dimensional spinodal decomposition	38
		5. Crystal structure of nanocolumns	39
		D. Magnetic properties	40

*Electronic address: ksato@mat.eng.osaka-u.ac.jp

†Electronic address: alberta.bonanni@jku.at

1. Crystalline (Ge,Mn) nanocolumns / Ge(001)	40
2. Crystalline (Ge,Mn) nanocolumns with partial relaxation / Ge(001)	42
3. Amorphous (Ge,Mn) nanocolumns / Ge(001)	43
4. Ge ₃ Mn ₅ clusters / Ge(001)	43
VII. Spinodal nanodecomposition in (Ge,Fe)	44
A. Introduction	44
B. MBE growth	44
C. Structural and chemical characterization	44
D. Magneto-optical characterization	45
VIII. Spinodal nanodecomposition in (Zn,Cr)Te	47
A. Introduction	47
B. Chemical phase separation and its control by the Fermi level position	48
1. Visualization of Cr distribution	48
2. Superparamagnetic behavior due to the Cr aggregation	49
3. Mechanism of Cr aggregation	50
4. Magneto-optical and magnetotransport properties	50
C. Crystallographic phase separation and konbu phase	51
1. Structural nanocharacterization	51
2. Magnetic properties	54
D. Summary	54
IX. Prospects of spinodal nanotechnology	55
X. Summary and outlook	56
List of abbreviations	58
Acknowledgments	58
References	59

I. INTRODUCTION

The detection of ferromagnetic features persisting up to above room temperature in a variety of magnetically doped semiconductors and oxides has been one of the most surprising developments in materials science over the recent years (Bonanni, 2007; Coey *et al.*, 2010; Dietl, 2003; Fukumura and Kawasaki, 2013; Kobayashi *et al.*, 2008; Kuzemsky, 2013; Liu *et al.*, 2005; Makarova, 2010; Nealon *et al.*, 2012; Pearton *et al.*, 2003; Roever *et al.*, 2011; Sawicki *et al.*, 2013; Yao *et al.*, 2012). In particular, the presence of robust ferromagnetism in technology-relevant semiconductors (e.g., GaN and Si) and oxides (e.g., ZnO and TiO₂) has promised to open the door to a wide exploitation in devices of remarkable spintronic functionalities found in dilute ferromagnetic semiconductors [such as (Ga,Mn)As] below their Curie temperature T_C , so far not exceeding 200 K (Dietl and Ohno, 2014; Jungwirth *et al.*, 2014; Sato *et al.*, 2010). However, it is increasingly clear that high- T_C non-metal ferromagnets represent a distinct class of systems in which the strength of ferromagnetic (FM) features correlates neither with the density of band holes necessary to mediate long-range interactions between diluted spins nor with an average concentration of magnetic ions.

In this review we focus on the latest progress in clarifying the origin of high- T_C ferromagnetism in dilute magnetic semiconductors (DMSs), such as group III pnictides, e.g., GaAs and GaN), group II chalcogenides, e.g., ZnTe), and group IV elemental semiconductors, e.g., Ge) doped with transition metal (TM) ions, either Cr, Mn, or Fe. Recent comprehensive studies have pointed out that in these systems, except for Mn in II-VI compounds (Giebultowicz *et al.*, 1993; Pajczkowska, 1978), the fundamental premise of DMSs on the random distribution of magnetic ions over cation sites is often not valid. As described here, this striking conclusion, and its consequences for electronic and magnetic properties, have been drawn from state-of-the-art theoretical modeling and experimental investigations. More specifically, the present understanding of these systems has been built by combining:

- *Ab initio* computational studies providing the magnitude of chemical interactions between magnetic cations depending on their distance, charge state, and location (surface vs. bulk); the interaction energies constitute the input parameters for kinetic simulations of spinodal nanodecomposition within the Monte Carlo method or by solving the relevant Cahn-Hilliard equation.
- Extensive epitaxy and post-growth processing protocols, including co-doping and annealing, allowing to establish the relationship between fabrication conditions and physical properties.
- Comprehensive nanocharacterization investigations employing ever improving methods of electron microscopy, synchrotron radiation, ion beams, and scanning probes that provide element-specific information on atom distributions, charge states, magnetic properties, and defects with spatial resolution down to the nm range.
- Scrupulous magnetization and magnetic resonance studies involving also the extensive examination of reference samples containing nominally no magnetic ions but otherwise grown and processed in the same way as the films under investigation.

According to the results reviewed in this paper, the above methodology has made it possible to bring to light theoretically and experimentally a number of unanticipated properties of magnetically doped semiconductors. The new findings can be summarized as follows:

1. In DMSs, open orbitals of TM impurities not only provide localized spins but also, via $p-d$ hybridization, contribute to the bonding, which usually results in attractive forces between magnetic cations and in a miscibility gap in the thermodynamic phase diagram of the alloy.
2. The actual TM distribution, for given fabrication conditions, post-growth processing, and epitaxial

- strain, is determined by a competition between attractive forces, entropy terms, and kinetic barriers at the growth surface or in the sample volume. This results in the co-existence of TM ions in random cation-substitutional positions and in regions with high concentrations of magnetic constituents, either commensurate with the host lattice (chemical phase separation) or in the form of precipitates (crystallographic phase separation). The process of TM aggregation is referred to as spinodal nanodecomposition though nucleation mechanisms (bimodal decomposition) is involved in many cases.
3. The buried regions with high concentrations of magnetic constituents (called condensed magnetic semiconductors - CMSs, even if an insulator-to-metal transition occurred locally) appear as TM-rich nanodots (distributed randomly over the sample volume or clustered in defined planes) or in the form of TM-rich nanocolumns extending along specific crystal directions.
 4. The incorporation and distribution of magnetic ions depend on co-doping by shallow impurities or electrically active defects, which rather than changing the carrier concentration alter the valence of the TM ions and, thus, the chemical forces and kinetic barriers controlling the aggregation of magnetic cations either at the growth surface or in the film volume.
 5. Because of the bonding to host atoms and the effects of strains, the structural and magnetic properties of particular CMS nanocrystals (NCs) may not yet been listed in chemical compendia, and have to be assessed experimentally.
 6. Depending on the predominant character of the exchange interactions, the spins within the *individual* CMS NCs exhibit FM, ferrimagnetic, or antiferromagnetic (AF) spin ordering that owing to the high concentrations of TM ions persists typically to above room temperature (RT). At the same time, local strains, the character of interfaces, internal spin-orbit interactions, and the shapes of TM-rich regions control the magnetic anisotropy of particular CMS NCs.
 7. Samples of nominally the same DMS with a given average TM concentration, can show diverse structural and macroscopic magnetic properties, as the relative abundance of randomly distributed TM ions and NCs formed by various phase separation processes depends on fabrication conditions, co-doping, and defect content. Except for DMSs with a large concentration of holes, randomly distributed TM spins can order only at low temperatures, whereas the NCs can lead a FM, AF, and/or superparamagnetic behavior persisting up to high temperatures.
 8. Due to the combine effects of magnetic anisotropy and dipole interactions, decomposed magnetic alloys rather than exhibiting superparamagnetic characteristics show typically temperature independent narrow and leaning magnetic hysteresis loops up to the ordering temperature of the relevant CMS (superferromagnetic characteristics), even if the diameters of TM-rich regions are in the sub 10 nm range. Ferromagnetic-like features can result also from uncompensated spins on the surface of AF NCs.
 9. The outstanding structure of decomposed alloys points to novel functionalities compared to hole-mediated uniform dilute FM semiconductors. In particular, the magnetotransport and magneto-optical properties of such systems, while correlate usually with the magnetic characteristics, reveal specificities of the nanocomposite media, such as the mixing between diagonal and non-diagonal components of the conductivity tensors and the persistence of magneto-optical effects into the spectral region below the band gap.
 10. Magnetic studies of thin epitaxial layers containing a small quantity of magnetic impurities are challenged by the uncontrolled contamination of samples by FM nano- and micro-particles.
- Altogether, one can now obtain various semiconductors with spatial distributions of TM cations on demand. In particular, by selecting appropriate growth conditions, layers' layout, co-doping, and/or processing protocols it becomes possible to fabricate either a uniform DMS or a decomposed alloy with a predefined (i) character of the phase separation (chemical vs. crystallographic); (ii) type of TM aggregation (nanodots vs. nanocolumns); (iii) plane at which nanodots assemble, and (iv) chemical and magnetic properties of the precipitates. This command over the structural and magnetic properties offers a spectrum of opportunities for the design and realization of modulated systems with properties and functionalities encountered neither in uniform DMSs nor in the case of self-assembled quantum dots or nanowires of non-magnetic semiconductors.
- As seen in the Table of Contents, the main body of the present review consists of three major parts.
- First, we discuss theoretical aspects of nanodecomposition in magnetically doped semiconductors (Sec. II). We start (Sec. II.A) by presenting first principles (*ab initio*) approaches and their applications (Sec. II.B) for determining the chemical forces between magnetic ions, either in bulk or at the growth surface, as well as their dependence on co-doping with shallow impurities. In Secs. II.C.1 and II.C.2 we describe Monte Carlo simulations of three-dimensional (3D) and two-dimensional (2D) spinodal decomposition, corresponding respectively to the spontaneous formation of TM-rich nanodots in the film volume and to the self-assembly of TM-rich

nanocolumns during the epitaxy. Next, in Sec. II.E the computed phase diagrams of some binary alloy are presented, allowing us to recall the notions of miscibility gap, nucleation, and spinodal decomposition. We also emphasize the importance of kinetic barriers in the process of TM aggregation. These concepts make it possible to discuss, in Sec. II.F, the Cahn-Hilliard equation quantifying the dynamics of spinodal decomposition. As a whole, theoretical modeling opens to the understanding of the physics of nanodecomposition for different combinations of hosts, TM ions, shallow impurities, and fabrication procedures.

Second, in Secs. III–VIII experimental studies of nanodecomposition in specific families of magnetically doped semiconductors are presented. Whenever possible the findings are discussed in the context of the theoretical predictions outlined in Sec. II. We start (Sec. III) with the model FM semiconductor (Ga,Mn)As. For this system pioneering works aiming at the fabrication of GaAs containing MnAs nanoprecipitates were carried out (Boeck *et al.*, 1996; Shi *et al.*, 1996). Furthermore, early *ab initio* studies of (Ga,Mn)As and related systems revealed the presence of strong attractive forces between TM cation pairs in DMSs (van Schilfgaarde and Mryasov, 2001). We describe the chemical and crystallographic phase separations occurring in (Ga,Mn)As under annealing or epitaxy at appropriately high temperatures. Structural information on Mn-rich (Mn,Ga)As NCs is linked to FM-like features as well as to device-relevant magnetic circular dichroism (MCD) and magnetotransport characteristics of this noncomposite system. The understanding of ferromagnetism in decomposed (Ga,Mn)As allows us to assess the origin of high- T_C in (Ga,Mn)P, (In,Mn)As, (Ga,Mn)Sb, and (In,Mn)Sb.

In Secs. IV and V we describe investigations of group III nitrides, doped with either Mn or Fe and, in some studies, co-doped with Si or Mg. In the case of (Ga,Mn)N (Sec. IV) a rich collection of magnetic properties at similar average Mn content is observed. The nanodecomposition scenario is confirmed by structural nanocharacterization demonstrating the correlation of high- T_C and low- T_C with respectively the presence and absence of a phase separation. Similar experiments point to spinodal decomposition, in the form of nanocolumns, in (Al,Cr)N (Gu *et al.*, 2005). Section V is devoted to (Ga,Fe)N, the subject of particularly comprehensive structural and magnetic studies. The collected data provide evidences for spinodal decomposition as well as for the precipitation of various Fe-rich (Fe,Ga) $_x$ N NCs whose composition x (and thus magnetic properties), abundance, and location in predefine planes can be controlled by growth conditions, co-doping by Si and Mg, and architecture.

Sections VI and V present the outcome of nanodecomposition studies on Mn- and Fe-doped Ge, respectively, in which the TM distribution is uniform or either chemical or crystallographic phase separation is observed depending on the growth temperature. In addition to detailed structural and magnetic investigations, compre-

hensive MCD and magnetotransport data are available for these systems. Particularly relevant are works on the formation of Mn-rich nanocolumns along the [001] growth direction in (Ge,Mn) deposited onto Ge(001) substrates.

As described in Sec. VIII, in the case of (Zn,Cr)Te spinodal decomposition results in either Cr-rich nanodots or nanocolumns assuming a $\langle 111 \rangle$ orientation, even for epitaxy on (001) substrates. Despite chemical heterogeneity there is a strict correlation between magnetization, MCD, and anomalous Hall effect (AHE) in these alloys. Furthermore, nanodecomposition and, thus, other associated properties are strongly affected by changing the concentrations of donors or acceptors, either by manipulating with stoichiometry via altering the intensities of the molecular beams or by co-doping with I or N, respectively. Pioneering work drawing attention to the possibility of spinodal nanodecomposition in (Zn,Cr)Se (Karzewski *et al.*, 2003) is also discussed.

In the third part of our review, Sec. IX, we discuss application prospects of the remarkable properties revealed for decomposed magnetically doped semiconductors over the recent years. We emphasize the possibility of bottom-up nanotechnology based on the control of spinodal nanodecomposition ('spinodal nanotechnology'). It is pointed out that decomposed magnetic alloys consisting, for instance, of a semiconductor with embedded NCs of a FM metal can exhibit functionalities that cannot be realized employing either uniform FM metal films or semiconductor quantum dot layers. Finally, in Sec. X, we summarize the main conclusions stemming from studies of heterogeneous DMSs and present an outlook on open questions and challenges ahead. Furthermore, a list of abbreviations is provided.

As seen, the physics of high- T_C ferromagnetism in magnetically doped oxides (Coey *et al.*, 2010; Fukumura and Kawasaki, 2013; Li *et al.*, 2012; Sawicki *et al.*, 2013), carbon derivatives (Kuzemsky, 2013; Makarova, 2010), and some other systems (Nealon *et al.*, 2012; Roever *et al.*, 2011; Rylkov *et al.*, 2012; Yao *et al.*, 2012) is beyond the scope of this review. In particular, the question of ferromagnetism originating from spins residing on defects (Coey *et al.*, 2010; Zhou, 2014) or on open p shells (Volnianska and Boguslawski, 2010), or mediated by defects or by residual impurities like hydrogen (Li *et al.*, 2012) is not addressed here. We only note that not only several authors have considered theoretically whether ferromagnetism would be possible without magnetic elements (Bouzerar and Ziman, 2006; Droghetti *et al.*, 2009; Du *et al.*, 2012; Elfimov *et al.*, 2002; Ivanovskii, 2007; Kenmochi *et al.*, 2004a, 2005, 2004b; Mavropoulos *et al.*, 2009; Volnianska and Boguslawski, 2010) but also the role of spinodal nanodecomposition was examined in this context (Seike *et al.*, 2012, 2013a,b).

As emphasized in our survey, the recent progress in understanding high- T_C DMSs results, to a large extent, from the application of various powerful nanocharacterization tools. Nevertheless, we do not discuss in details relevant experimental techniques, as many of them were

recently reviewed in a collection (Bonanni, 2011) that contains also useful information about the methodology of magnetic measurements on thin films employing superconducting quantum interference device (SQUID) magnetometry (Sawicki *et al.*, 2011). A related experimental challenge is the contamination by FM nano- and micro-particles that already reside in the substrate or can be incorporated during the growth, annealing, etching, handling, or storing of particular samples. Some instructive examples were disclosed (Abraham *et al.*, 2005; Grace *et al.*, 2009; Makarova *et al.*, 2006; Matsubayashi *et al.*, 2002) but presumably much more cases, even if spotted, have not been published.

II. THEORY OF SPINODAL NANODECOMPOSITION

A. Ab initio materials design

Ideally, theoretical studies should predict the microscopic TM distribution—including the presence of chemical and crystallographic phase separations—and the corresponding electronic and magnetic properties at given growth conditions and co-doping by shallow impurities. As already reviewed elsewhere (Sato *et al.*, 2010), first-principles methods for electronic structure calculations have played the important role in predicting various properties of homogeneous and heterogenous DMSs without referring to any experimental parameters. This is mainly due to the success of the local density approximation (LDA) in the density functional theory (DFT) (Dreizler and Gross, 1995; Hohenberg and Kohn, 1964; Kohn and Sham, 1965).

In the DFT, a many electron system is described by using the electron density $n(\mathbf{r})$, i.e., it is proven that the many electron wave function Φ and the expectation value of a physical quantity $\langle A \rangle$ can be written as a functional of $n(\mathbf{r})$, such as $\Phi[n(\mathbf{r})]$ and $A[n(\mathbf{r})]$, respectively. In particular, one can search for the ground state by minimizing the total energy functional $E[n(\mathbf{r})]$ with respect to $n(\mathbf{r})$. In the Kohn-Sham scheme, the total energy functional is formulated by referring to a one-electron system and given as,

$$E[n(\mathbf{r})] = T_{\text{op}}[n(\mathbf{r})] + \int n(\mathbf{r})v(\mathbf{r})d^3r + \frac{1}{2} \int \int e^2 \frac{n(\mathbf{r}) \cdot n(\mathbf{r}')}{|\mathbf{r} - \mathbf{r}'|} d^3r d^3r' + E_{\text{xc}}[n(\mathbf{r})]. \quad (1)$$

Here, $T_{\text{op}}[n(\mathbf{r})]$ is the electrons' kinetic energy, the second term is the energy of the electrons in an external potential $v(\mathbf{r})$, the third term is the classical Hartree interaction energy and the last term, the exchange-correlation energy. For the exchange-correlation energy, a rigorous expression is not known and an efficient approximation is needed (Dreizler and Gross, 1995).

The standard approximation is the LDA within which E_{xc} is taken as the exchange-correlation energy of homogeneous electron gas (Ceperly and Alder, 1980; Dreizler

and Gross, 1995; Perdew and Wang, 1986). Thus, within the LDA, E_{xc} is calculated as a function of the local electron density, i.e., $E_{\text{xc}}[n(\mathbf{r})] \sim E_{\text{xc}}(n(\mathbf{r}))$. This approximation sounds inaccurate since the electron density distribution in a real material varies strongly depending on the position \mathbf{r}). Furthermore, the computations are carried out for supercells containing typically less than 100 atoms and assuming periodic boundary conditions. Actually, despite these approximations, the LDA, or its spin-polarized version, the local spin density approximation (LSDA), are accurate enough for explaining many physical properties of various materials (Martin, 2004). Recently, LDA, LSDA, and their modifications are used not only for understanding experimental results but also for designing new functional materials.

It is well known that the phase diagrams of a number of alloys exhibit a solubility gap in a certain concentration range. Particularly low is the solubility of TM impurities in semiconductors. An exception here is a large solubility of Mn in II-VI compounds, in which Mn atoms remain distributed randomly over the substitutional cation sites up to concentrations often exceeding 50% (Furdyna and Kossut, 1988; Pajączkowska, 1978). The large solubility of Mn in II-VI compounds can be assigned to the truly divalent character of Mn whose d states little perturb the sp^3 tetrahedral sp bonds as both the lower d^5 (donor) and the upper d^6 (acceptor) Hubbard levels are respectively well below and above the band edges (Dietl, 1981, 2002; Zunger, 1986).

We describe now two *ab initio* approaches that have provided quantitative information on the *thermodynamic* stability of particular DMS alloys $A_{1-x}\text{TM}_x\text{B}$ as well as input parameters (such as the pairing energy E_d and mixing energy $\Delta E(x)$) for studies of decomposition dynamics by the Monte Carlo simulations and by the Cahn-Hilliard equation, respectively. Within the first method one evaluates a change of the system energy associated with bringing two or more TM ions to neighboring cation positions. If this pairing energy E_d is negative, i.e., there is an attractive chemical force between TM ions, their distribution may not be random. The second approach involves the evaluation of the alloy energy in comparison to weighted energies of the end compounds. A positive value of this mixing energy $\Delta E(x)$ points to the instability of the alloy.

B. Pairing energy

The pairing energy E_d (known also as heat of reaction or pair interaction energy) for a DMS alloy (A,TM)B is evaluated from total energies E corresponding to three different contents of TM cations in the supercell (van Schilfgaarde and Mryasov, 2001),

$$E_d = E[(A_{N-2}, \text{TM}_2)\text{B}_N] + E[A_N\text{B}_N] - 2E[(A_{N-1}, \text{TM})\text{B}_N], \quad (2)$$

where N is the total number of cations in the supercell. The magnitudes of E_d for TMs at the nearest neighbor cation positions were determined employing various DFT implementations for (Ga,Mn)As (Birowska *et al.*, 2012; Mahadevan *et al.*, 2005; Sato *et al.*, 2005; van Schilfhaarde and Mryasov, 2001); (Ga,V)As, (Ga,Cr)As, and (Ga,Fe)As (Mahadevan *et al.*, 2005); (Ga,Mn)N (Bogusławski and Bernholc, 2006; Chan *et al.*, 2008; Das *et al.*, 2003; Gonzalez Szwacki *et al.*, 2011; Raebiger *et al.*, 2014; Sato *et al.*, 2005; van Schilfhaarde and Mryasov, 2001); (Ga,Cr)N (Cui *et al.*, 2005; Gonzalez Szwacki *et al.*, 2011; Mahadevan *et al.*, 2005; van Schilfhaarde and Mryasov, 2001); (Ga,Fe)N (Gonzalez Szwacki *et al.*, 2011; Navarro-Quezada *et al.*, 2011); (Ge,Mn,Cr,Co) (Continenza *et al.*, 2006a); (Zn,Mn)Te (Kuroda *et al.*, 2007), and (Zn,Cr)Te (Da Silva *et al.*, 2008; Fukushima *et al.*, 2006b; Kuroda *et al.*, 2007; Raebiger *et al.*, 2014).

In the case of the nearest neighbor Mn cations in ZnTe, $E_d = 21$ meV (Kuroda *et al.*, 2007), the result consistent with a large solubility of Mn in II-VI compounds, as mentioned above. In contrast, $E_d = -160$ meV for Cr cations in $\text{Zn}_{0.95}\text{Cr}_{0.05}\text{Te}$ (Fukushima *et al.*, 2006b), which indicates that Cr cations should aggregate provided that diffusion barriers can be overcome at the growth or annealing temperature. Similarly, the pairing energy of Mn cation dimers was computed to be $E_d = -120$ meV in GaAs and -300 meV in GaN (van Schilfhaarde and Mryasov, 2001). Being determined by p - d hybridization, the magnitude of $|E_d|$ decays quickly with the distance between TM cations, as shown in Fig. 1.

A number of experimentally relevant extensions of this approach has been proposed.

Beyond dimers: The formation of larger TM cation clusters than dimers were considered and their magnetic properties assessed (Cui *et al.*, 2007; Das *et al.*, 2003; Gonzalez Szwacki *et al.*, 2011; Hynninen *et al.*, 2006b; Mahadevan *et al.*, 2005; Navarro-Quezada *et al.*, 2011; van Schilfhaarde and Mryasov, 2001). In this case (van Schilfhaarde and Mryasov, 2001),

$$E_d^{(n)} = E[(A_{N-n}, \text{TM}_n)\text{B}_N] + E[A_N\text{B}_N] - E[(A_{N-n+1}, \text{TM})\text{B}_N] - E[(A_{N-1}, \text{TM})\text{B}_N]. \quad (3)$$

This represents the energy change associated with the trapping of one more TM cation by a cluster consisting of $n - 1$ TM cations. Early studies (van Schilfhaarde and Mryasov, 2001) suggested that $E_d^{(n)} \simeq 0$ for $n = 3$ in the case of (Ga,Mn)As, (Ga,Mn)N, and (Ga,Cr)N, i.e., that decomposition of these alloys into systems containing clusters with three TM cations is favored energetically. This conclusion is not supported by a more recent investigation indicating that $E_d^{(n)}$ remains strongly negative up to at least $n = 4$ (Gonzalez Szwacki *et al.*, 2011), as shown in Fig. 2. This work pointed also out that coupling between pairs of Mn and of Cr ions is FM in wurtzite (wz) GaN, whereas the interaction between Fe ions is AF. These expectations are discussed in comparison to experimental results in Secs. IV and V.

The structure of Mn clusters in (Ga,Mn)N and the interactions of the magnetic Mn ions and clusters have been studied through first-principles calculations and T_C was evaluated using mean-field and Monte Carlo methods (Hynninen *et al.*, 2007). It was found that joining substitutional Mn ions to clusters is energetically favorable and especially the structures of two to four Mn ions formed around a single N ion are most stable. These clusters are always found to have a FM ground state, and FM intercluster interactions are also present even at relatively long distances. For randomly distributed Mn clusters, high T_C s are obtained at high Mn concentrations (Hynninen *et al.*, 2007). The calculated T_C is expected to depend dramatically on the microscopic cluster distribution (Hynninen *et al.*, 2006a), giving a possible explanation for the remarkable spread in experimental T_C values for (Ga,Mn)N (see Sec. IV.A). The complexity of the Mn-clustering has been highlighted by further DFT calculations where the coexistence of AF and FM coupling has been found for various configurations, different charge states and spatial distribution of the clusters (Cui *et al.*, 2007).

Nanocolumns and nanodots: It was noted that in the presence of attractive forces between TM cations, the

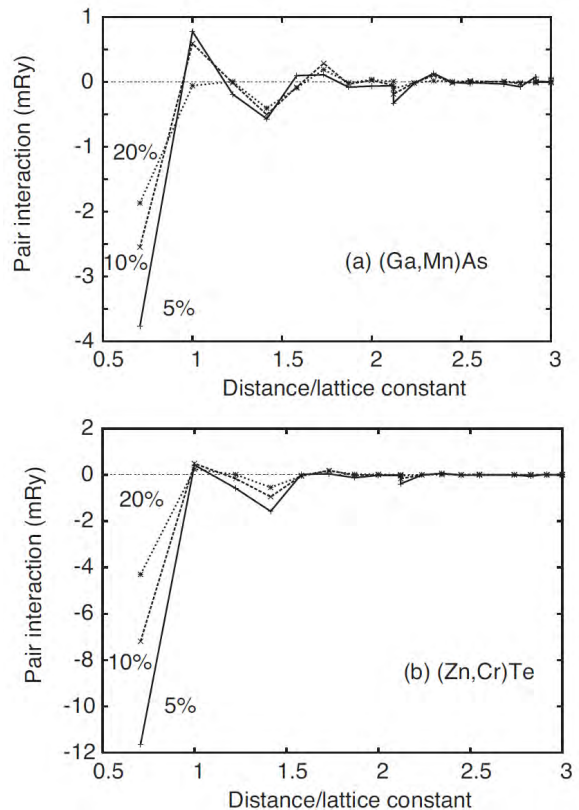


FIG. 1 Calculated pair interaction energies E_d as a function of the distance between TM pairs in (a) $\text{Ga}_{1-x}\text{Mn}_x\text{As}$ (from Sato *et al.*, 2005) and (b) $\text{Zn}_{1-x}\text{Cr}_x\text{Te}$ (from Fukushima *et al.*, 2006b) with various average concentrations x of TM ions.

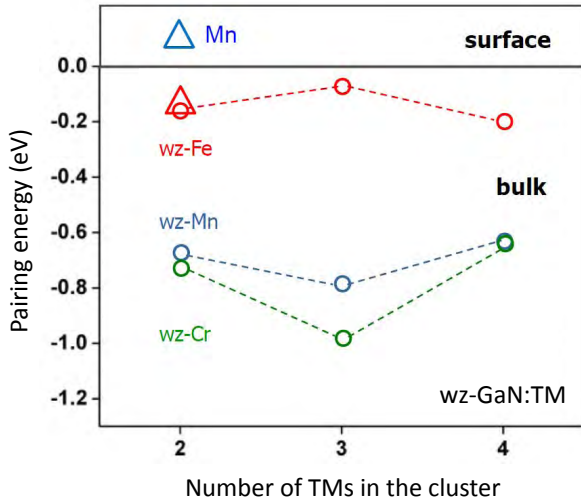


FIG. 2 (Color online) Pairing energies $E_d^{(n)}$ as a function of the number n of TM cations in Cr, Mn, and Fe clusters in bulk wz-GaN (circles) and on Ga(0001) surface (triangles). Adapted from Gonzalez Szwacki *et al.*, 2011.

layer-by-layer epitaxy can result in the growth of TM-rich nanocolumns (Fukushima *et al.*, 2006b). The resulting structure was named the 'konbu phase', where 'konbu' means seaweed in Japanese. The presence of the konbu phase was experimentally demonstrated in the case of (Al,Cr)N (Gu *et al.*, 2005), (Ge,Mn) (Sec. VI), and (Zn,Cr)Te (Sec. VIII). Often, however, the TM-rich regions appear in the form of nano-dots, the case of, e.g., annealed (Ga,Mn)As (see Sec. III). Since the cross section looks then like a marble ('dairiseki' in Japanese), the decomposed state is referred to as the 'dairiseki phase' (Sato *et al.*, 2005). Results of Monte-Carlo simulations designed to show the formation of either konbu or dairiseki phases are presented in Secs. II.C.1 and II.C.2.

Surface aggregation: Since the initial step of the TM aggregation is expected to occur on the epitaxy plane, pairing energies of TM impurities residing on surfaces relevant to epitaxial processes were evaluated (Birowska *et al.*, 2012; Gonzalez Szwacki *et al.*, 2011; Navarro-Quezada *et al.*, 2011). As presented in Fig. 2, E_d values for Mn and Cr cation dimers on the (0001) wz-GaN surface become positive ($E_d \simeq 170$ meV and 280 meV, respectively), whereas E_d remains negative for Fe pairs ($E_d = -120$ meV), favoring the formation of Fe-rich clusters during the epitaxy (Gonzalez Szwacki *et al.*, 2011). This explains a much lower solubility limit of Fe comparing to Mn in epitaxial films of wz-GaN but does not elucidate why it is difficult to grow epitaxially (Ga,Cr)N with a large concentration of randomly distributed Cr ions (see, Secs. IV and V). Furthermore, a question was addressed how the spatial distribution of TM ions in epitaxial films could be affected by non-equivalence of certain crystal directions on the surface. It was found for

(Ga,Mn)As deposited onto an unreconstructed surface of (001)GaAs that E_d is by 1 eV smaller for Mn pairs residing along the $[\bar{1}10]$ axis comparing to the $[110]$ case (Birowska *et al.*, 2012). Puzzling uniaxial anisotropies found in (Ga,Mn)As were explained by lowering of crystal symmetry associated with the non-random distribution of Mn dimer orientations, setting in during the epitaxy (Birowska *et al.*, 2012).

Role of co-doping: It was suggested that co-doping of DMSs with shallow donors or acceptors constitutes an efficient method of controlling the TM aggregation (Dietl, 2006). This way of affecting the process of nanodecomposition operates if there are band gap states derived from TM d orbitals that can trap carriers supplied by shallow impurities (for compilation of TM-related levels in various hosts see, e.g., Dietl and Ohno, 2003). The corresponding change in the charge state and valency of the magnetic ions modifies chemical and spin-dependent interactions between TM impurities. As an example, the energy of the *screened* Coulomb repulsion between two elementary charges residing on the nearest neighbor cation sites in the GaAs lattice is 280 meV. Accordingly, a surplus of charge on TM ions brought by co-doping with shallow dopants or by electrically active defects can outweigh the gain of energy stemming from p - d hybridization and impede the NC assembling (Boguslawski and Bernholc, 2006; Dietl, 2006; Ye and Freeman, 2006). This intuitive picture was checked by *ab initio* computations for (Ga,Mn)N (Boguslawski and Bernholc, 2006), (Ga,Fe)N (Navarro-Quezada *et al.*, 2011), (Zn,Cr)Te (Da Silva *et al.*, 2008; Kuroda *et al.*, 2007), and (Ga,Cr)As (Da Silva *et al.*, 2008). As shown in Fig. 3, the value of E_d attains a minimum in ZnTe when the two Cr cations are in the 2+ charge state (Da Silva *et al.*, 2008). However, the computation results shown in the same plot indicate that also in GaAs, E_d goes through a minimum for the Cr^{2+} case, rather than for the Cr^{3+} pairs, as might be expected for III-V compounds. Experimental verifications of these ideas have been found for (Ga,Fe)N co-doped with Si (Sec. V) and for (Zn,Cr)Te co-doped with I and N or deposited under growth conditions allowing to control the concentration of electrically active point defects (Sec. VIII). The effect of co-doping is also discussed theoretically in Sec. II.E exploiting the concept of the mixing energy.

Impurity and defect complexes: Electrically active impurities and defects not only alter the position of the Fermi level and, thus, the TM charge and spin state but can form with TM ions complexes characterized by specific structural and magnetic properties. Prompted by experimental results summarized in Secs. IV and V, magnitudes of $E_d^{(n,k)}$, where k denotes the number of shallow dopants in the cluster were evaluated for various complexes in wz-GaN, including Mn- Mg_k (Devillers *et al.*, 2012) as well as Fe_n - Mg_k and Fe_n - Si_k in the bulk and at the surface (Navarro-Quezada *et al.*, 2011). It was also established theoretically that Mn-D cation dimers, where D denotes either P, As, or Sb donor, allow to increase the

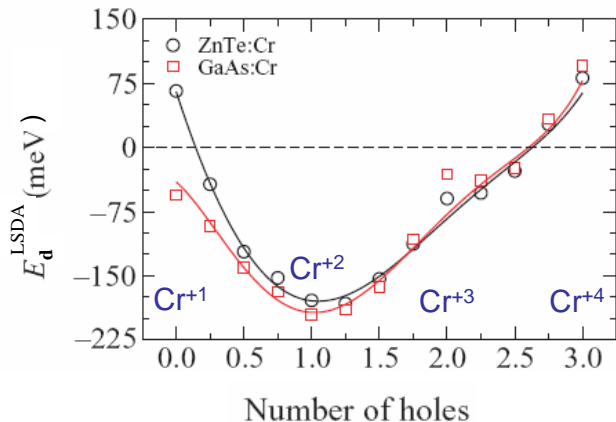


FIG. 3 Computed energy change resulting from bringing two Cr impurities to the nearest neighbor cation positions in ZnTe and GaAs depending on the charge state, i.e., the number of holes in the Cr d^5 shell. Adapted from Da Silva *et al.*, 2008.

incorporation of Mn in substitutional positions in both Si and Ge (Zhu *et al.*, 2008).

Crystallographic phase separation: The electronic structure and magnetic properties of antiperovskite GaMn_3N —frequently identified as a precipitated phase in $(\text{Ga},\text{Mn})\text{N}$ beyond the solubility limit of Mn into GaN (see Sec. IV.B)—have been studied by means of full potential linear muffin tin orbital (FP-LMTO) methods and compared to the results for cubic Mn_4N and Mn_3N . The total energy of these phases in different magnetic states, respectively FM, ferrimagnetic (FR), and AF is reported in Fig. 4.

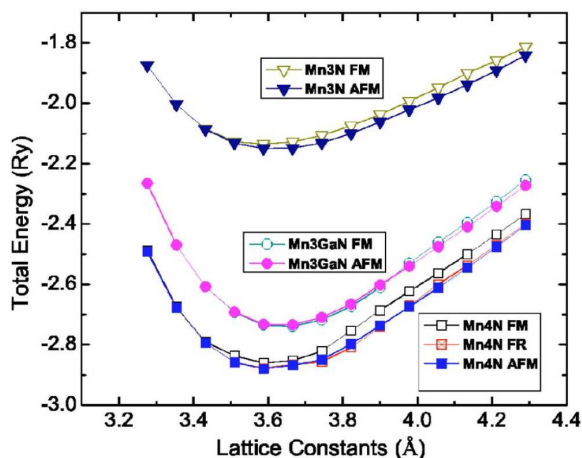


FIG. 4 (Color online) Total energy for Mn_4N , GaMn_3N , and Mn_3N in different magnetic ordering configurations. From Miao *et al.*, 2005.

C. Monte Carlo simulation of nanodecomposition

From paring energy considerations given in Sec. II.B, nanodecomposition is expected to occur in a number of DMSs. In order to predict the resulting TM distribution, it is relevant to simulate crystal growth. For this purpose, a hybrid method, combining *ab initio* and Monte Carlo simulations, was developed (Sato *et al.*, 2005).

Within this method, the alloy is described by an Ising model with the Hamiltonian of the system is written as,

$$H = \frac{1}{2} \sum_{i \neq j} V_{ij} \sigma_i \sigma_j, \quad (4)$$

where V_{ij} is the effective pair interaction energy between two TM cations at sites i and j , σ_i is the occupation index of the site i by the TM ion, i.e., $\sigma_i = 1$ if site i is occupied by a TM atom while $\sigma_i = 0$ if site i is occupied by a host atom. The effective interaction is calculated as $V_{ij} = V_{AA} + V_{BB} - 2V_{AB}$ for a two component alloy AB, where V_{AA} , V_{BB} and V_{AB} are the potential energies for the sites ij occupied by AA, BB, and AB atoms, respectively. The effective pair interactions V_{ij} are evaluated for the medium obtained within the coherent potential approximation (CPA) by using the generalized perturbation method proposed by Ducastelle and Gautier, 1976 in the formulation of Turchi *et al.*, 1988.

The calculated effective pair interactions in $(\text{Ga},\text{Mn})\text{As}$ and $(\text{Zn},\text{Cr})\text{Te}$ have been plotted in Fig. 1 as a function of the pair distance. By definition of V_{ij} , a negative V_{ij} indicates effective attractive interactions between the same kind of atoms and repulsive interactions between different kind of atoms. As shown in Fig. 1, pair interactions between magnetic impurities are effectively attractive.

Once the pair interactions in the Ising model are obtained, one can perform the Monte Carlo simulation of the Ising model to obtain the distribution of TM cations in a given semiconductor host at non-zero temperature. The Kawasaki dynamics is used to relax the system (Landau and Binder, 2000). First, a large supercell [typically $14 \times 14 \times 14$ face-centered cubic (fcc) conventional cubic cell] is considered and the magnetic cations are randomly distributed in the cell. Then, one pick up one host-TM pair and their position is exchange. When the change in the energy due to the exchange is negative, this process is allowed. When the energy is positive, it is decided whether this process is allowed or not by using the Metropolis criterion. This Monte Carlo step is repeated many times until the system reaches the thermal equilibrium. In the present study, a non-equilibrium states, namely the system is quenched within a very short time interval which is not sufficient for the complete relaxation of the impurity distribution and then frozen. This situation is simulated by interrupting the iteration after a certain number of Monte Carlo steps (Sato *et al.*, 2005). This procedure assumes that V_{ij} is the only relevant energy scale and, in particular, that there are no kinetic barriers for cation exchange and diffusion over the lattice

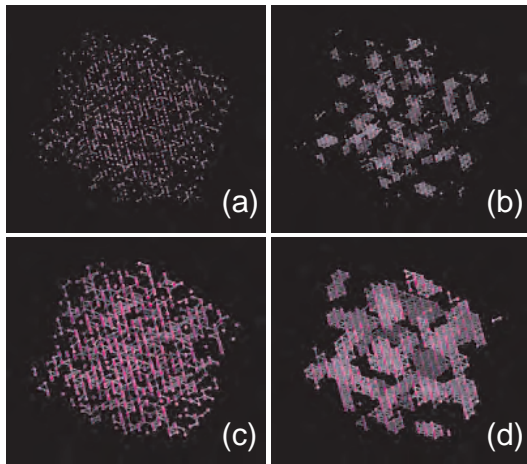


FIG. 5 (Color online) Mn configuration in (Ga,Mn)N. (a) and (c) refer to completely random configurations, (b) and (d) after 100 Monte Carlo steps (decomposed phase). Mn concentrations are 5% for (a) and (b), and 20% for (c) and (d). Nearest neighbor MnMn pairs are connected by bars. From Sato *et al.*, 2005.

sites. The role of such barriers is discussed in Secs. II.E and II.F.

1. Dairiseki phase

Figure 5 visualizes decomposition in (Ga,Mn)N, as revealed by Monte Carlo simulations. In the studied example, the average concentration of Mn in the simulation cell is 5% or 20 and 100 Monte Carlo steps per Mn site are performed at temperature $k_B T_b / V_{01} = 0.5$, where V_{01} is the chemical pair interaction energy between the nearest neighbors. Due to the chemical pair interactions, the Mn atoms attract each other, which results in the formation of clusters. In each cluster, the Mn atoms occupy nearest neighbor sites in order to decrease the energy as much as possible. As seen in Fig. 5(b), the Mn concentration in the cluster is almost 100% and the shape of the cluster is nearly spherical. If the Mn average concentration is low, and the clusters are separated. For higher concentrations, average size of clusters becomes larger and at 20% the clusters are connected and percolate through the cell [Fig. 5(d)]. Since the cross section of the decomposed system looks like a marble, the decomposed state of magnetically doped semiconductors was named the 'dairiseki phase' (Sato *et al.*, 2005), where 'dairiseki' means marble in Japanese.

As shown in the previous studies on ferromagnetism in DMSs with short range spin-spin interactions, at low concentrations T_C is suppressed (Sato *et al.*, 2010; Stefanowicz *et al.*, 2013). For example, below the percolation threshold (20% for the fcc structure (Stauffer and Aharony, 1994)) T_C is 0 for systems with interac-

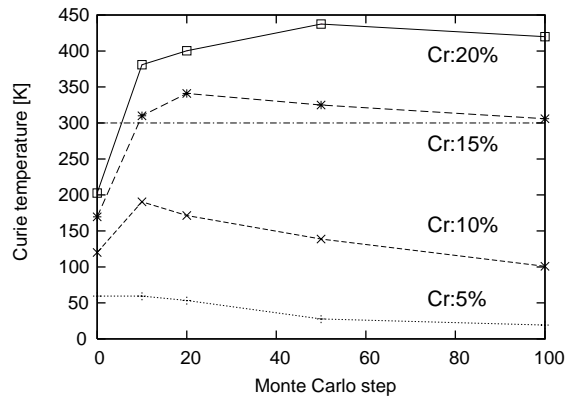


FIG. 6 Calculated Curie temperature of (Zn,Cr)Te as a function of Monte Carlo steps in the simulation of decomposition. Curie temperatures are calculated by using the random phase approximation. From Fukushima *et al.*, 2006a.

tions only between the nearest neighbors. As shown in Fig. 5(d), owing to decomposition there are many percolating paths already at 20% and the decomposition should affect considerably the magnetic properties of the system. In order to see effects of decomposition, T_C values were calculated as a function of the Monte Carlo steps (Fukushima *et al.*, 2006a). In order to include in the T_C calculations the distribution of magnetic impurities, the random phase approximation (RPA) proposed by Bouzerar *et al.*, 2005 and Hilbert and Nolting, 2004 was employed (Fukushima *et al.*, 2006a). It is known that this method correctly reproduces the magnetic percolation effects and predicts reasonable T_C magnitudes, close to the exact Monte Carlo values. Figure 6 shows the calculated T_C of (Zn,Cr)Te within the RPA as a function of MC steps.

As shown in Fig. 6, at low concentrations the decomposition works to lower T_C values. Due to decomposition many spatially isolated clusters are formed, as shown in Fig. 5(b). Since the exchange interactions between TM atoms are short range in this case, there is strong FM coupling between TM moments in the cluster, but FM correlations between clusters are weak. This is why T_C of the whole system is suppressed by decomposition. In the case of (Zn,Cr)Te after 100 MC steps, non-zero values of T_C is predicted, and the system is FM. However when the exchange interactions are more short range, the system becomes superparamagnetic after the decomposition. For higher concentrations, because of the increase of the number of the nearest neighbor pairs, T_C increases as the decomposition proceeds. The increase of T_C is observed already at 15%, which is below the percolation threshold, thus it is found that the decomposition lowers the magnetic percolation threshold effectively.

2. Konbu phase

In addition to growth temperature and TM concentration, one can control the dimensionality of the growth process. In the simulations presented in the previous subsection (Sec. II.C.1), the magnetic impurities can diffuse in any direction, therefore TM aggregation occurs in three dimensions. In actual experiments, molecular beam epitaxy (MBE) or metalorganic vapor phase epitaxy (MOVPE) are standard methods for crystal growth. On a surface with low coverage, the migration of atoms on the surface occurs relatively freely, but it is difficult to diffuse into the layers beneath, i.e., the diffusion is limited only to the uppermost layer. Thus under such crystal growth conditions, the dimensionality of the decomposition is automatically controlled. Since the decomposition occurs layer-by-layer and the exchange of atoms between layers is prohibited under this condition, one can expect anisotropic shape for the clusters formed by the decomposition. On the first layer, small clusters are formed due to the decomposition, then the impurity atoms deposited on the second layer gather around the nuclei in the first layer. This process is repeated for many times and finally clusters with elongated shape along the crystal growth direction are produced (Fukushima *et al.*, 2006b).

In Fig. 7 results of Monte Carlo simulations are shown for the layer-by-layer growth of (Zn,Cr)Te with the average Cr concentration of 5%. The growth direction is from the bottom to the top of the cube. As expected, the Cr cations form clusters with columnar shape. This state was named the 'konbu phase' (Fukushima *et al.*, 2006b), where 'konbu' means seaweed in Japanese. Apparently the size of the clusters is much larger than the clusters found in the dairiseki phase. In the konbu phase, the clusters are spatially well separated. The T_C value of each cluster is expected as high as the one of CrTe in a zinc-blende (zb) structure, presumably close to RT. The T_C magnitude of the konbu phase shown in Fig. 7(a) by using the RPA method is only 15 K. This low value is due to the absence of magnetic interactions between separated columnar structures. However, once the magnetic percolation paths are introduced between the structures, T_C should increase considerably. To visualize this effect, delta doping of Cr for the first and the last layers was assumed in the simulations [Fig. 7(b)], leading to T_C of 346 K (Fukushima *et al.*, 2006b). In reality, magnetization blocking phenomena brought about by magnetic anisotropy (see Sec.) and long-range dipole interactions between clusters' magnetizations and can lead to a large magnitude of apparent T_C .

D. Super-paramagnetic blocking phenomena

If we only focus on a thermodynamic quantity such as a T_C value, there is not much difference between the dairiseki phase and the konbu phase for low average TM concentrations. For both phases as a result of decom-

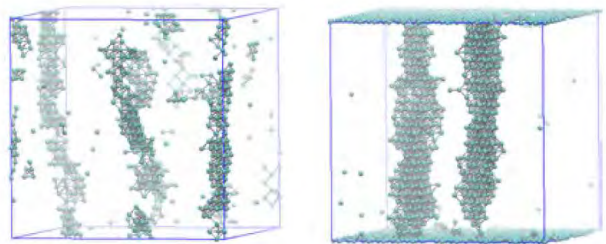


FIG. 7 (Color online) Monte Carlo simulations of phase separation in (Zn,Cr)Te under the layer-by-layer crystal growth condition (konbu phase). Average concentration of Cr is 5% for both (a) and (b), except for the first and the last layer in (b). In (b) delta-doping is simulated by depositing 80% of Cr on the first and the last layers. Cr positions in the crystal are indicated by small spheres and they are connected by bars if they occupy the nearest neighbor sites. Adapted from Fukushima *et al.*, 2006b.

position, T_C goes to 0 and the system becomes superparamagnetic, if the interactions are short range. On the other hand, if we look into the magnetization process, the dairiseki phase and the konbu phase behave very differently due to superparamagnetic blocking phenomena associated with shape anisotropy.

To reverse the magnetization direction of nanomagnets with in a single magnetic domain state, magnetic anisotropy energy should be overcome. For a system with uniaxial magnetic anisotropy, the magnetic anisotropy energy is $KV \sin^2 \theta$, where K , V and θ are anisotropy energy density, volume of the system, and angle between magnetization direction and magnetic easy axis, respectively. In general, shape and crystalline anisotropies contribute to the magnitude of K . The existence of the energy barrier between the easy directions results in a finite relaxation rate of the magnetization direction, $1/\tau \propto \exp(-KV/k_B T)$. Accordingly, for larger systems (but small enough to keep single domain nature), the relaxation time τ becomes longer and the magnetization direction is effectively fixed along the initial direction at low temperatures. This is the so-called superparamagnetic blocking phenomenon (Aharoni, 1996).

In the present cases of decomposed systems, the columnar structure contains high concentration of magnetic impurities. Due to the FM exchange interactions between magnetic impurities, the self-assembled structure with a high TM concentration behaves as a nanomagnet. The radius of the columnar structure is a few nanometers and within this length scale, we can expect that the structure contains a single magnetic domain.

As shown in the previous subsections (Secs. II.C.1 and II.C.2), it is possible to control the volume of the clusters formed by decomposition and, hence, sample magnetization via the superparamagnetic blocking phenomenon. In order to demonstrate this idea, the magnetization process was simulated by the Monte Carlo technique (Sato and Katayama-Yoshida, 2007) employing the method elabo-

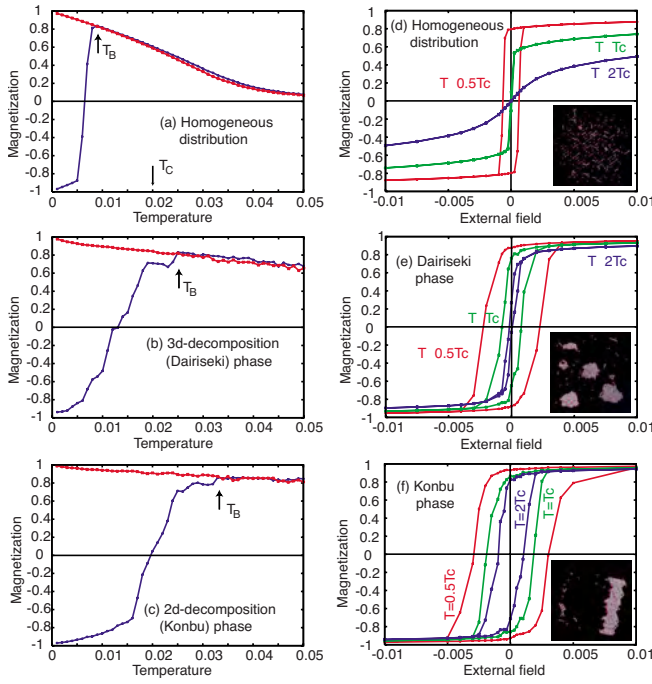


FIG. 8 (Color online) Superparamagnetic blocking phenomenon in (Ga,Mn)N according to Monte Carlo simulations. Left-hand panels: Magnetization as function of temperature starting from parallel or antiparallel configurations of initial magnetization to the external field. Right-hand panels: Magnetization as a function of external field. The simulations are performed for the uniform Mn distribution (a) and (d), the dairiseki phase (b) and (e), and the konbu phase (c) and (f). The insets in the lower panels show snapshots of the Mn distribution in (Ga,Mn)N for the respective phases. Temperature ($k_B T$) and the external magnetic field are scaled by the strength of the nearest-neighbor exchange energy J_{01} . From Sato *et al.*, 2007.

rated by Dimitrov and Wysin, 1996. In Fig. 8 the calculated temperature and field dependence of magnetization are shown taking the shape part of magnetic anisotropy into account. The simulations were performed for a uniform TM distribution, the dairiseki phase, and the konbu phase of (Ga,Mn)N. As shown in the magnetization curves, for the system with larger clusters, the cohesive field becomes greater and hysteresis loop opens wider, i.e., one obtains a harder magnet. Furthermore, magnetization as a function of temperature was calculate for increasing temperature starting from anti-parallel and parallel configurations of magnetization with respect to the external magnetic field. Above the blocking temperature T_b , the direction of the magnetization flips and the two lines coincide. It is clearly demonstrated in Figs.8(a)-(c) that T_b becomes higher for the dairiseki and the konbu phases.

Until now many experimental reports on the magnetism of TM-doped semiconductors have been published, but often they are not consistent, particularly for

wide band gap hosts. As shown in Sec.II.B, energies of chemical pair interactions between magnetic impurities are rather large, especially in wide bandgap DMSs, so that these systems have strong tendency towards decomposition. Since typically epitaxy is a non-equilibrium process, its outcome, particularly the degree of decomposition, depends sensitively on growth and processing conditions. As a result, the size, shape, and content of TM-rich NCs resulting from decomposition vary strongly from experiment to experiment. These considerations explain, at least partly, inconsistency in magnetic properties reported by various groups for the same material.

E. Mixing energy; nucleation and spinodal regions

In order to determine the temperature and TM concentration range corresponding to nanodecomposition, a lattice model, originally developed by Flory and Huggins for the polymer-mixing problem (Flory, 1942; Huggins, 1941; Rubinstein and Colby, 2003), was adapted for DMSs (Chan *et al.*, 2008; Hai *et al.*, 2011; Sato *et al.*, 2007). Within this approach, the free energy $F(x) = \Delta E(x) - TS(x)$ of a random alloy $A_{1-x}TM_xB$ is described by the mixing energy $\Delta E(x)$ and the entropy $S(x)$ per one cation of the form

$$\Delta E(x) = E(A_{1-x}TM_xB) - (1-x)E(AB) - xE(TMB); \quad (5)$$

$$S(x) = -k_B[x \ln x + (1-x) \ln(1-x)]. \quad (6)$$

If $\Delta E(x) > 0$, the alloy is unstable against decomposition into the end compounds (Swalin, 1970) but at $T > 0$ a tendency to randomization described by the entropy term becomes important. Figure 9 shows schematically the behavior of $F(x)$ for a convex function $\Delta E(x) > 0$ and $T > 0$. It is seen that for such a case $F(x)$ there are two points B_1 and B_2 at compositions x_1 and x_2 , between which $F(x) > F(x_1) + F(x_2)$. Hence, for $x_1 < x < x_2$ the thermal equilibrium state corresponds to the *binodal decomposition*, i.e., in the case of DMSs, to the nucleation of TM-rich NCs of content x_2 in the TM-poor matrix of the concentration x_1 . The region $x_1 < x < x_2$ corresponds to the miscibility gap at given temperature T .

Often, however, the alloy in some range between x_1 and x_2 is stable against *small* fluctuations $\pm \Delta x$ of local composition. Since changes in the local free energy density integrated over the volume encompassing many fluctuations is proportional to $(\Delta x)^2 \partial^2 F / \partial x^2$, the alloy can remain in a metastable state as long as $\partial^2 F / \partial x^2 > 0$, i.e., in the composition range, in which $F(x)$ is a concave function. In contrast, in the region between the points S_1 and S_2 in Fig.9, where $\partial^2 F / \partial x^2 < 0$, there is no thermodynamic barrier separating the homogenous and non-uniform alloy.

The resulting spontaneous up-hill diffusion process, called *spinodal decomposition*, leads to a system that is *structurally* homogenous but shows a modulation of the

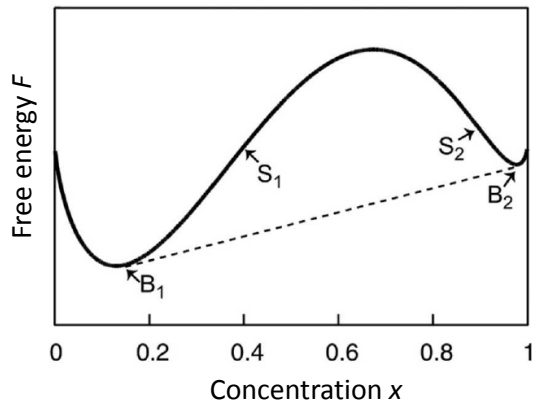


FIG. 9 Typical dependence of DMS free energy F on TM concentration x . Binodal decomposition can occur between points B_1 and B_2 , the ends of the common tangent segment of $F(x)$ (dashed line). Spinodal decomposition occurs between points S_1 and S_2 corresponding to $\partial^2 F/\partial x^2 = 0$. From Hai *et al.*, 2011.

TM concentration. This mechanism of chemical phase separation is suitable for fabricating a NC system with rather uniform NC size and inter-NC distance (Jones, 2002). An ordering in NC positions can be enhanced further on by strain, similarly to the case of self-assembling quantum dots in semiconductors (Stangl *et al.*, 2004). As discussed in Secs. III and VI, a periodic-like arrangement of TM-rich NCs has been found in Mn-doped GaAs and Mn-doped Ge, respectively.

The CPA approach (Sato *et al.*, 2007) and a cluster expansion method (Chan *et al.*, 2008) were employed to evaluate from first principles the energy $E(A_{1-x}TM_xB)$ and, thus, the mixing energy $\Delta E(x)$ of DMSs containing randomly distributed substitutional TM cations.

The CPA is particularly suitable for electronic structure calculations in the case of substitutional alloys (Akai, 1989; Akai and Dederichs, 1993; Shiba, 1971), such as DMSs. It is most efficiently combined with the Korringa-Kohn-Rostoker (KKR) method for the band structure calculation, particularly employing the MACHIKANEYAMA package (Sato *et al.*, 2010) developed by Akai (Akai, 2002). Within the CPA, a configuration average of the alloy electronic structure is calculated by using a mean-field like procedure. In a first step one considers a hypothetical atom that describes the averaged system. The crystal of hypothetical atoms constitutes an effective CPA medium. By using the multiple scattering theory the scattering path operator of the host and of the impurity atoms in the CPA medium is determined. The weighted average of these scattering path operators with respect to the concentration should be equal to the scattering path operator of the hypothetical atom itself. This is the self-consistent equation to be solved by an iterative method for determining the CPA medium, providing electronic density of states and the total energy E of the system. A more detailed expla-

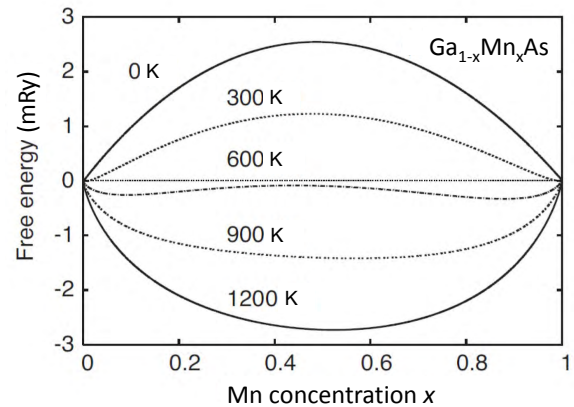


FIG. 10 Computed free energy $F(x)$ for $Ga_{1-x}Mn_xAs$ at various temperatures. As shown schematically in Fig. 9 this plot allows to determine composition ranges corresponding to binodal and spinodal decompositions at particular temperatures. From Sato *et al.*, 2007.

nation and practical formulation is provided by Gonis, 2000.

The CPA method was employed to evaluate $\Delta E(x)$ for $Zn_{1-x}Cr_xTe$, $Ga_{1-x}Mn_xAs$, $Ga_{1-x}Cr_xN$, and $Ga_{1-x}Mn_xN$ assuming zb structure and the experimental values of the lattice constants (Sato *et al.*, 2007). The convex form of $\Delta E(x)$ demonstrated that spinodal decomposition can appear in these systems. A similar conclusion was derived from cluster expansion studies of zb- $Ga_{1-x}Mn_xN$ (Chan *et al.*, 2008). Figure 10 shows, as an example, $F(x)$ for $Ga_{1-x}Mn_xAs$ at various temperatures (Sato *et al.*, 2007), which allows to determine the spinodal line, i.e., the position of S_1 and S_2 points as a function of temperature. Such a spinodal line is presented in Fig. 11 for in zb- $Ga_{1-x}Mn_xN$ (Chan *et al.*, 2008). It is seen that the upper critical solution temperature, above which the alloy is miscible for any x , is as high as 3000 K in this case. Hence, within the temperature range relevant for epitaxial growth and post-growth annealing, the DMSs in question can undergo spinodal decomposition.

According to Figs. 9–11, the range of compositions, at which alloy decomposition could appear, diminishes with increasing temperature. This is in qualitative *disagreement* with the long staying experimental observations which imply that *lowering* of epitaxy temperature is necessary for obtaining a uniform DMS (Munekata *et al.*, 1989), whereas annealing at *high* temperatures allows to generate phase separation (Boeck *et al.*, 1996). This apparent contradiction, i.e., the existence of lower critical solution temperature, points to the importance of *diffusion* (kinetic) barriers precluding aggregation of TM cations if growth or annealing temperature is too low even if there is no thermodynamic barrier for spinodal decomposition. To our knowledge, in the case of DMSs, only the barrier height for diffusion of interstitial Mn and Li ions in GaAs has so far been evaluated theoretically (Bergqvist *et al.*, 2010; Edmonds *et al.*, 2004). At

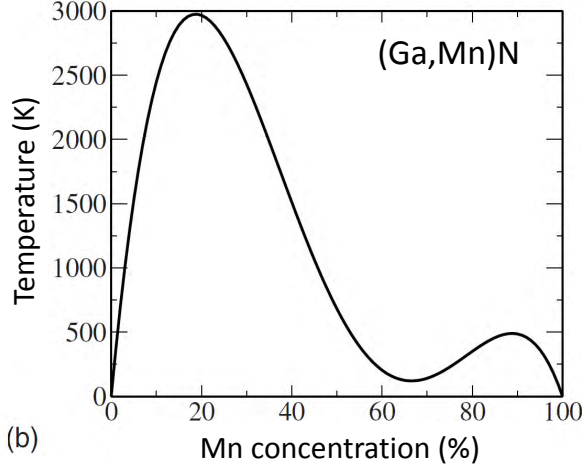


FIG. 11 Computed spinodal line for zinc-blende $\text{Ga}_{1-x}\text{Mn}_x\text{N}$. In the range of compositions x between the lines at given temperature T the alloy can undergo spinodal decomposition, so that at, e.g., 1000 K $\text{Ga}_{1-x}\text{Mn}_x\text{N}$ decomposes into compounds with $x = 0.03$ and 0.45 . From Chan *et al.*, 2008.

the same time, a phenomenological Cahn-Hilliard theory of spinodal decomposition, presented in Sec. II.F, was employed to describe properties of phase separation in DMSs (Hai *et al.*, 2011). The influence of growth and processing conditions on nanodecomposition is discussed from the experimental perspective in Secs. III–VIII.

Another important ingredient that has not been taken into account by the approaches leading to the results presented in Figs. 10 and 11 is the omission of interfacial energies. In particular, the comparison of free energies corresponding to the random alloy and the decomposed case has referred to the thermodynamic limit, i.e., energies of TM ions at interfaces between TM-rich and TM-poor phases have been disregarded. In general, energy lowering associated with the TM aggregation is smaller for interfacial ions comparing to the ions inside the cluster. This promotes the Oswald ripening, i.e., the formation of larger clusters at the expense of smaller ones. In extreme cases, small clusters, up to the so-call nucleation radius, are energetically unstable, which imposes a barrier for the nucleation process. Such a barrier can be lowered at crystal defects acting as nucleation centers or diffusion channels. According to the discussion of the pairing energies in Sec. II.B, even small clusters of TM cations are stable in a number of semiconductor compounds.

As already mentioned in Sec. II.B, according to *ab initio* studies, co-doping of DMSs by electrically active impurities or defects affects considerably the TM pairing energies. This conclusion is supported by studies of the mixing energy $\Delta E(x)$ of $(\text{Ga},\text{Mn})\text{As}$ (Bergqvist *et al.*, 2010; Sato and Katayama-Yoshida, 2007), $(\text{Ga},\text{Mn})\text{N}$, $(\text{Ga},\text{Mn})\text{Cr}$, and $(\text{Zn},\text{Cr})\text{Te}$ (Sato and Katayama-Yoshida, 2007) co-doped with donors. In particular, the mixing energies of $(\text{Ga},\text{Mn})\text{As}$ with interstitial impurities acting as donors, such as Li (Li_{int}) and Mg

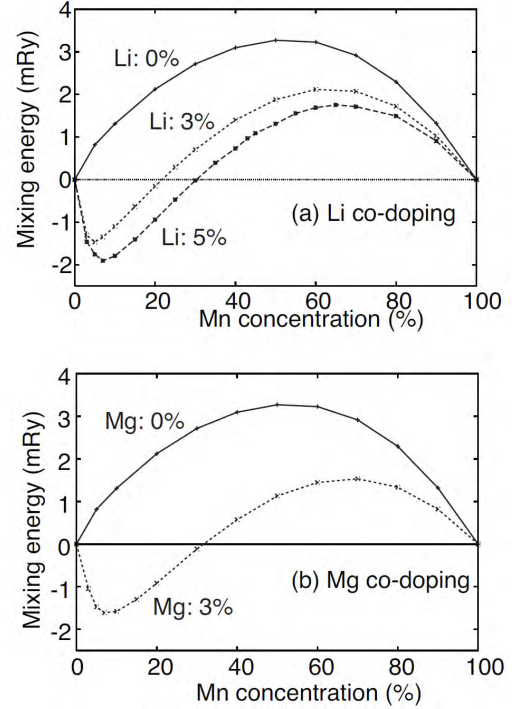


FIG. 12 Calculated mixing energy of $(\text{Ga},\text{Mn})\text{As}$ as a function of Mn concentration with (a) interstitial Li co-doping and (b) interstitial Mg co-doping. From Bergqvist *et al.*, 2010.

(Mg_{int}), were computed (Bergqvist *et al.*, 2010). As shown in Fig. 12, the effect of co-doping is dramatic and the mixing energy is significantly modified. Particularly at low concentrations of Mn, a negative and concave region is found in the calculated values of $\Delta E(x)$. This means that even at thermal equilibrium homogeneous doping of Mn is possible over a wide x range. Similar effects were also found for other combinations of the host semiconductors and different substitutional donor impurities (Sato and Katayama-Yoshida, 2007).

The advantage of interstitial impurities (particularly Li_{int}) over the substitutional ones is that interstitials can easily be removed by post-growth annealing. To check the effectiveness of this process, Monte Carlo simulations of diffusion of interstitial impurities in $(\text{Ga},\text{Mn})\text{As}$ were performed (Bergqvist *et al.*, 2010). The results imply that since the binding energy between Mn_{int} and Mn_{Ga} is much greater than in the case of Li_{int} , the low temperature annealing more effectively wipes away Li_{int} than Mn_{int} in $(\text{Ga},\text{Mn})\text{As}$.

F. Cahn-Hilliard theory of spinodal decomposition

One of the goal of decomposition theory is to describe spatial and temporal evolution of the local composition $x(\vec{r}, t)$ at a surface or in a volume of the alloy containing initially randomly distributed TM cations of the concentration \bar{x} . While it is rather difficult to determine $x(\vec{r}, t)$

in the nucleation regime, there exists a time-honored Cahn and Hilliard, 1958 theory of spinodal decomposition, discussed also in the context of phase separation in DMSs (Hai *et al.*, 2011). This approach exploits the Ginzburg-Landau theory of the continuous phase transitions, taking $u(\vec{r}, t) = x(\vec{r}, t) - \bar{x}$ as an order parameter. Furthermore, the interfacial effects are included to the lowest order in the gradient in the TM concentration $x(\vec{r})$. Under these assumptions the functional of the free energy assumes the form,

$$F_{\text{tot}}[u(\vec{r})] = N_0 \int d\vec{r} F[u(\vec{r})] + \frac{1}{2} \kappa |\nabla u(\vec{r})|^2. \quad (7)$$

where N_0 is the cation density and $F(x)$, in addition to the contributions given in Eqs. 5 and 6, can contain a term $ku^2(\vec{r}, t)/2$ describing an increase of the system energy associated with strain that builds in a decomposed system if the lattice constant depends on x . Along with the mixing energy $\Delta E(x)$, κ and k are parameters of the model, which in principle can be determined experimentally or by *ab initio* methods.

The distribution $u(\vec{r})$ under conditions of thermal equilibrium is provided by the variational minimization of $F_{\text{tot}}[u(\vec{r})]$, $\delta F_{\text{tot}}[u(\vec{r})]/\delta u(\vec{r}) = 0$ with the constrain, imposed by the mass conservation, that $u(\vec{r})$ integrated over the relevant crystal surface or volume vanishes. This procedure implies that (i) the decomposition occurs at temperatures below the critical temperature T_c , where $\partial^2 F(u, T)/\partial u^2|_0 < 0$; (ii) the compositions of TM-rich NCs and TM-poor matrix are determined from $\partial[F(u) - u(\partial F/\partial u)|_0]/\partial u = 0$ and (iii) the spatial width of the transition region between these two domains scales with $\kappa^{1/2}$.

However, from the experimental viewpoint particularly relevant is the evaluation of $u(\vec{r}, t)$ during the early stage of decomposition, i.e., far from thermal equilibrium. The starting point is the continuity equation,

$$\partial N_0 u(\vec{r}, t)/\partial t = -\nabla \cdot \vec{j}(\vec{r}, t), \quad (8)$$

where the current of TM cations $\vec{j}(\vec{r}, t)$ is driven by the gradient in the chemical potentials μ ,

$$\vec{j}(\vec{r}, t) = M \nabla \mu(\vec{r}, t). \quad (9)$$

Here, M is the TM mobility, one more material parameter. Since the chemical potential corresponds to a change of the free energy by adding or removing one atom, its local non-equilibrium value is given by a variational derivative,

$$\mu(\vec{r}, t) = -\delta F_{\text{tot}}[u(\vec{r}, t)]/\delta u(\vec{r}, t), \quad (10)$$

with the constrain $\int d\vec{r} u(\vec{r}, t) = 0$. This variational derivative and, thus, the chemical potential is not zero as $u(\vec{r}, t)$ does not yet correspond to the thermal equilibrium distribution. Inserting Eq. 10 into Eq. 9 and then Eq. 9 into 8, one obtains the Cahn-Hilliard equation in

the form

$$\partial u(\vec{r}, t)/\partial t = M \nabla^2 \partial [F(u) - u(\partial F(u)/\partial u)|_0]/\partial u - \kappa \nabla^2 u. \quad (11)$$

There is a comprehensive literature devoted to mathematical aspects of this differential equation [see, e.g., Novick-Cohen, 2008]. It is convenient to write its solution $u(\vec{r}, t)$ as a Fourier transform of a function $A(\vec{q}, t)$. If only the two lowest order terms are retained in the Taylor expansion of $F(u)$, a justified approximation at the early stage of decomposition, then

$$A(\vec{q}, t) = A_0(\vec{q}) \exp[R(\vec{q})t], \quad (12)$$

where the aggregation rate

$$R(q) = -M[\partial^2 F(u)/\partial u^2|_0 + \kappa q^2]q^2. \quad (13)$$

This formula shows that R is positive, at least for sufficiently small q values, in the spinodal decomposition range, $\partial^2 F(u)/\partial u^2|_0 < 0$. In such a case, R is governed by the cation mobility M which, because of diffusion barriers, decreases strongly on lowering temperature. This explains why low-temperature epitaxy can result in a metastable state corresponding to a DMS with a uniform distribution of magnetic ions. However, growth or annealing at appropriately high temperatures, or the presence of lattice defects, can enhance M and promote TM aggregation.

Because of the interfacial energy, on approaching thermal equilibrium conditions, the size of TM-rich NCs should increase whereas their concentration decrease. However, the formation of a periodic structure by spinodal decomposition at early times may render the Oswald ripening a prohibitively slow process, particularly in DMSs with $\bar{x} \ll 1/2$. In contrast, both NCs and the surrounding matrix can attain uniform TM concentrations, x_2 and x_1 , respectively, corresponding to the binodal points, B_2 and B_1 in Fig. 9 or even a transformation of TM-rich NCs to another crystallographic phase can take place. In either case, by determining q_c that maximizes $R(q)$ one can evaluate the expected distance $\lambda_c = 2\pi/q_c$ between TM-rich NCs,

$$\lambda_c = 4\pi[\kappa/|2\partial^2 F(u)/\partial u^2|_0|]^{1/2}, \quad (14)$$

where κ , representing the interfacial energy, is of the order of $|E_d|a^2$ and a is the lattice parameter. Since the magnitudes of pairing energy E_d and $\partial^2 F(u)/\partial u^2|_0$ are similar (cf. Figs. 1 and 10), the distance between TM-rich NCs is expected to set at about 10 lattice constants, the value in reasonable agreement with experimental results collected in Secs. III–VIII. Simple geometrical considerations provide an average radius of NCs at given \bar{x} , x_1 and x_2 , and λ_c .

Another interesting aspect is the dependence of $R(\vec{q})$ on the crystallographic direction of \vec{q} brought about by the elastic term $\frac{1}{2}ku^2$ in $F(u)$ (Hai *et al.*, 2011). According to theory developed for cubic crystals (Cahn, 1962), if elastic moduli fulfil the relation $2C_{44} - C_{11} + C_{12} > 0$,

the spinodal decomposition is predicted to proceed along $\langle 100 \rangle$ cubic directions. This inequality is obeyed in zb compounds of interest, GaAs, Ge, and ZnTe. Similarly to the case of self-assembling semiconductor quantum dots obtained in the Stranski-Krastanov heteroepitaxy regime (Stangl *et al.*, 2004), strain minimization can govern the NC arrangement.

Typically, the TM concentration of the host containing TM-rich NCs is non-zero, $x_1 > 0$. Accordingly, the magnetic response of decomposed alloy shows characteristics of the uniform DMS with TM content x_1 superimposed on magnetism of a system of NCs with the TM concentration x_2 . Since the crystallographic and chemical structure of the NCs is usually imposed by the host, magnetic properties of the individual NCs may not be listed in the existing materials compendia. Furthermore, magnetism of the NC ensemble is strongly affected by their distribution and coupling, either dipole-dipole type or mediated by strain and/or spins in the host.

III. SPINODAL NANODECOMPOSITION IN (Ga,Mn)As

It is well known that (Ga,Mn)As containing uniformly distributed magnetic atoms has become a model system for the entire class of dilute FM semiconductors (Dietl and Ohno, 2014; Jungwirth *et al.*, 2014; Tanaka *et al.*, 2014). Similarly, the decomposed (Ga,Mn)As system, consisting of MnAs or Mn-rich (Mn,Ga)As NCs embedded in Mn-poor (Ga,Mn)As, since its first fabrication (Boeck *et al.*, 1996; Shi *et al.*, 1996), has revealed properties relevant to the whole family of high T_C semiconductors. For instance, both crystallographic (Boeck *et al.*, 1996) and chemical (Moreno *et al.*, 2002) phase separations were put into the evidence, depending on fabrication and processing conditions. Furthermore, despite a small diameter down to 2 nm, the ensemble of zb Mn-rich NCs shows FM-like features persisting up to 360 K (Moreno *et al.*, 2002), to be compared to T_C of 318 K specific to free standing samples of MnAs that crystallizes in a hexagonal NiAs-type structure. Enhanced magneto-optical response was found in decomposed films of (Ga,Mn)As (Akinaga *et al.*, 2000a; Shimizu *et al.*, 2000).

A. Fabrication methods and nanocomposite structure

Various methods were found to provide decomposed (Ga,Mn)As. It can be obtained by MOVPE (Krug von Nidda *et al.*, 2006; Lampalzer *et al.*, 2004) or MBE at sufficiently high substrate temperatures (Hai *et al.*, 2011) or by post-growth annealing of either GaAs implanted with Mn (Ando *et al.*, 1998; Chen *et al.*, 2000; Shi *et al.*, 1996; Wellmann *et al.*, 1997) or fabricated by low-temperature (LT) MBE (Boeck *et al.*, 1996; DiPietro *et al.*, 2010; Kwiatkowski *et al.*, 2007; Moreno *et al.*, 2002; Rench *et al.*, 2011; Sadowski *et al.*, 2011; Shimizu *et al.*, 2001;

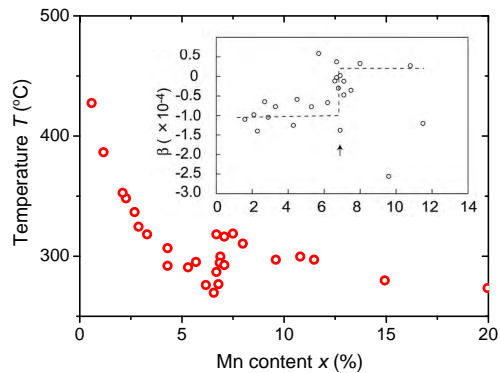


FIG. 13 (Color online) Phase decomposition diagram of (Ga,Mn)As alloy. Open circles are experimental values of temperature T_B at which RHEED stripes, witnessing 2D growth, change into dots. Inset shows the behavior of the in-plane lattice parameter. Adapted from Hai *et al.*, 2011.

Yokoyama *et al.*, 2005).

At the growth temperature specific to MOVPE, 500–600°C, one observes assembling of hexagonal MnAs NCs and their segregation towards the layer surface (Krug von Nidda *et al.*, 2006). They have typically elongated shape in the growth direction and their length reaches 100 nm.

According to the MBE growth diagram of $\text{Ga}_{1-x}\text{Mn}_x\text{As}$ (Dietl and Ohno, 2014; Hayashi *et al.*, 1997; Matsukura *et al.*, 2002; Ohno *et al.*, 1996), at temperatures above 350°C at $x = 1\%$ and above 200°C at $x = 10\%$ an onset of TM aggregation is observed. Growth temperatures below 200°C are required for maintaining 2D growth of (Ga,Mn)As incorporating more than 10% of uniformly distributed Mn cations (Chiba *et al.*, 2007; Mack *et al.*, 2008; Ohya *et al.*, 2007; Wang *et al.*, 2008). Results of detailed investigation by reflection high-energy electron diffraction (RHEED) of temperature $T_B(x)$ at which 2D growth disappears entirely, i.e., RHEED stripes transform into dots, are shown in Fig.13 (Hai *et al.*, 2011). As seen, $T_B(x)$ decreases monotonously with x reaching 270°C for $x = 6.7\%$ at which T_B abruptly rises to 320°C, the effect accompanied by a step-like increase in the in-plane lattice constant. For $x > 6.7\%$ a gradual decrease of T_B continues down to about 300°C at $x = 0.15\%$. This behavior, may indicate that zb-MnAs or Mn-rich (Mn,Ga)As NCs prevail for $x < 6.7\%$, whereas at higher x hexagonal MnAs NCs nucleate at $T \geq T_B$ on the growth surface.

High annealing temperatures, typically 500–700°C, are required to promote (Ga,Mn)As decomposition in films grown by low-temperature MBE (Boeck *et al.*, 1996; DiPietro *et al.*, 2010; Kwiatkowski *et al.*, 2007; Moreno *et al.*, 2002; Rench *et al.*, 2011; Sadowski *et al.*, 2011; Shimizu *et al.*, 2001; Yokoyama *et al.*, 2005), although at onset of Mn aggregation was already noted in films annealed at 400°C (Sadowski *et al.*, 2011). Similar or higher temperatures were employed to fabricate decomposed

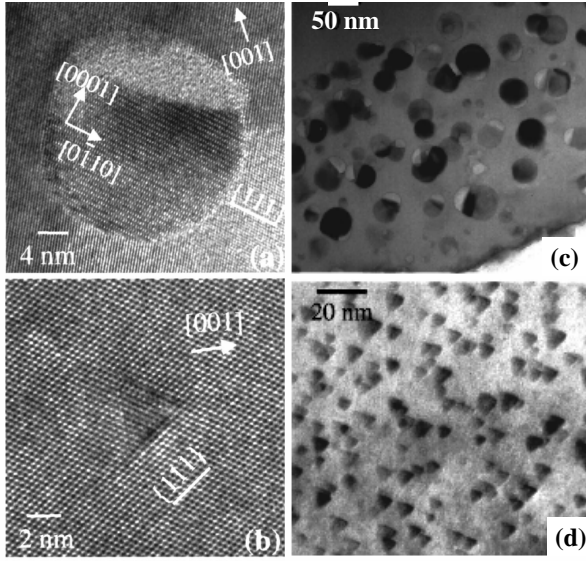


FIG. 14 Evidence for crystallographic and chemical phase separation in (Ga,Mn)As. High-resolution TEM (a,b) and cross-sectional bright-field TEM (c,d) images of Mn(Ga)As clusters embedded in a Ga(Mn)As matrix for: (a,c) sample I, which was subjected to rapid thermal annealing at 700°C and (b,d) sample II, which was annealed *in situ* at 600°C under MBE conditions. The formation of hexagonal MnAs NCs in sample I is the crystallographic phase separation, whereas the zb NCs are the evidence for the chemical separation. From Moreno *et al.*, 2002.

(Ga,Mn)As out of Mn-implanted GaAs (Ando *et al.*, 1998; Chen *et al.*, 2000; Shi *et al.*, 1996; Wellmann *et al.*, 1997). These temperatures, significantly surpassing T_B of Fig. 13, collaborate the fact that aggregation of Mn cations is kinetic-limited (see, Sec. II.F), as at given temperature atom diffusion is slower in the bulk than on the growth surface.

Depending on the magnitudes of the initial Mn concentration and annealing temperature, either hexagonal MnAs NCs with an NiAs structure and diameter ranging from 5 nm to 500 nm precipitate usually with no dislocations and with orientation $\text{MnAs}(0001) \parallel \text{GaAs}(111)B$ (crystallographic phase separation) (Ando *et al.*, 1998; Boeck *et al.*, 1996; Chen *et al.*, 2000; Krug von Nidda *et al.*, 2006; Moreno *et al.*, 2002; Rench *et al.*, 2011; Shi *et al.*, 1996; Wellmann *et al.*, 1997; Yokoyama *et al.*, 2005) or zb Mn-rich (Ga,Mn)As NCs aggregate (chemical phase separation) (Kwiatkowski *et al.*, 2007; Moreno *et al.*, 2002; Yokoyama *et al.*, 2005), according to high-resolution transmission electron microscopy (HRTEM), as shown in Fig. 14. A comprehensive x-ray diffraction (XRD) (Moreno *et al.*, 2003, 2005) and extended x-ray absorption fine structure (EXAFS) studies (Demchenko *et al.*, 2007) of hexagonal MnAs buried in the GaAs lattice provided detailed information on the magnitude of strain in reference to free-standing MnAs. The zb NCs can assume either tetrahedral (Moreno *et al.*, 2002) or spherical form (Kwiatkowski *et al.*, 2007; Sadowski

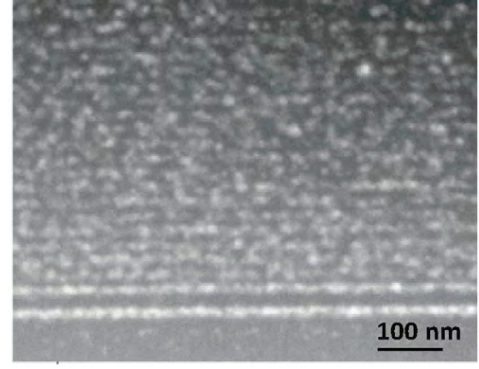


FIG. 15 Cross-sectional STEM image of the region close to the GaAs(001) substrate of a GaAs/(Ga,Mn)As superlattice with Mn content of 3.7% annealed at 560°C. Adapted from Sadowski *et al.*, 2013.

et al., 2011; Yokoyama *et al.*, 2005) with diameter typically from 2 to 6 nm; they are not stable against a transformation to the hexagonal phase for diameters exceeding 15 nm (Sadowski *et al.*, 2011). Hexagonal and cubic zb NCs coexist in annealed (Ga,Mn)As with Mn content of 2% and smaller (Sadowski *et al.*, 2011). It appears that main features of decomposed (Ga,Mn)As and (Ga,Mn)As:Be (Rench *et al.*, 2011) are similar.

The exact relative concentrations of Mn and Ga in the cubic NCs is barely known and may depend on details of the fabrication protocols; the Mn concentration as low as 20% was suggested (Lawniczak-Jablonska *et al.*, 2011). Under some processing conditions the obtained nanoparticles were found to be structurally disordered (Kwiatkowski *et al.*, 2007; Moreno *et al.*, 2002). In certain cases, presumably if growth of (Ga,Mn)As results in a substantial concentration of As antisites, hexagonal MnAs NCs obtained by annealing are accompanied by As precipitation and voids (Kovács *et al.*, 2011).

From application viewpoint particularly relevant is the preparation of magnetically active NCs that reside in a pre-define plane. This can be achieved by growing appropriately thin (Ga,Mn)As layers, in which Mn-rich NCs gather after annealing below 600°C (Sadowski *et al.*, 2013; Shimizu *et al.*, 2001), as shown in Fig. 15.

Furthermore, according to results presented in Fig. 16, rectangular-like distribution of MnAs NCs with a narrow dispersion of diameters was obtained by using the phase decomposition diagram of the (Ga,Mn)As alloy and spinodal decomposition induced by annealing.

More recently, the influence of laser irradiation on the self-assembly of MnAs NCs was investigated (Hai *et al.*, 2012). It was found that laser irradiation suppresses the temperature-induced transformation of small zb NCs into larger hexagonal MnAs NCs, and that the median diameter D_1 in the size distribution of small NCs depends on the incident photon energy $\hbar\omega$ following $D_1 \sim \omega^{-1/5}$. This behavior was explained by the desorption of Mn atoms from small NCs due to energy gain from optical transitions between their quantized energy levels.

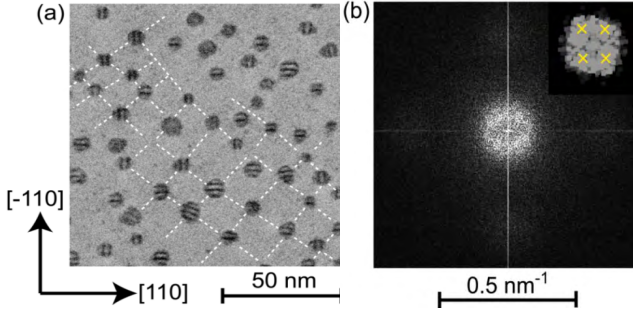


FIG. 16 (Color online) Periodic arrangement of MnAs NCs in GaAs. (a) Plain-view TEM image of hexagonal MnAs NCs fabricated using spinodal decomposition of a 5 nm-thick $\text{Ga}_{0.8}\text{Mn}_{0.2}\text{As}$ layer. (b) Fourier transform of the contrast of a $0.36 \times 0.36 \mu\text{m}^2$ TEM image. A ring structure with a radius of 0.063 nm^{-1} corresponding to a period of 16 nm is observed. The inset shows the pattern of the ring structure after applying a step-like high pass filter, revealing four fold symmetry, that is, rectangular lattice structure. Adapted from Hai *et al.*, 2011.

B. Magnetic properties

Figures 17(a,b) show magnetization loops at various temperatures for (Ga,Mn)As samples with hexagonal and cubic NCs, whose micrographs have been displayed in Figs. 14(a,b), respectively. As seen in 17(a), square hystereses pointing to the T_C value specific to bulk MnAs, $T_C \simeq 318 \text{ K}$ are observed for the film with hexagonal NCs (Moreno *et al.*, 2002), the finding reported also by others (Ando *et al.*, 1998; Rench *et al.*, 2011; Wellmann *et al.*, 1997; Yokoyama *et al.*, 2005). The data indicate that superparamagnetic blocking temperature T_b exceeds T_C , the conclusion consistent with an expected magnitude of the NC anisotropy energy, $E_a = VK$, for the large NCs in question.

In contrast, the behavior of magnetization in the case of the sample with cubic NCs [Fig. 17(b)] is intriguing and reveals surprising but generic aspects of decomposed magnetically doped systems:

- Despite a rather small size of zb NCs, even at high temperatures magnetization loops are opened and weakly temperature dependent. This indicates that $M(H, T)$ cannot be modeled by the Langevin function describing superparamagnetic systems above T_b , the conclusion emerging also from other studies of decomposed (Ga,Mn)As (Sadowski *et al.*, 2011; Yokoyama *et al.*, 2005). Given the NC volume V , this FM-like behavior points to a rather large magnitude of K or to a significant role played by spin-dependent interactions between the NCs (Hai *et al.*, 2007). For specific spatial distributions and densities of FM nanoparticles, long-range dipole interactions and/or exchange coupling lead to the so-called superferromagnetic phase (Bolcal *et al.*, 2012; Mørup *et al.*, 2010; Panov, 2012), whose char-

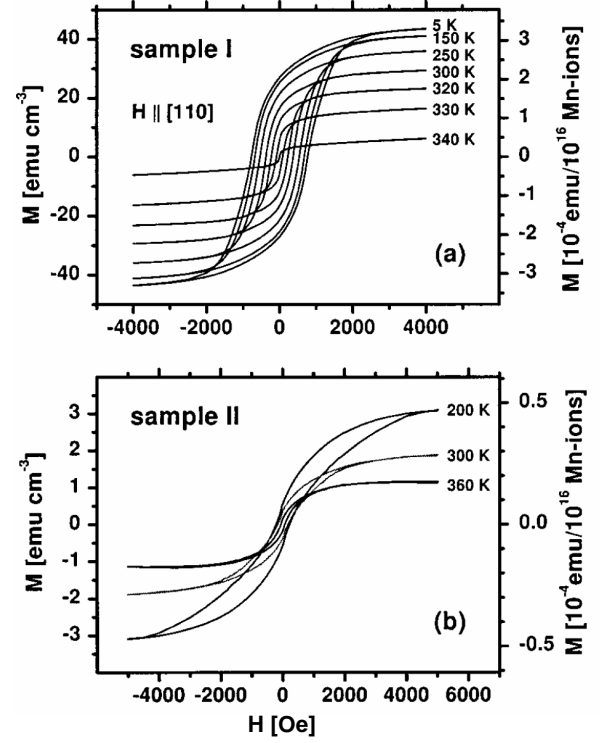


FIG. 17 Magnetization loops at various temperatures of annealed (Ga,Mn)As containing hexagonal (a) and zinc-blende (b) NCs, visualized in Fig. 14. From Moreno *et al.*, 2002.

acteristics are consistent with the data displayed in Fig. 17(b). In particular, a smaller magnitude of low temperature magnetization, as compared to the value expected from spin counting, is consistent with the superferromagnetic scenario.

- This set of data points to $T_C \gtrsim 360 \text{ K}$, for zb Mn-rich (Mn,Ga)As stabilized by the GaAs host (Moreno *et al.*, 2002; Sadowski *et al.*, 2011; Yokoyama *et al.*, 2005), the value substantially higher than $T_C \simeq 318 \text{ K}$ of free standing MnAs that crystallizes in the hexagonal structure. This T_C enhancement can be assigned to higher crystal symmetry, which typically leads to greater density of states at the Fermi level and, hence, to elevated T_C .
- While decomposed films discussed above show superferromagnetic features, in some other samples, containing similar NCs according to TEM studies, a standard superparamagnetic behavior was found (DiPietro *et al.*, 2010; Rench *et al.*, 2011; Sadowski *et al.*, 2011). Differing properties of nominally similar samples imply that magnetic characteristics of decomposed systems are rather sensitive to pertinent details of the system fabrication and the resulting morphology, including:

- the chemical structure and composition of

the individual NCs (i.e., TM concentration), which determine the electronic structure (e.g., the itinerant vs. localized character of d electrons) and, thus, magnetic characteristics such as the magnitude of T_C , magnetic moment, and energy of bulk and interfacial magnetic anisotropy

- the spatial distribution and density of the NCs' ensemble, which underlines the magnetic ground state originating from long-range dipole interactions
- the nature of host-mediated spin coupling among the NCs, which can depend on strain and interface between NCs and the host as well as on the TM, carrier, and defect concentrations in the host.

- Si co-doping enhances the formation of bigger MnAs nanoclusters (Shimizu and Tanaka, 2002b).

In the case of superparamagnetic samples, the temperature dependence of zero-field cooled magnetization demonstrates that the distribution of NCs' size is log-normal (DiPietro *et al.*, 2010; Rench *et al.*, 2011). At the same time, characteristics of magnetization relaxation are consistent with the superparamagnetic scenario and allow excluding spin-glass freezing as an origin of the magnetization maximum as a function of temperature (Sadowski *et al.*, 2011).

In general, magnetic response of decomposed (Ga,Mn)As contains contributions from both NCs with a high Mn concentration and (Ga,Mn)As with lower Mn content. In the cases discussed above, the NCs dominate magnetic response in the entire temperature range. However, for (Ga,Mn)As grown by MBE under conditions corresponding to the onset of phase separation, FM response of the (Ga,Mn)As host can prevail at low temperatures. Here, the NCs lead to pinning of domain walls and to enlargement of the coercive force (Wang *et al.*, 2006). Only at high temperatures, above T_C of the host, magnetization is dominated by the NCs (Wang *et al.*, 2006). Similar situation takes place in magnetic resonance studies: FM resonance of MnAs NCs dominates at high temperature, whereas a signal of dilute Mn ions takes over at low temperatures (Krug von Nidda *et al.*, 2006).

C. Magneto-optical phenomena

One of the attractive aspects of decomposed semiconductor alloys is that they show FM characteristics to above RT and at the same time they can be easily integrated with existing semiconductor devices. For instance, one can envisage magneto-optical insulators and modulators that would exploit a large magnitude of the Kerr effect characterizing FM metals and weak optical losses specific to semiconductors. Indeed, the giant Faraday effect and magnetic circular dichroism was found in

GaAs with hexagonal metallic MnAs NCs at RT (Akinaga *et al.*, 2000a). The Faraday rotation angle of the GaAs:MnAs layer reached about $0.2^\circ/\mu\text{m}$ at $0.98\ \mu\text{m}$.

Optical reflectivity of GaAs with hexagonal MnAs and zb-(Mn,Ga)As NCs is similar to that of the host GaAs matrix (Yokoyama *et al.*, 2005). However, magneto-optical spectra and intensities are different in these two kinds of decomposed (Ga,Mn)As; the intensity is weaker in the case zb NCs.

While the magnitude of the Verdet constant (i.e., the normalized Faraday rotation) is attractive and comparable or larger than the one characterizing magnetic materials employed in commercial optical insulators, it is hard to obtain a GaAs:MnAs layer thick enough to insure the required angle of polarization rotation, 45° . However, it is possible to enhance the rotation angle by extending the effective optical path length through a magnetic layer by using multiple reflections. By inserting a 140-nm thick GaAs:MnAs film in-between distributed Bragg reflectors (DBR) of GaAs/AlAs, the Faraday rotation angle was enhanced sevenfold at a wavelength of 970 nm at RT (Shimizu *et al.*, 2001). The MCD signal at RT as a function of the magnetic field showed saturation at about 1 kOe, the dependence corresponding to magnetization of GaAs:MnAs system. Furthermore, a similar structure showed the Kerr rotation of 1.54° at the designed wavelength of 980 nm under a relatively low magnetic field at RT (Ueda *et al.*, 2003). Theoretical modeling of optical and magneto-optical properties of these magneto-photon structures properly describes the experimental data.

As a further step, in order to reduce transmission losses associated with large MnAs NCs, the central GaAs:MnAs layer was replaced by a superlattice (SL) consisting of 2.8 nm thick AlAs and 5 nm thick GaAs:MnAs formed by annealing of (Ga,Mn)As with Mn content of $x = 0.047$ (Shimizu and Tanaka, 2001). In this way, the transmission coefficient at a local maximum at 990 nm was 30%, greatly improved from 2% in the previous multilayer without a SL. However, in this case, the enhancement in the Faraday rotation per unit magnetic layer thickness, compared to the GaAs:MnAs/AlAs SL structure without DBR, is only 3.3, presumably because of lower structural quality.

Another interesting structure, presented in Fig. 18, was optimized for the photon wavelength of $1.55\ \mu\text{m}$ (Shimizu and Tanaka, 2002b). Here, the central 230 nm thick layer consisted of GaAs:MnAs decomposed film co-doped with Si donors in order to reduce optical absorption associated with holes delivered by residual Mn ions in the GaAs host. The figure of merit (FOM), which is defined by the ratio of Faraday ellipticity (shown in Fig.18) to optical losses, is $0.074^\circ/\text{dB}$ at the wavelength of $1.54\ \mu\text{m}$, which is twice as large as the FOM of $0.037^\circ/\text{dB}$ at $0.98\ \mu\text{m}$ obtained in the studies (Shimizu *et al.*, 2001) referred to above.

At the same time, properties of *waveguide*-type optical insulators based on higher losses of backward propagat-

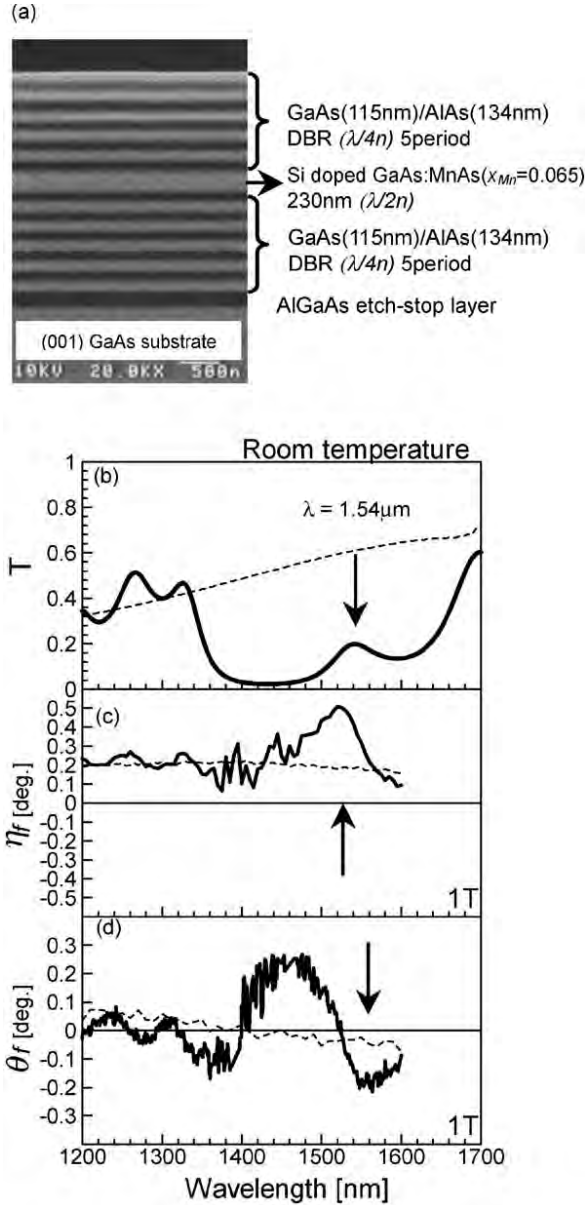


FIG. 18 An optimized structure with MnAs NCs for optical isolation. (a) A cross-sectional micrograph taken by scanning electron microscope of a Si-doped GaAs:MnAs layer placed between DBRs whose operational wavelength was set at $1.55 \mu\text{m}$. Solid lines in (a,b,c) show respectively optical transmission T ; Faraday ellipticity η_f (transmission MCD) and Faraday rotation θ_f at room temperature in the magnetic field of 1 T perpendicular to the plane of the sample shown in (a). Spectra of a Si-doped GaAs:MnAs single layer (200 nm) having the same Mn and Si concentration are also plotted as references (dotted lines). From Shimizu and Tanaka, 2002b.

ing light due to a nonreciprocal change of the refractive index were theoretically analyzed for an (In,Al)As waveguide with embedded MnAs nanoclusters (Shimizu and Tanaka, 2002a). Since also in this case the proposed optical isolator structure is composed of all semiconductor-based materials, it can be integrated with IIIV based

optoelectronic devices such as edge-emitting laser diodes. The device was assumed to be grown on an InP substrate and the operation wavelength was $1.55 \mu\text{m}$. Two designs were considered corresponding to the propagation of TM and TE modes, for which 119 dB/cm and 36 dB/cm of isolation were predicted, respectively.

D. Magnetoresistance

1. Films

Transport phenomena in granular metals exhibit a number of outstanding properties (Beloborodov *et al.*, 2007) that can be enriched by spin phenomena in decomposed magnetically doped semiconductors (Binns *et al.*, 2005; Michel *et al.*, 2008).

Magnetoresistance (MR) properties of GaAs/MnAs granular hybrid structures consisting of FM MnAs clusters within a paramagnetic GaAs:Mn host differ considerably from those of paramagnetic and FM (Ga,Mn)As alloys. According to experimental studies of decomposed samples obtained by various methods, giant positive MR dominates at high temperatures (typically above ~ 30 K) whereas negative MR takes over at low temperatures (Akinaga *et al.*, 2000b; Michel *et al.*, 2005; Wellmann *et al.*, 1998; Ye *et al.*, 2003). Large positive MR was also observed at RT in the impact ionization regime (Yokoyama *et al.*, 2006).

The positive MR effect is similar to the giant MR found in other metal-semiconductor hybrid systems (Akinaga *et al.*, 2000b; Solin *et al.*, 2000; Sun *et al.*, 2004). One of relevant mechanisms could be an admixture to the longitudinal voltage of the field-dependent Hall voltage, possibly enhanced by the AHE, a well known phenomenon in other heterogeneous systems (Solin *et al.*, 2000). A strong decrease of the positive MR for the in-plane magnetic field (Ye *et al.*, 2003) supports this scenario.

Two quantum mechanisms, considered widely in the case of homogeneous DMSs (Dietl, 2008b), can contribute to negative MR: (i) an orbital effect originating from the influence of the magnetic field upon interferences of self-crossing trajectories in either diffusing or hopping regime; (ii) a spin effect brought about by a destructive effect of the magnetic field upon spin-disorder scattering that controls interference of carrier-carrier interaction amplitudes in disordered systems. At the same time, giant MR (GMR) or tunneling MR (TMR) effects associated with the field-induced ordering of NCs' magnetic moments or spin-splitting of host's bands produced by stray fields can contribute to the magnitude of MR (Michel *et al.*, 2005). Furthermore, independently of the dominating MR mechanism, the spatial distribution of magnetic NCs is a factor affecting substantially the magnitude of MR and allowing its control (Michel *et al.*, 2008).

2. Spin-valve structures

The decomposed (Ga,Mn)As layers containing MnAs NCs with diameter of 10 nm were also formed in the fully epitaxial magnetic tunnel junctions (MTJs), GaAs:MnAs/Al(Ga)As/MnAs, in which a 20 nm MnAs layer constituted the second FM electrode and the barrier was either of AlAs (Hai *et al.*, 2006) or of GaAs (Hai *et al.*, 2008). The magnitude of tunneling magnetoresistance (TMR) was examined as a function of temperature and the barrier thickness d attending, at 7 K, 17% for $d_{\text{AlAs}} = 2.9$ nm (Hai *et al.*, 2006) and 8% for $d_{\text{GaAs}} = 10$ nm (Hai *et al.*, 2008). The observed oscillatory behavior of the TMR ratio with the increasing AlAs barrier thickness was explained by quantum interference of two X-valley related wave functions in the AlAs barrier. The ensemble of the results demonstrates that GaAs:MnAs layers can act as an efficient spin injector and a spin detector at low temperatures.

Figure 19(a,b) presents micrographs of a lateral nanodevice patterned of a MnAs/GaAs/GaAs:MnAs MTJ, which allowed to study TMR in the limit of tunneling across a *single* MnAs NC (Hai *et al.*, 2010). Sizable oscillations in differential conductance $dI_{\text{ds}}/dV_{\text{ds}}$ demonstrated that the Coulomb blockade regime was achieved at 2 K. As shown in Fig. 19(c), clear oscillations were also detected in TMR, defined as a relative difference in the resistance values without an external magnetic field (antiparallel arrangement of magnetization in the MnAs contacts) and in the magnetic field of 1 T (parallel magnetizations across the device). Modeling of the TMR results by the theory of Barnaś and Fert, 1998 led to the spin relaxation time τ_s of carriers in MnAs NCs as long as $10 \mu\text{s}$. The enhancement of τ_s was assigned to dimensional quantization of electronic states specific to nanoparticles (Hai *et al.*, 2010).

On the other hand, the magnetizing process of zb-MnAs NCs incorporated into tunnel junctions was found to generate a voltage and a huge magnetoresistance effect, which lasted for a time scale of 10^2 – 10^3 s (Hai *et al.*, 2009). This spin-motive force was explained by the transformation of magnetic energies of the NCs into the electric energy of the electron system in the Coulomb blockade regime. A similar long-living spin-motive force was observed by Miao *et al.*, 2014 in tunnel junctions with EuS barriers and Al nanoparticles. However, an external energy, brought about by, e.g., thermal or electromagnetic noise, should be provided to these systems to maintain such a long-living spin-motive force (Miao *et al.*, 2014; Ralph, 2011). The problem of spin-motive force and magnetotransport in nanoscale magnetic systems remains an outstanding experimental and theoretical topic in spinodal-decomposed magnetic semiconductors.

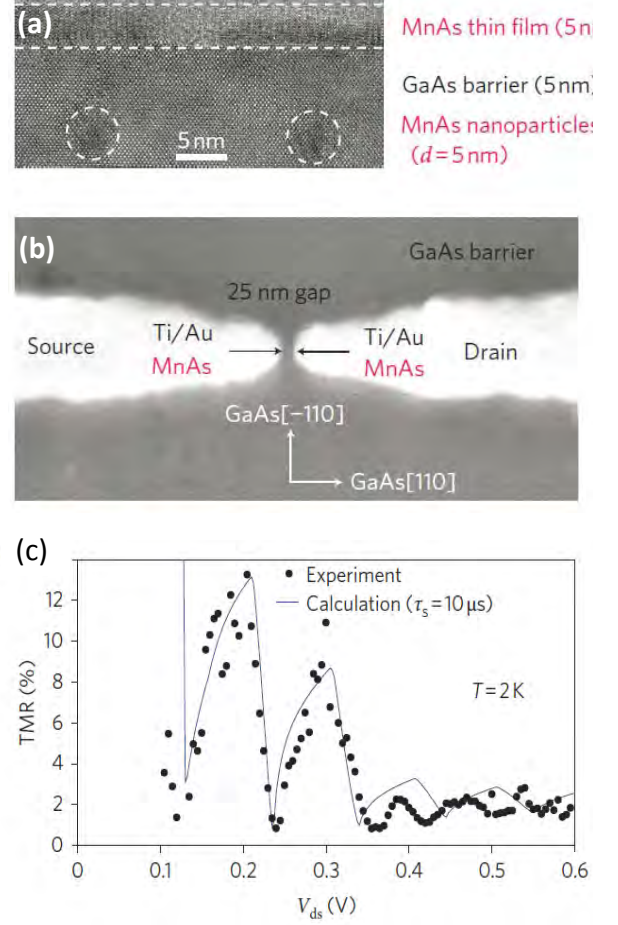


FIG. 19 (Color online) Magnetic tunnel junction involving a single MnAs NC. Cross-sectional TEM image prior to patterning of electrodes (a) and the top-view SEM image of the device (b). The values of $\text{TMR} = [R(\mu_0 H = 0) - R(\mu_0 H = 1 \text{ T})]/R(\mu_0 H = 1 \text{ T})$ as a function of V_{ds} (c). The line represents the theoretical calculation for carrier spin relaxation time within the MnAs NC $\tau_s = 10 \mu\text{s}$. Adapted from Hai *et al.*, 2010.

E. Spinodal nanodecomposition in other magnetic III-V compounds

Several properties outlined above for decomposed (Ga,Mn)As have been found in other III-V semiconductors doped with TM ions. These systems, if fabricated under specific growth conditions, show FM-like features with T_C magnitudes independent of an average Mn concentration but virtually identical to values characterizing relevant Mn pnictides, i.e., T_C of 291, 318, 573 K, for MnP, MnAs, and MnSb, respectively. To this category belong (Ga,Mn)P (de Andrés *et al.*, 2011), (In,Ga,Mn)As/InP (Hara and Fukui, 2006; Hara and Kuramata, 2005), (In,Mn)As (Khodaparast *et al.*, 2013), and (In,Mn)Sb (Lari *et al.*, 2012) grown by MOVPE as well as (Ga,Sb)Mn (Abe *et al.*, 2000) obtained by MBE and GaP:C implanted with Mn (Theodoropoulou

et al., 2002b). Particularly extensive studies have been performed for magnetically-doped GaN, as discussed in subsequent sections (Secs. IV and V).

IV. SPINODAL NANODECOMPOSITION IN (Ga,Mn)N

A. A controversial system

Various contradicting information about magnetism of (Ga,Mn)N has been reported in the literature.

Fabrication of single crystalline $\text{Ga}_{1-x}\text{Mn}_x\text{N}$ epitaxial films with an experimentally documented random distribution of Mn cations and a small concentration of donor-like defects or residual impurities (Bonanni *et al.*, 2011; Kunert *et al.*, 2012; Sarigiannidou *et al.*, 2006; Stefanowicz *et al.*, 2010) pointed to the presence of low-temperature ferromagnetism (Sarigiannidou *et al.*, 2006; Sawicki *et al.*, 2012; Stefanowicz *et al.*, 2013). In such samples the Fermi level is pinned by the mid-gap $\text{Mn}^{2+}/\text{Mn}^{3+}$ impurity band (Dietl and Ohno, 2014; Graf *et al.*, 2003; Woloś *et al.*, 2009) but Mn^{3+} ions prevail. A semiinsulating character of this material, exploited as a buffer in recent magnetotransport experiments on GaN:Si layers (Stefanowicz *et al.*, 2014), indicates that owing to strong p - d coupling holes are tightly bound to parent Mn acceptors (Dietl, 2008a; Woloś *et al.*, 2009). Accordingly, the impurity-band carriers remain localized by, presumably, a combine effect of the Mott-Hubbard and Anderson-Mott mechanism up to least $x = 10\%$. For the resulting high spin d -shell configuration of Mn^{3+} ions FM superexchange was predicted for tetrahedrally bound DMSs (Blinowski *et al.*, 1996), in agreement with the corresponding experimental results for $\text{Ga}_{1-x}\text{Mn}_x\text{N}$ (Bonanni *et al.*, 2011; Kondo *et al.*, 2002; Sarigiannidou *et al.*, 2006; Sawicki *et al.*, 2012; Stefanowicz *et al.*, 2013). Tight-binding and Monte-Carlo computations carried out within the superexchange scenario and taking into the Jahn-Teller distortion described quantitatively the experimentally found phase diagram $T_C(x)$ (Sawicki *et al.*, 2012; Stefanowicz *et al.*, 2013). The determined dependence $T_C(x) \propto x^\alpha$, where $\alpha = 2.2 \pm 0.2$ (Sawicki *et al.*, 2012; Stefanowicz *et al.*, 2013), characteristic for a short range superexchange of either sign (Sawicki *et al.*, 2013; Swagten *et al.*, 1992; Twardowski *et al.*, 1987), leads to a rather low magnitude of $T_C \lesssim 13$ K at small $x \lesssim 10\%$ in $\text{Ga}_{1-x}\text{Mn}_x\text{N}$ (Stefanowicz *et al.*, 2013). Within this scenario, ferromagnetism at RT is expected for $x \gtrsim 0.5$, if impurity band carriers will still remain localized at such high Mn concentrations. In contrast, within the p - d Zener model, long-range FM interactions mediated by band holes would result in $T_C > 300$ K at x as small as 5% in $\text{Ga}_{1-x}\text{Mn}_x\text{N}$ (Dietl *et al.*, 2000).

However, in other series of $\text{Ga}_{1-x}\text{Mn}_x\text{N}$ samples, grown by bulk-like methods with $x \leq 0.1$ (Zajac *et al.*, 2001) or by sputtering that allows to rise x up to 36% (Granville *et al.*, 2010), the interaction between Mn ions was established to be AF. This is consistent with the

dominance of Mn in the 2+ state in those cases (Graf *et al.*, 2003; Granville *et al.*, 2010; Zajac *et al.*, 2001) for which the tight binding theory referred to above predicts AF coupling (\cdot). A negative sign of Curie-Weiss temperature, found for MBE-grown films with x between 8% and 12% (Dhar *et al.*, 2003b), pointed also to the AF character of the spin interactions. The presence of spin-glass freezing at T_f between 3 and 4.4 K was revealed for these samples (Dhar *et al.*, 2003b). The nature of compensating donors providing electrons to Mn ions has not yet been firmly established.

Surprisingly, the appearance of FM-like features in (Ga,Mn)N, persisting up to temperatures well above 300 K, was announced by quite a few groups (Liu *et al.*, 2005; Pearton *et al.*, 2003), and assigned to double exchange that may appear when Mn^{3+} and Mn^{2+} ions coexist (Reed *et al.*, 2005; Sonoda *et al.*, 2007). In view of the technological importance of group III nitrides in today's photonics and electronics, the fabrication of a GaN-based functional FM semiconductor would constitute a major breakthrough. Since, however, neither spintronic devices nor phase diagram $T_C(x)$ have so far been reported in this case, it is tempting to assume that the high-temperature ferromagnetism in question is not under control. It is probable that spinodal nanodecomposition was involved. Theoretical aspects of nanodecomposition, for which (Ga,Mn)N has often served as a model system, are addressed in Sec. II. No magneto-optical effects associated with high- T_C ferromagnetism have been detected in (Ga,Mn)N (Ando, 2006).

B. Experimental evidences for spinodal nanodecomposition in (Ga,Mn)N

The FM response persisting at elevated temperature and in the absence of carriers mediating the interaction between magnetic ions, is presently widely recognized to originate in TM-doped semiconductors from regions of spinodal nanodecomposition in the form of either coherent chemical separation or crystallographic phase precipitation. In the case of (Ga,Mn)N the inclusion of FM NCs with different transition temperatures, such as Mn_4N ($T_C=784$ K) (Pop *et al.*, 1994), $\text{Mn}_{3-\delta}\text{Ga}$ ($T_C = 765$ K) (Niida *et al.*, 1996), or $\text{Ga}_{0.8}\text{Mn}_{3.2}\text{N}$ ($T_C=235$ K) (Garcia, 1985) has been identified.

As the appearance and the form of spinodal nanodecomposition depends sensitively on fabrication conditions, co-doping by shallow impurities, defect concentration, and post-growth processing, the detection of the subtle presence of phase separation requires a thorough characterization of individual samples with a combination of both local—high resolution TEM (HRTEM), 3D atom probe (3DAP),... —and averaging—SQUID magnetometry, synchrotron-based XRD (SXRD), x-ray XMCD, magnetotransport,... —techniques.

Early examples of extended characterization of (Ga,Mn)N and detection of crystallographic phase sepa-

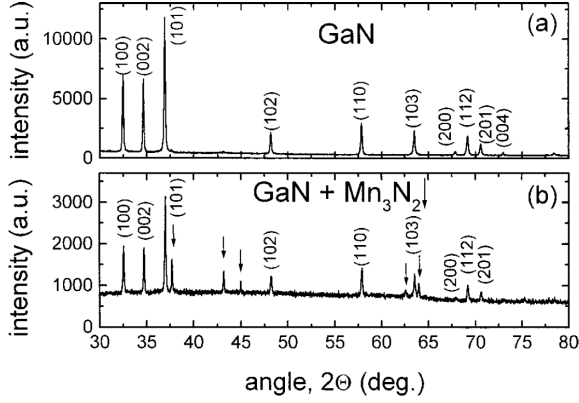


FIG. 20 XRD pattern of (Ga,Mn)N grown by the ammonothermal method with low (a) and high (b) Mn content. The Miller indices of the GaN crystal lattice planes are given for each diffraction line and arrows indicate diffraction lines originating from the Mn_3N_2 phase. From Zajac *et al.*, 2001.

ration are found in works reporting on samples fabricated by means of the ammonothermal technique with 0.25% of Mn (Zajac *et al.*, 2001). Here, the formation of a Mn_3N_2 was detected through XRD analysis, as reported in Fig. 20 and diffraction measurements as in Fig. 21 allowed also to identify $GaMn_3N$ phases in MBE layers containing more than 2% Mn (Giraud *et al.*, 2004; Yoon *et al.*, 2006).

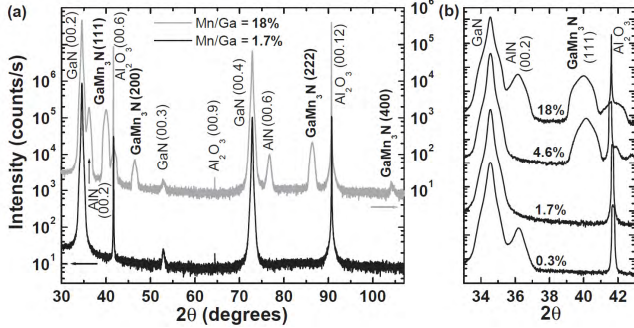


FIG. 21 Determination of NCs' structure in (Ga,Mn)N. (a) XRD patterns of (Ga,Mn)N epilayers. For a 18% Mn-doped GaN epilayer: presence of oriented clusters with perovskite structure. (b) X-ray absorption: the perovskite clusters at Mn contents larger than 2% are identified as $GaMn_3N$ NCs. From Giraud *et al.*, 2004.

Furthermore, through TEM bright-field micrographs it has been possible to recognize the presence of not better identified secondary phases in MBE (Ga,Mn)N grown onto a GaN buffer and employing specific growth conditions (Kunert *et al.*, 2012) or onto 4H-SiC(0001) substrates and containing 13.7% of Mn ions, as seen in Fig. 22, where the comparison between TEM micrographs from samples with respectively 7.6% (left panel) and 13.7% (right panel) is given (Dhar *et al.*, 2003a). From this work, the magnetization of the sample with

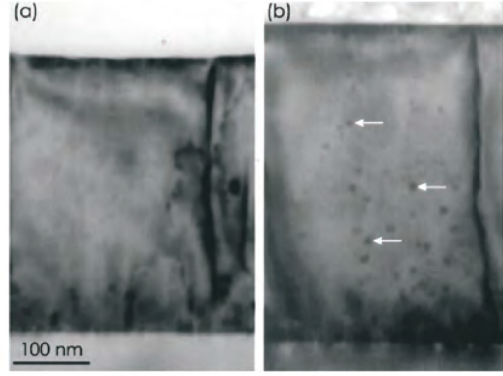


FIG. 22 Bright-field TEM of (Ga,Mn)N with nominal Mn concentrations: 7.6% (a) and 13.7% (b), respectively. The nm-scale clusters are indicated by arrows. From Dhar *et al.*, 2003a.

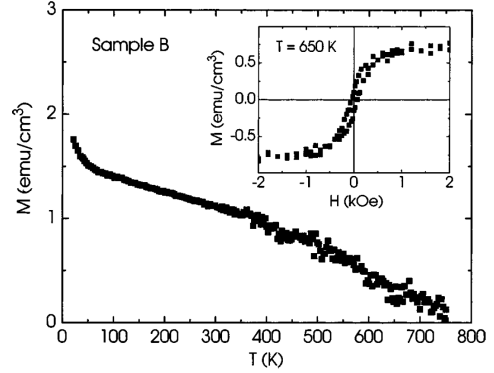


FIG. 23 Magnetization at 50 Oe for a (Ga,Mn)N sample with 13.7% of Mn. Inset: magnetization loop at 650 K. From Dhar *et al.*, 2003a.

the highest Mn concentration as a function of temperature and the magnetic field is reported in Fig. 23. Always worth to underline is that the measured magnetization of phase separated (Ga,Mn)N—and generally (Ga,TM)N—consists of different components, as exemplified in Fig. 24 and particular caution has to be given to discriminating between the various contributions, to the correct subtraction of the signal from the substrate and to possible sources of contamination (Bonanni *et al.*, 2007; Hwang *et al.*, 2007; Ney *et al.*, 2008).

As already mentioned, synchrotron radiation-based characterization techniques can supply precious information when standard methods, such as, e.g., conventional XRD, fail to provide the necessary sensitivity to the presence of spinodal nanodecomposition in the investigated materials (Navarro-Quezada *et al.*, 2010). An example is given by the application of synchrotron radiation microprobe to the identification and study of Mn-rich intermetallic Mn-Ga NCs in MBE (Ga,Mn)N with 11% of Mn (Martinez-Criado *et al.*, 2005). A combination of fluorescence mapping with spectroscopic techniques allowed to examine the composition of the clusters and their crys-

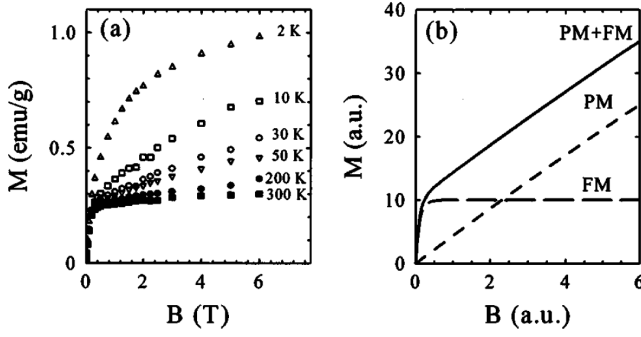


FIG. 24 Evidence for various contributions to (Ga,Mn)N magnetization. (a) Magnetization as a function of the magnetic field for several temperatures. (b) Schematic of the total magnetization (PM + FM) decomposition into paramagnetic (PM) and ferromagnetic (FM) contributions. From Zajac *et al.*, 2003.

tallographic orientation, as summarized in Fig. 25.

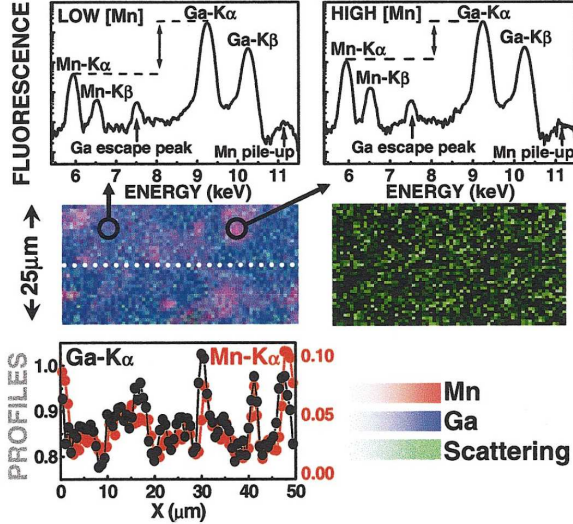


FIG. 25 (Color online) Decomposition of (Ga,Mn)N with an average Mn concentration of 11% studied by x-ray fluorescence mapping. Mn K_{α} , Ga K_{α} fluorescence line, and elastic (Compton) scattering signal, are shown. Ga and Mn profiles along the dotted scan line are presented in the lower panel indicating the formation of Mn-rich intermetallic Mn-Ga NCs. From Martinez-Criado *et al.*, 2005.

It has been reported that by employing H_2/N_2 instead of mere N_2 during the plasma-assisted MBE (PAMBE) of (Ga,Mn)N the solubility limit of Mn can be enhanced and the formation of secondary Mn-rich phases hindered (Cui and Li, 2002). Furthermore, again during a PAMBE process, it has been shown that by switching from N-rich to Ga-rich conditions the efficiency of Mn incorporation is diminished, while the crystalline quality is improved and the presence of mixed domains wz-zb is suppressed (Han *et al.*, 2007). The amount of Mn likely to be incorporated without precipitation has been found to depend critically

in MBE on the growth temperature T_g (Kondo *et al.*, 2002) and above a critical value of the Mn ions supply, $GaMn_3N$ NCs are found to form on the samples surface (Kocan *et al.*, 2006), as exemplified in Fig. 26.

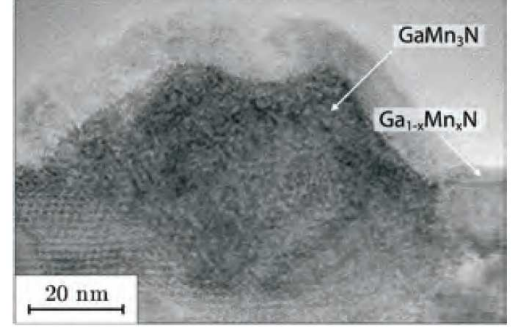


FIG. 26 Cross section HRTEM of a NC in a (Ga,Mn)N layer with nominal 33% Mn. From Kocan *et al.*, 2006.

The role of defects in the aggregation of Mn has been also taken into account (Larson and Satpathy, 2007) and, e.g., from x-ray absorption spectroscopy (XAS) and XMCD data complemented by *ab initio* calculations it has been concluded that Mn in GaN preferentially occupies Ga sites neighboring N split interstitial defects (Keavney *et al.*, 2005). The to-date literature lacks of a systematic study on the possible role of threading dislocations—especially in a system based on GaN—as preferential site for the aggregation of Mn. Energy filtered TEM (EFTEM) experiments should be considered, in particular in the perspective of identifying coherent regions (not crystallographically phase separated) with enhanced Mn concentration.

The high magnetic moment of Mn and its low solubility limit into GaN—common to all TMs—has prompted to optimize and exploit also Mn-induced phases onto a GaN surface: e.g., magnetic MnGa can grow with an abrupt interface and with a defined epitaxial orientation on wz-GaN, developing an ideal magnetic/semiconductor bilayer (Lu *et al.*, 2006). Furthermore, well ordered Mn submonolayers have been deposited onto wz-GaN by evaporation (Chinchore *et al.*, 2008) and (Ga,Mn)N nanostructures, though with a not-investigated structure and actual composition, and grown by MOVPE onto GaN are reported (Gupta *et al.*, 2006). A combined study by scanning tunneling microscopy (STM) and first-principles analysis states the feasibility of ordered Mn-induced nanostructures onto GaN(0001) at elevated temperatures, while the growth at RT leads to disordered phases (Qi *et al.*, 2010).

C. Co-doping with shallow impurities and δ -doping in (Ga,Mn)N

As mentioned above (Sec. IV.A), the charge state of a magnetic impurity in a semiconducting matrix, which can

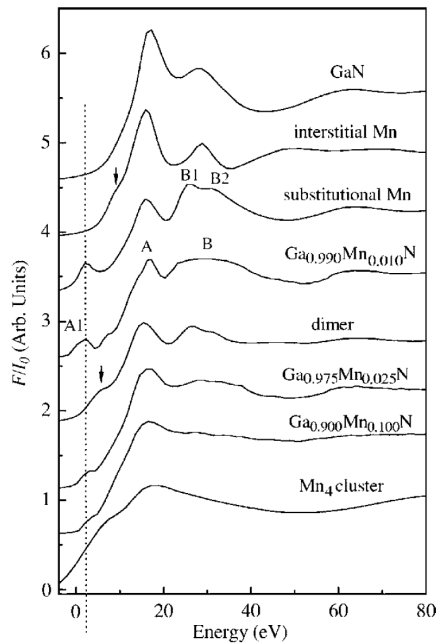


FIG. 27 Comparison of experimental Mn K -edge XANES spectra for $\text{Ga}_{1-x}\text{Mn}_x\text{N}$ with various Mn concentrations with computed spectra assuming various occupation sites in the GaN host crystal. From Wei *et al.*, 2006).

be altered in GaN by co-doping with electrically active impurities, is crucial for the magnetic properties of the material. Moreover, as discussed in Sec. II.B, engineering of the Fermi level position by co-doping can serve to modify the lattice position (e.g., interstitial vs. substitutional) and the distribution of magnetic impurities over cation sites (Dietl, 2006; Ye and Freeman, 2006).

In addition to infrared and magnetic-resonance spectroscopy (see, Bonanni *et al.*, 2011; Graf *et al.*, 2003; Wołoś and Kamińska, 2008), x-ray absorption near-edge spectroscopy (XANES) is a widely employed method to determine the valence state of Mn in GaN (Biquard *et al.*, 2003; Bonanni *et al.*, 2011; Sato *et al.*, 2002; Titov *et al.*, 2005; Wei *et al.*, 2006). As summarized in Fig. 27, from the analysis of the absorption-edge pre-peaks it is possible to infer the charge state of the TM ions. Furthermore, a careful modeling of the total signal can give information on the presence and nature of phase separation (Biquard *et al.*, 2003; Sato *et al.*, 2002; Titov *et al.*, 2005; Wei *et al.*, 2006). Another sensitive method is x-ray emission spectroscopy (XES) that was exploited to determine the evolution of Mn oxidation state with the Mg concentration in $(\text{Ga},\text{Mn})\text{N}:\text{Mg}$ (Devillers *et al.*, 2012).

The tuning of the Fermi level through co-doping with acceptors or donors is expected (Dietl, 2006)—and in other systems proven (Bonanni *et al.*, 2008; Kuroda *et al.*, 2007)—to affect the aggregation of TM ions in a semiconducting host and therefore the onset of spinodal nanodecomposition. In $(\text{Ga},\text{Mn})\text{N}$ the modulation of the Mn charge state has been mainly considered in relation to

its possible effect on the magnetic response. However, the reports are highly controversial: e.g., in some works the reduction from the neutral state Mn^{3+} to Mn^{2+} has been found to decrease the FM response of $(\text{Ga},\text{Mn})\text{N}$ layers (Yang *et al.*, 2008), while elsewhere it has been argued that paramagnetic $(\text{Ga},\text{Mn})\text{N}$ with a majority of Mn^{3+} can be rendered FM via double-exchange mechanisms if Mn^{3+} and Mn^{2+} coexist in the same sample (Sonoda *et al.*, 2007). Furthermore, co-doping with acceptors (Mg) is even reported to act not univocally, but depending on the quality of the matrix to either enhance or quench the FM response (Reed *et al.*, 2005). Again a hint of the crucial importance is a characterization of the material at the nanoscale, as co-doping often controls the formation of Mn-rich NCs that can dominate magnetic properties, especially at high temperatures.

Actually, it was demonstrated that co-doping of GaN with Mn and Mg during the MOVPE growth leads to the formation of Mn-Mg $_k$ impurity complexes, where k increases up to $k = 3$ with the ratio of Mg to Mn concentration according to the binomial distribution (Devillers *et al.*, 2012). These complexes show appealing optical properties, particularly broad-band infrared emission persisting up to RT (Devillers *et al.*, 2012).

Interestingly, MBE p - $(\text{Ga},\text{Mn})\text{N}$ spinodally decomposed in regions of GaMn_3N is seen to have an enhanced conductivity (Kim *et al.*, 2003) that could make this phase-separated system promising for functional effects.

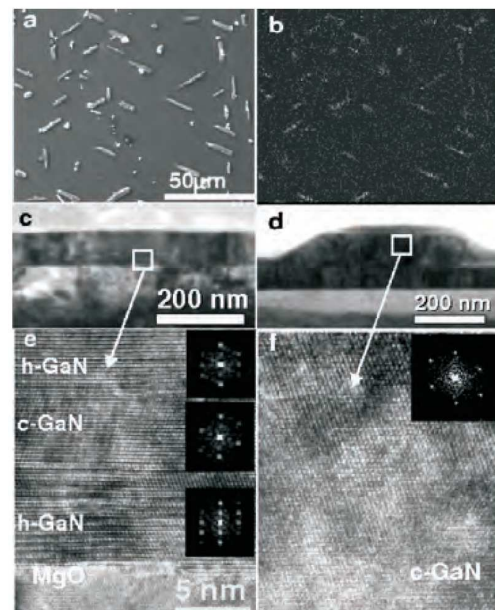


FIG. 28 Multilayer Mn/GaN film on MgO(111): top view SEM image (a) and Mn EDS map (b) showing 93% flat film regions and 7% Mn-rich protrusions. Bright-field TEM (c) and HRTEM (e) images of flat film regions. Bright-field TEM (d) and HRTEM (f) of a Mn-rich protrusion. From Lazarov *et al.*, 2008.

While thermodynamically stable $(\text{Ga},\text{Mn})\text{N}$ crystallizes in the wz-structure, it has been reported that MBE

layers can be locally stabilized by Mn δ -doping in the zb-phase (Lazarov *et al.*, 2008), as evidenced in Fig. 28. Furthermore, the energetics of cubic and hexagonal (Ga,Mn)N arrangements has been studied with *ab initio* pseudo-potential calculations and indeed δ -doping has resulted likely to stabilize the zb phase (Choi *et al.*, 2006).

V. SPINODAL NANODECOMPOSITION IN (Ga,Fe)N

A. Diluted Ga,Fe)N: current status

While extensive studies have been conducted on (Ga,Mn)N (Bonanni, 2007; Dietl, 2004; Graf *et al.*, 2003; Liu *et al.*, 2005; Pearton *et al.*, 2003) as promising workbench for future applications in spintronics, until very recently, only little was known about (Ga,Fe)N. Formerly, and to a broad extent still now, this system is being widely considered as semi-insulating substrate for high frequency devices, as AlGaIn/GaN high-mobility transistors (Heikman *et al.*, 2003; Kashiwagi *et al.*, 2007; Kubota *et al.*, 2009; Lo *et al.*, 2006; Muret *et al.*, 2007). In this context and generally in relation with a use of this material system in reliable devices, careful studies of the electronic structure of (Ga,Fe)N have been carried out and especially the knowledge of the exact position of the $\text{Fe}^{3+/2+}$ acceptor level within the band gap—used to predict band offsets in heterostructures on the basis of the internal reference rule (Langer and Heinrich, 1985)—has been considered of great importance. Furthermore, the behavior of d^5 and d^6 level systems in a trigonal crystal field of C_{3V} symmetry is of interest for general aspects of group and crystal-field theory (Lo *et al.*, 2006; Malguth *et al.*, 2008).

Furthermore, GaN doped with Fe impurities substitutional of Ga in their $\text{Fe}^{3+} d^5$ configuration (Baur *et al.*, 1994; Bonanni *et al.*, 2007; Malguth *et al.*, 2006a, 2008) attracted considerable attention as an ideal system for the study of the p - d exchange interaction in the strong coupling limit (Pacuski *et al.*, 2008). Indeed, magnetically-doped II-VI oxides and III-V nitrides, due to their small bond length and, thus, strong p - d hybridization, are expected to give rise to large values of the exchange energy $N_0|\beta|$, a prediction supported by photoemission experiments (Hwang *et al.*, 2005). Surprisingly, however, abnormally small field-induced exciton splittings in paramagnetic (Zn,Co)O (Pacuski *et al.*, 2006), (Zn,Mn)O (Pacuski *et al.*, 2011; Przędziecka *et al.*, 2006), and (Ga,Mn)N (Pacuski *et al.*, 2007; Sufczyński *et al.*, 2011) were reported. It was suggested (Dietl, 2008a) that due to the strong p - d coupling, the molecular and virtual crystal approximations fail in oxides and nitrides, making the apparent exchange splitting the valence band, quantified by $N_0\beta^{(\text{app})}$, reduced in absolute value and of opposite sign than expected, and observed in other II-VI DMSs. In this context, measurements of magnetization and magnetorefectivity in the free exciton region for (Ga,Fe)N epilayers were re-

ported (Pacuski *et al.*, 2008; Rousset *et al.*, 2013), and the obtained values for $N_0\beta^{(\text{app})}$ supported the theoretical expectations (Dietl, 2008a).

Moreover, recently reported DFT calculations supporting the notion that the spin-spin coupling in dilute (Ga,Fe)N is AF, while it becomes ferrimagnetic when holes are introduced into the system, have rekindled the discussion on the nature of the magnetic interactions in TM-doped DMS (Dalpian *et al.*, 2009). Additionally, DMSs in general and (Ga,Fe)N in particular, have become model systems to test various implementations of the DFT to disordered strongly correlated systems (Cui *et al.*, 2006; Mirbt *et al.*, 2002; Sanyal *et al.*, 2003; Sato and Katayama-Yoshida, 2002).

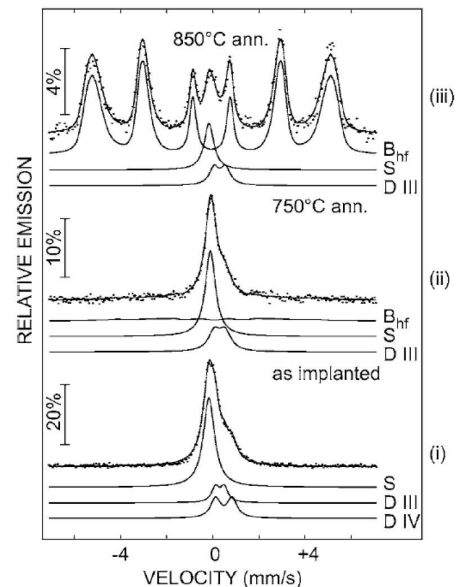


FIG. 29 Room temperature conversion electron Mössbauer spectroscopy spectra of a $4 \times 10^{16} \text{ cm}^{-2}$ Fe-implanted GaN sample: (i) as-implanted, annealed at 750°C , (iii) annealed at 850°C . From Talut *et al.*, 2006.

B. Fabrication and properties of spinodally decomposed (Ga,Fe)N

Both the above considerations and the search for high- T_C DMSs (Dietl *et al.*, 2000) impelled the research in various TM-doped GaN, and the Fe-doping has been pursued through a vast palette of fabrication techniques with variegated results. (Ga,Fe)N grown by means of radio-frequency plasma-assisted MBE (RF-MBE) at 800°C and with a Fe concentration up to $5 \times 10^{21} \text{ cm}^{-3}$ was shown to have superparamagnetic behavior and HRTEM images gave hints of some inhomogeneity in the layers (Kuwabara *et al.*, 2001b).

The same system fabricated by the ammonothermal technique (Dwiliński *et al.*, 1998; Gosk *et al.*, 2003) and by a chemical transport method (Gosk *et al.*, 2003) re-

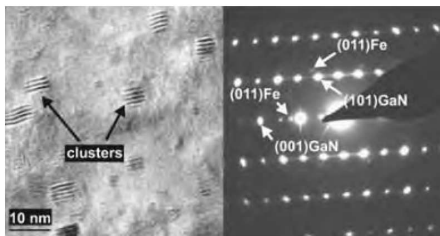


FIG. 30 GaN sample implanted with $4 \times 10^{16} \text{ cm}^{-2}$ Fe ions and annealed at 800°C : left panel - HRTEM: Fe clusters in the implanted region of the sample; right panel - selected area diffraction pattern of the same region. From Talut *et al.*, 2006.

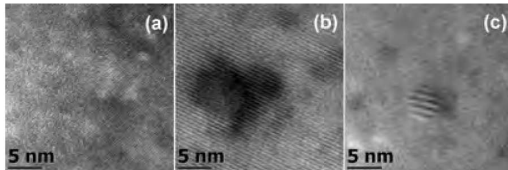


FIG. 31 HRTEM of (Ga,Fe)N showing (a) dilute case; (b) coherent spinodal decomposition (chemical phase separation), and (c) crystallographic phase separation. From Bonanni *et al.*, 2007.

vealed the coexistence of paramagnetic and FM contributions (see Sec. V.F), but the origin of this latter component was not investigated. The magnetic properties of nominally undoped and *p*-doped GaN implanted with Fe ions were reported, evidencing a FM response characterized by magnetization hysteresis loops persisting—depending on the provided dose (Pearson *et al.*, 2002)—up to RT (Shon *et al.*, 2004; Theodoropoulou *et al.*, 2002a).

The full width at half maximum (FWHM) of the GaN(0002) XRD rocking curves peaks acquired on Fe implanted GaN was found to increase as a function of the Fe dose, though without further analysis guiding to the presence of decomposition (Shon *et al.*, 2006). The emission channeling technique applied to Fe-implanted (Fe dose up to 10^{19} cm^{-3}) GaN samples confirmed the presence of a high percentage of TM ions (up to 80%) occupying substitutional Ga sites of the host crystal (Wahl *et al.*, 2001). Moreover, GaN films doped with Fe, with concentrations up to $3 \times 10^{19} \text{ cm}^{-3}$ were fabricated by MBE at growth temperatures (T_g) ranging from 380°C to 520°C directly on sapphire (0001) and FM behavior with $T_C = 100 \text{ K}$ was observed only in the samples grown at 400°C (Akinaga *et al.*, 2000c).

Films of (Ga,Fe)N (Fe density up to $6 \times 10^{21} \text{ cm}^{-3}$) fabricated by means of MBE at $T_g = 500 - 800^\circ\text{C}$ showed a superparamagnetic behavior (Kuwabara *et al.*, 2001a,b) assigned to Ga-Fe and/or Fe-N inclusions. EXAFS analysis suggests that the decrease of T_C is caused by a structural transition from *wz* to *zb*, and this transition was related to the origin of FM in Fe-doped GaN films (Ofuchi *et al.*, 2001).

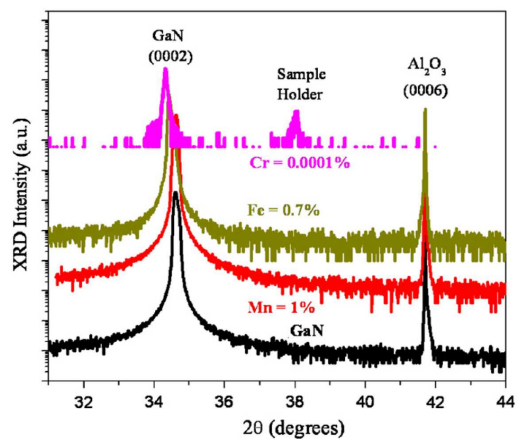


FIG. 32 (Color online) HRXRD for different MOVPE grown (Ga,TM)N. From Gupta *et al.*, 2008.

The MOVPE of (Ga,Fe)N was reported, with a focus on the actual Fe content in the layers and its effect onto the carrier concentration (Heikman *et al.*, 2003). MOVPE samples with a Fe-concentration up to 0.7% molar were claimed to give FM features up to RT even in the absence of holes, but without providing information on the actual distribution of the magnetic ions in the GaN matrix (Gupta *et al.*, 2008; Kane *et al.*, 2007).

Parallel works (Bonanni *et al.*, 2006; Przybylińska *et al.*, 2006) dealt with the extensive study and characterization of this material system with the precise objective of clarifying the correlation between the general properties—and in particular the magnetic ones—of the system and the distribution of the magnetic ions in the semiconducting matrix.

C. Fe distribution from nanoscale characterization

Especially the need to gain insight into the origin of the puzzling FM signatures detected in GaN upon doping with Fe and persisting up to above RT, has prompted lately a considerable experimental effort in the characterization of the system at the nanoscale. As discussed in this section, (Ga,Fe)N represents an interesting case, in which, for specific growth conditions, NCs formed by spinodal nanodecomposition gather in planes perpendicular to the growth direction.

Early steps were undertaken in the understanding of, e.g., the behavior of Fe-implanted GaN, where a combination of Mössbauer spectroscopy and HRTEM revealed the precipitation of Fe during implantation (Talut *et al.*, 2006). There, ^{57}Fe was employed as an atomic sensitive probe to investigate the local environment of Fe by Mössbauer spectroscopy and to study the precipitation at very early stage. MOVPE *p*-type Mg doped 10^{17} cm^{-3} *wz*-GaN(0001) films about $3 \mu\text{m}$ thick grown onto sapphire (0001) substrates were analyzed. The samples were implanted with 200 keV ^{57}Fe ions with fluences between

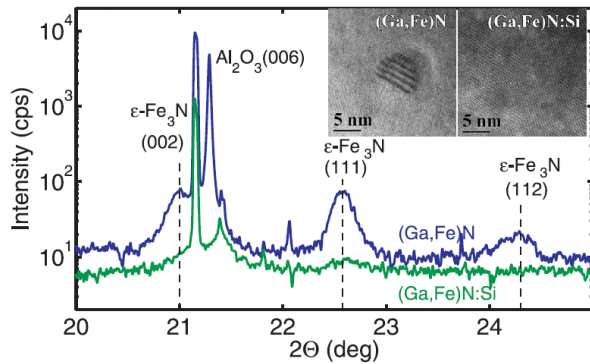


FIG. 33 (Color online) SAXRD for MOVPE grown (Ga,Fe)N with Fe density above the solubility limit. Secondary phases identified as ϵ -Fe₃N are evidenced in accord with HRTEM data (inset). The effect of co-doping by Si (see, Sec. V.E) is also shown. Adapted from Bonanni *et al.*, 2008.

$1 \times 10^{16} \text{ cm}^{-2}$ and $1.6 \times 10^{17} \text{ cm}^{-2}$ for a maximum Fe content of 1-18 at%.

Conversion electron Mössbauer spectroscopy (CEMS) in constant-acceleration mode at RT was applied to investigate the Fe lattice sites, electronic configuration, and magnetism. In samples implanted with fluences above $8 \times 10^{16} \text{ cm}^{-2}$, the formation of clusters was observed already in the as-implanted state. The CEMS spectra of the as-implanted state were found to consist of a singlet line and two quadrupole doublets. The singlet could be assigned to either superparamagnetic α -Fe or to paramagnetic γ -Fe with an isomer shift of -0.05 mm/s . The determined values was assigned to Fe³⁺ with three D_{III} and four D_{IV} nearest N neighbors with isomer shifts of 0.42 and 0.59 mm/s, respectively. The magnetically isolated Fe³⁺ ions were confirmed to be paramagnetic with no FM hyperfine splitting observable.

The presence of the Fe³⁺ state has been taken as a direct proof of its being substitutional of Ga sites in the wz structure, where Ga is surrounded by four N atoms and vice versa. However, only 23.6% of the total amount of Fe in the as-implanted samples appeared to substitute the Ga sites. The remanent magnetic ions were regarded to be either on interstitial sites or generating small precipitates of metallic γ - or α -Fe. Annealing at 850°C was found to trigger the formation of FM α -Fe, represented by a sextet with a mean magnetic hyperfine field of 318 kOe reported in Fig. 29.

A series of works with a first systematic study of the (Ga,Fe)N system fabricated by means of MOVPE from the impurity limit until the phase separation, was carried out (Bonanni *et al.*, 2007, 2008; Kowalik *et al.*, 2012; Pacuski *et al.*, 2008; Przybylińska *et al.*, 2006; Rovezzi *et al.*, 2009). It was shown that by controlling the growth parameters it is possible to incorporate the magnetic ions in different fashions, giving rise to respectively: (i) a DMS with Fe substitutional of Ga, in the charge state Fe³⁺ and responsible for the paramagnetic response of the samples; (ii) a system with spinodal decomposition (chemical

phase separation) in Fe-rich regions structurally coherent with the matrix; (iii) a crystallographic phase-separated material consisting of Fe_xN NCs embedded in the GaN host and likely to account for the FM signatures, as discussed in Sec. V.F.

The mentioned different arrangements are evidenced by the HRTEM images in Fig. 31, where (a) dilute, (b) chemically separated, and (c) crystallographically separated (Ga,Fe)N are, respectively, reported. Energy dispersive x-ray spectroscopy (EDS) measurements could confirm the enhanced concentration of Fe both in the coherent regions (b) and in the incoherent precipitates (c) (Bonanni *et al.*, 2007).

While often laboratory XRD does not evidence any phase separation in (Ga,Fe)N samples giving a FM response—an example is given in Fig. 32, where MOVPE (Ga,Fe)N with 0.7% Fe ions does not show diffraction peaks from secondary phases—SAXRD measurements on MOVPE (Ga,Fe)N with more than 0.4% Fe, reveal the presence of diffraction peaks identified as the (002) and (111) of the phase ϵ -Fe₃N—as reported in Fig. 33—a compound known to be FM with $T_C = 575 \text{ K}$.

The solubility limit in (Ga,Fe)N was found to be around 0.4% of the Fe ions under the optimized MOVPE growth conditions (Bonanni *et al.*, 2007). As discussed in Sec. II.B, an order of magnitude lower solubility limit of Fe comparing to Mn (see Sec. IV) under similar growth conditions is to be linked to a different sign of chemical forces between TM adatoms on the (0001)GaN surface during the epitaxy: according to *ab initio* studies the pairing interaction that is repulsive for surface cation Mn dimers, becomes attractive in the case of Fe ions (Gonzalez Szwacki *et al.*, 2011). Actually, a reduced magnitude of FM response with increasing the growth rate (Bonanni *et al.*, 2008) and lowering growth temperature (Navarro-Quezada *et al.*, 2010) constitutes an experimental hint about the importance of aggregation at the growth surface in the formation of Fe-rich NCs in (Ga,Fe)N.

An interesting aspect of spinodal nanodecomposition in (Ga,Fe)N was discovered by HRTEM (Navarro-Quezada *et al.*, 2011) and confirmed by x-ray photoemission electron microscopy (XPEEM) and XAS (Kowalik *et al.*, 2012). It was found that Fe-rich NCs tend to accumulate in a plane adjacent to the film surface. This observation allowed to develop a method of controlling the NCs' position (Navarro-Quezada *et al.*, 2012). As shown in Fig. 34, it was demonstrated that for an employed growth mode, the NCs gathered in a plane at which the Cp2Fe source flow was interrupted, i.e., at the interface between the (Ga,Fe)N layer and the GaN cap. This means that Fe-rich regions move together with the growth front as long as Fe is supply, reemphasizing the notion that the aggregation of TM ions occurs at the growth surface.

The command over the location of the NC array is obviously a major step toward applications of decomposed systems. Furthermore, a highly non-random distribution of NCs over the film volume indicates that the visual-

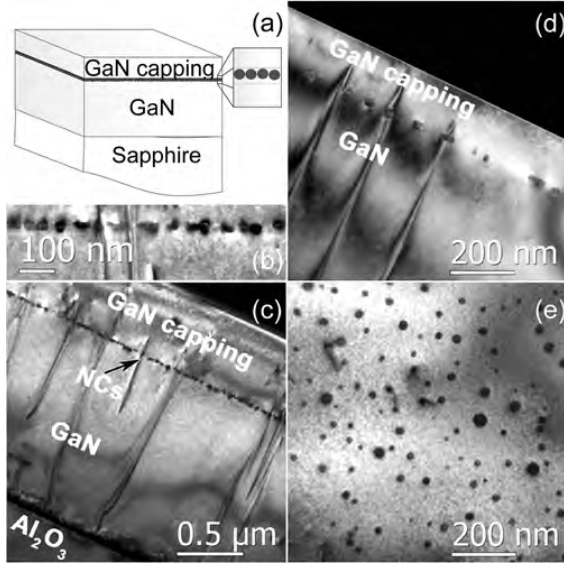


FIG. 34 Control over the spatial distribution of Fe-rich nanocrystals (NCs) in (Ga,Fe)N. (a) Schematic layout of the structure; (b) cross-sectional TEM: magnification of the region containing the array of NCs for the sample reported in (c); (c) and (d) cross section TEM images of the samples, showing the spatial distribution of the NCs into a planar array perpendicular to the growth direction and located at the interface to the cap layer, 500 nm and 150 nm below the sample surface, respectively; (e) plane-view TEM image of the sample in (c), giving the in-plane distribution of NCs. From Navarro-Quezada *et al.*, 2012).

ization of spinodal nanodecomposition can be quite challenging, as NCs may reside outside the probed region.

D. Phase diagram of the spinodal decomposition in (Ga,Fe)N

It is known that the increase of T_g promotes the aggregation of the TM ions incorporated in the semiconductor host and brings therefore the system far from the dilute state. Moreover, various Fe_xN phases with specific magnetic and structural properties are expected to be stable up to different temperatures. The MOVPE (Ga,Fe)N material system was studied as a function of T_g in the range between 800 and 950°C and for samples with a total concentration of Fe ions in the range $1 - 4 \times 10^{20} \text{ cm}^{-3}$ (Navarro-Quezada *et al.*, 2010). In that work, SXRD, EXAFS and XANES, combined with HRTEM and SQUID magnetometry permitted to detect and to identify particular Fe_xN phases in samples fabricated at different T_g , as well as to establish a correlation between the existence of the specific phases and the magnetic response of the system. It was found that already a 5% variation in the growth temperature is critical for the onset of new Fe_xN species and it could be confirmed that an increase in the growth temperature promoted the on-

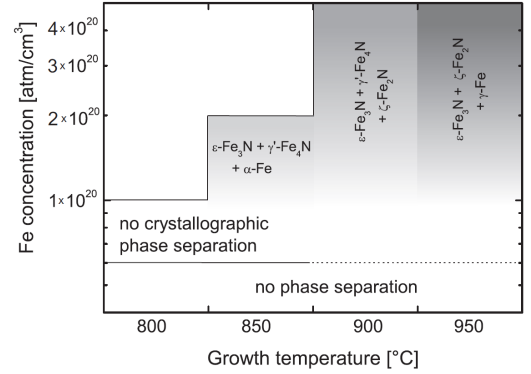


FIG. 35 A phase diagram of MOVPE (Ga,Fe)N as a function of the growth temperature. From Navarro-Quezada *et al.*, 2010.

set of spinodal decomposition, resulting in an enhanced density of Fe-rich NCs in the matrix and in a consequent increase of the FM response of the system.

In Fig. 36 SXRD spectra for (Ga,Fe)N samples grown at different temperatures, are reported. For layers fabricated at 800°C there is no evidence of secondary phases and only diffraction peaks originating from the sapphire substrate and from the GaN matrix are revealed, in agreement with HRTEM measurements showing no crystallographic phase separation. Moving to a T_g of 850°C different diffraction peaks belonging to secondary phases become evident, giving proof that at this T_g and at the given growth parameters the system undergoes spinodal decomposition and is phase separated. It was reported (Bonanni *et al.*, 2007) that when growing (Ga,Fe)N at this temperature, one dominant Fe-rich phase is formed, namely wz ϵ - Fe_3N , for which two main diffraction peaks are identified, corresponding to the (002) and the (111) reflexes, respectively. A closer analysis of the (111)-related feature and a fit with two gaussian curves centered at 35.2° and 35.4°, gives evidence of the presence of the (110) reflex from cubic metallic α -Fe. Moreover, the broad feature appearing around 38° is associated to the (200) reflex of fcc γ '- Fe_4N , that crystallizes in an inverse perovskite structure (Jack, 1952).

As the growth temperature is increased to 900°C there is no contribution left from the (110) α -Fe phase, and the signal from the (111) of ϵ - Fe_3N is significantly quenched, indicating the reduction in either size or density of the specific phase. Furthermore, an intense peak is seen at 34°, corresponding to the (121) contribution from orthorhombic ζ - Fe_2N . This phase crystallizes in the α - PbO_2 -like structure, where the Fe atoms show a slightly distorted hexagonal close packing (*hcp*), also found for ϵ - Fe_3N (Jacobs *et al.*, 1995). At a growth temperature of 950°C the diffraction peak of (200) γ '- Fe_4N recedes, indicating the decomposition of this fcc phase at temperatures above 900°C, in agreement with the phase diagram for free standing Fe_xN (Jacobs *et al.*, 1995), reporting cubic γ '- Fe_4N as stable at low temperatures. Only the

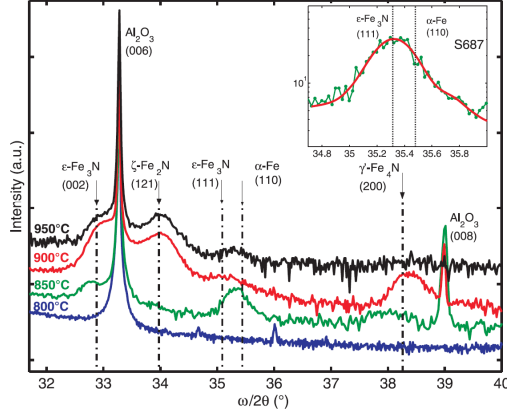


FIG. 36 Color online) SAXRD spectra for (Ga,Fe)N layers deposited at different growth temperatures. Inset: peak at 35.3° deconvoluted into two components assigned to diffraction maxima (111) of ε -Fe₃N and (110) of α -Fe [experiment (dotted line) and fit (smooth line)]. From Navarro-Quezada *et al.*, 2010.

(002) ε -Fe₃N- and the (121) ζ -Fe₂N-related diffraction peaks are preserved with a constant intensity and position with increasing temperature, suggesting that at high T_g these two phases and their corresponding orientations, are noticeably stable.

Following a procedure based on the Williamson-Hall formula method (Lechner *et al.*, 2009; Williamson and Hall, 1953), the approximate average NCs size is obtained from the FWHM of the diffraction peaks in the radial ($\omega/2\theta$) scans. The FWHM of the (002) ε -Fe₃N, of the (200) γ' -Fe₄N, and of the (121) ζ -Fe₂N diffraction peaks are comparable for samples grown at different temperatures, indicating that the average size of the corresponding NCs is also constant, as summarized in Fig. 37.

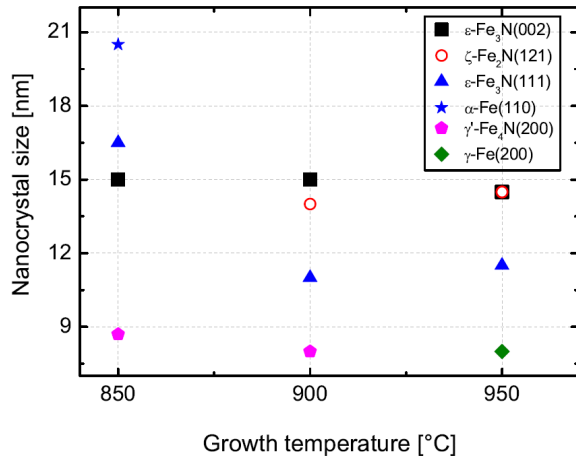


FIG. 37 (Color online) Average size vs. growth temperature T_g of nanocrystals in the different Fe_xN phases, as determined from SAXRD. From Navarro-Quezada *et al.*, 2010.

By summing up the SAXRD, EXAFS, and HRTEM find-

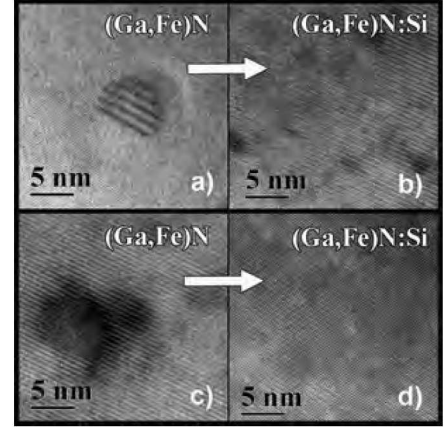


FIG. 38 HRTEM with mass contrast (b,c) of (Ga,Fe)N revealing the presence of Fe₃N precipitates (a), spinodal decomposition (c), and the effect of co-doping by Si (b,d) preventing the formation of the Fe-rich regions. Adapted from Bonanni *et al.*, 2008.

ings, a phase diagram of the Fe-rich phases formed in (Ga,Fe)N as a function of the growth temperature has been constructed and reported in Fig. 35, showing the dominant phases for each temperature interval. Moreover, according to the Fe vs. N phase diagram the orthorhombic phase (ζ -Fe₂N) contains a higher percentage of nitrogen (Jack, 1952) compared to the hexagonal one (ε -Fe₃N), and this guides to conjecture that the higher the growth temperature, the more nitrogen is introduced into the system. Furthermore, similarly to the case of (Ga,Mn)As (III) and (Ga,Mn)N (IV), NCs in (Ga,Fe)N can be built from compounds containing Ga. The presence of planar arrays of Ga_xFe_{4-x}N NCs was evidenced in a recent work (Navarro-Quezada *et al.*, 2012).

E. Co-doping with shallow impurities in (Ga,Fe)N

Remarkably, HRTEM, SAXRD, and SQUID data reveal that the aggregation of Fe ions in a GaN host, and therefore the onset of spinodal decomposition, can be affected by co-doping with shallow impurities, Si donors and Mg acceptors (Bonanni *et al.*, 2008; Navarro-Quezada *et al.*, 2011).

In Fig. 38 HRTEM images data for the two relevant spinodally decomposed initial regimes, namely (i) (Ga,Fe)N with embedded Fe-rich NCs [Fig. 38(a)] evidenced by Moiré fringes contrast and (ii) (Ga,Fe)N showing coherent chemical separation [Fig. 38(c)] generating mass contrast show the reduced aggregation of the Fe-rich regions as a consequence of co-doping with Si donors [Fig. 38(b),(d)].

This effect is further confirmed by the SAXRD results given already in Fig. 33, where the introduction of shallow donor impurities is found to hamper efficiently the precipitate aggregation, so that the SAXRD diffraction

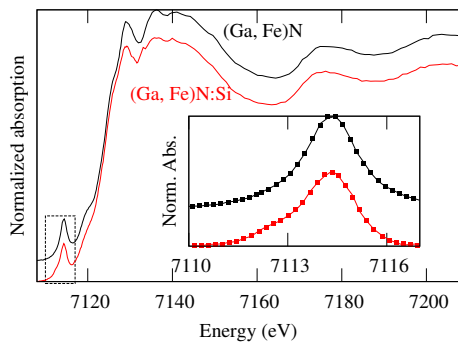


FIG. 39 (Color online) XANES spectra of (Ga,Fe)N and (Ga,Fe)N:Si. The region marked by the dashed box is expanded in the inset. Here the experimental data (lines) after a background subtraction are compared to the fitted values (dots). In addition to the peak at 7114.3 ± 0.1 eV assigned to the Fe^{3+} charge state, a shoulder at 7112.7 ± 0.1 eV is visible in the Si-doped sample pointing to the reduction of a part of the Fe ions to the Fe^{2+} charge state by Si doping. From Bonanni *et al.*, 2008.

peaks corresponding to $\varepsilon\text{-Fe}_3\text{N}$ are suppressed in the case of the co-doped samples (Bonanni *et al.*, 2008). The quenching of the FM contribution in the co-doped layers is further validated by the reduced number of average Fe ions involved in the FM response in co-doped (Ga,Fe)N samples.

In order to explain these key findings, it was noted, as discussed theoretically in Sec. II.B, that except for Mn in II-VI compounds (Kuroda *et al.*, 2007), owing to the presence of the open d shells in the vicinity of the Fermi level, the nearest neighbor pair of TM cations in semiconductors shows a large binding energy that promotes the magnetic ions aggregation. However, as also elaborated in Sec. II.B from a theoretical perspective, if carriers introduced by co-doping can be trapped by these ions, the pair binding energy will be altered, usually reduced by the corresponding Coulomb repulsion between charged TM impurities (Dietl, 2006; Ye and Freeman, 2006).

While the effect of shallow Si donors on the Fe aggregation and consequently on the onset of spinodal decomposition in (Ga,Fe)N is quite clear, since the presence of the mid-gap electron trap, i.e., the $\text{Fe}^{+3}/\text{Fe}^{+2}$ state, is well established in GaN (Malguth *et al.*, 2008). It was found that the Fe K-edge probed by the XAS shifts under Si doping from a position expected for the Fe^{3+} oxidation state towards that specific to the Fe^{+2} configuration (Rovezzi *et al.*, 2009), as evidenced by the XANES spectra in Fig. 39.

In contrast, the role of additional acceptors (Mg) is more complex in (Ga,Fe)N. The level $\text{Fe}^{+3}/\text{Fe}^{+4}$ is expected to reside rather in the valence band (Malguth *et al.*, 2008), but it was suggested that the potential introduced by a TM ion in GaN (and ZnO) is deep enough to bind a hole (Dietl, 2008a), shifting the $\text{Fe}^{+3}/\text{Fe}^{+4}$ up to the GaN band gap (Pacuski *et al.*, 2008). If this is the case, Mg co-doping could also hamper Fe aggregation.

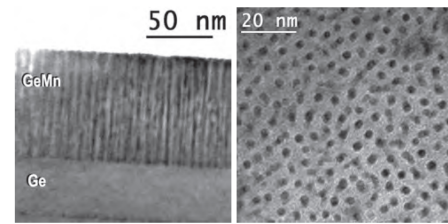


FIG. 40 (Color online) Magnetization of (Ga,Fe)N bulk crystals obtained by a chemical transport method showing a non-saturating linear in field component assigned to a Van Vleck-type paramagnetism of Fe^{2+} ions, together with a high- T_C ferromagnetic contribution visible in weak fields. From Gosk *et al.*, 2003.

It was found experimentally that the influence of Mg depended crucially on the way it was introduced to the system: uniform Mg co-doping reduced incorporation of Fe, diminishing in this way the NC abundance (Navarro-Quezada *et al.*, 2011). In contrast, co-doping of Mg in the δ fashion enhanced the NC formation, the effect discussed theoretically in terms of pairing energies of clusters containing different numbers of Fe and Mg cations in GaN (Navarro-Quezada *et al.*, 2011). The influence of Mg co-doping on magnetic properties is discussed below (Sec. V.F).

Significantly, based on these results, the previously observed effect of co-doping on ferromagnetism in (Ga,Mn)N, and assigned to the dependence of the double exchange mechanisms of the spin-spin coupling on the position of the Fermi level with respect to the center of the d band (Reed *et al.*, 2005), has to be reconsidered.

F. Magnetic properties of (Ga,Fe)N

Comprehensive nanocharacterization of (Ga,Fe)N has allowed to put on a more firm basis the origin of a complex magnetic response reported repetitively for this system. Two examples are given in Figs. 40 and 41, in which various contributions to magnetization are clearly seen. The richness of magnetic response correlates with the multi-phase character of (Ga,Fe)N with Fe concentrations beyond the solubility limit, as discussed above (Secs. VC-E).

In general, according to studies of magnetization (Bonanni *et al.*, 2007; Gosk *et al.*, 2003; Navarro-Quezada *et al.*, 2011, 2010), electron paramagnetic resonance (EPR) (Bonanni *et al.*, 2007; Malguth *et al.*, 2006a), ferromagnetic resonance (FMR) (Grois *et al.*, 2014), infrared spectroscopy (Malguth *et al.*, 2006a,b), magneto-optics (Pacuski *et al.*, 2008; Rousset *et al.*, 2013), and XMCD (Kowalik *et al.*, 2012) Fe dopants appear in distinct magnetic phases in (Ga,Fe)N, whose relative importance depends on growth conditions, Fe concentration, and co-doping by donors or acceptors.

Brillouin paramagnetism of Ga-substitutional Fe^{3+} ions: Because of a non-zero but relatively low solubil-

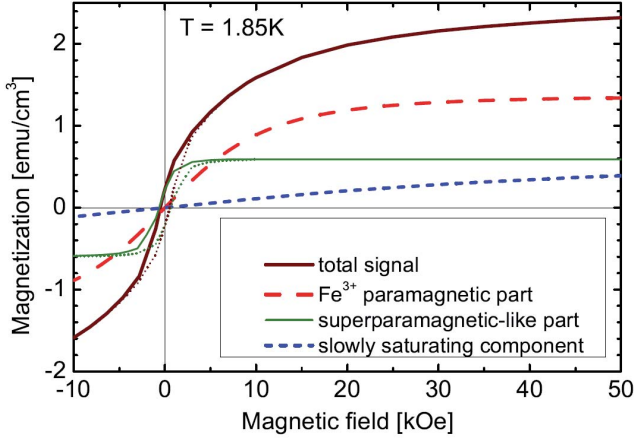


FIG. 41 (Color online) Crystallographically phase-separated (Ga,Fe)N - contributions to the total magnetization as a function of the magnetic field : (i) paramagnetic from non interacting Fe^{3+} , (ii) high- T_C superparamagnetic-like or superferromagnetic-like from the FM NCs and (iii) slowly saturating component, presumably coming from AF NCs. From Navarro-Quezada *et al.*, 2010.

ity limit, a paramagnetic contribution from diluted Fe^{3+} ions is always present (provided that density of compensating donors is sufficiently small), as confirmed by a quantitative interpretation of EPR spectra in terms of weakly interacting localized spins $S = 5/2$ occupying Ga-substitutional sites (Bonanni *et al.*, 2007; Malguth *et al.*, 2006a). These spins give rise to the Brillouin-like dependence of magnetization on the magnetic field and temperature visible in magneto-optical (Pacuski *et al.*, 2008; Rousset *et al.*, 2013) and magnetization measurements (Bonanni *et al.*, 2007, 2008; Navarro-Quezada *et al.*, 2010; Pacuski *et al.*, 2008).

Van Vleck paramagnetism due to Fe^{2+} ions: In addition to the Brillouin-like term described above, a term linear in the magnetic field was found to contribute to (Ga,Fe)N magnetization, and assigned to the Van Vleck paramagnetism of Fe^{2+} ions that can be present in (Ga,Fe)N due to residual or purposely introduced donors (Bonanni *et al.*, 2007; Gosk *et al.*, 2003; Malguth *et al.*, 2006b).

High- T_C ferromagnetism: A FM-like contribution to magnetization of (Ga,Fe)N, dominating at high temperatures, shows characteristics specific to the whole family of high- T_C DMSs and dilute magnetic oxides (Coey *et al.*, 2010; Sawicki *et al.*, 2013). As presented in Fig. 42, for any temperature and orientation of the magnetic field magnetic hysteresis loops $M(H, T)$ are leaning and narrow, so that the magnitude of spontaneous magnetization $M_s(T)$ is much smaller than the saturation magnetization M_{Sat} . Remarkably, $M_s(T)$ persists up to above RT and the values of normalized magnetization are approximately described by a temperature independent Langevin function $M(H)/M_{\text{Sat}} = \tanh(H/H_0)$, where in the case under consideration $H_0 \simeq 800$ Oe.

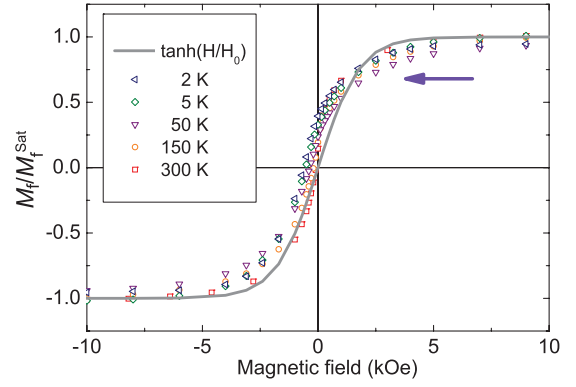


FIG. 42 (Color online) Normalized magnetization at various temperatures for (Ga,Fe)N co-doped by Mg in δ -like fashion with embedded Fe-rich nanocrystals. Points: experimental data; solid line: fit a Langevin-type function with $H_0 = 800$ Oe; arrow: sweep direction of the magnetic field. From Navarro-Quezada *et al.*, 2011.

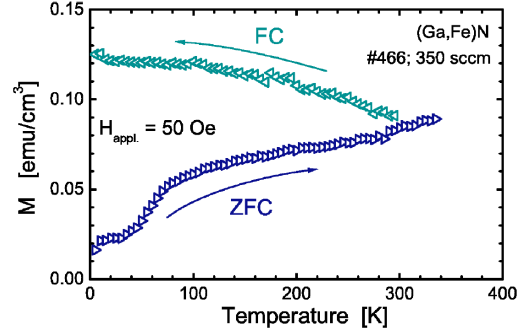


FIG. 43 (Color online) ZFC-FC magnetization at $H_{\text{appl.}} = 50$ Oe for a (Ga,Fe)N sample with crystallographic phase separation. From Bonanni *et al.*, 2007.

This behavior is in contrast to a square-like shape and strong temperature dependence of hysteresis in, e.g., dilute ferromagnetic semiconductors, such as (Ga,Mn)As. At the same time, if interpreted in terms of superparamagnetism it indicates that, for some NCs, the blocking temperature T_b is higher than RT. This conclusion was confirmed via zero-field cooled (ZFC) and field cooled (FC) SQUID magnetometry measurements at a low magnetic field of 50 Oe (Bonanni *et al.*, 2007), as shown in Fig. 43. However, the high magnitudes of T_b were surprising in view of relatively small values of NC diameters, collected in Fig. 37.

It was suggested that dipole-dipole interactions between densely packed magnetic constituents may lead to a magnetization that can be parametrized by a temperature-independent Langevin-type function (Coey *et al.*, 2010), a behavior refer to as superferromagnetism (Sawicki *et al.*, 2013). According to TEM (Navarro-Quezada *et al.*, 2010) and XPEEM (Kowalik *et al.*, 2012),

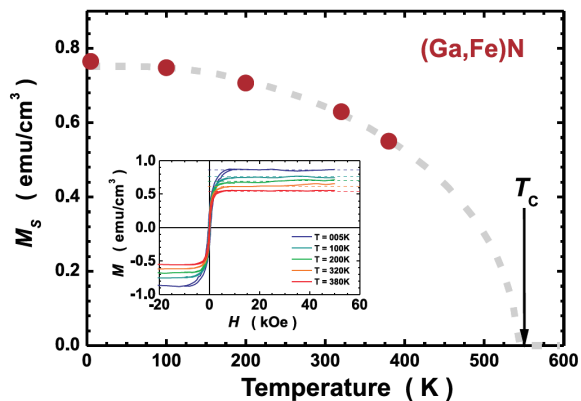


FIG. 44 (Color online) Saturation magnetization determined from the Arrott plots as a function of temperature for spinodally decomposed (Ga,Fe)N: the evaluated T_C of 575 K corresponds to the Curie temperature of ϵ -Fe₃N. Adapted from Bonanni *et al.*, 2007.

NCs tend to aggregate in planes perpendicular to the growth direction in the case of (Ga,Fe)N, which increases density of NCs and thus supports the superferromagnetism scenario (Navarro-Quezada *et al.*, 2011).

The above interpretation requires also that T_C of individual NCs is well above RT. According to results presented in Fig. 44, the value of M_{Sat} determined from Arrott plots as a function of temperature for the same type of samples, pointed to a $T_C = 575$ K. This value is in accord with the identification of the dominant secondary phases via SXRD and TEM as ϵ -Fe₃N in samples under consideration (Bonanni *et al.*, 2007). According to the phase diagram discussed in Sec. V.D, the abundance of ferromagnetic NCs (ϵ -Fe₃N, γ '-Fe₄N, α '-Fe, and their derivatives) increases with lowering the epitaxy temperature.

Recently, FMR was detected at RT in spinodally decomposed (Ga,Fe)N in which Ga_xFe_{4-x}N NCs formed a planar array (Grois *et al.*, 2014). The magnetic anisotropy was found to be primarily uniaxial with the hard axis normal to the NCs plane and to have a comparably weak in-plane hexagonal symmetry.

Antiferromagnetic contribution: According to the phase diagram discussed in Sec. V.D, an increase in the epitaxy temperature results in the formation of NCs with a higher degree of nitridation, for which AF coupling can prevail. In particular, γ '-GaFe₃N exhibits a weak AF coupling with a Curie-Weiss temperature of -20 K (Houben *et al.*, 2009), whereas orthorhombic ζ -Fe₂N is AF below 9 K (Hinomura and Nasu, 1996). Furthermore, it is also possible that wz-FeN NCs formed by chemical phase separation exhibit AF properties, as according to theoretical predictions presented in Sec. II.B, coupling between Fe cation pairs is AF in GaN. These considerations led to the conclusion that weakly saturating component of magnetization visible in Fig. 41, rather than resulting from a Van Vleck paramagnetism could

originate from antiferromagnetically ordered Fe-rich NCs (Navarro-Quezada *et al.*, 2010).

The presence of various Fe-rich phases with peculiar magnetic properties has been proven, but now it is mandatory to explore the routes that can lead to a single-phase system, especially in the perspective of exploiting hybrid AF/FM systems for, e.g., AF spintronics (Shick *et al.*, 2010).

VI. SPINODAL NANODECOMPOSITION IN (Ge,Mn)

A. Mn dilution in germanium

Almost all the theoretical predictions on the magnetic properties of magnetic semiconductors rely on the ideal dilution of magnetic TM atoms substituting the semiconducting host. d levels of Mn atoms in a tetrahedral environment are split into two energy levels: e_g (twice degenerated) and t_{2g} (three times degenerated) levels. In germanium, t_{2g} orbitals strongly hybridize with p orbitals in the germanium valence band forming bonding and anti-bonding states. The resulting magnetic moment per Mn atom is $3 \mu_B$ and two holes (when activated) are created in the germanium valence band. *Ab-initio* calculations have further shown that exchange coupling between Mn atoms mediated by holes oscillates following the Rudermann-Kittel-Kasuya-Yoshida (RKKY) magnetic interaction (Continenza *et al.*, 2006b; Zhao *et al.*, 2003). Among all TM atoms, Mn is the only one to provide both ferromagnetism and high localized spin moments in germanium. The Zener model complemented with mean field approximation further predicts T_C as high as 80 K in Ge_{0.975}Mn_{0.025} with a hole density of $3.5 \times 10^{20} \text{ cm}^{-3}$ (Dietl *et al.*, 2000). However exchange coupling was shown to be highly anisotropic, i.e., to depend on the crystal orientation between two Mn atoms (Continenza *et al.*, 2006b). Hence, for high Mn concentrations (up to few percents), the relative position of Mn atoms in the germanium crystal lattice should be known in detail to understand magnetic properties. Finally, from band structure calculations, Mn dilution in germanium is more favorable than in silicon to induce half-metallic character (100% spin polarization at the Fermi level) (Stroppa *et al.*, 2003). To conclude about theoretical works, (Ge,Mn) might be a very promising candidate as a DMS in future spintronic devices compatible with mainstream silicon technology.

Surprisingly, only few works have been published on ferromagnetism in TM-doped germanium until 2002. The evidence of FM order in an epitaxial layer of Mn-doped germanium was first reported in 2002 by Park (Park *et al.*, 2002b). Ge_{1-x}Mn_x ($0.6 < x < 3.5\%$) films were grown by LT-MBE on Ge(001) and GaAs(001) substrates. They exhibit p -type doping with hole densities up to 10^{19} – 10^{20} cm^{-3} and T_C increases linearly with Mn concentration from 25 K up to 116 K. Moreover they could demonstrate the interplay between band carriers

and Mn spins by measuring AHE as shown in Fig. 45(a). They could further modulate AHE by the application of a gate voltage as low as 0.5 V. However the magnetic moment per Mn atom (1.4-1.9 μ_B) was much less than the expected value for Mn substituting Ge (3 μ_B) and the authors reported the presence of small unidentified precipitates. Mn dilution in germanium can thus be questionable.

B. From Mn dilution to phase separation

Considering the very low solubility of Mn in germanium ($10^{-6}\%$) (Woodbury and Tyler, 1955), out-of-equilibrium growth techniques are required to dope germanium films with few % of Mn. Indeed, according to the binary phase diagram (Massalski, 1990) and DFT calculations (Arras *et al.*, 2011), the stable (Ge,Mn) alloy with the lowest Mn content is $\text{Ge}_8\text{Mn}_{11}$ and contains 57.9 at.% of Mn. Since the 1980's, seven stable (Ge,Mn) alloys have been synthesized: ϵ - $\text{GeMn}_{3.4}$ (Ohoyama *et al.*, 1961), ϵ_1 - $\text{GeMn}_{3.4}$, ς - Ge_2Mn_5 (Ohba *et al.*, 1987), κ - Ge_3Mn_7 , η - Ge_3Mn_5 (Ohoyama, 1961), GeMn_2 (Ellner, 1980) and $\text{Ge}_8\text{Mn}_{11}$ (Ohba *et al.*, 1984). Although some of them are FM, they all exhibit a metallic character that makes them poor candidates for spin injection in non-magnetic semiconductors due to conductivity mismatch (Fert and Jaffrès, 2001). Other (Ge,Mn) alloys could be prepared by melting Ge and Mn under very high pressure ($\simeq 4$ -6 GPa) by Takizawa. Metastable alloys such as Ge_5Mn_3 (Takizawa *et al.*, 1987), GeMn (Takizawa *et al.*, 1988), Ge_4Mn (Takizawa *et al.*, 1990) or GeMn_3 (Takizawa *et al.*, 2002) could be obtained. All these (Ge,Mn) alloys are Ge-rich and thus can exhibit a semiconducting character required for direct spin injection in semiconductors. At this stage, it should be noted that low temperature MBE could also allow to grow metastable (Ge,Mn) alloys thanks to high epitaxial strain.

The very low solubility of Mn in Ge was further theoretically demonstrated using *ab-initio* calculations. For instance, in order to increase Mn concentration, mixing substitutional and interstitial Mn in germanium lowers the free energy of the system (Arras *et al.*, 2012; Continenza *et al.*, 2007). At last, except in the work by Zeng (Zeng *et al.*, 2008), most groups have experimentally observed inhomogeneous Mn-doped germanium films. Inhomogeneities can be either secondary phase precipitates such as Ge_3Mn_5 clusters or Mn-rich nanostructures due to spinodal decomposition. Indeed spinodal decomposition leads to the formation of Mn-rich nanometer sized areas (either a metastable (Ge,Mn) alloy or Ge lattice with high Mn content) surrounded with an almost pure germanium matrix. In the next section, we make a thorough review of the results obtained on the (Ge,Mn) material.

1. Review of experimental results

As already mentioned, in order to prevent the formation of stable metallic (Ge,Mn) phases, out-of-equilibrium growth techniques are required. In the following, we summarize Mn implantation in germanium and MBE growth of thin (Ge,Mn) films. Ottaviano *et al.*, 2006 first performed Mn implantation in germanium (up to 4%) at 240°C and 270°C substrate temperatures. Before and after annealing (to improve the crystalline quality) Mn-rich precipitates are observed by TEM. These precipitates are amorphous before annealing and Ge_3Mn_5 clusters after annealing. In addition, x-ray absorption measurements showed that Mn-rich precipitates only form in the deeper part and substitutional Mn are detected close to the film surface (Ottaviano *et al.*, 2007). Ferromagnetic behavior was further observed by magneto-optical Kerr effect measurements up to 270 K (before annealing) and 255 K (after annealing). However the magnetic signal clearly arises from many different magnetic phases including Ge_3Mn_5 . Passacantando *et al.*, 2006 found similar results using different implantation doses in germanium wafers. At low implantation dose, Mn-rich precipitates are amorphous whereas they form Ge_3Mn_5 clusters at higher implantation doses as shown in Fig. 45(b). The second technique widely used to grow Mn-doped Ge films is low temperature MBE. Following the first results published by Park *et al.*, 2002b, many groups have attempted to dilute large amounts of Mn in Ge in order to raise T_C up to RT. D'Orazio *et al.*, 2004 investigated the magnetic and electrical properties of thin epitaxial $\text{Ge}_{1-x}\text{Mn}_x$ films ($0.027 < x < 0.044$) exhibiting ferromagnetism up to 250 K. Pinto *et al.*, 2005 and Morresi *et al.*, 2006 interpreted experimental observations in the framework of magnetic polaron percolation. However further structural characterizations showed that (Ge,Mn) epilayers contained Ge_3Mn_5 clusters surrounded with germanium containing almost 1.5% of substitutional paramagnetic Mn atoms. Similar results were also reported by others (Bihler *et al.*, 2006; Padova *et al.*, 2007, 2008). Finally, using high resolution TEM and energy dispersive x-ray spectroscopy, Sugahara *et al.*, 2005 could show the phase separation between Mn-rich amorphous clusters and a pure Ge matrix in thin epitaxial (Ge,Mn) films [see Fig. 45(c)].

The second metallic (Ge,Mn) phase that usually forms during MBE growth is $\text{Ge}_8\text{Mn}_{11}$. This phase exhibits two magnetic transitions at 150 K (AF/FM) and $T_C = 285$ K (FM/paramagnetic). $\text{Ge}_8\text{Mn}_{11}$ precipitates were observed by Park in thin $\text{Ge}_{1-x}\text{Mn}_x$ films ($0 < x < 0.12$) epitaxially grown between 250°C and 300°C (Park *et al.*, 2001). Using different methods to grow bulk single crystals, the same $\text{Ge}_8\text{Mn}_{11}$ phase could be detected by Cho *et al.*, 2002; Kang *et al.*, 2005 and Biegger *et al.*, 2007 performing chemical analysis at the micrometer scale, as shown in Fig. 45(d). More recently, by investigating Mn-doped (up to 4%) Ge films epitaxially grown on Ge(001) using various TEM techniques, Wang *et al.*, 2008 could

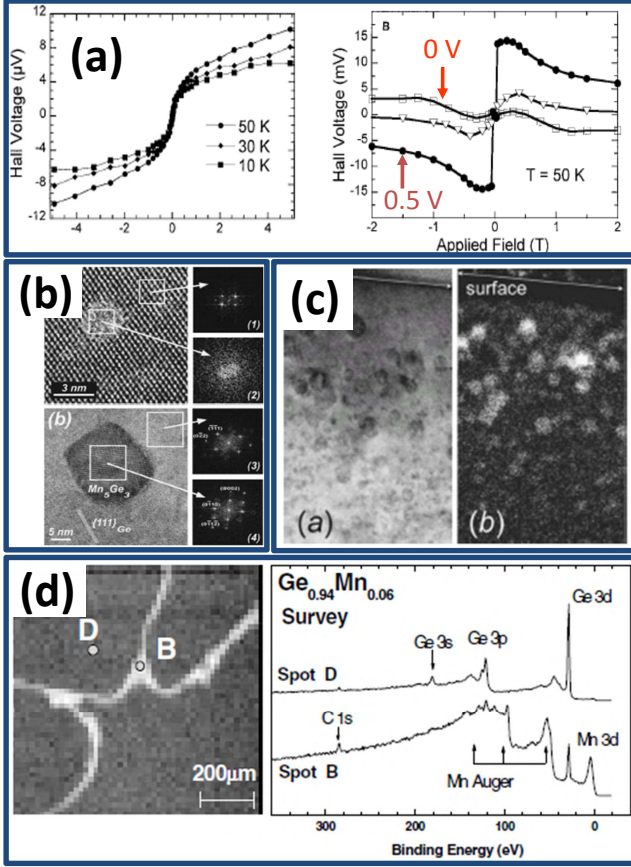


FIG. 45 (color online) Characterization of (Ge,Mn) samples obtained by various methods. (a) Anomalous Hall effect measured at 10, 30 and 50 K in a $\text{Mn}_{0.023}\text{Ge}_{0.937}$ film grown by LT-MBE (left) and voltage control of AHE (right). From Park *et al.*, 2002b. (b) HRTEM images of a Ge(100) wafer implanted at a dose of 1×10^{16} (up) and 4×10^{16} (down) Mn^+ ions/cm². At low dose, Mn-rich areas are amorphous whereas at high dose, they form Ge_3Mn_5 clusters. From Passacantando *et al.*, 2006. (c) TEM image of a GeMn film grown by LT-MBE showing amorphous $\text{Ge}_{1-x}\text{Mn}_x$ clusters (left) and corresponding energy dispersive x-ray spectroscopy image (right). Bright areas are Mn-rich. From Sugahara *et al.*, 2005. (d) Scanning photoelectron microscopy image of a $\text{Ge}_{0.94}\text{Mn}_{0.06}$ single crystal (left) and the survey spectra obtained at a bright spot (B) and a dark spot (D) respectively (right). From Kang *et al.*, 2005.

find the coexistence of $\text{Ge}_8\text{Mn}_{11}$ and Ge_2Mn_5 clusters. Moreover, by well adjusting growth parameters, these crystalline precipitates could be replaced by undefined Mn-rich nanostructures.

Since 2005, many groups have indeed reported the absence of any secondary phase precipitation in (Ge,Mn) films epitaxially grown at low temperature ($< 100^\circ\text{C}$). However, due to the very low solubility of Mn in Ge, the formation of Mn-rich nanostructures seems unavoidable mostly as a result of spinodal nanodecomposition. These

nanostructures are so hard to detect that only highly sensitive techniques such as TEM with nanoscale chemical analysis, 3DAP or XRD/XAS using synchrotron radiation can be used. From the low temperature MBE growth of $\text{Ge}_{0.94}\text{Mn}_{0.06}$ films, Sugahara *et al.*, 2005 found elongated Mn-rich amorphous precipitates surrounded with pure germanium. These precipitates exhibit ferromagnetism up to 100 K as given by MCD measurements. Their diameter is close to 5 nm and the Mn content in between 10% and 20%. Using almost the same growth conditions, Ahlers *et al.*, 2006; Bougeard *et al.*, 2006, 2009 observed the formation of Mn-rich cubic clusters coherently strained on the Ge matrix in addition to the precipitation of Ge_3Mn_5 clusters. Assuming zero Mn content in the Ge matrix, the maximum Mn content in the clusters is close to 15%. Their diameter is slightly less than 5 nm. Moreover they exhibit superparamagnetic behavior and a T_C value close to 200 K. Still using low temperature MBE growth and according to magnetic measurements only, Jaeger concluded that $\text{Ge}_{1-x}\text{Mn}_x$ films ($x=0.04$ and 0.2) contain two clusters populations (undefined Mn-rich precipitates and Ge_3Mn_5 clusters) along with diluted Mn atoms in the germanium matrix (Jaeger *et al.*, 2006). The overall population of Mn-rich precipitates behaves as a spin glass. The freezing temperatures are 12 and 15 K in $\text{Ge}_{0.96}\text{Mn}_{0.04}$ and $\text{Ge}_{0.8}\text{Mn}_{0.2}$ films, respectively. Finally Li also found elongated Mn-rich precipitates but coherently strained on the surrounding Ge matrix (Li *et al.*, 2007). In as-grown $\text{Ge}_{0.95}\text{Mn}_{0.05}$ samples, these precipitates show ferromagnetism at low temperature: remanence vanishes above 12 K. Post-growth annealing at 200°C leads to a rather substantial improvement in magnetic and electrical properties by converting interstitial Mn into substitutional Mn. They exhibit remanence up to 125 K, the magnetic moment per Mn atom reaches $1.5 \mu_B$ instead of $1.0 \mu_B$ in as-grown samples. Moreover, annealing triggers strong positive MR and AHE in (Ge,Mn) films.

To summarize, the key issue of (Ge,Mn) material is Mn-dilution: the very low solubility of Mn in Ge always results in Mn segregation and in the formation of Mn-rich precipitates. Low temperature growth techniques favor the formation of metastable (Ge,Mn) phases. As a consequence, slight differences in growth parameters can result in much different magnetic and electrical properties. In the following sections, we show how to control spinodal nanodecomposition in (Ge,Mn). The structure, magnetic and electrical properties of (Ge,Mn) films with spinodal nanodecomposition are reviewed.

C. Growth and structure of thin (Ge,Mn) films with spinodal decomposition

1. Sample preparation

Growth was performed using solid sources MBE by co-depositing Ge and Mn evaporated from standard Knud-

sen effusion cells (Devillers *et al.*, 2007a, 2006, 2007b; Jamet *et al.*, 2006). The deposition rate was kept constant and quite low ($\simeq 0.2 \text{ \AA}\cdot\text{s}^{-1}$). Germanium substrates were epi-ready Ge(001) wafers with a residual n-type doping and resistivity of 10^{15} cm^{-3} and $5 \text{ }\Omega\text{cm}$ respectively. After thermal desorption of the surface oxide, a 40 nm thick Ge buffer layer was grown at 250°C , resulting in a 2×1 surface reconstruction as observed by RHEED (see Fig. 46). Next, 80 nm thick $\text{Ge}_{1-x}\text{Mn}_x$ films were subsequently grown at low substrate temperature (between $T_g = 80^\circ\text{C}$ and $T_g = 200^\circ\text{C}$). Mn content has been determined by x-ray fluorescence measurements performed on thick samples ($\simeq 1 \mu\text{m}$ thick) and complementary Rutherford back scattering (RBS) on thin $\text{Ge}_{1-x}\text{Mn}_x$ films grown on silicon. Mn concentrations range from 1% to 11% Mn.

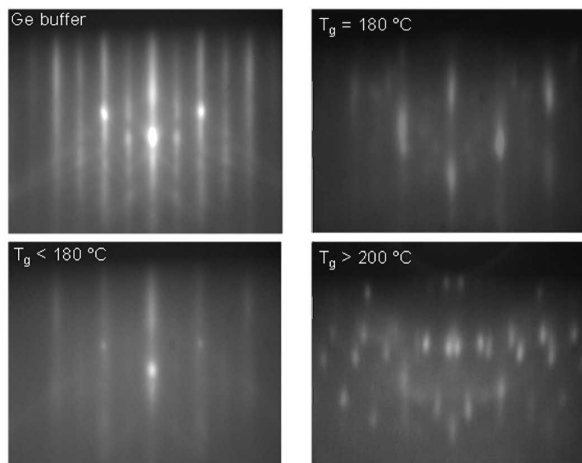


FIG. 46 RHEED patterns recorded for different growth temperatures of $\text{Ge}_{1-x}\text{Mn}_x$. Adapted from Devillers *et al.*, 2007a.

For $\text{Ge}_{1-x}\text{Mn}_x$ films grown at substrate temperatures below 180°C , after the first monolayer (ML) deposition, the 2×1 surface reconstruction almost totally disappears. After depositing few MLs (corresponding almost to 5 nm), a slightly diffuse 1×1 streaky RHEED pattern and a very weak 2×1 reconstruction (Fig. 46) indicate the predominantly 2D growth of a single crystalline film exhibiting the same lattice parameter as the Ge buffer layer. Increasing the layer thickness leads to an amplification of the surface roughness which is expected for the low temperature epitaxial growth of germanium (Chason *et al.*, 1989; Venkatasubramanian and Dorsey, 1993). For growth temperatures above 180°C additional spots appear in the RHEED pattern during the $\text{Ge}_{1-x}\text{Mn}_x$ growth (Fig. 46). These spots correspond to the formation of very small Ge_3Mn_5 crystallites.

2. Morphology of (Ge,Mn) films

From TEM images, vertical elongated nanostructures, i.e., nanocolumns were observed as shown in Fig. 47(a).

These observations are in very good agreement with the theoretical predictions of Sec. II. The formation of the konbu phase as a consequence of 2D spinodal decomposition in (Ge,Mn) is clearly demonstrated here as well as in (Zn,Cr)Te in Sec. VIII. Similar elongated nanostructures were also obtained in (Ge,Mn) by several groups in comparable growth conditions [Fig. 47(b-e)]. Nanocolumns span the entire $\text{Ge}_{1-x}\text{Mn}_x$ film thickness. Whatever the growth temperature and Mn concentration (except 0.1%) are, $\text{Ge}_{1-x}\text{Mn}_x$ films always exhibit the presence of nanocolumns with their axis along the growth direction [001]. Depending on growth conditions, the average columns diameter and density range between 2 and 7 nm, and between $10000 \mu\text{m}^{-2}$ and $40000 \mu\text{m}^{-2}$, respectively.

Further evidence of 2D spinodal nanodecomposition was provided by analyzing the periodic structures of the nanocolumns (Hai *et al.*, 2011; Yada *et al.*, 2011). Figure 48(a) presents a plain-view TEM image showing that the nanocolumns are uniform in diameter ($\sim 3 \text{ nm}$), and form either rectangular or triangular lattice structures, as indicated by thin dashed lines in Fig. 48(a). According to the Fourier transform of the TEM image, depicted in Fig. 48(b), the average distance between the nanocolumns is $\sim 9 \text{ nm}$.

The morphology of $\text{Ge}_{1-x}\text{Mn}_x$ films was further investigated using grazing incidence small angle x-ray scattering (GISAXS) from synchrotron radiation and atomic force microscopy (AFM), as depicted in Fig. 49.

As shown in Fig. 49(a), in addition to the specular reflection peak in the GISAXS spectrum, two pairs of correlation peaks were observed. The first one at large q_x value corresponds to a correlation length of $\simeq 10 \text{ nm}$ which is the average distance between nanocolumns. The oscillations along q_z are thickness oscillations and stand for the finite thickness of the $\text{Ge}_{1-x}\text{Mn}_x$ film. It demonstrates that nanocolumns span the entire film thickness. Furthermore there is a sizeable contrast of electronic density between nanocolumns and the surrounding matrix. At low q_x value, a second pair of correlation peaks corresponds to a distance of almost 50 nm. Moreover these peaks are much more elongated along q_z which is characteristic of a surface effect. Indeed, correlations are no more related to the presence of nanocolumns but to the surface roughness, as shown in Fig. 49(b). In order to investigate the columns chemical composition, electron energy loss spectroscopy (EELS) has been performed in cross section and plane view. The corresponding energy filtered TEM (EFTEM) images close to the Mn $L_{2,3}$ edge are displayed in Fig. 50 along with the corresponding Mn chemical profiles.

From EFTEM images, one can conclude that nanocolumns are Mn-rich and surrounded with an almost pure Ge matrix. The Mn signal in the Ge matrix is indeed below the resolution limit of EELS spectroscopy estimated to be around 1%. The most appropriate technique to estimate with more accuracy the Mn content in the Ge matrix is 3DAP. It leads to an average Mn concentration inside the Ge matrix below 0.05% ((Mouton

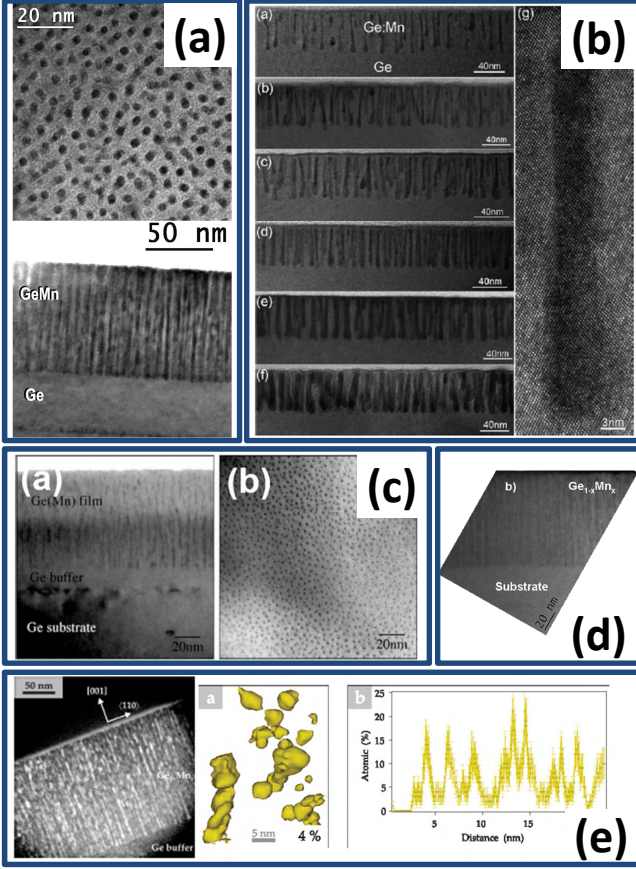


FIG. 47 (Color online) Characterization of $\text{Ge}_{1-x}\text{Mn}_x$ thin films grown by LT-MBE. (a) TEM plane view (up) and cross section (down) images of $\text{Ge}_{0.9}\text{Mn}_{0.1}$ containing Mn-rich nanocolumns. From Devillers *et al.*, 2007a. (b) TEM cross section images of films with $x = 2.5, 4, 4.5, 5.5, 7$, and 12% from top to bottom. The morphology of Mn-rich nanocolumns evolves from tadpole-like to cylinders when increasing Mn content. From Wang *et al.*, 2010. (c) and (d) TEM images of $\text{Ge}_{0.95}\text{Mn}_{0.05}$ (from Li *et al.*, 2007) and $\text{Ge}_{0.94}\text{Mn}_{0.06}$ (from Le *et al.*, 2010), respectively showing the presence of nanocolumns. (e) Vertical self-assembly of roughly spherical Mn-rich clusters: TEM cross section image in dark field with $x = 7.3\%$ (left) and APT data for $x = 2\%$ (right). From Bougeard *et al.*, 2009.

et al., 2012)). As a consequence, the Mn concentration in the nanocolumns shown in Fig. 50 is close to 30%. Hence the composition of nanocolumns is close to Ge_2Mn . Depending on the growth conditions, nanocolumns with Mn concentrations between 5 and 50% could be grown, all of them exhibiting FM properties (Devillers *et al.*, 2007a).

3. Lateral and vertical control of nanocolumns

In order to achieve lateral control of nanocolumns (size and density), the growth temperature and Mn concentra-

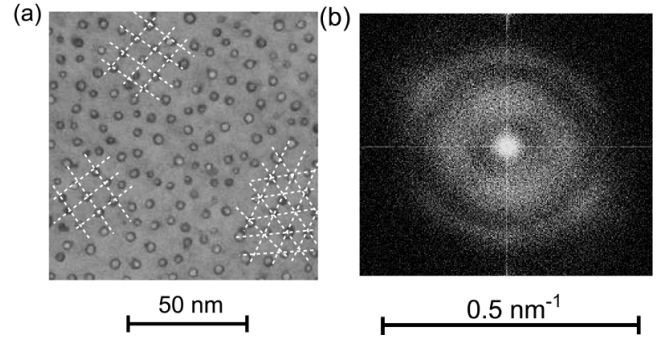


FIG. 48 (a) Plain-view TEM image of Mn-rich nanocolumns embedded in a Ge matrix fabricated by MBE of a 30 nm-thick $\text{Ge}_{0.94}\text{Mn}_{0.06}$ film onto a $\text{Ge}(001)$ substrate at 100°C with a growth rate of 150 nm/h. (b) Fourier transform of the contrast of a $0.36 \times 0.36 \mu\text{m}^2$ TEM image. Ring structures up to second harmonic are clearly seen, indicating strong 2D spinodal decomposition. Adapted from Hai *et al.*, 2011.

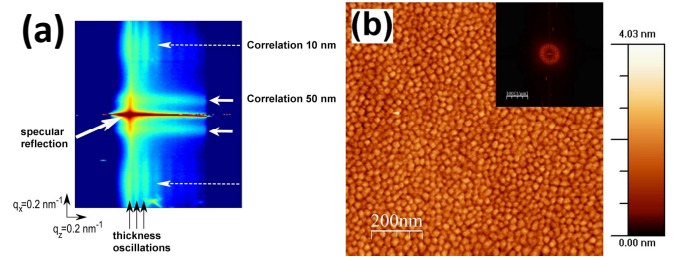


FIG. 49 (Color online) Characterization of a $\text{Ge}_{0.93}\text{Mn}_{0.07}$ film grown at 150°C . (a) GISAXS spectrum; the nanocolumns diameter is 5 nm and their density $8100 \mu\text{m}^{-2}$. Adapted from Tardif *et al.*, 2010b. (b) Corresponding AFM image of the film surface. The maximum roughness amplitude is of the order of 1 nm and corresponds to the formation of small islands at the film surface. The fast Fourier transform (inset) of this picture clearly exhibits the presence of a correlation ring between surface islands of the order of 30 nm. From Devillers, 2008.

tion were varied to study their respective influence. For this purpose, two series of $\text{Ge}_{1-x}\text{Mn}_x$ films were grown at two different growth temperatures: $T_g = 100^\circ\text{C}$ and $T_g = 150^\circ\text{C}$. In each case, the Mn concentration x was varied between 1 and 11%. All the samples were then observed by TEM in plane view: they all exhibit Mn segregation in Mn-rich nanocolumns surrounded with an almost pure Ge matrix. The results are shown in Fig. 51.

For samples grown at 100°C with Mn concentrations below 5% the nanocolumns mean diameter is 1.8 ± 0.2 nm. For higher Mn concentrations, it only slightly increases up to 2.8 nm at 11.3%. The evolution of columns density as a function of Mn concentration is also reported in Fig. 51. By increasing the Mn concentration up to 7% a significant increase of the columns density from 13000 to $35000 \mu\text{m}^{-2}$ was observed. Then the density seems to reach a plateau corresponding to almost $40000 \mu\text{m}^{-2}$.

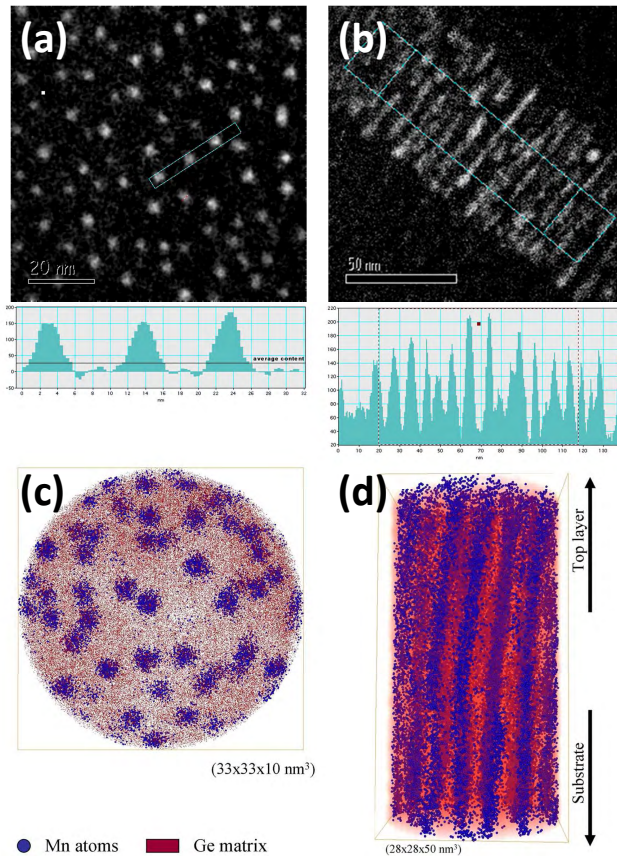


FIG. 50 (Color online) Characterization of a $\text{Ge}_{0.94}\text{Mn}_{0.06}$ film grown at 130°C . (a) and (b) Cross sectional and plane view EFTEM images. (c) and (d) 3DAP reconstructed 3D images. From Mouton *et al.*, 2012. Below EFTEM images are the corresponding Mn chemical profiles (bright areas are Mn-rich). From Jamet *et al.*, 2006.

Hence, increasing Mn concentration in samples grown at 100°C allows to control the columns density while keeping their diameter constant. Increasing the Mn content in the samples grown at 150°C from 1.3 to 11.3% leads to a slight decrease of the columns density as shown in Fig. 51. However, their average diameter increases significantly and size distributions become much broader. For the highest Mn concentration (11.3%) very small columns with a diameter of 2.5 nm are coexisting with very large columns with a diameter of 9 nm. Therefore increasing Mn concentration in samples grown at 150°C allows to control the columns diameter while keeping their density constant around $10000 \mu\text{m}^{-2}$. To summarize, by combining two growth parameters (temperature and Mn concentration), it is possible to control independently the diameter and density of nanocolumns. This ability is of great importance from a fundamental point of view to characterize nanocolumns but also for potential applications in spintronic devices. In Fig. 51, the volume fraction

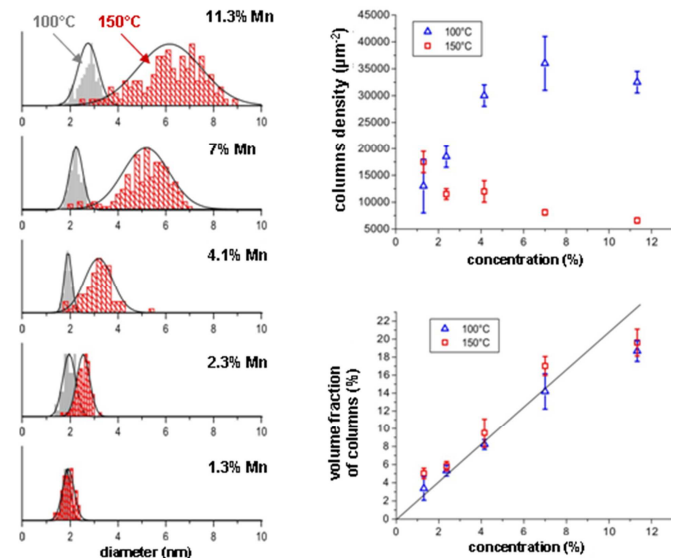


FIG. 51 (Color online) Lateral control of nanocolumns. From Devillers *et al.*, 2007a.

occupied by the columns in the film is reported as a function of Mn concentration showing a clear linear dependence for Mn contents up to almost 7%. The non-linear behavior above 7% can indicate that the mechanism of Mn incorporation is different in this concentration range, leading to an increase of Mn concentration in the columns and/or in the matrix.

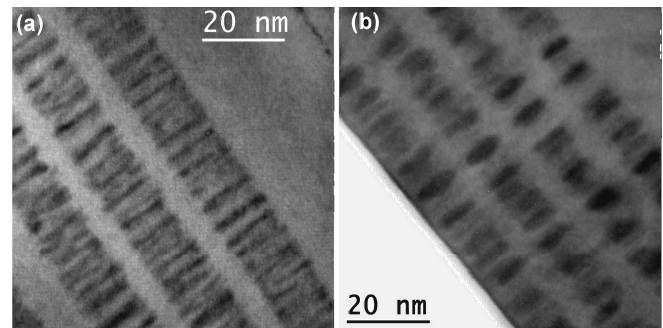


FIG. 52 (Color online) HRTEM images of $(\text{GeMn}/\text{Ge})_4$ superlattices observed along the $[110]$ crystal axis. From Devillers, 2008. In (a), no vertical correlation is observed whereas in (b) the vertical positions are clearly correlated and columns well aligned. In both cases, the germanium spacer is 5 nm thick.

Considering the vertical geometry of nanocolumns and the Mn concentration contrast between the columns and the Ge matrix, vertical transport will mainly take place through nanocolumns. Since nanocolumns are FM (see Sec. VI.D), they could be used as conduction channels for spin injection in non-magnetic semiconductors such as Si and Ge. The vertical control of nanocolumns is thus an important issue from a fundamental point of view as well

as for potential applications in spintronics. For this purpose, (GeMn/Ge) superlattices have been grown using different growth conditions. The (GeMn/Ge)₄ superlattice in Fig. 52(a) was grown in *standard* conditions (0.2 Å/s, 6% of Mn, $T_g = 100^\circ\text{C}$) leading to the formation of small nanocolumns with no vertical self-organization. The superlattice in Fig. 52(b) was grown at higher temperature (140°C) using a lower growth rate (0.13 Å/s) in order to favor the surface diffusion of Mn. Moreover the Mn content was increased up to 10% to grow larger columns. Assuming that the lattice parameters within the columns and the Ge matrix are different, larger columns lead to an enhanced residual strain field which favors the nucleation of nanocolumns on top of each other as in quantum dots superlattices (Tersoff *et al.*, 1996). By this method, the vertical self-organization of nanocolumns could be achieved (Wang *et al.*, 2011). Since the interface between nanocolumns and Ge spacer are quite abrupt, the diffusion of Mn along the growth direction is limited and then restricted to the top surface layer as discussed in the next section.

4. Two-dimensional spinodal decomposition

In order to understand the growth mechanism of nanocolumns, the first growth stage of (Ge,Mn) films on Ge(001) were investigated. For this purpose, scanning tunneling microscopy (STM) images have been recorded after depositing 0.44 Å of Mn on Ge(001) at 80°C [Fig. 53(a)].

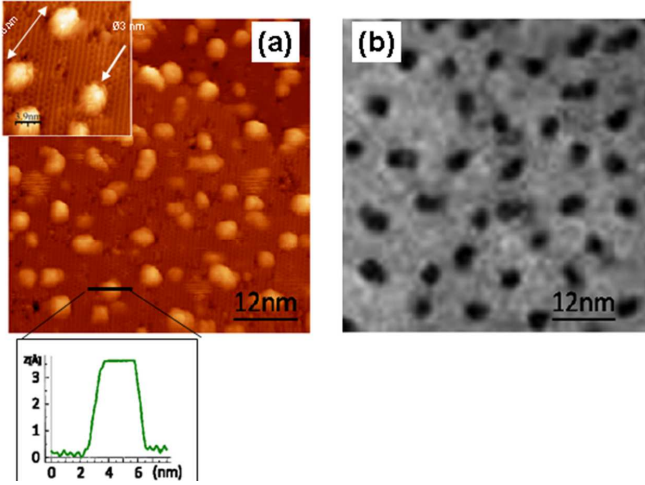


FIG. 53 (Color online) Formation of nanocolumns from self-assembled nanoislands. (a) STM image of a germanium surface after depositing 0.44 Å of Mn at 80°C (from Lethanh, 2006). The inset shows the diameter of self-assembled islands (≈ 3 nm) and the distance between nearest-neighbors (≈ 10 nm). The reported z-profile gives an estimation of their height: 3.5 Å. (b) Plane view TEM image of a 80 nm thick $\text{Ge}_{0.94}\text{Mn}_{0.06}$ film grown at 130°C (adapted from Jamet *et al.*, 2006).

They show the formation of self-assembled nanoislands. Their size and density are further comparable to the size and density of nanocolumns in as-grown (Ge,Mn) films [Fig. 53(b)]. Therefore, nanoislands are most probably Mn-rich nuclei at the origin of the formation of nanocolumns. Accordingly, this observation implies that the columns size and density are fully determined at the first growth stage. This growth mode leading to the formation of the konbu phase is summarized in Sec. II. It results from 2D spinodal decomposition due to Mn-Mn chemical pair attraction followed by layer-by-layer growth (Fukushima *et al.*, 2006b; Zheng *et al.*, 2010). The expected scenario for the growth of Mn-rich nanocolumns is thus illustrated in Fig. 54.

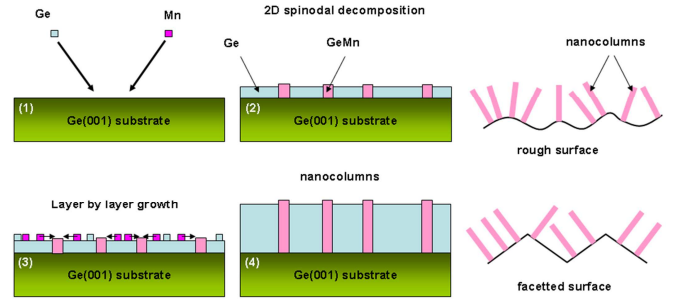


FIG. 54 (Color online) Nanocolumn growth and geometry. Left: four-steps scenario for the growth of Mn-rich nanocolumns in germanium. (1) Ge and Mn atoms are co-deposited by LT-MBE on the germanium surface. (2) Due to strong Mn-Mn pair attraction, a two-dimensional spinodal decomposition takes place at the first growth stage setting the size and density of nanocolumns. (3) Layer-by-layer growth with surface diffusion of Mn atoms. Due to Mn-Mn pair attraction, Mn atoms aggregate on top of Mn-rich areas. (4) Mn-rich nanocolumns perpendicular to the initial surface are obtained. Right: expected columns geometries for a rough and faceted initial surface. From Jamet, 2010.

As a consequence, nanocolumns will always grow perpendicular to the initial surface. Therefore, they will exactly follow the initial surface roughness or facets (Fig. 54). In order to support this conclusion, thin (Ge,Mn) films were grown in *standard* growth conditions on a rough GaAs(001) surface as well as on a faceted Ge surface (Yu *et al.*, 2010, 2011).

The resulting (Ge,Mn) films were then observed by TEM in cross section (Fig. 55). On GaAs(001), Mn-rich nanocolumns are clearly bent following the initial surface roughness. On the faceted Ge surface, nanocolumns have their axis perpendicular to the {113} facets (Yu *et al.*, 2010). Hence 2D spinodal decomposition and further layer-by-layer growth are most probably the mechanisms responsible for the formation of Mn-rich nanocolumns.

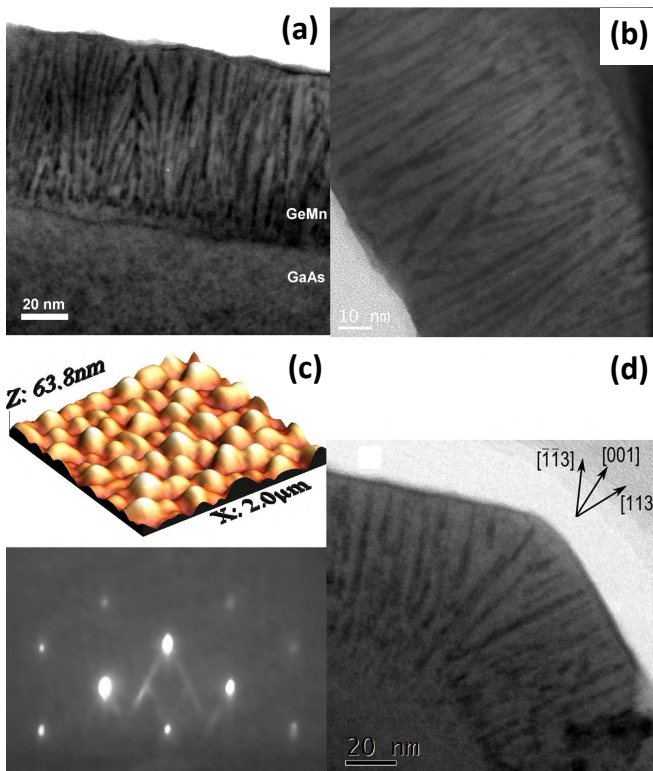


FIG. 55 (Color online) (a) Low and (b) HRTEM cross section images of a 80 nm thick $\text{Ge}_{0.9}\text{Mn}_{0.1}$ film grown at 100°C on $\text{GaAs}(001)$. Before the growth, the native oxide layer was first thermally removed from the $\text{GaAs}(001)$ substrate at 600°C leading to a rough Ga -rich surface. (c) AFM image and RHEED pattern of a faceted Ge surface obtained after anisotropic chemical etching revealing $\{113\}$ facets. (d) TEM cross section image of a 80 nm thick $\text{Ge}_{0.94}\text{Mn}_{0.06}$ film grown at 100°C on the faceted Ge surface. After Yu *et al.*, 2010.

5. Crystal structure of nanocolumns

The crystalline structure of (Ge,Mn) films was investigated using high resolution TEM observations as well as XRD and XAS. High resolution TEM observations in cross section show that $\text{Ge}_{1-x}\text{Mn}_x$ films grown below 180°C are single crystalline in epitaxial relationship with the substrate [Fig. 56(a)]. Furthermore nanocolumns can hardly be distinguished. The interface between the Ge buffer layer and the $\text{Ge}_{1-x}\text{Mn}_x$ film is flat and no defect propagates from the interface into the film. Diffraction scans performed in $\theta/2\theta$ mode were acquired on a high resolution diffractometer using synchrotron radiation. The scans only reveal the (004) Bragg peak of the germanium crystal, confirming the good epitaxial relationship between the layer and the substrate, and the absence of secondary phases to a good accuracy proven by a high ratio of the main peak intensity to noise, of the order of 10^7 [inset in Fig. 56(a)].

In order to get further insight into the crystalline structure of nanocolumns, grazing incidence SXRD was stud-

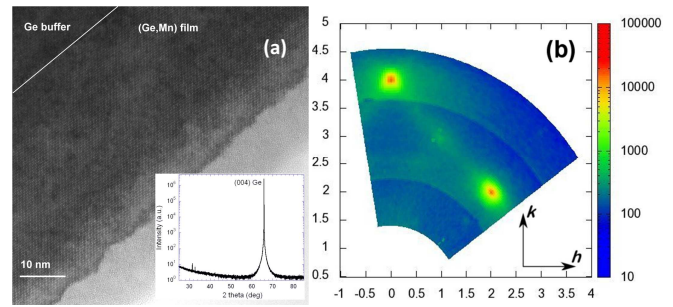


FIG. 56 (Color online) (a) HRTEM image of a 80 nm thick $\text{Ge}_{0.94}\text{Mn}_{0.06}$ sample grown at 130°C . Inset: XRD showing the single (004) Bragg peak of pure Ge . (b) $(h, k, 0)$ map of the reciprocal space performed on a $\text{Ge}_{0.94}\text{Mn}_{0.06}$ film grown at 150°C . Adapted from Tardif *et al.*, 2010b.

ied. The reciprocal space of a $\text{Ge}_{0.94}\text{Mn}_{0.06}$ film grown at 150°C [Fig. 56(b)] was mapped. In addition to the (400) and (220) Bragg peaks of germanium, two additional features were found: a broad (130) peak (which is forbidden in the diamond lattice) and a diffuse line connecting (400) and (220) Bragg peaks. At this stage, none of them could be related to the crystalline structure of nanocolumns (Tardif *et al.*, 2010b). (220) and (400) Bragg peaks further exhibit correlation rings related to anisotropic elastic strain in the germanium matrix between nanocolumns (Tardif *et al.*, 2010b). Since the internal crystalline structure of nanocolumns could not be resolved using XRD, three conclusions can be drawn: (i) nanocolumns exhibit the same diamond lattice as germanium with high Mn content, (ii) they are made of a metastable (Ge,Mn) phase showing a diffraction pattern similar to that of pure germanium and (iii) they are amorphous. In the following, the decisive role of the growth temperature on the columns crystalline structure is discussed.

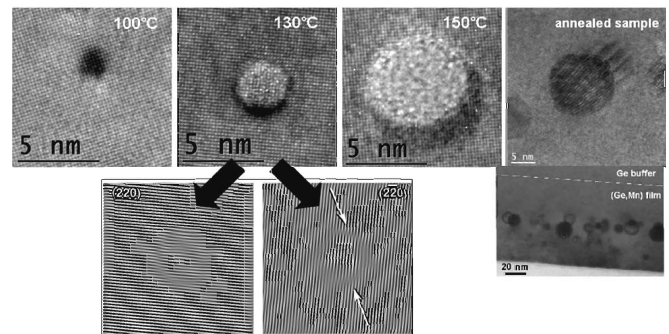


FIG. 57 (Color online) Crystalline structure of nanocolumns as a function of growth temperature. From left to right: $\text{Ge}_{0.99}\text{Mn}_{0.01}$ film grown at 100°C ; $\text{Ge}_{0.94}\text{Mn}_{0.06}$ film grown at 130°C ; $\text{Ge}_{0.887}\text{Mn}_{0.113}$ film grown at 150°C ; $\text{Ge}_{0.94}\text{Mn}_{0.06}$ film grown at 130°C and annealed at 650°C for 15 minutes. Adapted from Jamet *et al.*, 2006 and Devillers *et al.*, 2007a.

High resolution TEM observations in plane view

clearly demonstrate an evolution of the columns structure with growth temperature (Fig. 57). For $T_g = 100^\circ\text{C}$, small nanocolumns are fully strained on the surrounding Ge matrix and clearly exhibit a perfect cubic crystal. For $T_g = 130^\circ\text{C}$, crystalline columns were still observed. However, performing (220) and (2 $\bar{2}$ 0) Bragg filtering of diffraction spots, a pair of dislocations at the interface between the column and the Ge matrix is clearly visible. That leads to a lattice expansion of almost 4% in the column. Nanocolumns are thus only partially strained. For $T_g = 150^\circ\text{C}$, nanocolumns are amorphous. Finally, for samples grown at $T_g > 180^\circ\text{C}$ or annealed at high temperature, nanocolumns have collapsed into stable Ge_3Mn_5 clusters. For annealed samples, these clusters are further well buried inside the germanium film away from the surface.

Since magnetic properties highly depend on the relative position of Mn atoms in the nanocolumns, the local chemical environment of Mn atoms was probed by EXAFS measurements (Rovezzi *et al.*, 2008). By fitting EXAFS oscillations, the chemical environment of Mn atoms in the nanocolumns was found very similar to that of a Mn atom in an elementary tetrahedron of the Ge_3Mn_5 unit cell. This elementary tetrahedron corresponds to the building block of nanocolumns. However, at this stage, the structure of crystalline columns grown at low temperature still remains unknown. Nevertheless, a possible phase which exhibits a crystalline structure and composition compatible with the experimental findings was proposed by Arras *et al.*, 2012. This phase is called the α -phase and corresponds to a new class of materials based on the insertion of Mn atoms into a simple cubic crystal of Ge. Arras has shown that the incorporation of this phase (with a Mn content ranging from 10 to 50%) in the form of nanocolumns into the pure Ge matrix is energetically favorable (Arras *et al.*, 2012).

D. Magnetic properties

In this section, the magnetic properties of four different $\text{Ge}_{1-x}\text{Mn}_x$ films grown at different temperatures are investigated: crystalline columns with and without partial relaxation through the formation of a pair of dislocations, amorphous nanocolumns and Ge_3Mn_5 clusters. For this purpose, highly sensitive SQUID magnetometry as well as electron paramagnetic resonance (EPR) were thoroughly used.

1. Crystalline (Ge,Mn) nanocolumns / Ge(001)

Magnetic measurements on diluted $\text{Ge}_{0.999}\text{Mn}_{0.001}$ films grown at 100°C are first reported. Only a paramagnetic signal at low temperature by SQUID and the 6 isotropic hyperfine absorption lines characteristic of paramagnetic Mn atoms in EPR spectra (not shown) could be measured. This result is in good agreement with TEM

observations and EXAFS measurements. Indeed the absence of any contrast in TEM images rules out the presence of nanocolumns and EXAFS oscillations could be fitted with a single substitutional environment.

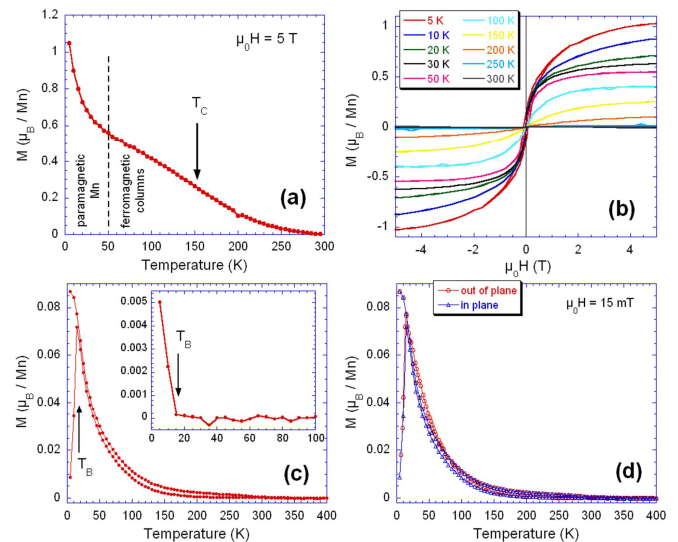


FIG. 58 (Color online) Magnetic characterization of a $\text{Ge}_{0.9}\text{Mn}_{0.1}$ film grown at 100°C . (a) Temperature dependence of the saturation magnetization (in μ_B/Mn). The applied field is 5 T. (b) Magnetization curves for different temperatures and (c) ZFC-FC measurements, pointing to with $T_C \approx 150$ K of nanocolumns. The in-plane applied field is 0.015 T. Inset: magnetic remanence after maximum field cooling under 5 T. (d) ZFC measurements performed with the field parallel and perpendicular to the film plane. From Jain *et al.*, 2010.

For more concentrated films grown at $T_g = 100^\circ\text{C}$, small nanocolumns spanning the whole film thickness are observed by TEM. Moreover they are well crystalline and in perfect epitaxial relationship with the Ge matrix (see Fig. 57). Assuming that the Mn concentration in the Ge matrix below 0.05%, the resulting Mn content in the columns is close to 50%. SQUID measurements performed on a $\text{Ge}_{0.9}\text{Mn}_{0.1}$ film are reported in Fig. 58. Two different contributions in Fig. 58(a) can be identified: a paramagnetic signal from isolated Mn atoms and the FM nanocolumns. It has been shown recently that the paramagnetic Mn atoms are located within a thin shell around nanocolumns (Prestat *et al.*, 2014). The T_C magnitude of the columns is of the order of 150 K, according to Figs. 58(b,c) (Jain *et al.*, 2010). In Fig. 58(b), magnetization curves are reversible above 15 K, also confirmed by ZFC-FC curves and dependence of remanence with temperature [Fig. 58(c)]. These nanocolumns are superparamagnetic with a blocking temperature of 15 ± 5 K. Moreover the narrow shape of the ZFC peak is related to the narrow size distribution of nanocolumns grown in this temperature range (see Fig. 51). To determine the magnetic anisotropy of these columns, ZFC-FC measurements were performed with the field parallel and perpen-

pendicular to the film plane. The susceptibility perpendicular to the plane seems slightly higher than that in the plane but a strong diamagnetic signal from the substrate and paramagnetic signal from diluted Mn atoms makes it difficult to quantify precisely this anisotropy.

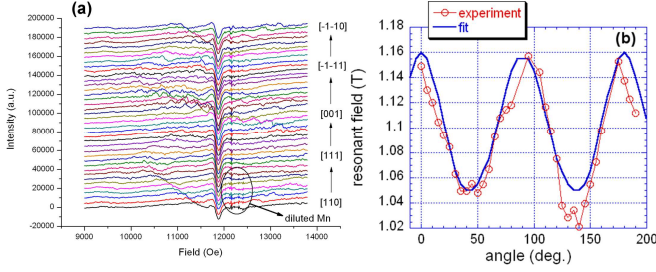


FIG. 59 (Color online) (a) EPR absorption spectra of a $\text{Ge}_{0.9}\text{Mn}_{0.1}$ film grown at 100°C as a function of the static field orientation at 5 K. The angle is defined between the [110] direction and the applied magnetic field. The working frequency is 34 GHz (Q-band set-up). Two different contributions can be observed: a FM broad peak of weak anisotropy and 6 hyperfine peaks from diluted paramagnetic Mn atoms. (b) Angular dependence of the resonance field. From Jain *et al.*, 2010.

EPR technique is hence used to differentiate the FM signal of nanocolumns from the paramagnetic diluted Mn atoms and estimate magnetic anisotropy (Jain *et al.*, 2010). The EPR spectra are observed as a function of the angle of applied magnetic field. The field is applied out-of-plane from the direction [110] to direction $[\bar{1}\bar{1}0]$ passing through the [001] direction. In Fig. 59 the EPR spectra of a $\text{Ge}_{0.9}\text{Mn}_{0.1}$ film with crystalline nanocolumns exhibit the hyperfine Mn lines corresponding to isolated paramagnetic Mn atoms and also a weak FM line attributed to nanocolumns. The angular dependence of the resonance field in Fig. 59(b) is fitted using the Smit-Beljers formalism (Smit and Beljers, 1955). For this purpose, it is assumed that nanocolumns are non-interacting and single domain at 5 K. The magnetic anisotropy energy of a single nanocolumn is written as: $F = K_2 m_z^2 + K_4 (m_x^2 m_y^2 + m_x^2 m_z^2 + m_y^2 m_z^2)$ where x , y and z axes are the [100], [010] and [001] crystal axes respectively. m_x , m_y and m_z are the coordinates of a unit vector along the column magnetization direction, K_2 and K_4 are second and fourth order magnetic anisotropy constants. Anisotropy fields are thus defined as: $\mu_0 H_{a2} = 2K_2/M_S$ and $\mu_0 H_{a4} = 2K_4/M_S$. From EPR data, the anisotropy fields can be deduced from EPR data: $\mu_0 H_{a2} \simeq -0.09$ T for the second order and $\mu_0 H_{a4} \simeq -0.11$ T for the fourth order with $\gamma/\gamma_e \simeq 1.07$ (where γ_e is the gyromagnetic ratio of a free electron). Hence, the nanocolumns exhibit a perpendicular uniaxial anisotropy and a cubic anisotropy with easy axis along [111]. The presence of cubic anisotropy supports the crystallinity of nanocolumns. Also, cubic anisotropy and uniaxial anisotropy constants are of the same order of magnitude making the two crystal axes [110] and

[001] close in energy. It thus explains the small difference between the ZFC curves for the field parallel and perpendicular to the film plane in the SQUID measurements of Fig. 58(d). Considering the saturation magnetization of these small nanocolumns $M_S = 140 \pm 20$ kA/m, the uniaxial anisotropy constant can be calculated: $K_2 \simeq -0.63 \times 10^4$ J/m³ which nicely corresponds to shape anisotropy $\mu_0 M_S^2/4 \simeq 0.62 \times 10^4$ J/m³ assuming that nanocolumns are infinite cylinders (Aharoni, 1996).

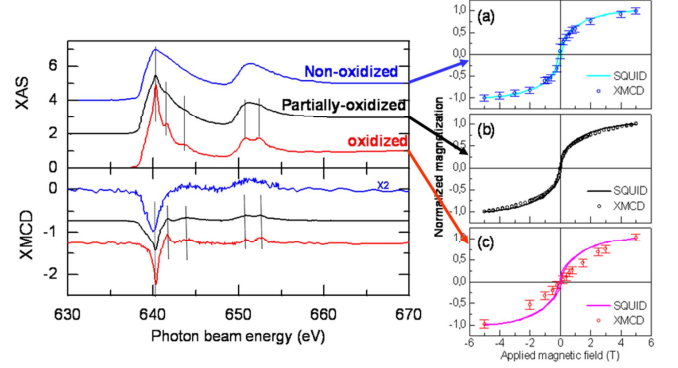


FIG. 60 (Color online) Isotropic XAS spectra at the Mn $L_{2,3}$ edge and corresponding XMCD signal recorded at 5 K under 5 T. Data were acquired in the total electron yield mode. Measurements were performed on a $\text{Ge}_{0.9}\text{Mn}_{0.1}$ film grown at 100°C exhibiting different surface states: non-oxidized, partially oxidized and oxidized. The spectra are shifted vertically for the sake of clarity. The XMCD signal recorded at the Mn L_3 edge is then compared with the SQUID signal at 5 K. Both XMCD and SQUID signals are normalized to their maximum value. Adapted from Tardif *et al.*, 2010a.

Finally in order to verify that the magnetic signal detected by SQUID magnetometry really comes from Mn-rich nanocolumns. For this purpose, XMCD measurements were carried out at the Mn $L_{2,3}$ edge (Ahlers *et al.*, 2009; Gambardella *et al.*, 2005). In Fig. 60, when the $\text{Ge}_{0.9}\text{Mn}_{0.1}$ film is properly capped with a Si/Ge layer to prevent surface oxidation (Tardif *et al.*, 2010a), the XMCD signal nicely fits the SQUID measurements. Moreover the magnetic moment per Mn atom deduced by sum rules (Thole *et al.*, 1992) from XMCD data also corresponds well to the magnetic moment measured by SQUID: $\simeq 1 \mu_B/\text{Mn}$. Electrical properties have been intensively investigated in such (Ge,Mn) films grown on semi-insulating GaAs substrates (Yu *et al.*, 2010). First, a negative giant MR signal has been detected at low temperature due to spin scattering on FM nanocolumns. In addition, two positive MR contributions were observed: the first one arises from ordinary or Lorentz MR and the second one was attributed to geometrically enhanced MR as a consequence of the conductivity contrast between the nanocolumns and the matrix (Solin *et al.*, 2000). Then AHE was demonstrated at low temperature but the interpretation of magnetotransport in such inhomogeneous system clearly remains a challenging task (Yu *et al.*, 2011).

2. Crystalline (Ge,Mn) nanocolumns with partial relaxation / Ge(001)

$\text{Ge}_{0.94}\text{Mn}_{0.06}$ films grown in a narrow temperature range around 130°C exhibit partial lattice relaxation (see Fig. 57) and ferromagnetism above RT up to 400 K as shown in Fig. 61 (Jamet *et al.*, 2006). This high- T_C FM behavior was also observed in nanowires and quantum dots (Cho *et al.*, 2008b; Kazakova *et al.*, 2005; van der Meulen *et al.*, 2009; Xiu *et al.*, 2010a).

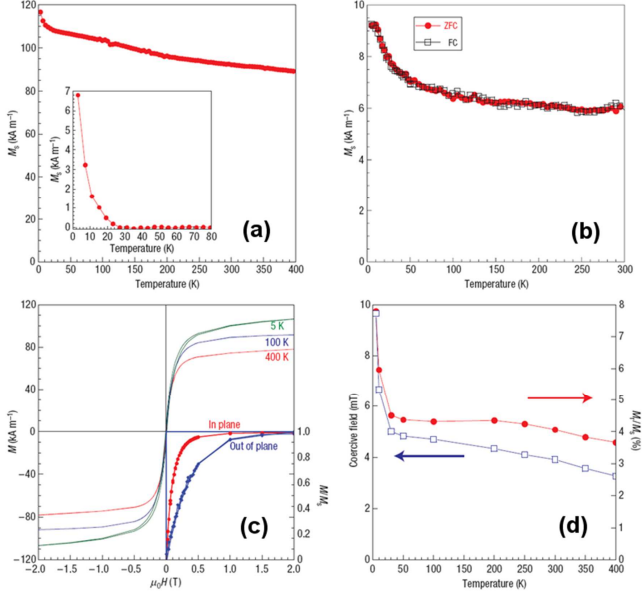


FIG. 61 (Color online) Magnetic characterization of $\text{Ge}_{0.94}\text{Mn}_{0.06}$ films grown around 130°C . (a) Temperature dependence of the saturation magnetization measured at 2 T. The inset shows the extrapolated matrix signal at low temperature after subtracting the nanocolumns magnetic signal. (b) ZFC-FC measurements performed at 0.01 T. Both curves superimposed. (c) Magnetization loops at 5, 100, and 400 K, after subtracting the diamagnetic contribution from the substrate. The inset demonstrates the easier saturation in-plane at 250 K. (d) Coercive field ($\mu_0 H_C$) and remanent magnetization (M_r/M_S) versus temperature. $\mu_0 H_C$ and M_r/M_S are given with a precision of the order of 10%. From Jamet *et al.*, 2006.

Figure 61(a) shows the temperature dependence of the magnetization at 2 T, measured by SQUID magnetometry. The magnetic moment per Mn atom is $4.7 \mu_B$ at 3 K. This value is close to $5 \mu_B$ expected for isolated Mn^{2+} ions according to Hund's rule. The large magnetization at high temperature is consistent with a FM phase with $T_C > 400$ K. ZFC-FC curves superimpose from 3 to 300 K [Fig. 61(b)], thus ruling out the presence of superparamagnetic particles except if their blocking temperature exceeds 300 K. Considering the Mn distribution in the GeMn films, this high T_C FM phase can be attributed to the nanocolumns. In the low temperature range, the magnetization increases when decreasing the temperature [inset in Fig. 61(a)]. The corresponding saturation

magnetization is small ($\simeq 9$ kA/m), and the additional susceptibility is described by a Curie-Weiss temperature between 10 and 15 K. A similar behavior was reported for a strongly diluted $\text{Ge}_{1-x}\text{Mn}_x$ layer. Assuming that isolated Mn atoms are present in the film, all magnetically active with a magnetic moment of $3 \mu_B$ (Schulthess and Butler, 2001), the Mn concentration in the nanocolumns reaches 33.7% (their composition is close to Ge_2Mn). The magnetic moment per Mn atom is close to $4.9 \mu_B$ from the saturation magnetization $\simeq 680$ kA/m. Magnetization loops [Fig. 61(c)] all exhibit a pronounced S-shape, a low remanent magnetization and a low coercive field [Fig. 61(d)]: in-plane and out-of-plane directions act as hard magnetic axes. The saturation is easier with the field applied in-plane [inset in Fig. 61(c)].

Nanocolumns are very close to each other and a strong magnetostatic or carrier mediated coupling is expected. Energy calculations using Fourier formalism (Beleggia *et al.*, 2004) were performed for an infinite square lattice of nanocolumns defined by the average experimental parameters (spacing 10 nm, diameter 3 nm and height 80 nm), taking into account the long range dipolar interaction and dipolar self energy of the nanocolumns. Three configurations have been tested: saturated out-of-plane ($\uparrow\uparrow$), saturated in-plane ($\rightarrow\rightarrow$) and anti-parallel out-of-plane with $M = 0$ ($\uparrow\downarrow$). Results are given in units of $\mu_0 M_S^2 V/2$ where V is the volume of the nanocolumns and M_S their magnetization at saturation. The smallest energy, $E_{\uparrow\downarrow} \simeq 0.01$, corresponds to the anti-parallel out-of-plane configuration: dipolar interactions favor an antiparallel arrangement of first neighbor nanocolumns. This finding is in good agreement with the low remanent magnetizations, low coercive fields and S-shaped in-plane and out-of-plane magnetization curves measured by SQUID. In real samples, the remanent magnetization is not zero because nanocolumns are randomly distributed, leading to many frustrated magnetic configurations. The model however fails to predict the right saturated configuration: we calculate $E_{\rightarrow\rightarrow} = 0.46$ and $E_{\uparrow\uparrow} = 0.08$, while experimentally the magnetization is easier to saturate in-plane ($E_{\rightarrow\rightarrow} < E_{\uparrow\uparrow}$). Thus an additional in-plane magneto-crystalline anisotropy has to be considered, competing with shape anisotropy, which favors the in-plane saturated state. This behavior has previously been observed in arrays of electrodeposited cobalt nanowires (Darques *et al.*, 2004). In (Ge,Mn) nanocolumns, this magneto-crystalline anisotropy originates from the broken in-plane cubic symmetry (columns are fully strained in only one direction) leading to a natural uniaxial anisotropy combined with large magneto-elastic effects (columns are 4% contracted). This feature also explains the very high (at least higher than 400 K) blocking temperature of nanocolumns. As previously discussed in III-V and II-VI FM semiconductors (Dietl *et al.*, 2001; Kossacki *et al.*, 2004), strain can modify the valence band dispersion and induce a large magnetic anisotropy. Carrier mediated FM coupling between the nanocolumns would also favor an in-plane sat-

urated state. It should also be noted in calculating the self-energy that the column aspect ratio can be overestimated since the columns are not perfect cylinders. Finally, these (Ge,Mn) films grown on Ge exhibit huge positive MR attributed to geometrically enhanced MR (Solin *et al.*, 2000) and more importantly AHE that might be attributed to the spin polarization of holes (Jamet *et al.*, 2006). That makes this system a promising candidate for spintronics applications.

3. Amorphous (Ge,Mn) nanocolumns / Ge(001)

For $\text{Ge}_{1-x}\text{Mn}_x$ films grown at higher temperatures ($T > 150^\circ\text{C}$) and high Mn concentration ($\geq 10\%$), amorphous nanocolumns are observed in TEM (see Fig. 57). As for small crystalline nanocolumns grown at 100°C (see Sec. VI.D.1), the Mn concentration in the columns is close to 50%. These amorphous nanocolumns have T_C close to 170 K. The contribution from isolated paramagnetic Mn atoms is still observed at low temperature, as shown in Fig. 62.

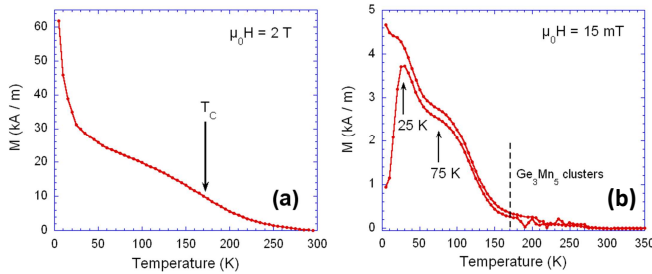


FIG. 62 (Color online) Magnetic characterization of a $\text{Ge}_{0.9}\text{Mn}_{0.1}$ film grown above 150°C with amorphous nanocolumns. (a) Temperature dependence of the saturation magnetization in the magnetic field of 2 T applied in the film plane along the [110] direction. (b) ZFC-FC measurements performed at 0.015 T. The ZFC curve exhibits two peaks with blocking temperatures around 25 K and 75 K, respectively, and points to $T_C \simeq 170$ K of nanocolumns. Non-zero magnetization at higher temperatures is due to Ge_3Mn_5 NCs. From Jain *et al.*, 2010.

In ZFC-FC curves [Fig. 62(b)] two peaks are present at around 25 K and 75 K in the ZFC curve as well as a weak contribution from Ge_3Mn_5 clusters. Those peaks are in agreement with the broad size distribution observed by TEM (see Fig. 51).

The magnetic anisotropy of these columns is studied by EPR (Jain *et al.*, 2010). The data are shown in Fig. 63 and the angular dependence of the resonance field is fitted using the Smit-Beljers formalism (Smit and Beljers, 1955) assuming that nanocolumns are non-interacting and single domain. A single perpendicular uniaxial anisotropy is found, the corresponding anisotropy field is: $\mu_0 H_{a2} \simeq -0.09$ T and $\gamma/\gamma_e \simeq 1.24$. From the saturation magnetization of amorphous nanocolumns $M_S = 220 \pm 20$ kA/m, the anisotropy energy density is calculated to

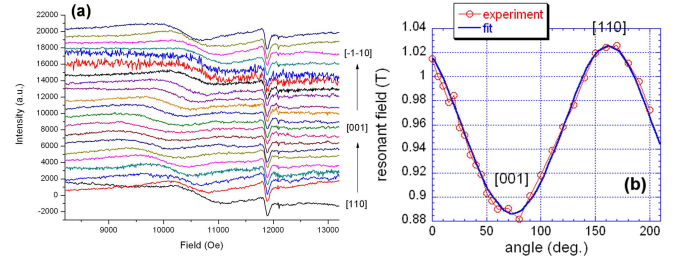


FIG. 63 (a) EPR absorption spectra of a $\text{Ge}_{0.9}\text{Mn}_{0.1}$ film grown at 150°C as a function of the static field orientation at 5 K. The angle is defined between the [110] direction and the applied magnetic field. The working frequency is 34 GHz (Q-band set-up). A single FM broad peak of weak anisotropy is observed. (b) Angular dependence of the resonance field. From Jain *et al.*, 2010.

be $K_2 \simeq -1.1 \times 10^4$ J/m³. This value corresponds to that of shape anisotropy $\mu_0 M_S^2/4 = 1.5 \times 10^4$ J/m³ of nanocolumns assuming their aspect ratio is high (Aharoni, 1996). As expected for amorphous nanocolumns, no cubic magneto-crystalline contribution is found. In the case of uniaxial magnetic anisotropy, the blocking temperature of nanocolumns can be easily estimated using the classical Néel-Brown formula (Jamet *et al.*, 2001): $KV = 25k_B T_B$, where K is the anisotropy constant, V the columns volume, k_B the Boltzmann constant and T_B the blocking temperature. From the average diameter and length of nanocolumns (6 nm and 80 nm respectively) given by TEM observations, one can estimate their volume and the blocking temperature: $T_B \simeq 72$ K which corresponds to the second broad peak in the ZFC curve. The first peak with a maximum close to 25 K can correspond either to shorter magnetic nanocolumns with an average length of $\simeq (25/72) \times 80$ nm = 28 nm or to the manifestation of a disordered magnetic state within the thin shell around nanocolumns and containing substitutional Mn atoms (Prestat *et al.*, 2014). In the first assumption it means that increasing the growth temperature partly activates Mn diffusion along the growth direction which leads to the formation of elongated clusters rather than continuous nanocolumns spanning the whole film thickness.

4. Ge_3Mn_5 clusters / Ge(001)

The growth of $\text{Ge}_{1-x}\text{Mn}_x$ films at high temperature ($>180^\circ\text{C}$) on Ge(001) or annealing $\text{Ge}_{1-x}\text{Mn}_x$ films grown at low temperature above 600°C leads to the formation of randomly distributed spherical Ge_3Mn_5 clusters. The RHEED pattern of annealed samples is very similar to that of Ge as in HRTEM the clusters are observed away from the surface (Fig. 57).

The structure of Ge_3Mn_5 clusters was investigated using grazing incidence SXR. The mean cluster diameter was estimated to be 10.6 ± 1 nm in agreement with

TEM observations. Moreover 97% of the clusters have their c -axis perpendicular to the film plane and 3% in-plane. Finally, by searching for all possible Ge_3Mn_5 reflections in the plane parallel to the sample surface, a slight in-plane distortion of the hexagonal lattice was found (Jain *et al.*, 2011). Magnetic properties were studied using SQUID magnetometry and EPR. Temperature dependent magnetization measurements clearly show the presence of two magnetic phases: the Ge_3Mn_5 with T_C of 300 ± 5 K and the paramagnetic contribution of isolated Mn atoms. Hysteresis curves at 5 K clearly show that most of Ge_3Mn_5 clusters exhibit perpendicular magnetic anisotropy. Since the clusters are spherical, perpendicular anisotropy arises from magneto-crystalline anisotropy. This result is in good agreement with XRD data. Indeed, bulk Ge_3Mn_5 crystal is hexagonal with uniaxial magnetic anisotropy along the c -axis. From hysteresis loops recorded with the field perpendicular to the film plane, the fraction of magnetic signal from Ge_3Mn_5 clusters is estimated to be 70%. The remaining signal likely comes from amorphous Mn-rich precipitates with very low coercive field. From the anisotropy field $\mu_0 H_a \simeq 0.6$ T and using the bulk M_S value (1100 kA/m) (Forsyth and Brown, 1990), the anisotropy constant can be calculated: $K = \mu_0 H_a M_S / 2 \simeq 3.3 \times 10^5$ J/m³ which is less than the reported bulk value 4.2×10^5 J/m³ (Tawara and Sato, 1963). This feature is explained by the in-plane distortion of the Ge_3Mn_5 crystal observed by XRD which is due to the epitaxy on the germanium matrix. It introduces an additional in-plane magneto-elastic component to magnetic anisotropy. Finally the same anisotropy field and perpendicular anisotropy were obtained from EPR measurements in good agreement with SQUID data (Jain *et al.*, 2011).

VII. SPINODAL NANODECOMPOSITION IN (Ge,Fe)

A. Introduction

Apart from Mn other TM atoms such as Cr, Co or Fe have also been incorporated into Ge films to obtain FM properties (Kim *et al.*, 2005; Kioseoglou *et al.*, 2004; Tsui *et al.*, 2004). In particular, FM order was predicted in Fe-doped germanium films (Weng and Dong, 2005; Zhou *et al.*, 2004) and experimentally demonstrated in Fe-implanted films (Venugopal *et al.*, 2002), Fe-doped germanium nanowires (Cho *et al.*, 2008a) or quantum dots (Xiu *et al.*, 2010b) as well as in Fe-doped bulk Ge single crystals (Choi *et al.*, 2003).

In order to enhance the solubility limit of Fe, LT-MBE was used to grow $\text{Ge}_{1-x}\text{Fe}_x$ films with x up to 17.5% (Shuto *et al.*, 2006b). In this section, we describe the growth, characterization, and magnetic properties of such $\text{Ge}_{1-x}\text{Fe}_x$ thin films, in particular, the relation between growth or annealing temperatures, defect formation, Fe distribution, and resulting magnetism (Shuto *et al.*, 2006a,b, 2007; Wakabayashi *et al.*, 2014a,b).

B. MBE growth

$\text{Ge}_{1-x}\text{Fe}_x$ thin films were grown on Ge (001) substrates by LT-MBE. After a LT Ge buffer layer was grown at the substrate temperature T_g of 100°C, a 16-nm-thick $\text{Ge}_{1-x}\text{Fe}_x$ film was grown at $T_g = 100, 200, 300,$ or 400°C. The Fe content (x) was varied from 2.0 to 24.0%. In-situ RHEED was used to monitor the crystallinity and surface morphology of the Ge buffer layer and the $\text{Ge}_{1-x}\text{Fe}_x$ film during the epitaxy. Although the diffraction pattern of the LT Ge buffer layer revealed intense and sharp 2×2 streaks, the pattern was quickly changed at the initial stage of $\text{Ge}_{1-x}\text{Fe}_x$ epitaxy. The $\text{Ge}_{1-x}\text{Fe}_x$ films grown at $T_g = 100$ and 200°C showed 2D growth mode and exhibited diamond-type crystal structure.

When the $\text{Ge}_{1-x}\text{Fe}_x$ film was grown at $T_g = 300$ (or 400°C), a spotty pattern was clearly observed in the RHEED image, indicating a 3D growth mode or surface roughening. Thus, the growth mode of the $\text{Ge}_{1-x}\text{Fe}_x$ film was changed from the 2D mode to the 3D mode between $T_g = 200^\circ\text{C}$ and 300°C . This growth mode change at around $T_g = 300^\circ\text{C}$ would be caused by the precipitates of Fe-Ge FM compounds in the film (crystallographic phase separation), as discussed below. This growth mode change at around $T_g = 300^\circ\text{C}$ would be caused by the precipitates of Fe-Ge FM compounds in the film (crystallographic phase separation), as discussed below.

C. Structural and chemical characterization

Figure 64(a) shows a HRTEM image of a $\text{Ge}_{1-x}\text{Fe}_x$ film ($x = 9.5\%$) grown at $T_g = 200^\circ\text{C}$, projected along the exact direction of Ge[110]. The image indicates that the $\text{Ge}_{1-x}\text{Fe}_x$ layer was homogeneously and epitaxially grown on the Ge buffer layer without any threading dislocations, and that the surface was atomically flat with a height of roughness less than 1 nm. These features were consistent with the RHEED observations, as mentioned earlier. However, when the lattice image was projected along the angle slightly tilted from the Ge[110] direction, cluster-like dark contrast regions appeared in the epitaxially grown $\text{Ge}_{1-x}\text{Fe}_x$ layer, as shown in Fig. 64(b). It is well recognized in TEM observations that the contrast due to the difference in chemical compositions is enhanced when the projection direction is slightly tilted from the exact zone axis. Using spatially resolved transmission electron diffraction (TED) and EDS, the crystal structure and chemical composition of the dark region [denoted as *1 in Fig. 64(b)] and surrounding bright region [denoted as *2 in Fig. 64(b)] were investigated. The TED image of point *1 (the right inset) showed the diffraction pattern of the diamond structure projected from its [110] direction with weak extra spots caused by stacking fault defects. On the contrary, point *2 (the left inset) in the bright region exhibited the diffraction pattern of the diamond structure without any extra spots. This means that no other crystal structures except the

diamond crystal structure were formed both in the dark and in the bright regions, although the dark region included tiny stacking fault defects.

The local Fe composition at point *1 measured by EDS was $\sim 12\%$, which is higher than that ($\sim 4\%$) at point *2. Therefore, the contrast in the HRTEM image shown in Fig. 64(b) was due to the nonuniform distribution of the Fe composition. Similar structural features were also observed for a $\text{Ge}_{1-x}\text{Fe}_x$ film with $x = 6.0\%$, in which dark and bright contrast regions appeared in the TEM image caused by nonuniform Fe distribution. Tiny stacking fault defects were also detected in the dark contrast regions. The local Fe composition in the dark and bright contrast regions of this film was about 8.0% and 1.5% , respectively. Thus, both the Fe compositions in dark and bright contrast regions increased with increasing x .

Thus, RHEED, HRTEM, TED, and EDS studies lead to the conclusion that $\text{Ge}_{1-x}\text{Fe}_x$ films grown at 200°C on Ge(001) maintain the diamond crystal structure without any intermetallic Fe-Ge compounds or Fe inclusions. Similarly, the diamond structure is preserved under annealing (Ge,Fe) below 600°C (Wakabayashi *et al.*, 2014a). However, the films grown at 200°C or annealed exhibit a nonuniform distribution of Fe composition x , i.e., they undergo spinodal nanodecomposition in the form of chemical phase separation.

In worth noting that since EDS provides chemical information averaged over the specimen width, the amplitude of actual x fluctuations can be even larger than implied by the values of x determined for points *1 and *2.

D. Magneto-optical characterization

Figure 65(a) shows MCD spectra taken at 10 K in reflection configuration for $\text{Ge}_{1-x}\text{Fe}_x$ ($x = 9.5\%$) films grown at $T_g = 100, 200, 300,$ and 400°C , with magnetic field perpendicular to the sample plane. As seen, when the $\text{Ge}_{1-x}\text{Fe}_x$ film was grown at $T_g = 100$ (or 200°C), its MCD spectrum showed a clear E_1 peak whose intensity was significantly enhanced compared with that of bulk Ge [uppermost curve in Fig. 65(a)], implying the presence of s, p - d exchange splitting of bands. An offset-like broad signal was also observed in the whole energy range examined here. The magnetic-field dependence of the MCD intensity at the critical point E_1 exhibited a FM hysteresis loop, and the hysteresis shape at any other photon energies in the offset-like signal was identical with that at E_1 , indicating the $\text{Ge}_{1-x}\text{Fe}_x$ film grown at $T_g = 100$ – 200°C was magnetically homogeneous without Fe-Ge FM precipitates. Note that the E_0 of the sample was not clearly distinguished due to measurement-light interference caused by adsorbed moisture on the sample surface (Shuto *et al.*, 2006b).

When the $\text{Ge}_{1-x}\text{Fe}_x$ film was grown at $T_g = 300$ (or 400°C), the MCD intensity at the critical point E_1 was not enhanced at all, but the MCD spectrum of bulk Ge

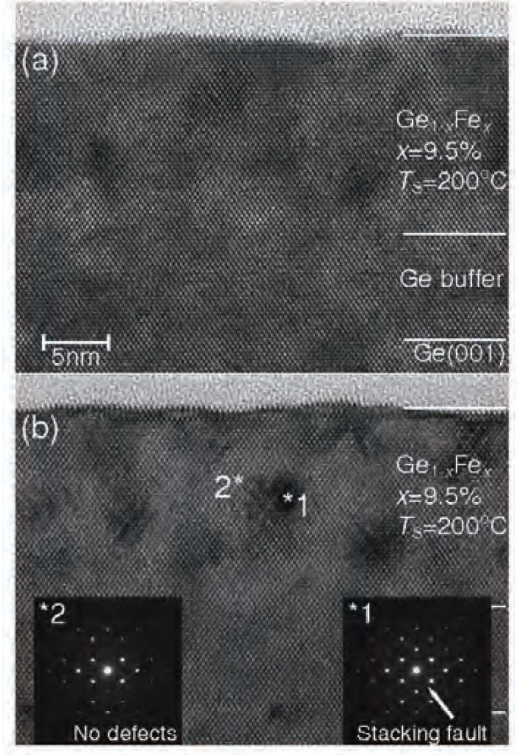


FIG. 64 HRTEM lattice images projected along (a) the exact direction of the Ge[110] axis and (b) the direction slightly tilted from the Ge[110] axis for $\text{Ge}_{1-x}\text{Fe}_x$ thin films with $x = 9.5\%$ grown at $T_g = 200^\circ\text{C}$. Insets: diffraction images at the dark region (*1) and at the surrounding bright region (*2). From Shuto *et al.*, 2007.

was overlapped with an offset-like MCD signal: The magnitude of the E_1 peak [denoted as δ shown in Fig. 65(a)] that was measured from the bottom of the offset-like signal level was equal to that of bulk Ge. The MCD hysteresis loop measured at E_1 (2.30 eV) was not identical with that measured at other energy points (for example, 2.95 eV) as shown in Fig. 65(b), indicating crystallographic phase separation. The MCD hysteresis loop at E_1 can be divided into two components, i.e., the paramagnetic component of the host Ge matrix and the FM component of FM precipitates.

Figure 66 shows T_C values of $\text{Ge}_{1-x}\text{Fe}_x$ films as a function of Fe content x , where T_C was evaluated from the Arrott-plots using temperature-dependent MCD hysteresis loops at the E_1 critical point.

For the $\text{Ge}_{1-x}\text{Fe}_x$ films grown at $T_g = 200^\circ\text{C}$, T_C linearly increased with increasing x in the range between $x = 0$ and 17.5% . Above $x = 17.5\%$, T_C was saturated at around 170 - 180 K (Shuto *et al.*, 2007). T_C of $\text{Ge}_{1-x}\text{Fe}_x$ films grown at $T_g = 100^\circ\text{C}$ also linearly increased with increasing x , but T_C was significantly reduced in comparison with that of the samples grown at $T_g = 200^\circ\text{C}$.

When $\text{Ge}_{1-x}\text{Fe}_x$ films were grown at $T_g = 300$ and 400°C , their T_C values were quite higher than those of the samples grown at $T_g = 100$ and 200°C . For example,

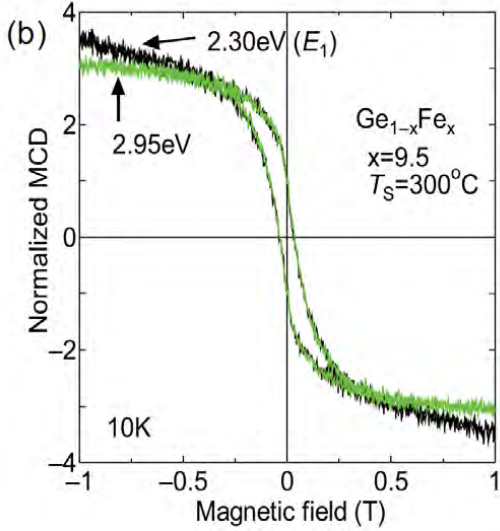
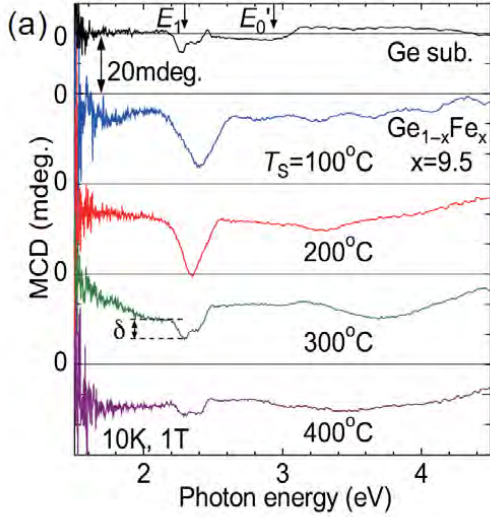


FIG. 65 (a) Growth temperature dependence of the MCD spectra of $\text{Ge}_{1-x}\text{Fe}_x$ ($x = 9.5\%$) films grown at $T_g = 100 - 400^\circ\text{C}$, measured at 10K with magnetic field of 1T perpendicular to the sample plane with reflection configuration. (b) Magnetic-field dependence of MCD intensities at 2.30 eV (E_1) and at other energy point (2.95 eV) for the $\text{Ge}_{1-x}\text{Fe}_x$ ($x = 9.5\%$) films grown at $T_g = 300^\circ\text{C}$, where the data were normalized by their MCD intensities at the magnetic field of 0T. Adapted from Shuto *et al.*, 2006a.

T_C values were 120 K and 200 K in the cases of $T_g = 300$ and 400°C , respectively, even when x was only 2.0%. On the contrary, T_C values were below 10 K in the cases of $T_g = 100$ and 200°C with $x = 2.0\%$. This behavior of T_C at $T_g = 300$ and 400°C can be attributed to the precipitates of FM compounds described above.

The apparent values of $T_C^{(app)}$ not only increases with the growth temperature but can be enhanced by annealing (Wakabayashi *et al.*, 2014a). In either case, the mag-

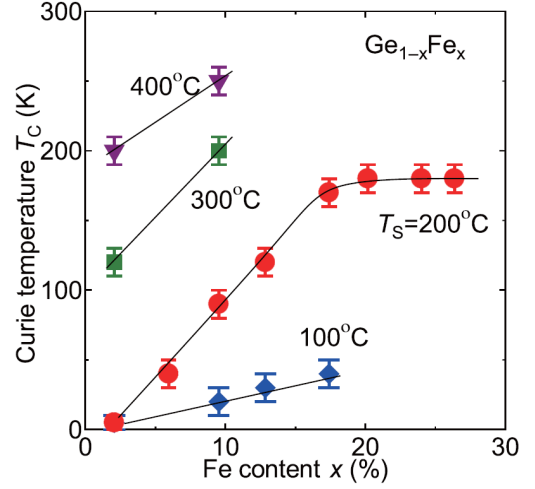


FIG. 66 Curie temperature T_C of $\text{Ge}_{1-x}\text{Fe}_x$ films as a function of Fe content x . $\text{Ge}_{1-x}\text{Fe}_x$ films were grown at $T_g = 100, 200, 300,$ and 400°C . From Shuto *et al.*, 2006a.

nitude of $T_C^{(app)}$ correlates with the non-uniformity of the Fe distribution and the stacking fault density (Wakabayashi *et al.*, 2014a,b). Meanwhile, channeling Rutherford backscattering and particle-induced x-ray emission measurements revealed that about 15% of the Fe atoms reside in the tetrahedral interstitial sites and that the substitutional Fe concentration, in agreement with the decomposition scenario, is barely correlated with the magnitude of $T_C^{(app)}$ (Wakabayashi *et al.*, 2014b). At the same time, all the (Ge,Fe) films show a weak spin-glass-like behavior in a low-temperature region (below ~ 26 K), which is insensitive to the annealing temperature. However, the ferromagnetism associated with the non-uniform Fe distribution dominates magnetic properties of the system.

In summary, studies of $\text{Ge}_{1-x}\text{Fe}_x$ as a function of epitaxy temperature and TM content clearly show an evolution of the alloy character from a dilute magnetic semiconductor to a decomposed system, first involving chemical and then crystallographic phase separation. This evolution is accompanied by changes in spectral dependencies of MCD that is initially enhanced in the region of optical transitions specific to the host semiconductor but as nanodecomposition progresses this magnetization dependent enhancement starts to extend over a wide spectral region indirectly pointing to a metallic character of Fe-rich regions. The apparent T_C values determined from the MCD hysteresis loops show a clear correlation with the degree of nanocomposition, i.e., with the upper limit of local TM concentrations as well as with the appearance of structural defects.

VIII. SPINODAL NANODECOMPOSITION IN (Zn,Cr)Te

A. Introduction

Among various DMSs, Cr-doped II-VI compounds have been studied for a long time, attracting attention due to their peculiar magnetic and magneto-optical properties. Excitonic magnetospectroscopy indicated that the p - d exchange interaction is FM (Mac *et al.*, 1996), in contrast to the AF interaction in Mn-doped II-VI compounds. According to the Schrieffer-Wolff transformation, the FM p - d interaction results from the position of the Cr $3d$ donor level *above* the top of the valence band (Kacman, 2001; Mizokawa and Fujimori, 1997).

Concerning the spin dependent coupling between Cr spins in (II,Cr)VI, it was theoretically predicted that the superexchange interaction becomes FM for d^4 ions in the tetrahedral crystal field (Blinowski *et al.*, 1996). Later, a FM ordering of Cr spins in II-VI compounds was found by DFT first-principle calculations (Sato and Katayama-Yoshida, 2002). Hence, the theoretically expected ferromagnetism can be understood in the picture of double-exchange interaction between the Cr $3d$ electrons in the localized level within the band-gap (Fukushima *et al.*, 2004; Sato and Katayama-Yoshida, 2002) or as FM superexchange interaction of highly localized Cr spins (Blinowski *et al.*, 1996). In either case, the FM interaction between Cr spins is short-range, extending over few nearest neighbors.

Experimentally, the FM behavior was observed in (Zn,Cr)Te (Saito *et al.*, 2002) and (Zn,Cr)Se (Karczewski *et al.*, 2003) with Cr contents reaching a few percent, and later ferromagnetism at RT was achieved in $Zn_{1-x}Cr_xTe$ with a high Cr content $x = 0.2$ (Saito *et al.*, 2003). The FM transition temperature T_C was reported to increase almost linearly with Cr content x , reaching 300 K at $x = 0.2$, in agreement with the *ab initio* prediction (Fukushima *et al.*, 2004). In addition, the intrinsic nature of ferromagnetism appeared to be confirmed by the similar magnetic-field dependencies of magnetization and MCD (Saito *et al.*, 2003). However, according to Karczewski *et al.*, 2003, the ferromagnetism in $Zn_{1-x}Cr_xSe$ resulted from the precipitation of a FM compound, as T_C was independent of x .

It was also found that the FM properties of (Zn,Cr)Te were significantly affected by the co-doping of donor or acceptor impurities; the ferromagnetism was suppressed by co-doping with acceptor impurity nitrogen (N) (Ozaki *et al.*, 2005) while it was enhanced due to co-doping with iodine (I) donor impurities (Ozaki *et al.*, 2006). In particular, for a fixed Cr content $x = 0.05$, the FM transition temperature T_C increased up to 300 K with the co-doping of iodine at a concentration of the order of 10^{18} cm^{-3} , from $T_C \sim 30 \text{ K}$ in a layer without co-doping (referred to as undoped sample). However, it was difficult to understand the realization of high-temperature ferromagnetism at a low Cr content, $x \simeq 0.05$, which is below the percolation limit of the zb structure, if we as-

sume a short-range interaction between Cr spins. Moreover, the combined analysis of the nano-scale chemical probing using TEM and the magnetization measurements with SQUID revealed that there is a systematic correlation between FM properties and the heterogeneity of the Cr distribution (Kuroda *et al.*, 2007). In I-doped (Zn,Cr)Te crystals exhibiting ferromagnetism at RT, it was found that the Cr distribution is strongly inhomogeneous, i.e., nanoscale regions are formed, in which the concentration of Cr cations is high. According to the current understanding, in these Cr-rich volumes, Cr spins are ordered ferromagnetically due to the short distance between them. These FM clusters give rise to superparamagnetism controlled by the magnetic anisotropy of individual Cr-rich NCs and interactions among them.

The electronic structure of the Cr ions and host bands was investigated in $Zn_{1-x}Cr_xTe$ ($x = 0.03$ and 0.15) using XMCD and photoemission spectroscopy (Kobayashi *et al.*, 2008). It was concluded that neither double exchange mechanism nor carrier-induced ferromagnetism are important, and the inhomogeneous distribution of Cr atoms dominantly influences the FM properties of $Zn_{1-x}Cr_xTe$.

In the case of (Zn,Cr)Te, similarly to other DMSs discussed in this survey, both chemical and crystallographic phase separations can be induced depending on Cr content and growth conditions (Kobayashi *et al.*, 2012; Kuroda *et al.*, 2007). The pairing energy of Cr ions, which is the driving force of the phase separation (see, Secs.II.B), is expected to vary with the Cr charge state (Dietl, 2006). Since the Cr $3d$ electrons form deep donor and acceptor levels in the band-gap of ZnTe (Godlewski and Kamińska, 1980), the studies of (Zn,Cr)Te demonstrated that the shift of the Fermi level produced by a change in the concentration of electrically active defects or shallow impurities alters the Cr charge state, which affects the Coulomb interaction between Cr ions and hence their aggregation (Kuroda *et al.*, 2007).

In this section, we review recent experimental studies on spinodal nano-decomposition in (Zn,Cr)Te grown by MBE (Ishikawa *et al.*, 2009; Kobayashi *et al.*, 2012; Kuroda *et al.*, 2007; Nishio *et al.*, 2009) as well as associated magneto-optical (Kuroda *et al.*, 2007; Ozaki *et al.*, 2006) and magnetotransport properties (Kuroda *et al.*, 2007). In the first part (Sec.VIII.B) we describe the properties of (Zn,Cr)Te films grown in the [001] crystallographic direction under the standard condition of MBE growth for the host binary compound ZnTe – at a substrate temperature of $T_g = 300^\circ\text{C}$ and at a fixed growth rate of $\sim 1 \text{ \AA}/\text{sec}$. We discuss also the effect of co-doping by I donors and N acceptors as well of varying the stoichiometry by changing the ratio of Zn and Te fluxes. The influence of the growth rate and temperature on the structural and magnetic properties of (Zn,Cr)Te:I is presented in Sec.VIII.C. The accumulated data demonstrate the possibility of controlling the Cr aggregation by growth conditions and co-doping with shallow impurities, corroborating the theoretical considerations on

the pairing energy presented in Sec. II.B, as well as provide experimental illustration of the daireseki and konbu phases discussed theoretically in Secs. II.C.1 and II.C.2. This control over the size and shape of Cr-rich regions substantiates the prospects of spinodal nanotechnology discussed in Sec. IX.

B. Chemical phase separation and its control by the Fermi level position

1. Visualization of Cr distribution

Figure 67 shows the EDS mapping images of the local Cr composition in I-doped, undoped, and N-doped $\text{Zn}_{1-x}\text{Cr}_x\text{Te}$ films with relatively low and high values of the average Cr content $x \simeq 0.05$ and 0.2 . In the case of the low Cr composition $x \simeq 0.05$, the Cr mapping images exhibit clear differences in the uniformity of Cr distribution between particular samples (Kuroda *et al.*, 2007): uniform distributions in the undoped films grown under Te-rich flux (Fig. 67A) and in the N-doped film (D) versus non-uniform distributions in the undoped film grown under Zn-rich flux (B) and in the I-doped film (C). In the case of non-uniform distributions, the typical length scale of the compositional fluctuation is estimated to be 20–50 nm. According to the spot analysis of the EDS spectra, a typical value of the local Cr composition inside the Cr-rich regions is $x \sim 0.1$.

The TEM observation of the series of the films with the Cr composition $x \simeq 0.05$ revealed that the structural properties are not much affected by the co-doping of iodine or nitrogen, or the growth under different Zn/Te flux ratios. As a typical example of the series of the films, the result of the I-doped film is shown in Fig. 68. The TEM image in Fig. 68(a) exhibits mostly zb crystalline structure, but there appear many stacking faults along the $\{111\}$ planes. It was suggested that strain associated with a preferential formation of TM cation dimers along the $[\bar{1}10]$ direction accounts for the appearance of such faults during the growth (Birowska *et al.*, 2012). In addition, the electron diffraction from regions close to the bottom [Fig. 68(b)] and the top [Fig. 68(c)] of the $\text{Zn}_{1-x}\text{Cr}_x\text{Te}$ layer exhibits different images, indicating the deterioration of crystallinity as the growth proceeds. In the diffraction image close to the bottom [Fig. 68(b)], there appear additional weak spots at one-third positions between the fundamental spots of a hexagonal arrangement of the zb structure, corresponding to a triplet periodicity in the stacking sequence along the $\{111\}$ planes in the observed stacking faults. On the other hand, the diffraction image close to the film top [Fig. 68(c)] shows hexagonal patterns revealing the presence of zb nanocrystals with different crystallographic orientations at the end of the growth process. However, any apparent precipitates of other crystal structures were detected neither in the lattice image nor in the diffraction pattern.

For the high Cr composition of $x \sim 0.2$, the Cr distri-

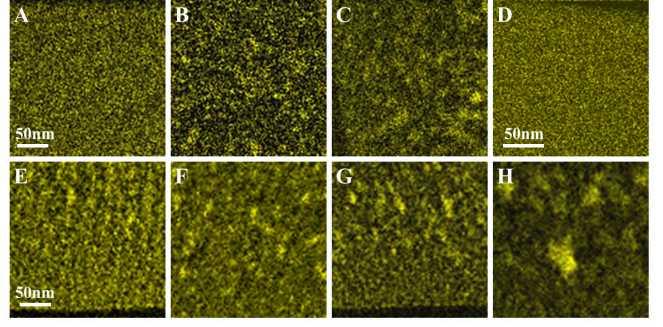


FIG. 67 (Color online) Mapping images of the emission intensity of the EDS Cr K_{α} line for cross-sectional pieces of $\text{Zn}_{1-x}\text{Cr}_x\text{Te}$ films with average Cr contents $x \simeq 0.05$ (A-D) and $x \simeq 0.2$ (E-H). A, E: undoped films grown under Te-rich flux; B, F: undoped films grown under Zn-rich flux; C, G, H: I-doped films with iodine concentrations of $\sim 2 \times 10^{18} \text{ cm}^{-3}$ (C, G) and $\sim 1 \times 10^{19} \text{ cm}^{-3}$ (H); D: N-doped film with a nitrogen concentration of $\sim 2 \times 10^{20} \text{ cm}^{-3}$. All these films were grown in the $[001]$ crystallographic direction using GaAs (001) substrates under the standard condition of the MBE growth for ZnTe (the substrate temperature $T_g = 300^\circ\text{C}$ and the growth rate around $1 \text{ \AA}/\text{sec}$). Adapted from Kuroda *et al.*, 2007 and Ishikawa *et al.*, 2009.

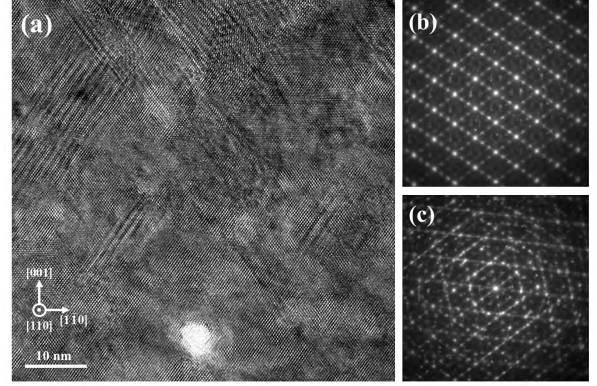


FIG. 68 TEM and electron diffraction images of the I-doped $\text{Zn}_{0.95}\text{Cr}_{0.05}\text{Te}$ film (sample C in Fig. 67). Cross-sectional lattice image (a). Electron diffraction image from a region close to the interface with the ZnTe buffer layer (b) and from a region close to the surface (c). From Kuroda *et al.*, 2007.

bution is always non-uniform, irrelevant of the co-doping or the Zn/Te flux ratio, but the degree of inhomogeneity changes depending on the co-doping or the Zn/Te flux ratio (Ishikawa *et al.*, 2009). As shown in Fig. 67E-H, the inhomogeneity of Cr distribution in the undoped film grown under Te-rich flux is not significant, whereas the Cr distribution in the I-doped films and the undoped film grown under Zn-rich flux is strongly inhomogeneous. In particular, the size of Cr-rich regions becomes larger in the I-doped film with a higher iodine concentration of $\sim 1 \times 10^{19} \text{ cm}^{-3}$ (H). A typical length scale of the Cr-rich regions is estimated to be 30–70 nm. According

to the EDS spot analysis, a maximum value of the local Cr composition in the Cr-rich regions is $x = 0.4\text{--}0.5$. It is concluded from these results that the inhomogeneity of Cr distribution is enhanced either by co-doping with iodine or by the growth under the Zn-rich condition for both low and high Cr contents.

2. Superparamagnetic behavior due to the Cr aggregation

The measurements of the temperature and magnetic-field dependencies of magnetization $M(T, H)$ using SQUID revealed that the magnetic properties also depend significantly on the Zn/Te flux ratio or co-doping with donor or acceptor impurities (Ishikawa *et al.*, 2009; Kuroda *et al.*, 2007). In Fig. 69, the temperature dependence of magnetization is compared for undoped films grown under Te-rich flux and I-doped films. As seen, superparamagnetic features, such as the irreversibility between magnetizations determined under FC and ZFC conditions, and a cusp in the $M(T)$ dependence taken in the ZFC process, are more pronounced in the case of the I-doped films than for the undoped films grown under Te-rich flux. The magnitude of blocking temperature T_b , i.e., a temperature value corresponding to the maximum in the $M(T)$ dependence taken in the ZFC process, is much higher for the I-doped films than in the case of undoped films grown in the Te-rich flux. The paramagnetic Curie-Weiss temperature θ_P obtained from the linear fitting of the temperature dependence of the inverse magnetic susceptibility $\chi(T)$ is also higher in case of the I-doped films comparing to the undoped films grown under Te-rich flux.

The magnitudes of three characteristic temperatures, T_b , θ_P , and the apparent Curie temperature $T_C^{(\text{app})}$ deduced from the Arrott plot analysis of the $M(H)$ dependence, are plotted in Fig. 70 for samples with the average Cr contents $x \simeq 0.05$ and 0.2 as a function the iodine concentration and Te/Zn flux ratio. In the case of $x \simeq 0.05$, these temperatures are closely correlated with the uniformity of the Cr distribution: $T_C^{(\text{app})}$, T_b , and θ_P assume maximum values at the iodine concentration $\sim 2 \times 10^{18} \text{ cm}^{-3}$ for the I-doped films and Te/Zn flux ratio 0.7 (Zn-rich flux) for the undoped films, which correspond to the most pronounced inhomogeneity of the Cr distribution. On the other hand, in the case of $x \sim 0.2$, $T_C^{(\text{app})}$ and θ_P are already high even in the undoped film grown under Te-rich flux and do not increase much for the growth under Zn-rich flux or the co-doping of iodine. In contrast, T_b shows a sizable change depending on the flux ratio or the I-doping; in the undoped films, T_b increases with the decrease of the Te/Zn flux ratio, and in the I-doped films, T_b increases with the increase of iodine concentration at first and reaches a maximum at $\sim 5 \times 10^{18} \text{ cm}^{-3}$, and then decreases gradually with a further increase of iodine content. These findings indicate that the magnitude of T_b shows a close correlation with the degree of inhomogeneity in the Cr distribution

at high Cr compositions.

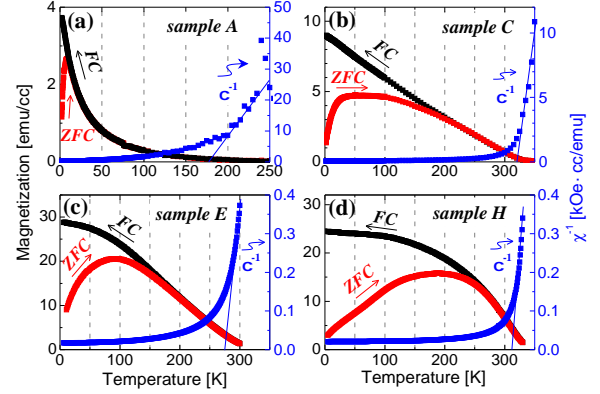


FIG. 69 (Color online) Temperature dependence of magnetization and the inverse magnetic susceptibility of $\text{Zn}_{1-x}\text{Cr}_x\text{Te}$ films: (a) undoped $\text{Zn}_{0.95}\text{Cr}_{0.05}\text{Te}$ film grown under Te-rich flux (sample A in Fig.67); (b) I-doped $\text{Zn}_{0.95}\text{Cr}_{0.05}\text{Te}$ film (sample C); (c) undoped $\text{Zn}_{0.81}\text{Cr}_{0.19}\text{Te}$ film grown under Te-rich flux (sample E); (d) I-doped $\text{Zn}_{0.81}\text{Cr}_{0.19}\text{Te}$ film (sample H). Adapted from Kuroda *et al.*, 2007.

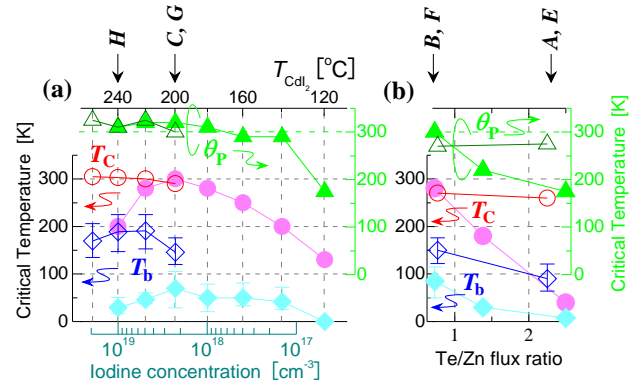


FIG. 70 (Color online) Plots of the three characteristic temperatures for I-doped and undoped $\text{Zn}_{1-x}\text{Cr}_x\text{Te}$ films with $x \simeq 0.05$ and $x \sim 0.2$: the apparent Curie temperature $T_C^{(\text{app})}$ (circles), the paramagnetic Curie-Weiss temperature θ_P (triangles) and the blocking temperature T_b (diamonds) are plotted as a function of the iodine concentration for I-doped films (a), and as a function of Te/Zn flux ratio for undoped films (b). For clarity, the vertical scale for θ_P (right) is shifted from that for $T_C^{(\text{app})}$ and T_b (left). The data for $x \simeq 0.05$ and 0.2 are represented by full and open symbols, respectively. The labels A-H above the figure serve to identify the films shown in Fig. 67. From Ishikawa *et al.*, 2009.

These experimental observations demonstrate that the magnetic properties of $(\text{Zn,Cr})\text{Te}$ films are closely correlated with the uniformity of Cr distribution. In particular, non-uniform Cr distributions give rise to higher values of characteristic temperatures introduced above.

Since the FM exchange interaction between Cr spins is considered to be of short-range (Bergqvist *et al.*, 2004), the long-range FM order cannot be expected for average Cr compositions below the percolation limit for the nearest neighbor coupling in the fcc lattice, $x < 0.20$, if we assume a random distribution of Cr ions. On the other hand, if the alloy is phase-separated into regions with low and high Cr contents, Cr spins inside the Cr-rich regions can order ferromagnetically, so that the crystal containing these FM nanoclusters is expected to exhibit superparamagnetic features. Below the blocking temperature T_b , whose magnitude is given by the product of the mean cluster volume V and the density of the magnetic anisotropy energy K , FM-like properties are observed in superparamagnetic systems, including magnetization hysteresis and remanence. A clear correlation between the values of T_b and the inhomogeneity of Cr distribution confirms this interpretation. In addition, rather broad peaks in the $M(T)$ curves obtained under the ZFC condition reflect a dispersion in values of blocking temperatures. The apparent Curie temperature $T_C^{(\text{app})}$, corresponding to temperature at which hysteretic behaviors due to the magnetic anisotropy of the clusters disappear entirely, is determined by an upper bound of the T_b distribution. On the other hand, the paramagnetic Curie-Weiss temperature θ_P , deduced from the fitting of the linear dependence in the $\chi^{-1}(T)$ curves in the high-temperature range, is determined by interactions between Cr spins inside the Cr-rich NCs and, therefore, is virtually independent of their volume V . This is consistent with the observation that θ_P is less dependent on the uniformity of the Cr distribution than $T_C^{(\text{app})}$ and T_b .

Altogether, the data imply that zb Cr-rich (Cr,Zn)Te with the ZnTe lattice parameter is characterized by $T_C \simeq 300$ K. A ferromagnetic ground state was theoretically predicted for such zb-CrTe (Zhao and Zunger, 2005).

3. Mechanism of Cr aggregation

Similarly to the most combinations of magnetic elements and host semiconductors, the solubility of Cr in ZnTe is low and the incorporation of Cr beyond a certain limit results in the crystallographic or chemical phase separation. The driving force of the phase separation is an attractive interaction between magnetic cations. The key to understanding the observation that the uniformity of Cr distribution varies with the Zn/Te flux ratio or the co-doping of donor or acceptor impurities is the dependence of the attractive interaction on the Fermi level position within the band-gap (Dietl, 2006; Ye and Freeman, 2006). In the case of intrinsic ZnTe, Cr assumes the 2+ charge state. However, this charge state can be changed by trapping a hole or an electron since the substitutional Cr forms the deep donor $\text{Cr}^{2+/3+}$ and acceptor $\text{Cr}^{1+/2+}$ levels within the band-gap of the host ZnTe (Godlewski and Kamińska, 1980). Therefore, the

co-doping with shallow impurities changes the Cr valence and, thus, the Cr-Cr interaction. In particular, an additional Coulomb repulsion between those Cr ions that have trapped a carrier hinders the Cr aggregation, leading to a uniform distribution of Cr cations. This is in contrast to a non-uniform distribution driven by the attractive interaction between isoelectronic Cr^{2+} ions, associated with the contribution of TM 3d states to bonding, as discussed in Sec. II.B.

In order to understand the observed phenomena based on the above model, it should be taken into account that ZnTe crystals, due to the native formation of Zn vacancies, have a tendency to become p-type even without intentional doping (Baron *et al.*, 1998). In (Zn,Cr)Te films grown under the Te-rich condition, the Zn vacancies are formed, so that a part of the Cr ions assumes the Cr^{3+} charge state. The growth under the Zn-rich condition or co-doping with iodine donors restore the isoelectronic Cr^{2+} configuration, as the Zn vacancies are suppressed by a surplus supply of Zn or compensated by the I donors. In the I-doped films, the degree of inhomogeneity and the value of the blocking temperature T_b (and also $T_C^{(\text{app})}$ for $x \simeq 0.05$) attain a maximum when the iodine and Zn vacancy concentrations become equal, so that the charge state of all Cr ions is 2+. In contrast, co-doping with N increases the concentration of Cr^{3+} ions (as observed by XMCD (Yamazaki *et al.*, 2011)), which diminishes attractive forces between Cr cations and results in their uncorrelated distribution.

4. Magneto-optical and magnetotransport properties

Magneto-optical properties were investigated for crystals exhibiting a high temperature ferromagnetism assigned, as explained above, to a non-uniform Cr distribution. Figure 71 shows the result of the MCD measurement on an I-doped $\text{Zn}_{1-x}\text{Cr}_x\text{Te}$ film with a relatively low Cr content of $x = 0.07$ and $T_C^{(\text{app})} \simeq 300$ K (Ozaki *et al.*, 2006). As shown in Fig. 71(a), the MCD spectrum exhibits a broad band below the band-gap energy 2.38 eV of ZnTe, in contrast to a sharp peak in the spectrum of ZnTe. According to Fig. 71(b), the MCD intensity at a fixed photon energy shows virtually identical magnetic-field dependence as magnetization measured by SQUID. These features of MCD were also observed in undoped films $x = 0.07$ grown under Te-rich flux (Kuroda *et al.*, 2005), in which smaller scale inhomogeneities in the Cr distribution lead to lower value of $T_C^{(\text{app})}$, of the order of 100 K.

The broad band in the MCD spectrum could be attributed to optical transitions from the valence band to the Cr 3d level in the middle of the band-gap, with a significant broadening of the absorption energy due to the lattice relaxation (Godlewski and Kamińska, 1980) or may originate from the presence of Cr-rich regions that affect MCD in a wide spectral region *via* magnetization-dependent boundary conditions for light propagation

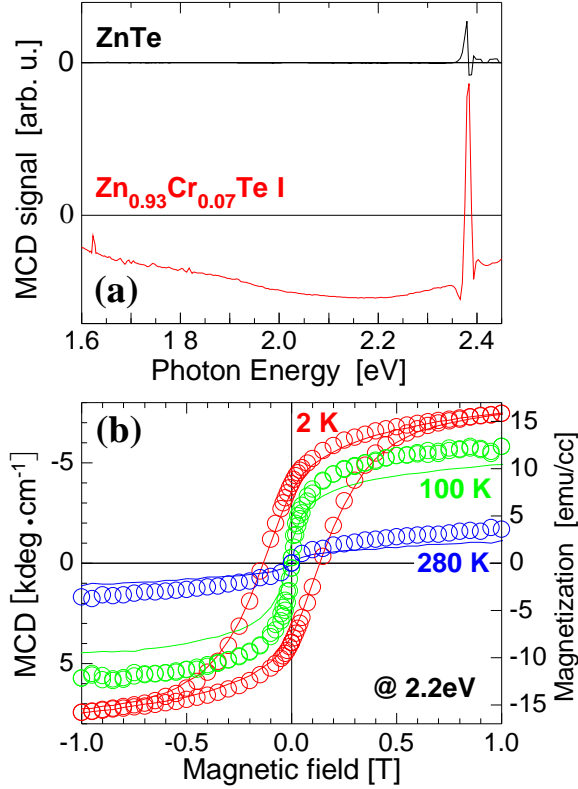


FIG. 71 (Color online) Results of MCD studies on an I-doped $\text{Zn}_{0.93}\text{Cr}_{0.07}\text{Te}$ film. The measurement was performed in the transmission mode in the magnetic field perpendicular to the film plane (Faraday configuration). (a) The MCD spectra at 2 K and 1 T, with the reference data for a ZnTe film. (b) Magnetic-field dependence of the MCD intensities at a photo energy of 2.2 eV (circles), together with magnetization values measured by SQUID (lines). From Ozaki *et al.*, 2006.

(the Kerr effect). The consistency between magneto-optical and magnetization data, observed also in the case of decomposed (Ga,Mn)As, (Ge,Mn), and (Ge,Fe), as discussed in Secs. III.C, VI.B.1, and VII.D, respectively, suggests that in these systems magneto-optical response is dominated by regions with high TM concentrations, which account for the FM properties.

In addition, the anomalous Hall effect was observed in an I-doped $\text{Zn}_{1-x}\text{Cr}_x\text{Te}$ film (Kuroda *et al.*, 2007, Supplementary Information). The observation of the magneto-optical and magneto-transport properties peculiar to DMSs even in phase-separated (Zn,Cr)Te layers suggests a possibility of new functionalities in hybrid structure consisting of TM-rich nanocrystals embedded in a semiconductor matrix, as discussed in Sec. IX.

C. Crystallographic phase separation and konbu phase

1. Structural nanocharacterization

Structural, compositional, and magnetic properties were investigated for a series of I-doped $\text{Zn}_{1-x}\text{Cr}_x\text{Te}$ films varying substrate temperature during the growth, growth rate, and crystallographic orientation of the substrate (Nishio *et al.*, 2009). It was found that the substrate temperature is a critical factor controlling the phase separation. For the lower average Cr content $x \simeq 0.05$, the structural properties of I-doped $\text{Zn}_{1-x}\text{Cr}_x\text{Te}$ films change with the substrate temperature T_g , while the uniformity of Cr distribution is not much different. Figure 72 shows the results of TEM and EDS studies of I-doped $\text{Zn}_{1-x}\text{Cr}_x\text{Te}$ ($x \simeq 0.05$) films grown in the [001] direction at various values of T_g . As shown in the TEM and diffraction images (left column), the crystallinity exhibits a marked variation with T_g ; at an intermediate temperature of $T_g = 270^\circ\text{C}$, the crystal consists dominantly of the zb structure, but the stacking faults along the $\{111\}$ planes are observed in the lattice image and additional spots corresponding the triplet periodicity of the stacking faults appear in the diffraction image. The crystallinity is deteriorated by decreasing T_g down to 240°C , exhibiting polycrystalline features in addition to the stacking faults, while it looks much improved by increasing T_g up to 360°C , the TEM and diffraction images exhibiting almost perfect zb structure without the stacking faults. On the other hand, as shown in the Cr mapping images (right column), the Cr distribution is inhomogeneous in all the films, but the degree of inhomogeneity seems to be slightly reduced with the increase of T_g . The results of XAS measurements at Cr K-edge for the same series of I-doped $\text{Zn}_{1-x}\text{Cr}_x\text{Te}$ ($x \simeq 0.05$) films suggested a change in the local crystallographic structure depending on the substrate temperature (Ofuchi *et al.*, 2009), which is correlated with the results of the TEM observation.

A natural explanation of the above results would be that lattice defects appearing at low T_g lower kinetic barriers for Cr diffusion, so that the Cr aggregation is efficient even at low T_g .

In contrast, for the higher average Cr content $x \sim 0.2$, the substrate temperature affects significantly the form of the phase separation (Nishio *et al.*, 2009). Figure 73 presents Cr mapping images of the films grown onto either (001) or (111) substrates at intermediate and high substrate temperatures, $T_g = 300^\circ\text{C}$ and 360°C . As shown in Fig. 73(a), the Cr-rich regions form isolated NCs at $T_g = 300^\circ\text{C}$, whereas according to Figs. 73(b,c), in the case of films grown at $T_g = 360^\circ\text{C}$, Cr-rich regions look like continuous nanocolumns aligned approximately along the $\langle 111 \rangle$ direction of the host crystal. As estimated by the EDS spot analysis, a maximum value of the local Cr composition is $x = 0.4\text{--}0.5$, both in the case of Cr-rich NCs and nanocolumns.

Figure 74 shows TEM and EELS images allowing to shed some light on the crystal structure of Cr-rich re-

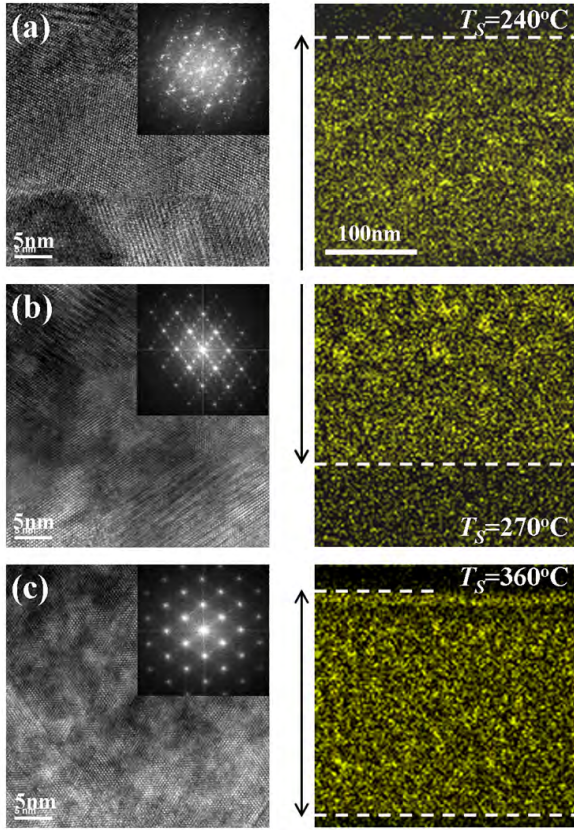


FIG. 72 (Color online) TEM and diffraction images (left) and EDS mapping images of Cr (right) for cross-sectional pieces of I-doped $\text{Zn}_{1-x}\text{Cr}_x\text{Te}$ films ($x \simeq 0.05$) grown in the [001] direction at various substrate temperatures. (a) $T_g = 240^\circ\text{C}$; (b) $T_g = 270^\circ\text{C}$; (c) $T_g = 360^\circ\text{C}$. In the EDS mapping images, the range of the $\text{Zn}_{1-x}\text{Cr}_x\text{Te}$:I layer and the boundary with the ZnTe buffer layer are indicated by arrows and dashed lines, respectively. From Nishio *et al.*, 2009.

gions in an I-doped $\text{Zn}_{1-x}\text{Cr}_x\text{Te}$ films ($x = 0.25$) grown at $T_g = 360^\circ\text{C}$ (Kobayashi *et al.*, 2012). In the TEM image in Fig. 74(a), Moiré fringes appear in many regions, which suggests that these regions are composed of a mixed phase with different crystal structures, pointing to the presence of crystallographic phase separation. By comparing the TEM image [Fig. 74(a)] with the EELS image [Fig. 74(b)] of the same area, it is confirmed that the Moiré regions in the TEM image correspond to the regions with a high value of Cr content. In a magnified lattice image in Fig. 74(c), the Moiré region is boarded by the two $\{111\}_{zb}$ planes, and there appears another region exhibiting a different structure, identified as a hexagonal structure from the arrangement of diffraction spots in the FFT image shown in Fig. 74(d). The lattice parameters deduced from the spacing between the spots are $c = 6.32 \text{ \AA}$ and $a = 4.18 \text{ \AA}$, close to the values reported for bulk CrTe in the NiAs structure (Dijkstra *et al.*, 1989; Ohta *et al.*, 1993). This suggests that the precipitates consist of NiAs-type CrTe or of non-stoichiometric

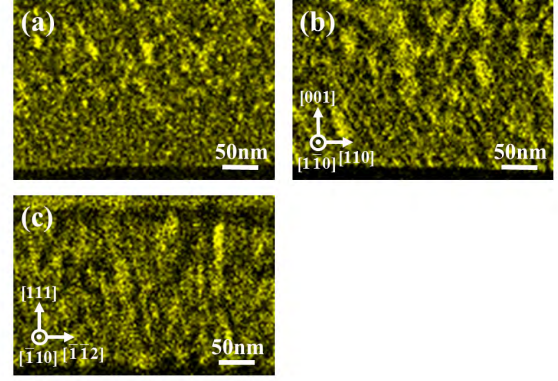


FIG. 73 (Color online) Cross-sectional EDS mapping images of Cr for $\text{Zn}_{1-x}\text{Cr}_x\text{Te}$:I films ($x \simeq 0.25$) grown (a) at a substrate temperature $T_g = 300^\circ\text{C}$ in the [001] direction, (b) at $T_g = 360^\circ\text{C}$ in the [001] direction, and (c) at $T_g = 360^\circ\text{C}$ in the [111] direction, imposed by crystallographic orientations of GaAs substrates. Cr-rich regions are formed as isolated NCs in (a), while they are elongated and form continuous nanocolumns in (b), (c). From Nishio *et al.*, 2009.

$\text{Cr}_{1-\delta}\text{Te}$ in a hexagonal structure. According to the TEM and diffraction images in Fig. 74, the c -axis of elongated hexagonal NCs is nearly parallel to the $\{111\}_{zb}$ planes of the host. In the case of $T_g = 360^\circ\text{C}$, a 3D analysis using atom probe tomography revealed that the Cr-aggregated regions were formed as thin plates with the base plane nearly parallel to the $\{111\}_{zb}$ planes (Kodzuka, 2012).

The above observations of the crystallographic phase separation support theoretical computations indicating that zb -CrTe with the lattice parameter of ZnTe is unstable against the formation of CrTe in the NiAs crystal structure (Zhao and Zunger, 2005).

In the conventional ω - 2θ XRD scan, which probes XRD from the film plane, only maxima corresponding to the zb host crystal were detected for the (001) $\text{Zn}_{1-x}\text{Cr}_x\text{Te}$:I films with $x \sim 0.2$. However, hexagonal $\text{Cr}_{1-\delta}\text{Te}$ precipitates that have principal diffraction planes inclined against the film plane, can be detected in the ω -scan, as shown in Fig. 75. This measurement was performed with the incident and reflected x-ray in the $(\bar{1}\bar{1}0)$ plane of the host zb structure. By locking 2θ to the values corresponding to the $(\bar{1}\bar{1}01)$ and $(\bar{1}\bar{1}02)$ planes of the hexagonal $\text{Cr}_{1-\delta}\text{Te}$, the diffractions from these planes were detected in an almost symmetric way in respect to ω . The values of ω of the diffraction peaks are close to the ones expected from the crystallographic relation of these NCs to the host crystal revealed by the TEM observation. On the other hand, in the same ω -scan measurement in another configuration with the incident and reflected x-ray in the $(110)_{zb}$ plane, the intensity of the diffraction from the hexagonal nanocrystals was much reduced (Kobayashi *et al.*, 2013). This result suggests that the hexagonal $\text{Cr}_{1-\delta}\text{Te}$ tends to stack preferentially on the $(111)_{zb}$ plane [or Zn-terminated $(111)A$ plane] rather

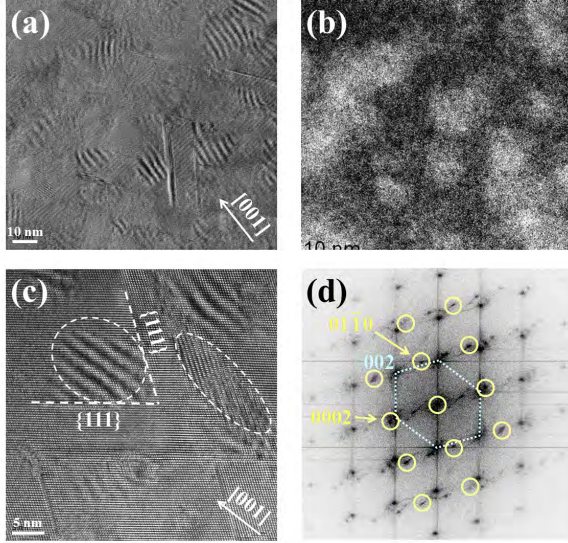


FIG. 74 (Color online) TEM and EELS images of the I-doped $\text{Zn}_{0.75}\text{Cr}_{0.25}\text{Te}$ film grown in the [001] direction at $T_g = 360^\circ\text{C}$ [the same film as shown in Fig. 73(b)] giving evidence for crystallographic phase separations. (a) TEM image. (b) Cr mapping image of the same area obtained by EELS. (c) Lattice image in a magnified scale. A Moiré region boarded by the two $\{111\}_{\text{zb}}$ planes and a region of a different crystallographic structure are observed (encircled by broken lines). (d) FFT image determined from the data in (c). The set of diffraction spots of a hexagonal arrangement (connected by dotted line) originates from the zb structure and that of a rectangular arrangement (denoted by circles) originates from the hexagonal structure whose c -plane is almost parallel to the $\{111\}_{\text{zb}}$ planes. From Kobayashi *et al.*, 2012.

than $(\bar{1}\bar{1}\bar{1})_{\text{zb}}$ plane [or Te-terminated (111)B plane]. This preference could be understood from the arrangement of atoms on the interface between the hexagonal $\text{Cr}_{1-\delta}\text{Te}$ and the host zb crystals.

The intensity of the above diffraction from the hexagonal $\text{Cr}_{1-\delta}\text{Te}$ gives us an estimate of the amount of the precipitates formed in the crystal. The ω -scan measurement on the series of $\text{Zn}_{1-x}\text{Cr}_x\text{Te}:\text{I}$ films grown at different substrate temperatures revealed how the amount of the precipitates depends on the growth temperature. As clearly seen in Fig. 76, in which the diffraction intensity from the $(\bar{1}\bar{1}01)$ plane of the hexagonal $\text{Cr}_{1-\delta}\text{Te}$ is plotted as a function of the substrate temperature T_g , the hexagonal precipitates are formed in a larger quantity at a higher T_g .

As described above, it was revealed that the substrate temperature during the growth affects the Cr aggregation significantly; the Cr-aggregated regions are formed in almost spherical NCs at a low T_g while they are formed in thin plates at higher T_g . In addition, the amount of the hexagonal precipitates increases with the increase of T_g . The observed variation in the shape of Cr-aggregated regions with the substrate temperature reflects a differ-

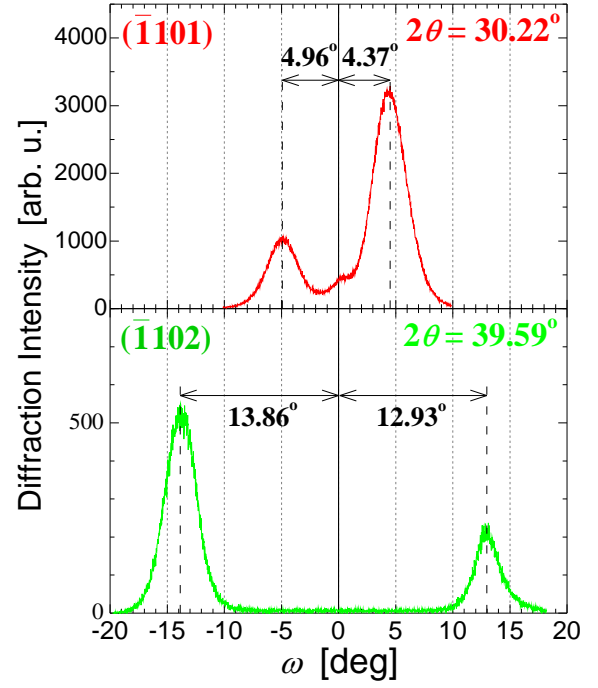


FIG. 75 (Color online) XRD ω -scan profiles of an I-doped $\text{Zn}_{0.73}\text{Cr}_{0.27}\text{Te}$ film grown in the [001] orientation at $T_g = 390^\circ\text{C}$. The diffraction profiles from the plane ($2\theta = 30.22^\circ$) (upper panel) and the plane ($2\theta = 39.59^\circ$) (lower panel) are plotted, respectively. This measurement was performed in the configuration with the incident and reflected x-ray in the $(\bar{1}\bar{1}0)$ plane of the host zb structure. From Kobayashi *et al.*, 2012.

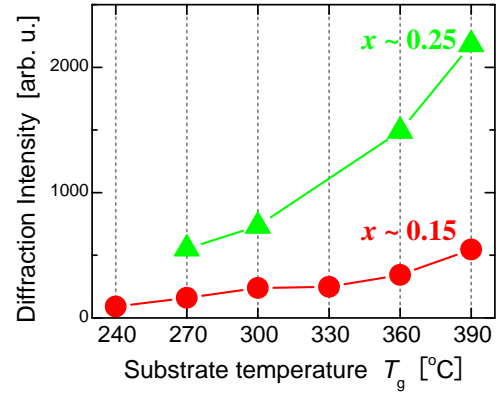


FIG. 76 (Color online) The diffraction intensity from the $(\bar{1}\bar{1}01)$ plane of the hexagonal $\text{Cr}_{1-\delta}\text{Te}$ nanocrystals is plotted as a function of the substrate temperature T_g for the two series of $\text{Zn}_{1-x}\text{Cr}_x\text{Te}:\text{I}$ films with $x \approx 0.15$ and 0.25 . After Kuroda *et al.*, unpublished.

ence in the dimensionality of the spinodal decomposition,

which results in the formation of the dairiseki or konbu phase, as discussed in Secs. II.C.1 and II.C.2. According to a theoretical consideration (Fukushima *et al.*, 2006b), the spinodal decomposition in the layer-by-layer growth mode results in the formation of one-dimensional columnar regions with high content of the magnetic element. With an enhanced migration of impinging atoms on the growing surface at a higher substrate temperature, Cr atoms tend to aggregate in such places on the top surface where Cr-aggregated areas are already formed in the layer just below the growing surface. As a result, the Cr-rich regions form continuous nanocolumns, instead of isolated clusters appearing in the case of slow surface migration. Once Cr-aggregated regions are formed inside the crystal, they can transform at sufficiently high T_g into a stable $\text{Cr}_{1-\delta}\text{Te}$ hexagonal compound that assumes crystal orientation insuring the best much of atom positions with the host, i.e., minimizing the interfacial energy.

2. Magnetic properties

Three characteristic temperatures $T_C^{(\text{app})}$, θ_P , and T_b are presented in Fig. 77 as a function of T_g for the two series of I-doped $\text{Zn}_{1-x}\text{Cr}_x\text{Te}$ films with the low and high average Cr contents of $x \simeq 0.05$ (full symbols) and 0.25 (empty symbols). In the case of $x \simeq 0.05$, the film grown at the lowest T_g of 240°C did not exhibit ferromagnetism even at 2 K, presumably due to the deterioration of crystallinity. In contrast, the films obtained at T_g from 270°C to 390°C show high temperature ferromagnetism, consistent with the presence of Cr-rich regions. The observed values $T_C^{(\text{app})} \simeq 300$ K and $\theta_P \simeq 330$ K for films with $x \simeq 0.25$ are consistent with the fact that $\text{Cr}_{1-\delta}\text{Te}$ in bulk form exhibits ferromagnetism with $T_C = 325\text{--}360$ K for a relatively a small amount of Cr deficiency (Shimada *et al.*, 1996), though T_C decreases when the amount of Cr deficiency increases further on (Ohta *et al.*, 1993). Furthermore, in agreement with TEM data pointing to smaller volumes of Cr-rich regions in the case of samples with lower x , the magnitudes of T_b are significantly lower for $x \simeq 0.05$ comparing to the values found for $x \simeq 0.25$. However, rather surprisingly, $T_C^{(\text{app})}$ and θ_P tend to decrease from 300 K down to 250 K with T_g for samples with $x \simeq 0.05$. This result points to a complex interplay between the degree of host crystallinity, TM aggregation, and resulting T_C of embedded NCs.

It can be expected that strain and shape of NCs affect their magnetic anisotropy. Figure 78 presents magnetization loops $M(H)$ for magnetic fields perpendicular and parallel to the film plane for the I-doped (111) $\text{Zn}_{1-x}\text{Cr}_x\text{Te}$ film ($x = 0.22$), in which Cr-rich NCs show the elongated shape with long axes almost perpendicular to the film plane (Nishio *et al.*, 2009). As seen, hysteretic behaviors are more pronounced (i.e., the coercive force is larger) for the perpendicular magnetic field. This suggests that the easy direction is parallel to the long axis

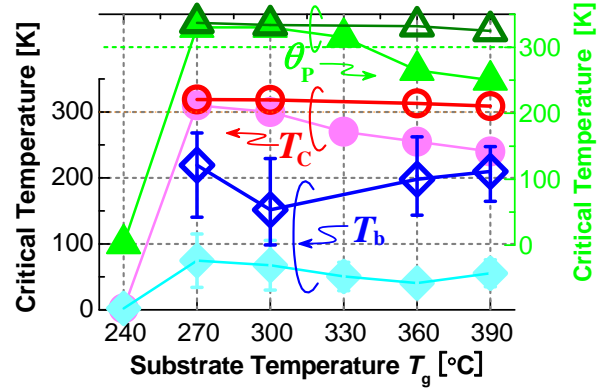


FIG. 77 (Color online) Plot of three characteristic temperatures $T_C^{(\text{app})}$ (circles), θ_P (triangles), and T_b (diamonds) as a function of the substrate temperature T_g for I-doped $\text{Zn}_{1-x}\text{Cr}_x\text{Te}$ films with the low ($x \simeq 0.05$) and high ($x \simeq 0.25$) average Cr contents (full and empty symbols, respectively). After Kuroda *et al.*, unpublished.

of the NCs, the expected result for the shape-dependent direction of the demagnetization field and weak in-plane crystalline magnetic anisotropy.

D. Summary

The comprehensive studies of $(\text{Zn,Cr})\text{Te}$ described in this section show that the Cr distribution is affected significantly by co-doping with donor or acceptor impurities or by the growth under different Zn/Te flux ratios. This behavior originates from the influence of co-doping and growth conditions upon the position of the Fermi level in the band gap, which controls the Cr charge state: from Cr^{+1} for high I donor concentrations to Cr^{3+} at high density of N acceptor impurities or Zn vacancies. These findings corroborate the influence of Coulomb interactions upon the chemical forces between TM ions. The magnetic properties are closely correlated with the heterogeneity of the Cr distribution. In particular, the Cr-rich regions give rise to the appearance of high-temperature ferromagnetism. The systematic investigations on $(\text{Zn,Cr})\text{Te}$ films grown under various MBE conditions revealed that the growth temperature plays a crucial role in the phase separation: the crystallographic structure and the shape of the Cr-rich regions change with the substrate temperature during the growth. The ability to fabricate in a self-organized fashion hybrid systems consisting of FM nano-clusters embedded in the semiconductor matrix, as realized in $(\text{Zn,Cr})\text{Te}$ and other DMSs, opens doors for studies of various functionalities of these novel nanocomposites.

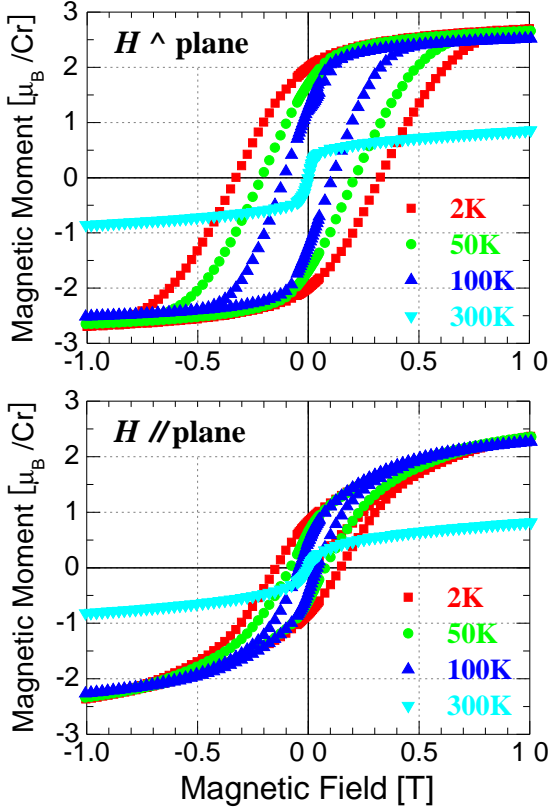


FIG. 78 (Color online) Magnetization loops in $\text{Zn}_{0.78}\text{Cr}_{0.22}\text{Te}:\text{I}$ film grown in the $[111]$ direction at $T_g = 360^\circ\text{C}$ (the same film as shown in Fig. 73(c)). The upper (bottom) panel shows the results obtained for magnetic fields parallel (perpendicular) to the growth direction. The coercive field H_c for the parallel configuration ($\mu_0 H_c = 0.33\text{ T}$ at 2 K) is much larger than for the perpendicular configuration ($\mu_0 H_c = 0.14\text{ T}$ at 2 K). From Nishio *et al.*, 2009.

IX. PROSPECTS OF SPINODAL NANOTECHNOLOGY

It is believed that the application of embedded metallic NCs will revolutionize the performance of various commercial devices, such as flash memories. Similarly colloidal or embedded semiconducting NCs, i.e., semiconductor quantum dots and nanowires, are extensively studied as perspective media for lightning, low current semiconductor lasers, solar cells, single-photon emitters and detectors, quantum processors and memories.

In view of the results presented in the previous sections, the incorporation of TM impurities into semiconductors opens the door to fabrication of dense arrays of TM-rich NCs coherently embedded into a semiconductor matrix. Depending on growth and processing conditions as well as on the combination of host semiconductor, TM impurity, and co-doping the self-assembled NCs can be metallic or semiconducting, form nanodots or nanocolumns, exhibit FM, ferrimagnetic, or AF spin

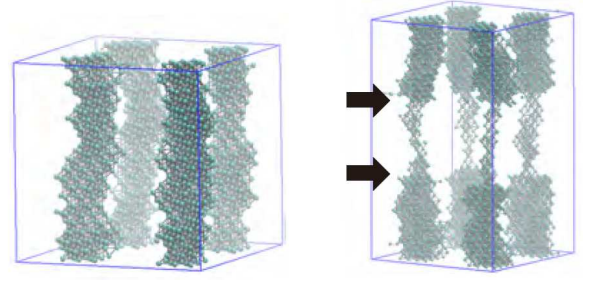


FIG. 79 (Color online) Demonstration of the nanocolumn shape control by Monte Carlo simulations of $(\text{Zn,Cr})\text{Te}$ epitaxy (the konbu phase). Positions of Cr cations are shown. Nano-scale seeding by zinc-blende CrTe (a). During the deposition (between two arrows), the Cr concentration is reduced to control the shape of the metallic and FM CrTe nanocolumns embedded in ZnTe (b). Adapted from Fukushima *et al.*, 2007.

ordering persisting usually to above RT. Thus, spinodal nanotechnology not only allows one to explore the feasibility of device fabrication with a new and versatile bottom-up method but also enlarges considerably the spectrum of possible functionalities offered by nanoscale heterogeneous systems (Dietl, 2008c; Katayama-Yoshida *et al.*, 2007).

As an example, Fig. 79 presents results of Monte Carlo simulations in which the Cr flux was altered during the 2D growth of CrTe nanocolumns (the *konbu* phase) embedded in ZnTe (Fukushima *et al.*, 2007). This example suggests that dense arrays of various nanodevices can be fabricated by selecting appropriate growth protocols. For instance, by reducing the flux for time corresponding to the growth of a few monolayers, the formation of magnetic tunnel junctions is predicted for nanocolumns of a FM metal (Fukushima *et al.*, 2007). Such junctions can serve for low-power high-density magnetic storage, including spin-torque magnetic random access memories and, if sufficiently high TMR will be found, for the field programmable logic, i.e., TMR-based connecting/disconnecting switches (Reiss and Meyners, 2006), and even all-magnetic logic, characterized by low power consumption and radiation hardness. Furthermore, nanocolumns might form racetracks for domain-wall based 3D memories (Thomas *et al.*, 2007).

Another kind of possible spintronic applications makes use of the coupling between FM leads and carriers in a semiconductor matrix. In particular, in the proposal of a scalable processor (Dery *et al.*, 2007), the magnetization-dependent interaction between neighbor FM contacts is mediated by spin currents injected from the FM contact to the semiconductor. Furthermore, in the pioneering design of quantum processors involving the couplings between single spins on quantum dots, nanomagnets serve to introduce differences in spin resonance frequencies of particular dots, which makes it possible to address individual spins (Loss and DiVincenzo, 1998). Actually, top-

down methods were already employed to pattern nanostructures with tiny magnets whose stray fields controlled spin currents (Wróbel *et al.*, 2004) and spin resonance frequencies (Pioro-Ladrière *et al.*, 2008) at the nanoscale.

As already discussed in Secs. III, VI, VII, and VIII, a number of decomposed alloys exhibits spin-related magnetotransport and magneto-optical phenomena typically persisting up to T_C of the relevant NCs. In particular, AHE was observed in (Ge,Mn) (Jamet *et al.*, 2006) and (Zn,Cr)Te (Kuroda *et al.*, 2007). A sizable magnitude of AHE together with heterogeneity-induced mixing between diagonal and off-diagonal conductivity components, resulted in a large positive MR of (Ge,Mn) (Jamet *et al.*, 2006). A related effect was also observed in granular films with MnSb (Akinaga *et al.*, 2000b) and MnAs (Yokoyama *et al.*, 2006) NCs. Furthermore, TMR was found in a device containing MnAs and GaAs:MnAs electrodes (Hai *et al.*, 2008, 2006). All these findings could possibly be exploited in magnetic field sensors with characteristics (*e.g.*, impedance) that could be tailored over a wide range.

At the same time, as elaborated in Secs. III, VI, VII, and VIII, magnetic circular dichroism (MCD) was reported for decomposed (Ga,Mn)As, (Ge,Mn), (Ge,Fe), and (Zn,Cr)Te as well as for other systems such as (Ga,Mn)P (Monette *et al.*, 2010). A combination of strong and spectrally broad MCD specific to FM metals and weak losses characterizing the semiconductor hosts suggests possible applications of decomposed semiconductor alloys as optical isolators (Amemiya *et al.*, 2006) as well as 3D tunable photonic crystals and spatial light modulators for advanced photonic applications (Park *et al.*, 2002a).

Metallic nanocolumns and nanodots could also serve as high quality nanocontacts in nanoelectronics and optoelectronics as well as metallic elements in nanoplasmonics. Dense arrays of nanocolumns are also attractive for thermoelectric applications (power generators and coolers) as a specific form of density of states in 1D systems is expected to result in a significant enhancement of the Seebeck and Peltier effects (Shinya *et al.*, 2014; Vu *et al.*, 2011). Furthermore, the growth process presented in Fig. 79 can be adapted to fabricate devices for all-metal nanoelectronics based, for instance, on single-electron transistors. Actually, the Coulomb blockade was demonstrated for a single MnAs NC, tunnel-coupled to MnAs electrodes patterned lithographically (Hai *et al.*, 2010). A long spin relaxation time, of the order of 10 μ s, was evaluated from these data.

If, in contrast, nanocolumns were semiconducting, appropriate band gap engineering could improve efficiency of photovoltaic solar cells by leading to spatial separation of photoelectrons and photoholes in such all-semiconductor superstructures (Oshitani *et al.*, 2011; Tani *et al.*, 2010, 2011, 2012a,b,c). As a one more example of possible functionalities worth mentioning is the case of catalysts for automotive-emissions control. Here, by using decomposed alloy with spatially separated NCs

containing the relevant metal, *e.g.*, Pt, the destructive process of metal agglomeration could be much reduced (Hamada *et al.*, 2011; Kizaki and Katayama-Yoshida, 2013; Kizaki *et al.*, 2008).

X. SUMMARY AND OUTLOOK

We have reviewed the recent progress in the understanding of high-temperature ferromagnetism in a range of magnetically doped semiconductors, including primarily (Ga,Mn)As, (Ga,Mn)N, (Ga,Fe)N, (Ge,Mn), (Ge,Fe), and (Zn,Cr)Te. As we have emphasized, the abundance of contradicting views on the mechanisms accounting for surprisingly large magnitudes of Curie temperature T_C resulted from intertwined theoretical and experimental challenges requiring the application of cutting-edge computational and materials nano-characterization methods that have mostly become available only recently. In this way, semiconductors doped by transition metals (TMs) have emerged as outstanding systems to test our understanding of unanticipated relationships between (i) growth conditions, co-doping, and processing; (ii) alloy nanostructure, and (iii) pertinent macroscopic properties.

The key ingredient of the materials families that have been described in this review is spinodal nanodecomposition leading to the formation of TM-rich nanocrystals (NCs) either commensurate with the TM-depleted host (chemical phase separation) or precipitating in another crystallographic and/or chemical form (crystallographic phase separation). Whether magnetic ions are distributed randomly or form aggregates is determined by the competition between attractive forces among TM cations (revealed by *ab initio* computations) and kinetic barriers for TM diffusion at the growth surface or in the bulk. Accordingly, the alloy decomposition is more efficient at high growth temperatures and slow growth rates, and depends also on the Fermi level position (co-doping) that changes TMs valence and their diffusion coefficients. Remarkably, according to both theoretical simulations and experimental results the TM-rich regions (condensed magnetic semiconductors - CMSs) assume the form of either nanodots (the *dairiseki* phase) or nanocolumns (the *konbu* phase). Furthermore, the nanodots can be distributed randomly or accumulate in a plane adjacent to the interface or surface. Similarly, nanocolumns can extend along the growth direction or assume another spatial orientation.

A rich spectrum of forms assumed by spinodal nanodecomposition, such as chemical phase separation or aggregation of precipitates in one plane, have elucidated the reason why uncovering the presence of a non-random distribution of magnetic ions was so challenging in DMS research and, in particular, why the application of standard in-house structure characterization techniques (*e.g.*, x-ray diffraction) was often misleading. The comprehensive element-specific nano-characterization investigations

described in this review have demonstrated the existence of a tight correlation between the presence of TM-rich NCs and high- T_C ferromagnetism. Within this scenario the puzzling T_C independence of the average TM concentration x has been explained. However, it has been found that the reverse is not true, i.e., variations of T_C with x do not prove a uniform distribution of TM ions. Furthermore, according to the evidence, spontaneous magnetization of decomposed systems is usually smaller than expected from the TM concentration, as typically a part of TM ions is distributed randomly giving rise to a paramagnetic, and not FM or superparamagnetic response. It also happens that NCs formed by spinodal decomposition are weak ferromagnets or even antiferromagnets [see, e.g., the data for (Ga,Fe)N in Sec. V] or that coupling between them results rather in a superferromagnetic behavior than in a superparamagnetic phase (Sawicki *et al.*, 2013).

It was often argued that the presence of the magnetic circular dichroism (MCD) points to a random distribution of TM ions over cation sites (Ando, 2006). Actually, because of boundary conditions for electromagnetic waves, the dielectric function of heterogeneous media contains contributions from all constituents. Hence, TM-rich NCs not only give a specific contribution to the magnetic response but, in general, can also affect, in a magnetization-dependent fashion, magneto-optical properties, as observed for (Ga,Mn)As, (Ge,Mn), (Ge,Fe), and (Zn,Cr)Te (Secs. III, VI, VII, and VIII, respectively). In particular, metallic NCs rather than enhancing MCD only at host critical points of the Brillouin zone, produce a large MCD signal over a wide spectral range. However, no enhancement of MCD has been reported for (Ga,Mn)N and (Ga,Fe)N (Secs. IV and V, respectively). Presumably, in the case of (Ga,Mn)N, Mn-rich NCs are wide band-gap insulators, whereas in (Ga,Fe)N the NCs aggregate in a narrow plane parallel to the film surface, which reduces their coupling to light.

A similar question arises to what extent magnetotransport studies could tell whether the TM distribution is uniform or one deals rather with spinodal nanodecomposition. A weak negative contribution to the Hall signal, resembling the anomalous Hall effect (AHE), can originate from stray fields generated by magnetic NCs. More often, spin-depending coupling between host charge current and magnetic NCs results in a sizable AHE, as observed in (Ge,Mn) and (Zn,Cr)Te, and mentioned in Secs. VI and VIII. Particularly challenging is the question of magnetoresistance (MR). Here positive MR, specific to semiconductor-metallic nanocomposite (Solin *et al.*, 2000), may appear, particularly if the magnitude of AHE is significant, the effect being discussed for (Ge,Mn) in Sec. VI. Moreover, as in other non-magnetic and magnetic semiconductors, one expects a range of MRs associated with quantum localization phenomena (Dietl, 2008b). In particular, strong spin disorder scattering near T_C accounts for colossal negative MR. However, a weak negative MR away from T_C , according to straight-

forward and parameter-free theoretical modeling, originates rather from the influence of magnetic flux upon interference of scattered carrier de Broglie waves (weak localization MR) than from spin disorder scattering. This is in contrast with magnetically doped *metals* in which effects of spin disorder scattering dominate, as competing scattering mechanisms and associated localization effects are typically weak.

Despite the recent progress, there is a number of challenging and open questions ahead. As an example we note that an important theoretical issue is the determination of kinetic barriers for TM diffusion at the growth surface and in the bulk, crucial parameters to simulate quantitatively the NC assembly during epitaxy, co-doping, or post-growth annealing. Furthermore, since CMSs assume a form imposed by the matrix, their chemical composition and associated properties are by no means obvious. In particular, it is hardly known whether open d shells remain localized in CMSs (as in the parent DMS) or rather a Mott-Hubbard transition occurs, leading to itinerant magnetism specific to certain end compounds such as MnAs and CrTe. It was actually suggested that Mn-rich zinc-blende (zb) NCs in decomposed (Ga,Mn)As contain only about 20% of Mn and retain the properties of (Ga,Mn)As in which spins are localized (Lawniczak-Jablonska *et al.*, 2011). A related question concerns the crystalline magnetic anisotropy of particular combinations of CMSs and hosts. This anisotropy, together with shape anisotropy and dipolar or exchange coupling between NCs, accounts for macroscopic magnetic properties, including the apparent magnitude of T_C and the character of magnetic hystereses. A theoretical and experimental evaluation of this anisotropy awaits for future studies.

Furthermore, FM-like features brought about by uncompensated spins at the surface of antiferromagnetic (AF) NCs, as discussed theoretically (Dietl *et al.*, 2007), have not yet been put into evidence experimentally in the materials considered here. We also note that the FM proximity effect or the exchange bias in the case of AF CMSs can lead to spin polarization of a semiconductor surrounding a given NC. Such induced polarization will persist up to the spin ordering temperature of the CMS and, according to the RKKY theory, will extend over a distance of the order of the inverse Fermi vector in the presence of band carriers and perhaps over two or three bond lengths in their absence. This effect was examined in Fe/(Ga,Mn)As heterostructures (Maccherozzi *et al.*, 2008) but not yet in decomposed alloys, in which it can lead to an erroneous conclusion that the host is intrinsically FM up to high temperatures.

Whilst theoretical and experimental results described in this review have concerned with a limited set of compounds, there is a ground to expect that the developed methodology, the observed phenomena, and the conclusions drawn from theoretical and experimental results apply to a much broader class of magnetically doped materials and also to many other alloys. We are quite certain

that with a further development and with a wide-spread use of powerful nanocharacterization tools, the family of decomposed alloys will steadily grow. Future work will also show the role of structural defects, residual impurities (e.g. H) or contaminants (e.g. Fe-rich nanoparticles) in the appearance of high- T_C ferromagnetism in semiconductors and oxides.

It is clear that the understanding of the origin of high- T_C ferromagnetism and detailed knowledge on the TM distribution are preconditions for a meaningful design of devices that could exploit the outstanding properties of magnetically doped semiconductors and insulators. As discussed in Sec. IX, the demonstrated and predicted functionalities of decomposed magnetic alloys might be of interest not only for spintronics but also for electronics, photonics, plasmonics, photovoltaics, thermoelectrics, and catalysis. In general terms, the future studies of these systems will contribute to address the timely question on to what extent and when bottom-up technologies will start to be competitive with the top-down approaches dominating today.

List of abbreviations

1D, 2D, 3D	one-, two-, three-dimensional
AF	antiferromagnetic
AP	atom probe
AFM	atomic force microscopy
AHE	anomalous Hall effect
CEMS	Conversion electron Mössbauer spectroscopy
CMS	condensed magnetic semiconductor
CPA	coherent potential approximation
DFT	density functional theory
DMS	dilute magnetic semiconductors
DFS	dilute ferromagnetic semiconductor
EDS	energy dispersive x-ray spectroscopy (the same as EDX)
EELS	electron energy loss spectroscopy
EPR	electron paramagnetic resonance
EF	energy-filtered
EXAFS	extended x-ray Absorption Fine Structure
FC	field cool
fcc	face-centered cubic
FM	ferromagnetic
FMR	ferromagnetic resonance
GGA	generalized gradient approximations
GISAXS	grazing incidence small angle x-ray scattering
GMR	giant magnetoresistance
HR	high resolution
LDA	local density approximation
LSDA	local spin density approximation
LT	low-temperature
MBE	molecular beam epitaxy
MOVPE	metal organic vapor phase deposition (the same as MOCVD)
MCD	magnetic circular dichroism
MR	magnetoresistance
NC	nanocrystal
RHEED	reflection high-energy electron diffraction
RPA	random phase approximation

RKKY	Ruderman-Kittel-Kasuya-Yosida
SEM	scanning electron microscopy
SIMS	secondary ions mass spectroscopy
SQUID	superconducting quantum interference device
STM	scanning tunneling microscopy
SXRD	synchrotron x-ray diffraction
TEM	transmission electron microscopy
TM	transition metal
TMR	tunneling magnetoresistance
wz	wurtzite
XANES	x-ray absorption near edge structure
XAS	x-ray absorption spectroscopy
XES	x-ray emission spectroscopy
XMCD	x-ray magnetic circular dichroism
XPEEM	x-ray photoemission electron microscopy
XRd	x-ray diffraction
ZFC	zero-field cooled
zb	zinc-blende

Acknowledgments

The work of T.D. and A.B. was supported by the European Research Council through the FunDMS Advanced Grant (No. 227690) within the "Ideas" 7th Framework Programme of the EC, by Wroclaw Research Centre EIT+ within the project "The Application of Nanotechnology in Advanced Materials" - NanoMat (P2IG.01.01.02-02-002/08) co-financed by the European Regional Development Fund (operational Programme Innovative Economy, 1.1.2), and also (T.D.) by National Center of Science in Poland (Decision No. 2011/02/A/ST3/ 00125), whereas (A.B.) by the Austrian Fonds zur Förderung der wissenschaftlichen Forschung – FWF (P18942, P20065, P22471, P22477, and N107-NAN). K.S. acknowledges the financial support from a Grand-in-Aid for Scientific Research for young researchers and on Innovative Areas "Materials Design through Computics: Complex Correlation and Non-Equilibrium Dynamics", the GCOE program "Core Research and Engineering of Advanced Materials-Interdisciplinary Education Center for Materials Science", and a JST Strategic Japanese-German Cooperative Program "Computational design and evaluation of spintronics materials". M. J. and A. Ba. was supported by the French Agence Nationale pour la Recherche (ANR project GeMO) and the Nanoscience Foundation of Grenoble (RTRA project IMAGE). M. T. and P. N. H. acknowledge the financial support from the Grant-in-Aid for Specially Promoted Research (No. 23000010) and Grant-in-Aid for Young Scientists (A) (No. 24686040), the Project for Developing Innovation Systems of MEXT, the FIRST program, the Global COE program (C04), and the ATI foundation. The study of S. K. was partially supported by Grant-in-Aids for Scientific Research from Ministry of Education, Science, Sports and Culture of the Japanese Government. HKY acknowledges the financial support provided by the Japan Society for the Promotion of Science (JSPS) Core-to-Core Program "Computational Nano-Materials Design on Green Energy", and Advanced Low Carbon Technology Research and Devel-

opment Program (ALCA) of Japan Science and Technology Agency (JST) "Spinodal Nanotechnology for Super-High Efficiency Energy Conversion".

References

- Abe, E., F. Matsukura, H. Yasuda, Y. Ohno, and H. Ohno, 2000, "Molecular beam epitaxy of III-V diluted magnetic semiconductor (Ga,Mn)Sb," *Physica E* **7**, 981
- Abraham, D. W., M. M. Frank, and S. Guha, 2005, "Absence of magnetism in hafnium oxide films," *Appl. Phys. Lett.* **87**, 252502
- Aharoni, A., 1996, "Introduction to the theory of ferromagnetism," in *The International Series of Monographs on Physics*, International Series of Monographs on Physics, Vol. 109, edited by J. Birman, S. F. Edwards, R. H. Friend, C. H. Llewellyn Smith, M. Rees, D. Sherrington, and G. Veneziano (Oxford Science Publications)
- Ahlers, S., D. Bougeard, N. Sircar, G. Abstreiter, A. Trampert, M. Opel, and R. Gross, 2006, "Magnetic and structural properties of $\text{Ge}_x\text{Mn}_{1-x}$ films: Precipitation of intermetallic nanomagnets," *Phys. Rev. B* **74**, 214411
- Ahlers, S., P. R. Stone, N. Sircar, E. Arenholz, O. D. Dubon, and D. Bougeard, 2009, "Comparison of the magnetic properties of gemn thin films through mn l-edge x-ray absorption," *Appl. Phys. Lett.* **95**, 151911
- Akai, H., 1989, "Fast Korringa-Kohn-Rostoker coherent potential approximation and its application to FCC Ni-Fe systems," *J. Phys.: Condens. Matt.* **1**, 8045
- Akai, H., 2002, <http://kkr.phys.sci.osaka-u.ac.jp/>
- Akai, H., and P. H. Dederichs, 1993, "Local moment disorder in ferromagnetic alloys," *Phys. Rev. B* **47**, 8739
- Akinaga, H., S. Miyanishi, K. Tanaka, W. Van Roy, and K. Onodera, 2000a, "Magneto-optical properties and the potential application of GaAs with magnetic MnAs nanoclusters," *Appl. Phys. Lett.* **76**, 97
- Akinaga, H., M. Mizuguchi, K. Ono, and M. Oshima, 2000b, "Room-temperature thousandfold magnetoresistance change in MnSb granular films: Magnetoresistive switch effect," *Appl. Phys. Lett.* **76**, 357
- Akinaga, H., S. Nemeth, J. De Boeck, L. Nistor, H. Bender, G. Borghs, H. Ofuchi, and M. Oshima, 2000c, "Growth and characterization of low-temperature grown GaN with high Fe doping," *Appl. Phys. Lett.* **77**, 4377
- Amemiya, T., H. Shimizu, Y. Nakano, Pham Nam Hai, M. Yokoyama, and M. Tanaka, 2006, "Semiconductor waveguide optical isolator based on nonreciprocal loss induced by ferromagnetic MnAs," *Appl. Phys. Lett.* **89**, 021104
- Ando, K., 2006, "Seeking room-temperature ferromagnetic semiconductors," *Science* **312**, 1883
- Ando, K., A. Chiba, and H. Tanoue, 1998, "Uniaxial magnetic anisotropy of submicron MnAs ferromagnets in GaAs semiconductors," *Appl. Phys. Lett.* **73**, 387
- de Andrés, A., A. Espinosa, C. Prieto, M. García-Hernández, R. Ramírez-Jiménez, S. Lambert-Milot, and R. A. Masut, 2011, "MnP films and MnP nanocrystals embedded in GaP epilayers grown on GaP(001): Magnetic properties and local bonding structure," *J. Appl. Phys.* **109**, 113910
- Arras, E., D. Caliste, T. Deutsch, F. Lancon, and P. Pochet, 2011, "Phase diagram, structure, and magnetic properties of the ge-mn system: A first-principles study," *Phys. Rev. B* **83**, 174103
- Arras, E., F. Lancon, and I. Slipukhina, 2012, "Interface-driven phase separation in multifunctional materials: The case of the ferromagnetic semiconductor gemn," *Phys. Rev. B* **85**, 115204
- Barnaś, J., and A. Fert, 1998, "Effects of spin accumulation on single-electron tunneling in a double ferromagnetic microjunction," *Europhys. Lett.* **44**, 85
- Baron, T., K. Saminadayar, and N. Magnea, 1998, "Nitrogen doping of Te-based II-VI compounds during growth by molecular beam epitaxy," *J. Appl. Phys.* **83**, 1354
- Baur, J., K. Maier, M. Kunzer, U. Kaufmann, and J. Schneider, 1994, "Determination of the GaN/AlN band offset via the (-/0) acceptor level of iron," *Appl. Phys. Lett.* **65**, 2211
- Beleggia, M., S. Tandon, Y. Zhu, and M. De Graef, 2004, "On the magnetostatic interactions between nanoparticles of arbitrary shape," *J. Magn. Magn. Mater.* **278**, 270
- Beloborodov, I. S., A. V. Lopatin, V. M. Vinokur, and K. B. Efetov, 2007, "Granular electronic systems," *Rev. Mod. Phys.* **79**, 469
- Bergqvist, L., O. Eriksson, J. Kudrnovský, V. Drchal, P. Korzhavyi, and I. Turek, 2004, "Magnetic percolation in diluted magnetic semiconductors," *Phys. Rev. Lett.* **93**, 137202
- Bergqvist, L., K. Sato, P. H. Dederichs, and H. Katayama-Yoshida, 2010, *Phys. Rev. B*, submitted
- Biegger, E., L. Staheli, M. Fonin, U. Rudiger, and Y. S. Dedkov, 2007, "Intrinsic ferromagnetism versus phase segregation in Mn-doped Ge," *J. Appl. Phys.* **101**, 103912
- Bihler, C., H. Huebl, M. S. Brandt, S. T. B. Goennenwein, M. Reinwald, U. Wurstbauer, M. Döppe, D. Weiss, and W. Wegscheider, 2006, "Magnetic anisotropy of $\text{Ga}_{1-x}\text{Mn}_x\text{As}$ thin films on GaAs(311)A probed by ferromagnetic resonance," *Appl. Phys. Lett.* **89**, 012507
- Binns, C., K. N. Trohidou, J. Bansmann, S. H. Baker, J. A. Blackman, J.-P. Bucher, D. Kechrakos, A. Kleibert, S. Louch, K.-H. Meiwes-Broer, G. M. Pastor, A. Perez, and Y. Xie, 2005, "The behaviour of nanostructured magnetic materials produced by depositing gas-phase nanoparticles," *J. Phys. D: Appl. Phys.* **38**, R357
- Biquard, X., O. Proux, J. Cibert, D. Ferrand, H. Mariette, R. Giraud, and B. Barbara, 2003, "Local structure and valence state of Mn in $\text{Ga}_{1-x}\text{Mn}_x\text{N}$ epilayers," *J. Supercond.* **16**, 127
- Birowska, M., C. Śliwa, J. A. Majewski, and T. Dietl, 2012, "Origin of bulk uniaxial anisotropy in zinc-blende dilute magnetic semiconductors," *Phys. Rev. Lett.* **108**, 237203
- Blinowski, J., P. Kacman, and J. A. Majewski, 1996, "Ferromagnetic superexchange in Cr-based diluted magnetic semiconductors," *Phys. Rev. B* **53**, 9524
- Boeck, J. De, R. Oesterholt, A. Van Esch, H. Bender, C. Bruynseraede, C. Van Hoof, and G. Borghs, 1996, "Nanometer-scale magnetic MnAs particles in GaAs grown by molecular beam epitaxy," *Appl. Phys. Lett.* **68**, 2744
- Bogusławski, P., and J. Bernholc, 2006, "Properties of wurtzite $w\text{-MnN}$ and of $w\text{-MnN}$ inclusions in $(\text{Ga,Mn})\text{N}$," *Appl. Phys. Lett.* **88**, 092502
- Bolcal, E., V. Dimitrov, B. Aktaş, H. Aslan, and A. Bozkurt, 2012, "Ground state and magnetostatic properties of a dipole system arranged in two-dimensional lattice," *Acta Phys. Polon. A* **121**, 257, <http://przyrbwn.icm.edu.pl/APP/PDF/121/a121z1p80.pdf>
- Bonanni, A., 2007, "Ferromagnetic nitride-based semiconduc-

- tors doped with transition metals and rare earths,” *Semicond. Sci. Technol.* **22**, R41
- Bonanni, A., 2011, “(Nano)characterization of semiconductor materials and structures,” *Semicon. Sci. Technol.* **26**, 060301
- Bonanni, A., M. Kiecana, C. Simbrunner, T. Li, M. Sawicki, M. Wegscheider, M. Quast, H. Przybylińska, A. Navarro-Quezada, R. Jakiela, A. Wolos, W. Jantsch, and T. Dietl, 2007, “Paramagnetic GaN:Fe and ferromagnetic (Ga,Fe)N: The relationship between structural, electronic, and magnetic properties,” *Phys. Rev. B* **75**, 125210
- Bonanni, A., A. Navarro-Quezada, T. Li, M. Wegscheider, Z. Matěj, V. Holý, R. T. Lechner, G. Bauer, M. Rovezzi, F. D’Acapito, M. Kiecana, M. Sawicki, and T. Dietl, 2008, “Controlled aggregation of magnetic ions in a semiconductor: An experimental demonstration,” *Phys. Rev. Lett.* **101**, 135502
- Bonanni, A., M. Sawicki, T. Devillers, W. Stefanowicz, B. Faina, Tian Li, T. E. Winkler, D. Sztenkiel, A. Navarro-Quezada, M. Rovezzi, R. Jakiela, A. Grois, M. Wegscheider, W. Jantsch, J. Suffczyński, F. D’Acapito, A. Meingast, G. Kothleitner, and T. Dietl, 2011, “Experimental probing of exchange interactions between localized spins in the dilute magnetic insulator (Ga,Mn)N,” *Phys. Rev. B* **84**, 035206
- Bonanni, A., C. Simbrunner, M. Wegscheider, H. Przybylinska, A. Wolos, H. Sitter, and W. Jantsch, 2006, “Doping of GaN with Fe and Mg for spintronics applications,” *phys. stat. sol. (b)* **243**, 1701
- Bougeard, D., S. Ahlers, A. Trampert, N. Sircar, and G. Abstreiter, 2006, “Clustering in a precipitate free GeMn magnetic semiconductor,” *Phys. Rev. Lett.* **97**, 237202
- Bougeard, D., N. Sircar, S. Ahlers, V. Lang, G. Abstreiter, A. Trampert, J.-M. LeBeau, S. Stemmer, D. W. Saxey, and A. Cerezo, 2009, “Ge_{1-x}Mn_x clusters: Central structural and magnetic building blocks of nanoscale wire-like self-assembly in a magnetic semiconductor,” *Nano Lett.* **9**, 3743
- Bouzerar, G., and T. Ziman, 2006, “Model for vacancy-induced d^0 ferromagnetism in oxide compounds,” *Phys. Rev. Lett.* **96**, 207602
- Bouzerar, G., T. Ziman, and J. Kudrnovský, 2005, “Calculating the Curie temperature reliably in diluted III-V ferromagnetic semiconductors,” *Europhys. Lett.* **69**, 812
- Cahn, J. W., 1962, “On spinodal decomposition in cubic crystals,” *Acta Metall.* **10** (3), 179, ISSN 0001-6160
- Cahn, J. W., and J. E. Hilliard, 1958, “Free energy of a nonuniform system. i. interfacial free energy,” *J. Chem. Phys.* **28**, 258
- Ceperly, D. M., and B. J. Alder, 1980, “Ground state of the electron gas by a stochastic method,” *Phys. Rev. Lett.* **45**, 566
- Chan, J. A., Jefferson Z. Liu, H. Raebiger, S. Lany, and A. Zunger, 2008, “Relative stability, electronic structure, and magnetism of MnN and (Ga,Mn)N alloys,” *Phys. Rev. B* **78**, 184109
- Chason, E., J. Y. Tsao, K. M. Horn, and S. T. Picraux, 1989, “Dynamics of growth roughening and smoothing on Ge (001),” *J. Vac. Sci. Technol. B* **7**, 332
- Chen, Chenjia, Ming Cai, Xuezhong Wang, Shifa Xu, Ming Zhang, Xiaomin Ding, and Yunxi Sun, 2000, “Ferromagnetic properties and structures of the Mn-implanted GaAs semiconductor,” *J. Appl. Phys.* **87**, 5636
- Chiba, D., Y. Nishitani, F. Matsukura, and H. Ohno, 2007, “Properties of Ga_{1-x}Mn_xAs with high Mn composition ($x > 0.1$),” *Appl. Phys. Lett.* **90**, 122503
- Chinchore, A., K. Wang, W. Lin, J. Pak, and A. R. Smith, 2008, “Atomic layer structure of manganese atoms on wurtzite gallium nitride (000 $\bar{1}$),” *Appl. Phys. Lett.* **93**, 181908
- Cho, S., S. Choi, S. C. Hong, Y. Kim, J. B. Ketterson, B. J. Kim, Y. C. Kim, and J. H. Jung, 2002, “Ferromagnetism in Mn-doped Ge,” *Phys. Rev. B* **66**, 033303
- Cho, Y. J., C. H. Kim, H. S. Kim, W. S. Lee, S.-H. Park, J. Park, S. Y. Bae, B. Kim, H. Lee, and J.-Y. Kim, 2008a, “Ferromagnetic Ge_{1-x}M_x (M = Mn, Fe, and Co) nanowires,” *Chem. Mater.* **20**, 4694
- Cho, Y. J., C. H. Kim, H. S. Kim, W. S. Lee, S. H. Park, J. Park, S. Y. Bae, B. Kim, H. Lee, and J. Y. Kim, 2008b, “Ferromagnetic Ge_{1-x}M_x (M = Mn, Fe, and Co) nanowires,” *Chem. Mater.* **20**, 4694
- Choi, E. A., J. Kang, and K. J. Chang, 2006, “Energetics of cubic and hexagonal phases in Mn-doped GaN: First-principles pseudopotential calculations,” *Phys. Rev. B* **74**, 245218
- Choi, S., S. C. Hong, S. Cho, Y. Kim, J. B. Ketterson, C.-U. Jung, K. Rhie, B.-J. Kim, and Y. C. Kim, 2003, “Ferromagnetic properties in Cr, Fe-doped Ge single crystals,” *J. Appl. Phys.* **93**, 7670
- Coe, J. M. D., P. Stamenov, R. D. Gunning, M. Venkatesan, and K. Paul, 2010, “Ferromagnetism in defect-ridden oxides and related materials,” *New J. Phys.* **12**, 053025
- Continenza, A., G. Profeta, and S. Picozzi, 2006a, “Transition metal doping and clustering in Ge,” *Appl. Phys. Lett.* **89** (20), 202510, doi:\bibinfo{doi}{10.1063/1.2388894}
- Continenza, A., G. Profeta, and S. Picozzi, 2006b, “Transition metal impurities in Ge: Chemical trends and codoping studied by electronic structure calculations,” *Phys. Rev. B* **73**, 035212
- Continenza, A., G. Profeta, and S. Picozzi, 2007, “Transition metal doping in Ge,” *J. Magn. Magn. Mat.* **310**, 2147
- Cui, X. Y., B. Delley, A. J. Freeman, and C. Stampfl, 2006, “Magnetic metastability in tetrahedrally bonded magnetic III-nitride semiconductors,” *Phys. Rev. Lett.* **97**, 016402
- Cui, X. Y., B. Delley, A. J. Freeman, and C. Stampfl, 2007, “Neutral and charged embedded clusters of Mn in doped GaN from first principles,” *Phys. Rev. B* **76**, 045201
- Cui, X. Y., J. E. Medvedeva, B. Delley, A. J. Freeman, N. Newman, and C. Stampfl, 2005, “Role of embedded clustering in dilute magnetic semiconductors: Cr doped GaN,” *Phys. Rev. Lett.* **95**, 256404
- Cui, Y., and L. Li, 2002, “Suppression of phase segregation during molecular-beam epitaxial growth of GaMnN using nitrogen-hydrogen plasma,” *Appl. Phys. Lett.* **80**, 4139
- Da Silva, Juarez L. F., Gustavo M. Dalpian, and Su-Huai Wei, 2008, “Carrier-induced enhancement and suppression of ferromagnetism in Zn_{1-x}Cr_xTe and Ga_{1-x}Cr_xAs: origin of the spinodal decomposition,” *New J. Phys.* **10**, 113007
- Dalpian, G. M., Juarez L. F. Da Silva, and Su-Huai Wei, 2009, “Ferrimagnetic Fe-doped GaN: An unusual magnetic phase in dilute magnetic semiconductors,” *Phys. Rev. B* **79**, 241201(R)
- Darques, M., A. Encinas, L. Vila, and L. Piraux, 2004, “Tailoring of the c-axis orientation and magnetic anisotropy in electrodeposited Co nanowires,” *J. Phys.: Condens. Matter* **16**, S2279
- Das, G. P., B. K. Rao, and P. Jena, 2003, “Ferromagnetism in Mn-doped GaN: From clusters to crystals,” *Phys. Rev. B* **68**, 035207

- Demchenko, I. N., K. Lawniczka-Jablonska, T. Story, V. Osinniy, R. Jakiela, J. Z. Domagala, J. Sadowski, M. Klepka, A. Wolska, and M. Chernyshova, 2007, "Modification of the local atomic structure around Mn atoms in (Ga,Mn)As layers by high temperature annealing," *J. Phys.: Condens. Matter* **19**, 496205
- Dery, H., P. Dalal, L. Cywiński, and L. J. Sham, 2007, "Spin-based logic in semiconductors for reconfigurable large-scale circuits," *Nature* **447**, 573
- Devillers, T., 2008, "Etude des propriétés physiques des phases de Ge(1-x)Mn(x) ferromagnétiques pour l'électronique de spin. physics. université joseph fourier-grenoble i, 2008,"
- Devillers, T., M. Jamet, A. Barski, V. Poydenot, P. Bayle-Guillemaud, E. Bellet-Amalric, S. Cherifi, and J. Cibert, 2007a, "Structure and magnetism of self-organized Ge_{1-x}Mn_x nanocolumns on Ge(001)," *Phys. Rev. B* **76**, 205306
- Devillers, T., M. Jamet, A. Barski, V. Poydenot, R. Dujardin, P. Bayle Guillemaud, J. Rothman, E. Bellet Amalric, J. Cibert, R. Mattana, and S. Tatarenko, 2006, "Ferromagnetism of self-organized Ge_{1-x}Mn_x nano-pillars," *phys. stat. sol. (c)* **3**, 4123
- Devillers, T., M. Jamet, A. Barski, V. Poydenot, R. Dujardin, P. Bayle Guillemaud, J. Rothman, E. Bellet Amalric, J. Cibert, R. Mattana, and S. Tatarenko, 2007b, "Structural and magnetic properties of GeMn layers; high Curie temperature ferromagnetism induced by self organized GeMn nano-columns," *phys. stat. sol. (a)* **204**, 130
- Devillers, T., M. Rovezzi, N. Gonzalez Szwacki, S. Dobkowska, W. Stefanowicz, D. Sztenkiel, A. Grois, J. Suffczyński, A. Navarro-Quezada, B. Faina, T. Li, P. Glatzel, F. d'Acapito, R. Jakiela, M. Sawicki, J. A. Majewski, T. Dietl, and A. Bonanni, 2012, "Manipulating Mn-Mg_k cation complexes to control the charge- and spin-state of Mn in GaN," *Sci. Rep.* **2**, 722
- Dhar, S., O. Brandt, A. Trampert, L. Däweritz, K. J. Friedland, K. H. Ploog, J. Keller, B. Beschoten, and G. Güntherodt, 2003a, "Origin of high-temperature ferromagnetism in (Ga,Mn)N layers grown on 4H-SiC(0001) by reactive molecular-beam epitaxy," *Appl. Phys. Lett.* **82**, 2077
- Dhar, S., O. Brandt, A. Trampert, K. J. Friedland, Y. J. Sun, and K. H. Ploog, 2003b, "Observation of spin-glass behavior in homogeneous (Ga,Mn)N layers grown by reactive molecular-beam epitaxy," *Phys. Rev. B* **67**, 165205
- Dietl, T., 1981, "Semimagnetic semiconductors in high magnetic fields," in *Physics in High Magnetic Fields*, edited by S. Chikazumi and N. Miura (Springer, Berlin) p. 344
- Dietl, T., 2002, "Ferromagnetic semiconductors," *Semicond. Sci. Technol.* **17**, 377
- Dietl, T., 2003, "Dilute magnetic semiconductors: Functional ferromagnets," *Nat. Mater.* **2**, 646
- Dietl, T., 2004, "Spintronics in nitrides," in *Materials Research Society Fall Meeting, Boston, USA, Nov. 2004, MRS Proceedings*, Vol. 831, edited by C. Wetzel, B. Gil, M. Kuzuhara, and M. Manfra, p. E91
- Dietl, T., 2006, "Self-organised growth controlled by charge states of magnetic impurities," *Nature Mat.* **5**, 673
- Dietl, T., 2008a, "Hole states in wide band-gap diluted magnetic semiconductors and oxides," *Phys. Rev. B* **77**, 085208
- Dietl, T., 2008b, "Interplay between carrier localization and magnetism in diluted magnetic and ferromagnetic semiconductors," *J. Phys. Soc. Jpn.* **77**, 031005
- Dietl, T., 2008c, "Origin and control of ferromagnetism in dilute magnetic semiconductors and oxides (invited)," *J. Appl. Phys.* **103**, 07D111
- Dietl, T., T. Andrearczyk, A. Lipińska, M. Kiecana, Maureen Tay, and Yihong Wu, 2007, "Origin of ferromagnetism in Zn_{1-x}Co_xO from magnetization and spin-dependent magnetoresistance measurements," *Phys. Rev. B* **76**, 155312
- Dietl, T., and H. Ohno, 2003, "Ferromagnetic III-V and II-VI semiconductors," *MRS Bulletin*, 714
- Dietl, T., and H. Ohno, 2014, "Dilute ferromagnetic semiconductors: Physics and spintronic structures," *Rev. Mod. Phys.* **86**, 187
- Dietl, T., H. Ohno, and F. Matsukura, 2001, "Hole-mediated ferromagnetism in tetrahedrally coordinated semiconductors," *Phys. Rev. B* **63**, 195205
- Dietl, T., H. Ohno, F. Matsukura, J. Cibert, and D. Ferrand, 2000, "Zener model description of ferromagnetism in zinc-blende magnetic semiconductors," *Science* **287**, 1019
- Dijkstra, J., H. H. Weitering, C. F. van Bruggen, C. Haas, and R. A. de Groot, 1989, "Band-structure calculations, and magnetic and transport properties of ferromagnetic chromium tellurides (CrTe, Cr₃Te₄, Cr₂Te₃)," *J. Phys.: Condens. Matter* **1**, 9141
- Dimitrov, D. A., and G. M. Wysin, 1996, "Magnetic properties of superparamagnetic particles by a Monte Carlo method," *Phys. Rev. B* **54**, 9237
- DiPietro, R. S., H. G. Johnson, S. P. Bennett, T. J. Nummy, L. H. Lewis, and D. Heiman, 2010, "Determining magnetic nanoparticle size distributions from thermomagnetic measurements," *Appl. Phys. Lett.* **96**, 222506
- D'Orazio, F., F. Lucari, N. Pinto, L. Morresi, and R. Murri, 2004, "Toward room temperature ferromagnetism of Ge:Mn systems," *J. Magn. Magn. Mat.* **272**, 2006
- Dreizler, R., and E. Gross, 1995, in *Density Functional Theory* (Plenum Press, New York)
- Droghetti, A., N. Baadji, and S. Sanvito, 2009, "MgN: A possible material for spintronic applications," *Phys. Rev. B* **80**, 235310
- Du, Aijun, Stefano Sanvito, and Sean C. Smith, 2012, "First-principles prediction of metal-free magnetism and intrinsic half-metallicity in graphitic carbon nitride," *Phys. Rev. Lett.* **108**, 197207
- Ducastelle, F., and F. Gautier, 1976, "Generalized perturbation theory in disordered transitional alloys: Applications to the calculation of ordering energies," *J. Phys. F: Met. Phys.* **6**, 2039
- Dwiliński, R., R. Doradziński, J. Garczyński, L. Sierzputowski, J. M. Baranowski, and M. Kamińska, 1998, "AMMONO method of GaN and AlN production," *Diamond Relat. Mater.* **7**, 1348
- Edmonds, K. W., P. Bogusławski, K. Y. Wang, R. P. Campion, N. R. S. Farley, B. L. Gallagher, C. T. Foxon, M. Sawicki, T. Dietl, M. B. Nardelli, and J. Bernholc, 2004, "Mn interstitial diffusion in (Ga,Mn)As," *Phys. Rev. Lett.* **92**, 037201
- Elfimov, I. S., S. Yunoki, and G. A. Sawatzky, 2002, "Possible path to a new class of ferromagnetic and half-metallic ferromagnetic materials," *Phys. Rev. Lett.* **89**, 216403
- Ellner, M., 1980, "Kristallstrukturdaten von Mn₂Ge," *J. Appl. Cryst.* **13**, 99
- Fert, A., and H. Jaffrès, 2001, "Conditions for efficient spin injection from a ferromagnetic metal into a semiconductor," *Phys. Rev. B* **64**, 184420
- Flory, J. P., 1942, "Thermodynamics of high polymer solu-

- tions," *J. Chem. Phys.* **10**, 51
- Forsyth, J. B., and P. J. Brown, 1990, "The spatial distribution of magnetisation density in Mn_5Ge_3 ," *J. Phys.: Condens. Matter* **2**, 2713
- Fukumura, T., and M. Kawasaki, 2013, "Magnetic oxide semiconductors: On the high-temperature ferromagnetism in TiO_2 - and ZnO -based compounds," in *Functional Metal Oxides* (Wiley-VCH Verlag GmbH & Co. KGaA) pp. 89–131
- Fukushima, T., K. Sato, and H. Katayama-Yoshida, 2007, "Ab initio design of fabrication process and shape control of self-organized tera-bit-density nano-magnets in dilute magnetic semiconductors by two-dimensional spinodal decomposition," *phys. stat. sol. (c)* **3**, 4139
- Fukushima, T., K. Sato, H. Katayama-Yoshida, and P. H. Dederichs, 2004, "Theoretical prediction of Curie temperature in $(\text{Zn,Cr})\text{S}$, $(\text{Zn,Cr})\text{Se}$ and $(\text{Zn,Cr})\text{Te}$ by first principles calculations," *Jpn. J. Appl. Phys.* **43**, L1416
- Fukushima, T., K. Sato, H. Katayama-Yoshida, and P. H. Dederichs, 2006a, "Ab initio study of spinodal decomposition in $(\text{Zn,Cr})\text{Te}$," *Phys. Stat. Sol. A* **203**, 2751
- Fukushima, T., K. Sato, H. Katayama-Yoshida, and P. H. Dederichs, 2006b, "Spinodal decomposition under layer by layer growth condition and high Curie temperature quasi-one-dimensional nano-structure in dilute magnetic semiconductors," *Jpn. J. Appl. Phys.* **45**, L416
- Furdyna, J. K., and J. Kossut, 1988, *Diluted Magnetic Semiconductors*, Semiconductors and Semimetals, Vol. 25 (Academic Press, New York)
- Gambardella, P., H. Brune, S. S. Dhesi, P. Bencok, S. R. Krishnakumar, S. Gardonio, M. Veronese, C. Grazioli, and C. Carbone, 2005, "Paramagnetic mn impurities on ge and gaas surfaces," *Phys. Rev. B* **51**, 045337
- Garcia, J., 1985, "Magnetic susceptibility, magnetization and specific heat of $\text{Mn}_{3.2}\text{Ga}_{0.8}\text{N}$," *J. Magn. Magn. Mater.* **51**, 365
- Giebultowicz, T. M., P. Kłowski, N. Samarth, H. Luo, J. K. Furdyna, and J. J. Rhyne, 1993, "Neutron-diffraction studies of zinc-blende MnTe epitaxial films and MnTe/ZnTe superlattices: The effect of strain and dilution on a strongly frustrated fcc antiferromagnet," *Phys. Rev. B* **48**, 12817
- Giraud, R., S. Kuroda, S. Marquet, E. Bellet-Amalric, X. Biquard, B. Barbara, D. Fruchart, D. Ferrand J. Cibert, and H. Mariette, 2004, "Ferromagnetic $(\text{Ga,Mn})\text{N}$ epilayers versus antiferromagnetic GaMn_3N clusters," *Europhys. Lett.* **65**, 553
- Godlewski, M., and M. Kamińska, 1980, "The chromium impurity photogeneration transitions in ZnS , ZnSe and ZnTe ," *J. Phys. C: Solid State Phys.* **13**, 6537
- Gonis, A., 2000, in *Theoretical Materials Science* (Materials Research Society, Warrendale PA)
- Gonzalez Szwacki, N., J. A. Majewski, and T. Dietl, 2011, "Aggregation and magnetism of Cr, Mn, and Fe cations in GaN ," *Phys. Rev. B* **83**, 184417
- Gosk, J., M. Zajac, M. Byszewski, M. Kamińska, J. Szczytko, A. Twardowski B. Strojek, and S. Podsiąło, 2003, "Magnetic properties of $(\text{Ga,Fe})\text{N}$," *J. Supercond. Nov. Magn.* **16**, 79
- Grace, P. J., M. Venkatesan, J. Alaria, J. M. D. Coey, G. Kopnov, and R. Naaman, 2009, "The origin of the magnetism of etched Silicon," *Adv. Mater.* **21**, 71
- Graf, T., S. T. B. Goennenwein, and M. S. Brandt, 2003, "Prospects for carrier-mediated ferromagnetism in GaN ," *phys. stat. sol. (b)* **239**, 277
- Granville, S., B. J. Ruck, F. Budde, H. J. Trodahl, and G. V. M. Williams, 2010, "Nearest-neighbor mn antiferromagnetic exchange in $\text{Ga}_{1-x}\text{Mn}_x\text{N}$," *Phys. Rev. B* **81**, 184425
- Grois, A., T. Devillers, Tian Li, and A. Bonanni, 2014, "Planar array of self-assembled $\text{Ga}_x\text{Fe}_{4-x}\text{N}$ nanocrystals in GaN : magnetic anisotropy determined via ferromagnetic resonance," *Nanotechnology* **25** (39), 395704
- Gu, L., S. Y. Wu, H. X. Liu, R. K. Singh, N. Newman, and D. J. Smith, 2005, "Characterization of $\text{Al}(\text{Cr})\text{N}$ and $\text{Ga}(\text{Cr})\text{N}$ dilute magnetic semiconductors," *J. Magn. Magn. Mater.* **290**, 1395
- Gupta, S., W. E. Fenwick, A. Melton, T. Zaidi, H. Yua, V. Rengarajan, J. Nause, A. Ougazzaden, and I. T. Ferguson, 2008, "MOVPE growth of transition-metal-doped GaN and ZnO for spintronic applications," *J. Cryst. Growth* **310**, 5032
- Gupta, S., H. Kang, M. Strassburg, A. Asghar, M. Kane, W. E. Fenwick, N. Dietz, and I. T. Ferguson, 2006, "A nucleation study of group III-nitride multifunctional nanostructures," *J. Cryst. Growth* **287**, 596
- Hai, Pham Nam, W. Nomura, T. Yatsui, M. Ohtsu, and M. Tanaka, 2012, "Effects of laser irradiation on the self-assembly of MnAs nanoparticles in a GaAs matrix," *Appl. Phys. Lett.* **101**, 193102
- Hai, Pham Nam, S. Ohya, M. Tanaka, S. E. Barnes, and S. Maekawa, 2009, "Electromotive force and huge magnetoresistance in magnetic tunnel junctions," *Nature* **458**, 489
- Hai, Pham Nam, S. Ohya, and M. Tanaka, 2010, "Long spin-relaxation time in a single metal nanoparticle," *Nature Nanotech.* **5**, 593
- Hai, Pham Nam, Y. Sakata, M. Yokoyama, S. Ohya, and M. Tanaka, 2008, "Spin-valve effect by ballistic transport in ferromagnetic metal (MnAs)/semiconductor (GaAs) hybrid heterostructures," *Phys. Rev. B* **77**, 214435
- Hai, Pham Nam, K. Takahashi, M. Yokoyama, S. Ohya, and M. Tanaka, 2007, "Magnetic properties of MnAs nanoclusters embedded in a GaAs semiconductor matrix," *J. Magn. Magn. Mater.* **310**, 1932
- Hai, Pham Nam, S. Yada, and M. Tanaka, 2011, "Phase decomposition diagram of magnetic alloy semiconductor," *J. Appl. Phys.* **109**, 073919
- Hai, Pham Nam, M. Yokoyama, S. Ohya, and M. Tanaka, 2006, "Tunneling magnetoresistance of MnAs thin film/ $\text{GaAs}/\text{AlAs}/\text{GaAs}:\text{MnAs}$ nanoclusters and its AlAs barrier thickness dependence," *Appl. Phys. Lett.* **89**, 242106
- Hamada, I., A. Uozumi, Y. Morikawa, A. Yanase, and H. Katayama-Yoshida, 2011, "A density functional theory study of self-regenerating catalysts $\text{LaFe}_{1-x}\text{M}_x\text{O}_{3-y}$ ($\text{M} = \text{Pd}, \text{Rh}, \text{Pt}$)," *J. Am. Chem. Soc.* **133**, 18506
- Han, Y., M. W. Fay, P. D. Brown, S. V. Novikov, K. W. Edmonds, B. L. Gallagher, R. P. Champion, and C. T. Foxon, 2007, "Microstructural characterization of low-temperature grown GaMnN on $\text{GaAs}(001)$ substrates by plasma-assisted MBE," *Semicond. Sci. Technol.* **22**, 1131
- Hara, S., and T. Fukui, 2006, "Hexagonal ferromagnetic MnAs nanocluster formation on $\text{GaInAs}/\text{InP}(111)\text{B}$ layers by metal-organic vapor phase epitaxy," *Appl. Phys. Lett.* **89**, 113111
- Hara, S., and A. Kuramata, 2005, "Ferromagnetic nanoclusters hybridized in Mn-incorporated GaInAs layers during metal-organic vapour phase epitaxial growth on InP layers

- under low growth temperature conditions,” *Nanotechnology* **16**, 957
- Hayashi, T., M. Tanaka, T. Nishinaga, H. Shimada, H. Tsuchiya, and Y. Otuka, 1997, “(GaMn)As: GaAs-based III-V diluted magnetic semiconductors grown by molecular beam epitaxy,” *J. Cryst. Growth* **175176**, Part **2**, 1063
- Heikman, S., S. Keller, T. Mates, S. P. DenBaars, and U. K. Mishra, 2003, “Growth and characteristics of Fe-doped GaN,” *J. Cryst. Growth* **248**, 513
- Hilbert, S., and W. Nolting, 2004, “Disorder in diluted spin systems,” *Phys. Rev. B* **70**, 165203
- Hinomura, T., and S. Nasu, 1996, “ ^{57}Fe Mössbauer study of Fe nitrides,” *Nouvo Cimento* **18**, 253
- Hohenberg, P., and W. Kohn, 1964, “Inhomogeneous electron Gas,” *Phys. Rev.* **136**, 864
- Houben, A., J. Burghaus, and R. Dronskowski, 2009, “The ternary nitrides GaFe₃N and AlFe₃N: Improved synthesis and magnetic properties,” *Chem. Mater.* **21**, 4332
- Huggins, M. L., 1941, “Solutions of long chain compounds,” *J. Chem. Phys.* **9**, 440
- Hwang, J. I., Y. Ishida, M. Kobayashi, H. Hirata, K. Takubo, T. Mizokawa, A. Fujimori, J. Okamoto, K. Mamiya, Y. Saito, Y. Muramatsu, H. Ott, A. Tanaka, T. Kondo, and H. Munekata, 2005, “High-energy spectroscopic study of the III-V nitride-based diluted magnetic semiconductor Ga_{1-x}Mn_xN,” *Phys. Rev. B* **72**, 085216
- Hwang, J. I., Y. Osafune, M. Kobayashi, K. Ebata, Y. Ooki, Y. Ishida, A. Fujimori, Y. Takeda, T. Okane, Y. Saitoh, K. Kobayashi, and A. Tanaka, 2007, “Depth profile high-energy spectroscopic study of Mn-doped GaN prepared by thermal diffusion,” *J. Appl. Phys.* **101**, 103709
- Hynninen, T., H. Raebiger, and J. von Boehm, 2007, “Structural and magnetic properties of (Ga,Mn)N from first principles,” *Phys. Rev. B* **75**, 125208
- Hynninen, T., H. Raebiger, J. von Boehm, and A. Ayuela, 2006a, “High Curie temperatures in (Ga,Mn)N from Mn clustering,” *Appl. Phys. Lett.* **88**, 122501
- Hynninen, T., H. Raebiger, and J. von Boehm, 2006b, “A multiscale study of ferromagnetism in clustered (Ga,Mn)N,” *J. Phys.: Condensed Matter* **18** (5), 1561
- Ishikawa, K., N. Nishizawa, S. Kuroda, H. Ikeda, K. Takita, M. Mitome, Y. Bando, and T. Dietl, 2009, “Inhomogeneous Cr distribution and superparamagnetic behavior in magnetic semiconductor (Zn, Cr)Te,” *Physics of Semiconductors*, AIP Conf. Proc. **1199**, 419
- Ivanovskii, A. L., 2007, “Magnetic effects induced by sp impurities and defects in nonmagnetic sp materials,” *Physics-Uspokhi* **50** (10), 1031
- Jack, K. H., 1952, “The iron-nitrogen system: the crystal structures of ϵ -phase iron nitrides,” *Acta Cryst.* **5**, 404
- Jacobs, H., D. Rechenbach, and U. Zachwieja, 1995, “Structure determination of γ' -Fe₄N and ϵ -Fe₃N,” *J. Alloys Compd.* **227**, 10
- Jaeger, C., C. Bihler, T. Vallaitis, S. T. B. Goennenwein, M. Opel, R. Gross, and M. S. Brandt, 2006, “Spin-glass-like behavior of Ge:Mn,” *Phys. Rev. B* **74**, 045330
- Jain, A., M. Jamet, A. Barski, T. Devillers, C. Porret, P. Bayle-Guillemaud, S. Gambarelli, V. Maurel, and G. Desfonds, 2010, “Investigation of magnetic anisotropy of (ge,mn) nanocolumns,” *Appl. Phys. Lett.* **97**, 202502
- Jain, A., M. Jamet, A. Barski, T. Devillers, I.-S. Yu, C. Porret, P. Bayle-Guillemaud, V. Favre-Nicolin, S. Gambarelli, V. Maurel, G. Desfonds, J.-F. Jacquot, and S. Tardif, 2011, “Structure and magnetism of ge₃mn₅ clusters,” *J. Appl. Phys.* **109**, 013911
- Jamet, M., 2010 unpublished
- Jamet, M., A. Barski, T. Devillers, V. Poydenot, R. Dujardin, P. Bayle-Guillemaud, J. Rothman, E. Bellet-Amalric, A. Marty, J. Cibert, R. Mattana, and S. Tatarenko, 2006, “High-Curie-temperature ferromagnetism in self-organized Ge_{1-x}Mn_x nanocolumns,” *Nature Mater.* **5**, 653
- Jamet, M., W. Wernsdorfer, C. Thirion, D. Mailly, V. Dupuis, P. Mélinon, and A. Pérez, 2001, “Magnetic anisotropy of a single cobalt nanocluster,” *Phys. Rev. Lett.* **86**, 4676
- Jones, R. A. L., 2002, in *Soft Condensed Matter* (Oxford University Press, Oxford)
- Jungwirth, T., J. Wunderlich, V. Novák, K. Olejník, B. L. Gallagher, R. P. Campion, K. W. Edmonds, A. W. Rushforth, A. J. Ferguson, and P. Němec, 2014, “Spin-dependent phenomena and device concepts explored in (Ga,Mn)As,” *Rev. Mod. Phys.* **86**, 855–896
- Kacman, P., 2001, “Spin interactions in diluted magnetic semiconductors and magnetic semiconductor structures,” *Semicond. Sci. Technol.* **16**, R25
- Kane, M. H., S. Gupta, W. E. Fenwick, N. Li, E.-H. Park, M. Strassburg, and I. T. Ferguson, 2007, “Comparative study of Mn and Fe incorporation into GaN by metalorganic chemical vapor deposition,” *phys. ptat. sol. (a)* **204**, 61
- Kang, J. S., G. Kim, S. C. Wi, S. S. Lee, S. Choi, Sunglae Cho, S. W. Han, K. H. Kim, H. J. Song, H. J. Shin, A. Sekiyama, S. Kasai, S. Suga, and B. I. Min, 2005, “Spatial chemical inhomogeneity and local electronic structure of Mn-doped Ge ferromagnetic semiconductors,” *Phys. Rev. Lett.* **94**, 147202
- Karczewski, G., M. Sawicki, V. Ivanov, C. Rueter, G. Grabecki, F. Matsukura, L. W. Molenkamp, and T. Dietl, 2003, “Ferromagnetism in (Zn,Cr)Se layers grown by molecular beam epitaxy,” *J. Supercond. Nov. Magn.* **16**, 55
- Kashiwagi, T., S. Sonoda, H. Yashiro, Y. Akasaka, and M. Hagiwara, 2007, “ESR in a GaN thin film doped with Fe,” *J. Mag. Mag. Mat.* **310**, 2152
- Katayama-Yoshida, H., K. Sato, T. Fukushima, M. Toyoda, H. Kizaki, V. A. Dinh, and P. H. Dederichs, 2007, “Theory of ferromagnetic semiconductors,” *phys. stat. sol. (a)* **204**, 15
- Kazakova, O., J. S. Kulkarni, J. D. Holmes, and S. O. Demokritov, 2005, “Room-temperature ferromagnetism in Ge_{1-x}Mn_x nanowires,” *Phys. Rev. B* **72**, 094415
- Keavney, D. J., S. H. Cheung, S. T. King, M. Weinert, and L. Li, 2005, “Role of defect sites and Ga polarization in the magnetism of Mn-Doped GaN,” *Phys. Rev. Lett.* **95**, 257201
- Kenmochi, K., V. A. Dinh, K. Sato, A. Yanase, and H. Katayama-Yoshida, 2004a, “Materials design of transparent and half-metallic ferromagnets of MgO, SrO and BaO without magnetic elements,” *J. Phys. Soc. Jap.* **73**, 2952
- Kenmochi, K., K. Sato, A. Yanase, and H. Katayama-Yoshida, 2005, “Materials design of ferromagnetic diamond,” *Jpn. J. Appl. Phys.* **44**, L51
- Kenmochi, K., M. Seike, K. Sato, A. Yanase, and H. Katayama-Yoshida, 2004b, “New class of diluted ferromagnetic semiconductors based on CaO without transition metal elements,” *Jpn. J. Appl. Phys.* **43**, L934
- Khodaparast, G. A., Y. H. Matsuda, D. Saha, G. D. Sanders,

- C. J. Stanton, H. Saito, S. Takeyama, T. R. Merritt, C. Feeser, B. W. Wessels, X. Liu, and J. Furdyna, 2013, "Cyclotron resonance in ferromagnetic InMnAs and InMnSb," *Phys. Rev. B* **88**, 235204
- Kim, G., S. C. Wi, S. S. Lee, J.-S. Kang, S. Y. Choi, S. Cho, S. W. Han, K. H. Kim, H. J. Song, and H. J. Shin, 2005, "Scanning photoelectron microscopy study of $\text{Ge}_{1-x}\text{T}_x$ ($T = \text{Cr}, \text{Fe}$) diluted ferromagnetic semiconductor single crystals," *J. Appl. Phys.* **97**, 10A307
- Kim, K. H., K. J. Lee, D. J. Kim, H. J. Kim, Y. E. Ihm, D. Djayaprawira, M. Takahashi, C. S. Kim, C. G. Kim, and S. H. Yoo, 2003, "Magnetotransport of p -type GaMnN assisted by highly conductive precipitates," *Appl. Phys. Lett.* **82**, 1775
- Kioseoglou, G., A. T. Hanbicki, C. H. Li, S. C. Erwin, R. Goswami, and B. T. Jonker, 2004, "Epitaxial growth of the diluted magnetic semiconductors $\text{Cr}_y\text{Ge}_{1-y}$ and $\text{Cr}_y\text{Mn}_x\text{Ge}_{1-x-y}$," *Appl. Phys. Lett.* **84**, 1725
- Kizaki, H., and H. Katayama-Yoshida, 2013, "Spinodal nano decomposition in perovskite three-way catalysts: First-principles calculations and Monte Carlo simulations," *Chem. Phys. Lett.* **579**, 85
- Kizaki, H., K. Kusakabe, S. Nogami, and H. Katayama-Yoshida, 2008, "Generation of nano-catalyst particles by spinodal nano-decomposition in perovskite," *Appl. Phys. Exp.* **1**, 104001
- Kobayashi, H., Y. Nishio, K. Kanazawa, S. Kuroda, M. Mitome, and Y. Bando, 2012, "Structural analysis of the phase separation in magnetic semiconductor (Zn,Cr)Te," *Physica B* **407**, 2947
- Kobayashi, H., K. Yamawaki, Y. Nishio, K. Kanazawa, S. Kuroda, M. Mitome, and Y. Bando, 2013, "Structural analysis of Cr aggregation in ferromagnetic semiconductor (Zn,Cr)Te," *Physics of Semiconductors, AIP Conf. Proc.* **1566**, 341
- Kobayashi, M., Y. Ishida, J. I. Hwang, G. S. Song, C. S. Fujimori, A. Yang, Lee. L., H.-J. Lin, D. J. Huang, C. T. Chen, Y. Takeda, K. Terai, S.-I. Fujimori, T. Okane, Y. Saitoh, H. Yamagami, K. Kobayashi, A. Tanaka, H. Saito, and K. Ando, 2008, "Local electronic structure of Cr in the II-VI diluted ferromagnetic semiconductor $\text{Zn}_{1-x}\text{Cr}_x\text{Te}$," *New J. Phys.* **10**, 055011
- Kocan, M., J. Malindretos, M. Roeber, J. Zenneck, T. Niermann, D. Mai, M. Bertelli, M. Seibt, and A. Rizzi, 2006, "Mn incorporation in GaN thin layers grown by molecular-beam epitaxy," *Semicond. Sci. Technol.* **21**, 1348
- Kodzuka, M., 2012, *Application of atom probe to microstructure analysis of thin film materials* (PhD Thesis, University of Tsukuba)
- Kohn, W., and L. Sham, 1965, "Self-consistent equations including exchange and correlation effects," *Phys. Rev.* **140**, A1133
- Kondo, T., S. Kuwabara, H. Owa, and H. Munekata, 2002, "Molecular beam epitaxy of (Ga,Mn)N," *J. Cryst. Growth* **237**, 1353
- Kossacki, P., W. Pacuski, W. Maślana, J. A. Gaj, M. Bertolini, D. Ferrand, S. Tatarenko, and J. Cibert, 2004, "Spin engineering of carrier-induced magnetic ordering in (Cd,Mn)Te quantum wells," *Phys. E* **21**, 943
- Kovács, A., T. Kasama, J. Sadowski, T. Dietl, and R. E. Dunin-Borkowski, 2011, "Aberration-corrected electron microscopy of MnAs and As nanocrystals and voids in annealed (Ga,Mn)As," *J. Phys. Conference Series* **326**, 012018
- Kowalik, I. A., A. Persson, M. Á. Niño, A. Navarro-Quezada, B. Faina, A. Bonanni, T. Dietl, and D. Arvanitis, 2012, "Element-specific characterization of heterogeneous magnetism in (Ga,Fe)N films," *Phys. Rev. B* **85**, 184411
- Krug von Nidda, H.-A., T. Kurz, A. Loidl, Th. Hartmann, P. J. Klar, W. Heimbrot, M. Lampalzer, K. Volz, and W. Stolz, 2006, "Tuning the magnetic properties of GaAs:Mn/MnAs hybrids via the MnAs cluster shape," *J. Phys. Cond. Matter* **18**, 6071
- Kubota, M., T. Onuma, Y. Ishihara, A. Usui, A. Uedono, and S. F. Chichibu, 2009, "Thermal stability of semi-insulating property of Fe-doped GaN bulk films studied by photoluminescence and monoenergetic positron annihilation techniques," *J. Appl. Phys.* **105**, 083542
- Kunert, G., S. Dobkowska, Tian Li, H. Reuther, C. Kruse, S. Figge, R. Jakiela, A. Bonanni, J. Grenzer, W. Stefanowicz, J. von Borany, M. Sawicki, T. Dietl, and D. Hommel, 2012, " $\text{Ga}_{1-x}\text{Mn}_x\text{N}$ epitaxial films with high magnetization," *Appl. Phys. Lett.* **101**, 022413
- Kuroda, S., N. Nishizawa, T. Kumekawa, S. Marcet, and K. Takita, 2005, "Growth and magnetic properties of novel ferromagnetic semiconductor (Zn,Cr)Te," *Sci. Technol. Adv. Mater.* **6**, 558
- Kuroda, S., N. Nishizawa, K. Takita, M. Mitome, Y. Bando, K. Osuch, and T. Dietl, 2007, "Origin and control of high-temperature ferromagnetism in semiconductors," *Nature Mat.* **6**, 440
- Kuwabara, S., K. Ishii, S. Haneda, T. Kondo, and H. Munekata, 2001a, "Preparation of wurtzite GaN-based magnetic alloy semiconductors by molecular beam epitaxy," *Physica E* **10**, 233
- Kuwabara, S., T. Kondo, T. Chikyow, P. Ahmet, and H. Munekata, 2001b, "Molecular beam epitaxy of wurtzite GaN-based magnetic alloy semiconductors," *Jpn. J. Appl. Phys.* **40**, L724
- Kuzemsky, A. L., 2013, "Unconventional and exotic magnetism in carbon-based structures and related materials," *Int. J. Mod. Phys. B* **27**, 1330007
- Kwiatkowski, A., D. Wasik, M. Kamińska, R. Bożek, J. Szczytko, A. Twardowski, J. Borysiuk, J. Sadowski, and J. Gosk, 2007, "Structure and magnetism of MnAs nanocrystals embedded in GaAs as a function of *post-growth* annealing temperature," *J. Appl. Phys.* **101**, 113912
- Lampalzer, M., S. Nau, C. Pietzonka, W. Treutmann, K. Volz, and W. Stolz, 2004, "Te-co-doping experiments in ferromagnetic Mn(Ga)As/GaAs cluster hybrid layers by MOVPE," *J. Cryst. Growth* **272**, 772
- Landau, D. P., and K. Binder, 2000, in *A Guide to Monte Carlo Simulations in Statistical Physics* (Cambridge University Press, Cambridge)
- Langer, J. M., and H. Heinrich, 1985, "Deep-level impurities: A possible guide to prediction of band-edge discontinuities in semiconductor heterojunctions," *Phys. Rev. Lett.* **55**, 1414
- Lari, L., S. Lea, C. Feeser, B. W. Wessels, and V. K. Lazarov, 2012, "Ferromagnetic InMnSb multi-phase films study by aberration-corrected (scanning) transmission electron microscopy," *J. Appl. Phys.* **111**, 07C311
- Larson, P., and S. Satpathy, 2007, "Effect of vacancies on ferromagnetism in GaN:Mn dilute magnetic semiconductors from first-principles," *Phys. Rev. B* **76**, 245205
- Lawniczak-Jablonska, K., J. Libera, A. Wolska, M. T. Klepka, P. Dłuzewski, J. Sadowski, D. Wasik, A. Twardowski, A. Kwiatkowski, and K. Sato, 2011, "The source of room

- temperature ferromagnetism in granular GaMnAs layers with zinc blende clusters,” *phys. status solidi (RRL)* **5**, 62
- Lazarov, V. K., S. H. Cheung, Y. Cui, L. Li, and M. Gajdardziska-Josifovska, 2008, “Role of Mn and H in formation of cubic and hexagonal GaMnN,” *Appl. Phys. Lett.* **92**, 101914
- Le, T.-G., D. N. H. Nam, M.-T. Dau, T. K. P. Luong, N. V. Khiem, V. Le Thanh, L. Michez, and J. Derrien, 2010, “The effects of Mn concentration on structural and magnetic properties of $\text{Ge}_{1-x}\text{Mn}_x$ diluted magnetic semiconductors,” *J. Phys.: Conf. Series* **282**, 012012
- Lechner, R. T., V. Holý, S. Ahlers, D. Bougeard, J. Stangl, A. Trampert, A. Navarro-Quezada, and G. Bauer, 2009, “Self-assembled Mn_3Ge_3 nanomagnets close to the surface and deep inside a $\text{Ge}_{1-x}\text{Mn}_x$ epilayer,” *Appl. Phys. Lett.* **95**, 023102
- Lethanh, V., 2006 private communication
- Li, A. P., C. Zeng, K. van Benthem, M. F. Chisholm, J. Shen, S. V. S. Nageswara Rao, S. K. Dixit, L. C. Feldman, A. G. Petukhov, M. Foygel, and H. H. Weitering, 2007, “Dopant segregation and giant magnetoresistance in manganese-doped germanium,” *Phys. Rev. B* **75**, 201201(R)
- Li, Li, Y. Guo, X. Y. Cui, Rongkun Zheng, K. Ohtani, C. Kong, A. V. Ceguerra, M. P. Moody, J. D. Ye, H. H. Tan, C. Jagadish, Hui Liu, C. Stampfl, H. Ohno, S. P. Ringer, and F. Matsukura, 2012, “Magnetism of Co-doped ZnO epitaxially grown on a ZnO substrate,” *Phys. Rev. B* **85**, 174430
- Liu, C., F. Yun, and H. Morkoç, 2005, “Ferromagnetism of ZnO and GaN: A review,” *J. Mater. Sci.: Mater. Electron.* **16**, 555
- Lo, Ikai, J. K. Tsai, M. H. Gau, Y. L. Chen, Z. J. Chang, W. T. Wang, J. C. Chiang, K. R. Wang, Chun-Nan Chen, T. Aggerstam, and S. Lourduoss, 2006, “Study of two-subband population in Fe-doped $\text{Al}_x\text{Ga}_{1-x}\text{N}/\text{GaN}$ heterostructures by persistent photoconductivity effect,” *Phys. Rev. B* **74**, 245325
- Loss, D., and D. P. DiVincenzo, 1998, “Quantum computation with quantum dots,” *Phys. Rev. A* **57**, 120
- Lu, E., D. C. Ingram, A. R. Smith, J. W. Knepper, and F. Y. Yang, 2006, “Reconstruction control of magnetic properties during epitaxial growth of ferromagnetic $\text{Mn}_{3-\delta}\text{Ga}$ on wurtzite GaN(0001),” *Phys. Rev. Lett.* **97**, 146101
- Mac, W., A. Twardowski, and M. Demianiuk, 1996, “s,p-d exchange interaction in Cr-based diluted magnetic semiconductors,” *Phys. Rev. B* **54**, 5528
- Maccherozzi, F., M. Sperl, G. Panaccione, J. Minar, S. Polesya, H. Ebert, U. Würstbauer, M. Hochstrasser, G. Rossi, G. Woltersdorf, W. Wegscheider, and C. H. Back, 2008, “Evidence for a magnetic proximity effect up to room temperature at Fe/(Ga,Mn)As interfaces,” *Phys. Rev. Lett.* **101**, 267201
- Mack, S., R. C. Myers, J. T. Heron, A. C. Gossard, and D. D. Awschalom, 2008, “Stoichiometric growth of high Curie temperature heavily alloyed GaMnAs,” *Appl. Phys. Lett.* **92**, 192502
- Mahadevan, Priya, J. M. Osorio-Guillén, and A. Zunger, 2005, “Origin of transition metal clustering tendencies in GaAs based dilute magnetic semiconductors,” *Appl. Phys. Lett.* **86**, 172504
- Makarova, T., 2010, “Nanomagnetism in otherwise nonmagnetic materials,” in *Handbook in Nanophysics: Principles and Methods* (ERC Press) p. 25.1
- Makarova, T. L., B. Sundqvist, R. Höhne, P. Esquinazi, Y. Kopelevich, P. Scharff, V. Davydov, L. S. Kashevarova, and A. V. Rakhmanina, 2006, “Retraction: Magnetic carbon,” *Nature* **440**, 707
- Malguth, E., A. Hoffmann, W. Gehlhoff, O. Gelhausen, M. R. Phillips, and X. Xu, 2006a, “Structural and electronic properties of Fe^{3+} and Fe^{2+} centers in GaN from optical and EPR experiments,” *Phys. Rev. B* **74**, 165202
- Malguth, E., A. Hoffmann, and M. R. Phillips, 2008, “Fe in III-V and II-VI semiconductors,” *phys. stat. sol. (b)* **245**, 455
- Malguth, E., A. Hoffmann, and X. Xu, 2006b, “Internal $^5e \rightarrow ^5t_2$ transition of Fe^{2+} in GaN,” *Phys. Rev. B* **74**, 165201
- Martin, R. M., 2004, in *Electronic structure* (Cambridge University Press)
- Martinez-Criado, G., A. Somogyi, S. Ramos, J. Campo, R. Tucoulou, M. Salome, J. Susini, M. Hermann, M. Eickhoff, and M. Stutzmann, 2005, “Mn-rich clusters in GaN: Hexagonal or cubic symmetry?,” *Appl. Phys. Lett.* **86**, 131927
- Massalski, T. B., 1990, “Binary alloy phase diagrams,” American Society for Metals, Metals Pair, OH, 1990 **2**
- Matsubayashi, K., M. Maki, T. Tsuzuki, T. Nishioka, and N. K. Sato, 2002, “Parasitic ferromagnetism in a hexaboride?,” *Nature* **420**, 143
- Matsukura, F., H. Ohno, and T. Dietl, 2002, “III-V ferromagnetic semiconductors,” in *Handbook of Magnetic Materials*, Vol. 14, edited by K. H. J. Buschow (Elsevier) p. 1
- Mavropoulos, P., M. Ležić, and S. Blügel, 2009, “Ferromagnetism in nitrogen-doped MgO: Density-functional calculations,” *Phys. Rev. B* **80**, 184403
- van der Meulen, M. I., N. Petkov, M. A. Morris, O. Kazakova, X. Han, K. L. Wang, A. P. Jacob, and J. D. Holmes, 2009, “Single crystalline $\text{Ge}_{1-x}\text{Mn}_x$ nanowires as building blocks for nanoelectronic,” *Nano Lett.* **9**, 50
- Miao, Guo-xing, Joonyeon Chang, Badih A. Assaf, D. Heiman, and J. S. Moodera, 2014 04, “Spin regulation in composite spin-filter barrier devices,” *Nat. Commun.* **5**, 3682
- Miao, M. S., A. Herwadkar, and W. R. L. Lambrecht, 2005, “Electronic structure and magnetic properties of Mn_3GaN precipitates in $\text{Ga}_{1-x}\text{Mn}_x\text{N}$,” *Phys. Rev. B* **72**, 033204
- Michel, C., M. T. Elm, B. Goldlücke, S. D. Baranovskii, P. Thomas, W. Heimbrod, and P. J. Klar, 2008, “Tailoring the magnetoresistance of MnAs/GaAs:Mn granular hybrid nanostructures,” *Appl. Phys. Lett.* **92**, 223119
- Michel, C., C.H. Thien, S. Ye, P.J. Klar, W. Heimbrod, S.D. Baranovskii, P. Thomas, M. Lampalzer, K. Volz, W. Stolz, and B. Goldlücke, 2005, “Spin-dependent localization effects in GaAs:Mn/MnAs granular paramagnetic-ferromagnetic hybrids at low temperatures,” *Superlatt. Microstruct.* **37**, 321
- Mirbt, S., B. Sanyal, and P. Mohn, 2002, “Magnetic properties of 3d impurities substituted in GaAs,” *J. Phys.: Condens. Matter* **14**, 3295
- Mizokawa, T., and A. Fujimori, 1997, “p-d exchange interaction for 3d transition-metal impurities in II-VI semiconductors,” *Phys. Rev. B* **56**, 6669
- Monette, G., C. Lacroix, S. Lambert-Milot, V. Boucher, D. Ménard, and S. Francoeur, 2010, “Giant magneto-optical Faraday effect in GaP epilayers containing MnP magnetic nanoclusters,” *journal J. Appl. Phys.* **107**, 09A949
- Moreno, M., B. Jenichen, V. Kaganer, W. Braun, A. Trampert, L. Däweritz, and K.H. Ploog, 2003, “MnAs nanoclus-

- ters embedded in GaAs studied by x-ray diffuse and coherent scattering,” *Phys. Rev. B* **67**, 235206
- Moreno, M., V. M. Kaganer, B. Jenichen, A. Trampert, L. Däweritz, and K. H. Ploog, 2005, “Micromechanics of MnAs nanocrystals embedded in GaAs,” *Phys. Rev. B* **72**, 115206
- Moreno, M., A. Trampert, B. Jenichen, L. Däweritz, and K. H. Ploog, 2002, “Correlation of structure and magnetism in GaAs with embedded Mn(Ga)As magnetic nanoclusters,” *J. Appl. Phys.* **92**, 4672
- Morresi, L., N. Pinto, M. Ficcadenti, R. Murri, F. D’Orazio, and F. Lucari, 2006, “Magnetic and transport polaron percolation in diluted GeMn films,” *Mater. Sci. Eng. B* **126**, 197
- Mørup, S., M. F. Hansen, and C. Frandsen, 2010, “Magnetic interactions between nanoparticles,” *Beilstein J. Nanotechnol.* **1**, 182
- Mouton, L., R. Lardé, E. Talbot, E. Cadel, C. Genevois, D. Blavette, V. Baltz, E. Prestat, P. Bayle Guillemaud, A. Barski, and M. Jamet, 2012, “Composition and morphology of self-organized Mn-rich nanocolumns embedded in Ge: Correlation with the magnetic properties,” *J. Appl. Phys.* **112**, 113918
- Munekata, H., H. Ohno, S. von Molnar, A. Segmüller, L. L. Chang, and L. Esaki, 1989, “Diluted magnetic III–V semiconductors,” *Phys. Rev. Lett.* **63**, 1849
- Muret, P., J. Pernot, M. Azize, and Z. Bourigoua, 2007, “Photoinduced current transient spectroscopy of deep levels and transport mechanisms in iron-doped GaN thin films grown by low pressure-metalorganic vapor phase epitaxy,” *J. Appl. Phys.* **102**, 053701
- Navarro-Quezada, A., T. Devillers, Tian Li, and A. Bonanni, 2012, “Planar arrays of magnetic nanocrystals embedded in GaN,” *Appl. Phys. Lett.* **101**, 081911
- Navarro-Quezada, A., N. Gonzalez Szwacki, W. Stefanowicz, Tian Li, A. Grois, T. Devillers, M. Rovezzi, R. Jakiela, B. Faina, J. A. Majewski, M. Sawicki, T. Dietl, and A. Bonanni, 2011, “Fe-Mg interplay and the effect of deposition mode in (Ga,Fe)N doped with Mg,” *Phys. Rev. B* **84**, 155321
- Navarro-Quezada, A., W. Stefanowicz, Tian Li, B. Faina, M. Rovezzi, R. T. Lechner, T. Devillers, F. d’Acapito, G. Bauer, M. Sawicki, T. Dietl, and A. Bonanni, 2010, “Embedded magnetic phases in (Ga,Fe)N: Key role of growth temperature,” *Phys. Rev. B* **81**, 205206
- Nealon, G. L., B. Donnio, R. Greget, J.-P. Kappler, E. Terazzi, and J.-L. Gallani, 2012, “Magnetism in gold nanoparticles,” *Nanoscale* **4**, 5244
- Ney, A., T. Kammermeier, V. Ney, K. Ollefs, and S. Ye, 2008, “Limitations of measuring small magnetic signals of samples deposited on a diamagnetic substrate,” *J. Magn. Magn. Mater.* **320**, 3341
- Niida, H., T. Hori, H. Onodera, Y. Yamaguchi, and Y. Nakagawa, 1996, “Magnetization and coercivity of $\text{Mn}_{3-\delta}\text{Ga}$ alloys with a D_{022} -type structure,” *J. Appl. Phys.* **79**, 5946
- Nishio, Y., K. Ishikawa, S. Kuroda, M. Mitome, and Y. Bando, 2009, “Formation of Cr-rich nano-clusters and columns in (Zn,Cr)Te grown by MBE,” in *MRS Proceedings*, Vol. 1183, pp. FF01–11
- Novick-Cohen, A., 2008, “The CahnHilliard equation,” in *Evolutionary Equations*, Handbook of Differential Equations, Vol. 4, edited by C.M. Dafermos and E. Feireisl, Chap. 4 (Elsevier, Amsterdam) p. 201
- Ofuchi, H., K. Ishikawa, K. Zhang, S. Kuroda, M. Mitome, and Y. Bando, 2009, “Fluorescence XAFS analysis of local structures in iodine-doped $\text{Zn}_{1-x}\text{Cr}_x\text{Te}$,” *J. Phys.: Conf. Ser.* **190**, 012103
- Ofuchi, H., M. Oshima, M. Tabuchi, Y. Takeda, H. Akinaga, Š. Németh, J. De Boeck, and G. Borghs, 2001, “Fluorescence x-ray absorption fine structure study on local structures around Fe atoms heavily doped in GaN by low-temperature molecular-beam epitaxy,” *Appl. Phys. Lett.* **78**, 2470
- Ohba, T., K. Kifune, and Y. Komura, 1987, “Structure determination of $\zeta_2\text{-Mn}_5\text{Ge}_2$ using a mixed crystal,” *Acta Cryst.* **B43**, 489
- Ohba, T., N. Watanabe, and Y. Komura, 1984, “Temperature dependence of the lattice constants and the structure of $\text{Mn}_{11}\text{Ge}_8$ at 295 and 116 k,” *Acta Cryst.* **B40**, 351
- Ohno, H., A. Shen, F. Matsukura, A. Oiwa, A. Endo, S. Katsumoto, and Y. Iye, 1996, “(Ga,Mn)As: A new diluted magnetic semiconductor based on GaAs,” *Appl. Phys. Lett.* **69**, 363
- Ohoyama, T., 1961, “X-ray and magnetic studies of the manganese-germanium system,” *J. Phys. Soc. Jpn.* **16**, 1995
- Ohoyama, T., K. Yasukochi, and K. Kanematsu, 1961, “A new phase of an intermetallic compound $\text{Mn}_{3.4}\text{Ge}$ and its magnetism,” *J. Phys. Soc. Jpn.* **16**, 352
- Ohta, S., T. Kanomata, T. Kaneko, and H. Yoshida, 1993, “Pressure effect on the Curie temperature and thermal expansion of CrTe,” *J. Phys.: Condens. Matter* **5**, 2759
- Ohya, S., K. Ohno, and M. Tanaka, 2007, “Magneto-optical and magnetotransport properties of heavily Mn-doped GaMnAs,” *Appl. Phys. Lett.* **90**, 112503
- Oshitani, M., K. Sato, and H. Katayama-Yoshida, 2011, *Appl. Phys. Exp.* **4**, 022302
- Ottaviano, L., M. Passacantando, A. Verna, F. D’Amico, and R. Gunnella, 2007, “Mn $L_{2,3}$ x-ray absorption spectra of a diluted Mn–Ge alloy,” *Appl. Phys. Lett.* **90**, 242105
- Ottaviano, L., M. Passacantando, A. Verna, R. Gunnella, E. Principi, A. D. Cicco, G. Impellizzeri, and F. Priolo, 2006, “Direct structural evidences of Mn dilution in Ge,” *J. Appl. Phys.* **100**, 063528
- Ozaki, N., N. Nishizawa, S. Marcet, S. Kuroda, O. Eryu, and K. Takita, 2006, “Significant enhancement of ferromagnetism in $\text{Zn}_{1-x}\text{Cr}_x\text{Te}$ doped with iodine as an n -type dopant,” *Phys. Rev. Lett.* **97**, 037201
- Ozaki, N., J. Okabayashi, T. Kumekawa, N. Nishizawa, S. Marcet, S. Kuroda, and K. Takita, 2005, “Suppression of ferromagnetism due to hole doping in $\text{Zn}_{1-x}\text{Cr}_x\text{Te}$ grown by molecular-beam epitaxy,” *Appl. Phys. Lett.* **87**, 192116
- Pacuski, W., D. Ferrand, J. Cibert, C. Deparis, J. A. Gaj, P. Kossacki, and C. Morhain, 2006, “Effect of the $s,p-d$ exchange interaction on the excitons in $\text{Zn}_{1-x}\text{Co}_x\text{O}$ epilayers,” *Phys. Rev. B* **73**, 035214
- Pacuski, W., D. Ferrand, J. Cibert, J. A. Gaj, A. Golnik, P. Kossacki, S. Marcet, E. Sarigiannidou, and H. Mariette, 2007, “Excitonic giant Zeeman effect in GaN:Mn^{3+} ,” *Phys. Rev. B* **76**, 165304
- Pacuski, W., P. Kossacki, D. Ferrand, A. Golnik, J. Cibert, M. Wegscheider, A. Navarro-Quezada, A. Bonanni, M. Kiecana, M. Sawicki, and T. Dietl, 2008, “Observation of strong-coupling effects in a diluted magnetic semiconductor $\text{Ga}_{1-x}\text{Fe}_x\text{N}$,” *Phys. Rev. Lett.* **100**, 037204
- Pacuski, W., J. Suffczyński, P. Osewski, P. Kossacki, A. Golnik, J. A. Gaj, C. Deparis, C. Morhain, E. Chikoidze, Y. Dumont, D. Ferrand, J. Cibert, and T. Dietl, 2011, “In-

- fluence of $s,p-d$ and $s-p$ exchange couplings on exciton splitting in $\text{Zn}_{1-x}\text{Mn}_x\text{O}$,” *Phys. Rev. B* **84**, 035214
- Padova, P. D., J.-P. Ayoub, I. Berbezier, J.-M. Mariot, A. Taleb-Ibrahimi, M. C. Richter, O. Heckmann, A. M. Testa, D. Fiorani, B. Olivieri, S. Picozzi, and K. Hricovini, 2007, “ $\text{Mn}_x\text{Ge}_{1-x}$ thin layers studied by TEM, X-ray absorption spectroscopy and SQUID magnetometry,” *Surf. Sci.* **601**, 2628
- Padova, P. D., J.-P. Ayoub, I. Berbezier, P. Perfetti, C. Quaresima, A. M. Testa, D. Fiorani, B. Olivieri, J.-M. Mariot, A. Taleb-Ibrahimi, M. C. Richter, O. Heckmann, and K. Hricovini, 2008, “ $\text{Mn}_{0.06}\text{Ge}_{0.94}$ diluted magnetic semiconductor epitaxially grown on Ge(001): Influence of Mn_5Ge_3 nanoscopic clusters on the electronic and magnetic properties,” *Phys. Rev. B* **77**, 045203
- Pajczkowska, A., 1978, “Physicochemical properties and crystal growth of $A^{II}B^{VI} - \text{MnB}^{VI}$ systems,” *Prog. Cryst. Growth Charact.* **1**, 289
- Panov, A. V., 2012, “Dipolar ordering of random two-dimensional spin ensemble,” *Appl. Phys. Lett.* **100**, 052406
- Park, J., J. Cho, K. Nishimura, and M. Inoue, 2002a, “Magneto-optical spatial light modulator for volumetric digital recording system,” *Jpn. J. Appl. Phys.* **41**, 1813
- Park, Y. D., A. T. Hanbicki, S. C. Erwin, C. S. Hellberg, J. M. Sullivan, J. E. Mattson, T. F. Ambrose, A. Wilson, G. Spanos, and B. T. Jonker, 2002b, “A group-IV ferromagnetic semiconductor: $\text{Mn}_x\text{Ge}_{1-x}$,” *Science* **295**, 651
- Park, Y. D., A. Wilson, A. T. Hanbicki, J. E. Mattson, T. Ambrose, G. Spanos, and B. T. Jonker, 2001, “Magnetoresistance of Mn:Ge ferromagnetic nanoclusters in a diluted magnetic semiconductor matrix,” *Appl. Phys. Lett.* **78**, 2739
- Passacantando, M., L. Ottaviano, F. D’Orazio, F. Lucari, M. De Biase, G. Impellizzeri, and F. Priolo, 2006, “Growth of ferromagnetic nanoparticles in a diluted magnetic semiconductor obtained by mn+ implantation on ge single crystals,” *Phys. Rev. B* **73**, 195207
- Pearnton, S. J., C. R. Abernathy, M. E. Overberg, G. T. Thaler, D. P. Norton, N. Theodoropoulou, A. F. Hebard, Y. D. Park, F. Ren, J. Kim, and L. A. Boatner, 2003, “Wide band gap ferromagnetic semiconductors and oxides,” *J. Appl. Phys.* **93**, 1
- Pearnton, S. J., M. E. Overberg, G. Thaler, C. R. Abernathy, N. Theodoropoulou, A. F. Hebard, S. N. G. Chu, R. G. Wilson, J. M. Zavada, A. Y. Polyakov, A. V. Osinsky, P. E. Norris, P. P. Chow, A. M. Wowchack, J. M. Van Hove, and Y. D. Park, 2002, “Characterization of high dose Mn, Fe and Ni implantation into p-GaN,” *J. Vac. Sci. Technol. A* **20**, 721
- Perdew, J. P., and Y. Wang, 1986, “Accurate and simple density functional for the electronic exchange energy: Generalized gradient approximation,” *Phys. Rev.* **33**, 8800
- Pinto, N., L. Morresi, M. Ficcadenti, R. Murri, F. D’Orazio, F. Lucari, L. Boarino, and G. Amato, 2005, “Magnetic and electronic transport percolation in epitaxial $\text{Ge}_{1-x}\text{Mn}_x$ films,” *Phys. Rev. B* **72**, 165203
- Pioro-Ladrière, M., T. Obata, Y. Tokura, Y.-S. Shin, T. Kubo, K. Yoshida, T. Taniyama, and S. Tarucha, 2008, “Electrically driven single-electron spin resonance in a slanting Zeeman field,” *Nat. Phys.* **4**, 776
- Pop, I., M. Andreucut, I. Burda, R. Munteanu, and K. Criveanu, 1994, “Itinerant ferromagnetism in Mn_4N ,” *Mater. Chem. Phys.* **37**, 52
- Prestat, E., P. Dalmas de Réotier, A. Yaouanc, A. Suter, T. Prokscha, E. Morenzoni, A. Marty, A. Barski, P. Bayle Guillemaud, and M. Jamet, 2014, “Evidence for a core-shell nanostructure in Ge:Mn,” to be submitted
- Przeździecka, E., E. Kamińska, M. Kiecana, M. Sawicki, L. Kłopotowski, W. Pacuski, and J. Kossut, 2006, “Magneto-optical properties of the diluted magnetic semiconductor p -type ZnMnO ,” *Solid State Commun.* **139**, 541
- Przybylińska, H., A. Bonanni, A. Wolos, M. Kiecana, M. Sawicki, T. Dietl, H. Malissa, C. Simbrunner, M. Wegscheider, H. Sitter, K. Rumpf, P. Granitzer, H. Krenn, and W. Jantsch, 2006, “Magnetic properties of a new spintronic material-GaN:Fe,” *Mater. Sci. Engineer. B* **126**, 222
- Qi, Y., G.F. Sun, M. Weinert, and L. Li, 2010, “Electronic structures of Mn-induced phases on GaN(0001),” *Phys. Rev. B* **80**, 235323
- Raebiger, H., H. Nakayama, and T. Fujita, 2014, “Control of defect binding and magnetic interaction energies in dilute magnetic semiconductors by charge state manipulation,” *J. Appl. Phys.* **115**, 012008, doi:\bibinfo{doi}{10.1063/1.4838016}
- Ralph, D. C., 2011, “The electromotive force of MnAs nanoparticles,” *Nature* **474**, E6
- Reed, M. J., F. E. Arkun, E. A. Berkman, N. A. Elmasry, J. Zavada, M. O. Luen, M. L. Reed, and S. M. Bedair, 2005, “Effect of doping on the magnetic properties of GaMnN: Fermi level engineering,” *Appl. Phys. Lett.* **86**, 102504
- Reiss, G., and D. Meyners, 2006, “Reliability of field programmable magnetic logic gate arrays,” *Appl. Phys. Lett.* **88**, 043505
- Rench, D. W., P. Schiffer, and N. Samarth, 2011, “Structural and magnetic characteristics of MnAs nanoclusters embedded in Be-doped GaAs,” *Phys. Rev. B* **84**, 094434
- Roever, M., J. Malindretos, A. Bedoya-Pinto, A. Rizzi, Ch. Rauch, and F. Tuomisto, 2011, “Tracking defect-induced ferromagnetism in GaN:Gd,” *Phys. Rev. B* **84**, 081201
- Rousset, J.-G., J. Papierska, W. Pacuski, A. Golnik, M. Nawrocki, W. Stefanowicz, S. Stefanowicz, M. Sawicki, R. Jakiela, T. Dietl, A. Navarro-Quezada, B. Faina, T. Li, A. Bonanni, and J. Suffczyński, 2013, “Relation between exciton splittings, magnetic circular dichroism, and magnetization in wurtzite $\text{Ga}_{1-x}\text{Fe}_x\text{N}$,” *Phys. Rev. B* **88**, 115208
- Rovezzi, M., F. D’Acapito, A. Navarro-Quezada, B. Faina, Tian Li, A. Bonanni, F. Filippone, A. A. Bonapasta, and T. Dietl, 2009, “Local structure of (Ga,Fe)N and (Ga,Fe)N:Si investigated by x-ray absorption fine structure spectroscopy,” *Phys. Rev. B* **79**, 195209
- Rovezzi, M., T. Devillers, E. Arras, F. d’Acapito, A. Barski, M. Jamet, and P. Pochet, 2008, “Atomic structure of Mn-rich nanocolumns probed by x-ray absorption spectroscopy,” *Appl. Phys. Lett.* **92**, 242510
- Rubinstein, M., and R. H. Colby, 2003, in *Polymer Physics* (Oxford University Press, Oxford)
- Rylkov, V. V., S. N. Nikolaev, K. Yu. Chernoglazov, B. A. Aronzon, K. I. Maslakov, V. V. Tugushev, E. T. Kulatov, I. A. Likhachev, E. M. Pashaev, A. S. Semisalov, N. S. Perov, A. B. Granovskii, E. A. Ganshin, O. A. Novodvorskii, O. D. Khranova, E. V. Khaidukov, and V. Ya. Panchenko, 2012, “High-temperature ferromagnetism in $\text{Si}_{1-x}\text{Mn}_x$ ($x \simeq 0.5$) nonstoichiometric alloys,” *JETP Lett.* **96**, 255
- Sadowski, J., J. Z. Domagala, R. Mathieu, A. Kovacs, and P. Dłużewski, 2013, “Formation of two-dimensionally confined superparamagnetic (Mn, Ga)As nanocrystals in high-temperature annealed (Ga, Mn)As/GaAs superlattices,” *J.*

- Phys.: Cond. Matter **25**, 196005
- Sadowski, J., J. Z. Domagala, R. Mathieu, A. Kovács, T. Kasama, R. E. Dunin-Borkowski, and T. Dietl, 2011, "Formation process and superparamagnetic properties of (Mn,Ga)As nanocrystals in GaAs fabricated by annealing of (Ga,Mn)As layers with low Mn content," Phys. Rev. B **84**, 245306
- Saito, H., V. Zayets, S. Yamagata, and K. Ando, 2002, "Magneto-optical studies of ferromagnetism in the II-VI diluted magnetic semiconductor $Zn_{1-x}Cr_xTe$," Phys. Rev. B **66**, 081201
- Saito, H., V. Zayets, S. Yamagata, and K. Ando, 2003, "Room-temperature ferromagnetism in a II-VI diluted magnetic semiconductor $Zn_{1-x}Cr_xTe$," Phys. Rev. Lett. **90**, 207202
- Sanyal, B., O. Bengone, and S. Mirbt, 2003, "Electronic structure and magnetism of Mn-doped GaN," Phys. Rev. B **68**, 205210
- Sarigiannidou, E., F. Wilhelm, E. Monroy, R. M. Galera, E. Bellet-Amalric, A. Rogalev, J. Goulon, J. Cibert, and H. Mariette, 2006, "Intrinsic ferromagnetism in wurtzite (Ga,Mn)N semiconductor," Phys. Rev. B **74**, 041306(R)
- Sato, K., L. Bergqvist, J. Kudrnovský, P. H. Dederichs, O. Eriksson, I. Turek, B. Sanyal, G. Bouzerar, H. Katayama-Yoshida, V. A. Dinh, T. Fukushima, H. Kizaki, and R. Zeller, 2010, "First-principles theory of dilute magnetic semiconductors," Rev. Mod. Phys. **82**, 1633
- Sato, K., T. Fukushima, and H. Katayama-Yoshida, 2007, "Super-paramagnetic blocking phenomena and room-temperature ferromagnetism in wide band-gap dilute magnetic semiconductor (Ga, Mn)N," Jpn. J. Appl. Phys. **46**, L682
- Sato, K., and H. Katayama-Yoshida, 2002, "First principles materials design for semiconductor spintronics," Semicond. Sci. Technol. **17**, 367
- Sato, K., and H. Katayama-Yoshida, 2007, "Design of colossal solubility of magnetic impurities for semiconductor spintronics by the Co-doping method," Jpn. J. Appl. Phys. **46**, L1120
- Sato, K., H. Katayama-Yoshida, and P. H. Dederichs, 2005, "High Curie temperature and nano-scale spinodal decomposition phase in diluted magnetic semiconductors," Jpn. J. Appl. Phys. **44**, L948
- Sato, M., H. Tanida, K. Kato, T. Sasaki, Y. Yamamoto, S. Sonoda, S. Shimizu, and H. Hori, 2002, "Local structure around Mn in ferromagnetic GaMnN film studied by X-ray absorption fine structure," Jap. J. Appl. Phys. **41**, 4513
- Sawicki, M., T. Devillers, S. Gałęski, C. Simserides, S. Dobkowska, B. Faina, A. Grois, A. Navarro-Quezada, K. N. Trohidou, J. A. Majewski, T. Dietl, and A. Bonanni, 2012, "Origin of low-temperature magnetic ordering in $Ga_{1-x}Mn_xN$," Phys. Rev. B **85**, 205204
- Sawicki, M., E. Guziewicz, M. I. Łukasiewicz, O. Proselkov, I. A. Kowalik, W. Lisowski, P. Dłuzewski, A. Wittlin, M. Jaworski, A. Wolska, W. Paszkowicz, R. Jakiela, B. S. Witkowski, L. Wachnicki, M. T. Klepka, F. J. Luque, D. Arvanitis, J. W. Sobczak, M. Krawczyk, A. Jablonski, W. Stefanowicz, D. Sztenkiel, M. Godlewski, and T. Dietl, 2013, "Homogeneous and heterogeneous magnetism in (Zn,Co)O: From a random antiferromagnet to a dipolar superferromagnet by changing the growth temperature," Phys. Rev. B **88**, 085204
- Sawicki, M., W. Stefanowicz, and A. Ney, 2011, "Sensitive SQUID magnetometry for studying nanomagnetism," Semicon. Sci. Technol. **26**, 064006
- Schulthess, T. C., and W. H. Butler, 2001, "Electronic structure and magnetic interactions in Mn doped semiconductors," J. Appl. Phys. **89**, 7021
- Seike, M., V. A. Dinh, T. Fukushima, K. Sato, and H. Katayama-Yoshida, 2012, "Self-organized nanostructures and high blocking temperatures in MgO-based d^0 ferromagnets," Jap. J. Appl. Phys. **51**, 050201
- Seike, M., T. Fukushima, K. Sato, and H. Katayama-Yoshida, 2013a, "Design of self-organized nanostructures to achieve high blocking temperatures in MgO-based d^0 ferromagnets," J. Korean Phys. Soc. **62**, 1807
- Seike, M., T. Fukushima, K. Sato, and H. Katayama-Yoshida, 2013b, "Self-organized ferromagnetic nanowires in MgO-based magnetic tunnel junctions," Solid State Commun. **167**, 14
- Shi, Jing, S. Gider, K. Babcock, and D. D. Awschalom, 1996, "Magnetic clusters in molecular beams, metals, and semiconductors," Science **271**, 937
- Shiba, H., 1971, "A reformulation of the coherent potential approximation and its applications," Prog. Theor. Phys. **46**, 77
- Shick, A. B., S. Khmelevskiy, O. N. Mryasov, J. Wunderlich, and T. Jungwirth, 2010, "Spin-orbit coupling induced anisotropy effects in bimetallic antiferromagnets: A route towards antiferromagnetic spintronics," Phys. Rev. B **81**, 212409
- Shimada, K., T. Saitoh, H. Namatame, A. Fujimori, S. Ishida, S. Asano, M. Matoba, and S. Anzai, 1996, "Photoemission study of itinerant ferromagnet $Cr_{1-\delta}Te$," Phys. Rev. B **53**, 7673
- Shimizu, H., M. Miyamura, and M. Tanaka, 2000, "Enhanced magneto-optical effect in a GaAs:MnAs nanoscale hybrid structure combined with GaAs/AlAs distributed Bragg reflectors," J. Vacuum Sci. Techn. B **18**, 2063
- Shimizu, H., M. Miyamura, and M. Tanaka, 2001, "Magneto-optical properties of a GaAs:MnAs hybrid structure sandwiched by GaAs/AlAs distributed Bragg reflectors: Enhanced magneto-optical effect and theoretical analysis," Appl. Phys. Lett. **78**, 1523
- Shimizu, H., and M. Tanaka, 2001, "Magneto-optical properties of semiconductor-based superlattices having GaAs with MnAs nanoclusters," J. Appl. Phys. **89**, 7281
- Shimizu, H., and M. Tanaka, 2002a, "Design of semiconductor-waveguide-type optical isolators using the nonreciprocal loss/gain in the magneto-optical waveguides having MnAs nanoclusters," Appl. Phys. Lett. **81**, 5246
- Shimizu, H., and M. Tanaka, 2002b, "Magneto-optical properties of a Si-doped GaAs:MnAs-based magneto-phonic crystal operating at $1.55 \mu m$," Physica E **13**, 597
- Shinya, H., A. Masago, T. Fukushima, H. Funashima, and H. Katayama-Yoshida, 2014, "First-principles investigations of defect and phase stabilities in thermoelectric $(GeTe)_x(AgSbTe_2)_{1-x}$," Jpn. J. Appl. Phys. **53**, 111201
- Shon, Y., Y. Hae Kwon, Y. S. Park, Sh. U. Yuldashev, Seung Joo Lee, C. S. Park, K. J. Chung, S. J. Yoon, H. J. Kim, W. C. Lee, D. J. Fu, T. W. Kangb, X. J. Fan, Y. J. Park, and H. T. Oh, 2004, "Ferromagnetic behavior of p -type GaN epilayer implanted with Fe^+ ions," J. Appl. Phys. **95**, 761
- Shon, Y., S. Lee, H. C. Jeon, Y. S. Park, D. Y. Kim, T. W.

- Kang, J. S. Kim, E. K. Kim, D. J. Fu, X. J. Fan, Y. J. Park, J. M. Baik, and J. L. Lee, 2006, "Origin of clear ferromagnetism for p -type GaN implanted with Fe^+ (5 and 10 at. %)," *Appl. Phys. Lett.* **89**, 082505
- Shuto, Y., M. Tanaka, and S. Sugahara, 2006a, "Epitaxial growth and magnetic properties of a new group-IV ferromagnetic semiconductor: $\text{Ge}_{1-x}\text{Fe}_x$," *phys. stat. solidi (c)* **3**, 4110
- Shuto, Y., M. Tanaka, and S. Sugahara, 2006b, "Magneto-optical properties of group-IV ferromagnetic semiconductor $\text{Ge}_{1-x}\text{Fe}_x$ grown by low-temperature molecular beam epitaxy," *J. Appl. Phys.* **99**, 08D516
- Shuto, Y., M. Tanaka, and S. Sugahara, 2007, "Structural and magnetic properties of epitaxially grown $\text{Ge}_{1-x}\text{Fe}_x$ thin films: Fe concentration dependence," *Appl. Phys. Lett.* **90**, 132512
- Smit, J., and H. G. Beljers, 1955, *Phillips Res. Rep.* **10**, 113
- Solin, S. A., T. Thio, D.R. Hines, and J. J. Heremans, 2000, "Enhanced room-temperature geometric magnetoresistance in inhomogeneous narrow-gap semiconductors," *Science* **289**, 1530
- Sonoda, S., I. Tanaka, F. Oba, H. Ikeno, H. Hayashi, T. Yamamoto, Y. Yuba, Y. Akasaka, K. Yoshida, M. Aoki, M. Asari, T. Araki, Y. Nanishi, K. Kindo, and H. Hori, 2007, "Awakening of ferromagnetism in GaMnN through control of Mn valence," *Appl. Phys. Lett.* **90**, 012504
- Stangl, J., V. Holý, and G. Bauer, 2004, "Structural properties of self-organized semiconductor nanostructures," *Rev. Mod. Phys.* **76**, 725
- Stauffer, D., and A. Aharony, 1994, in *Introduction to percolation theory (revised 2nd ed.)* (Taylor and Francis, 1994)
- Stefanowicz, S., G. Kunert, C. Simserides, J. A. Majewski, W. Stefanowicz, C. Kruse, S. Figge, Tian Li, R. Jakiela, K. N. Trohidou, A. Bonanni, D. Hommel, M. Sawicki, and T. Dietl, 2013, "Phase diagram and critical behavior of a random ferromagnet $\text{Ga}_{1-x}\text{Mn}_x\text{N}$," *Phys. Rev. B* **88**, 081201(R)
- Stefanowicz, W., R. Adhikari, T. Andrearczyk, B. Faina, M. Sawicki, J. A. Majewski, T. Dietl, and A. Bonanni, 2014, "Experimental determination of Rashba spin-orbit coupling in wurtzite n -GaN:Si," *Phys. Rev. B* **89**, 205201
- Stefanowicz, W., D. Sztienkiel, B. Faina, A. Grois, M. Rovezzi, T. Devillers, A. Navarro-Quezada, Tian Li, R. Jakiela, M. Sawicki, T. Dietl, and A. Bonanni, 2010, "Structural and paramagnetic properties of dilute $\text{Ga}_{1-x}\text{Mn}_x\text{N}$," *Phys. Rev. B* **81**, 235210
- Stroppa, A., S. Picozzi, A. Continenza, and A. J. Freeman, 2003, "Electronic structure and ferromagnetism of Mn-doped group-IV semiconductors," *Phys. Rev. B* **68**, 155203
- Suffczyński, J., A. Grois, W. Pacuski, A. Golnik, J. A. Gaj, A. Navarro-Quezada, B. Faina, T. Devillers, and A. Bonanni, 2011, "Effects of s , p - d and s - p exchange interactions probed by exciton magnetospectroscopy in $(\text{Ga},\text{Mn})\text{N}$," *Phys. Rev. B* **83**, 094421
- Sugahara, S., K. L. Lee, S. Yada, and M. Tanaka, 2005, "Precipitation of amorphous ferromagnetic semiconductor phase in epitaxially grown Mn-doped Ge thin films," *Jpn. J. Appl. Phys.* **44**, L1426
- Sun, Zhi-gang, M. Mizuguchi, and H. Akinaga, 2004, "Au/GaAs magnetoresistive-switch-effect devices fabricated by wet etching," *Japan. J. Appl. Phys.* **43**, 2101
- Swagten, H. J. M., A. Twardowski, P. J. T. Eggenkamp, and W. J. M. de Jonge, 1992, " d - d exchange interaction in the diluted magnetic semiconductor $\text{Zn}_{1-x}\text{Co}_x\text{Se}$," *Phys. Rev. B* **46**, 188–192
- Swalin, R. A., 1970, in *Thermodynamics of Solids* (Wiley, New York)
- Takizawa, H., T. Sato, T. Endo, and M. Shimada, 1987, "High-pressure synthesis and electrical properties of Mn_3Ge_5 with $\text{Mn}_{11}\text{Si}_{19}$ -type structure," *J. Solid State Chem.* **68**, 234
- Takizawa, H., T. Sato, T. Endo, and M. Shimada, 1988, "High-pressure synthesis and electrical and magnetic properties of MnGe and CoGe with the cubic B20 structure," *J. Solid State Chem.* **73**, 40
- Takizawa, H., T. Sato, T. Endo, and M. Shimada, 1990, "High pressure synthesis and electrical and magnetic properties of MnGe_4 and CoGe_4 ," *J. Solid State Chem.* **88**, 384
- Takizawa, H., T. Yamashita, K. Uheda, and T. Endo, 2002, "High-pressure synthesis of ferromagnetic Mn_3Ge with the Cu_3Au -type structure," *J. Phys.: Condens. Matter* **14**, 11147
- Talut, G., H. Reuther, A. Mücklich, F. Eichhorn, and K. Potzger, 2006, "Nanocluster formation in Fe implanted GaN," *Appl. Phys. Lett.* **89**, 161909
- Tanaka, M., S. Ohya, and Pham Nam Hai, 2014, "Recent progress in III-V based ferromagnetic semiconductors: Band structure, Fermi level, and tunneling transport," *Appl. Phys. Rev.* **1**, 011102
- Tani, Y., K. Sato, and H. Katayama-Yoshida, 2010, "Materials design of spinodal nanodecomposition in $\text{CuIn}_{1-x}\text{Ga}_x\text{Se}_2$ for high-efficiency solar energy conversion," *Appl. Phys. Express* **3**, 101201
- Tani, Y., K. Sato, and H. Katayama-Yoshida, 2011, "First principles materials design of negative activation energy and transparent conducting sulfides in n -type $\text{CuAl}_{1-x}\text{Sn}_x\text{S}_2$ and p -Type $\text{Cu}_{1-x}\text{VCu}_x\text{AlS}_2$," *Appl. Phys. Express* **4**, 021201
- Tani, Y., K. Sato, and H. Katayama-Yoshida, 2012a, "Computational nano-materials design of low cost and high efficiency $\text{Cu}_2\text{ZnSn}[\text{Se}_{1-x}\text{S}_x]_4$ photovoltaic solar cells by self-organized two-dimensional spinodal nanodecomposition," *Jap. J. Appl. Phys.* **51**, 050202
- Tani, Y., K. Sato, and H. Katayama-Yoshida, 2012b, "First-principles materials design of CuInSe_2 -based high-efficiency photovoltaic solar cells," *Physica B* **407**, 3056
- Tani, Y., K. Sato, and H. Katayama-Yoshida, 2012c, "Materials design of $\text{CuIn}_{1-x}\text{Zn}_{0.5x}\text{Sn}_{0.5x}\text{Se}_2$ for low cost photovoltaic solar cells," *J. Non-Cryst. Solids* **358**, 2420
- Tardif, S., S. Cherifi, M. Jamet, T. Devillers, A. Barski, N. Darowski, D. Schmitz, P. Thakur, J. C. Cezar, and N. B. Brookes, 2010a, "Exchange bias in GeMn nanocolumns: The role of surface oxidation," *Appl. Phys. Lett.* **97**, 062501
- Tardif, S., V. Favre-Nicolin, F. Lancon, E. Arras, M. Jamet, A. Barski, C. Porret, P. Bayle-Guillemaud, T. Devillers, and M. Rovezzi, 2010b, "Strain and correlation of self-organized $\text{Ge}_{1-x}\text{Mn}_x$ nanocolumns embedded in $\text{Ge}(001)$," *Phys. Rev. B* **82**, 104101
- Tawara, Y., and K. Sato, 1963, "On the magnetic anisotropy of single crystal of Mn_5Ge_3 ," *J. Phys. Soc. Jpn.* **18**, 773
- Tersoff, J., C. Teichert, and M. G. Lagally, 1996, "Self-organization in growth of quantum dot superlattices," *Phys. Rev. Lett.* **76**, 1675
- Theodoropoulou, N., A. F. Hebard, S. N. G. Chu, M. E. Overberg, C. R. Abernathy, S. J. Pearton, R. G. Wilson, and J. M. Zavada, 2002a, "Use of ion implantation to facilitate the discovery and characterization of ferromagnetic semiconductors," *J. Appl. Phys.* **91**, 7499

- Theodoropoulou, N., A. F. Hebard, M. E. Overberg, C. R. Abernathy, S. J. Pearton, S. N. G. Chu, and R. G. Wilson, 2002b, "Unconventional carrier-mediated ferromagnetism above room temperature in ion-implanted (Ga, Mn)P:C," *Phys. Rev. Lett.* **89**, 107203
- Thole, B. T., B. Carra, F. Sette, and G. van der Laan, 1992, "X-ray circular dichroism as a probe of orbital magnetization," *Phys. Rev. Lett.* **68**, 1943
- Thomas, L., M. Hayashi, Xin Jiang, R. Moriya, C. Rettner, and S. Parkin, 2007, "Resonant amplification of magnetic domain-wall motion by a train of current pulses," *Science* **315**, 1553
- Titov, A., X. Biquard, D. Halley, S. Kuroda, E. Bellet-Amalric, H. Mariette, J. Cibert, A. E. Merad, G. Merad, M. B. Kanoun, E. Kulatov, and Yu. A. Uspenskii, 2005, "X-ray absorption near-edge structure and valence state of Mn in (Ga,Mn)N," *Phys. Rev. B* **72**, 115209
- Tsui, F., L. He, A. Tkachuk, S. Vogt, and Y. S. Chu, 2004, "Evidence for strain compensation in stabilizing epitaxial growth of highly doped germanium," *Phys. Rev. B* **69**, 081304(R)
- Turchi, P. E. A., G. M. Stocks, W. H. Butler, D. M. Nicholson, and A. Gonis, 1988, "First-principles study of ordering properties of substitutional alloys using the generalized perturbation method," *Phys. Rev. B* **37**, 5982
- Twardowski, A., H. J. M. Swagten, W. J. M. de Jonge, and M. Demianiuk, 1987, "Magnetic behavior of the diluted magnetic semiconductor $Zn_{1-x}Mn_xSe$," *Phys. Rev. B* **36**, 7013-7023
- Ueda, K., H. Shimizu, and M. Tanaka, 2003, "Magneto-optical kerr effect of semiconductor-based multilayer structures containing a GaAs:MnAs granular thin film," *Japan. J. Appl. Phys.* **42**, L914
- van Schilfgaarde, Mark, and O. N. Mryasov, 2001, "Anomalous exchange interactions in III-V dilute magnetic semiconductors," *Phys. Rev. B* **63**, 233205
- Venkatasubramanian, R., and D. L. Dorsey, 1993, "Molecular-beam epitaxial growth surface roughening kinetics of Ge (001): A theoretical study," *J. Vac. Sci. Technol. B* **11**, 253
- Venugopal, R., B. Sundaravel, I. H. Wilson, F. W. Wang, and X. X. Zhang, 2002, "Structural and magnetic properties of fe-ge layer produced by Fe ion-implantation into germanium," *J. Appl. Phys.* **91**, 1410
- Volnianska, O., and P. Boguslawski, 2010, "Magnetism of solids resulting from spin polarization of p orbitals," *J. Phys.: Condens. Matter* **22**, 073202
- Vu, Nguyen Dang, K. Sato, and H. Katayama-Yoshida, 2011, "Giant Peltier effect in self-organized quasi-one-dimensional nano-structure in Cu-Ni alloy," *Appl. Phys. Exp.* **4**, 015203
- Wahl, U., A. Vantomme, G. Langousche, J. G. Correia, L. Peralta, and The ISOLDE Collaboration, 2001, "Direct evidence for implanted Fe on substitutional Ga sites in GaN," *Appl. Phys. Lett.* **78**, 3217
- Wakabayashi, Y. K., Y. Ban, S. Ohya, and M. Tanaka, 2014a, "Annealing-induced enhancement of ferromagnetism and nanoparticle formation in the ferromagnetic semiconductor GeFe," *Phys. Rev. B* **90**, 205209
- Wakabayashi, Y. K., S. Ohya, Y. Ban, and M. Tanaka, 2014b, "Important role of the non-uniform Fe distribution for the ferromagnetism in group-IV-based ferromagnetic semiconductor GeFe," *J. Appl. Phys.* **116**, 173906
- Wang, K.-Y., M. Sawicki, K.W. Edmonds, R.P. Champion, A.W. Rushforth, A.A. Freeman, C.T. Foxon, B.L. Gallagher, and T. Dietl, 2006, "Control of coercivities in (Ga,Mn)As thin films by small concentrations of MnAs nanoclusters," *Appl. Phys. Lett.* **88**, 022510
- Wang, Y., F. Xiu, Y. Wang, X. Kou, A. P. Jacob, K. L. Wang, and J. Zou, 2010, "Mn-rich clusters in gemm magnetic semiconductors: Structural evolution and magnetic property," *J. Alloys Compd.* **508**, 273
- Wang, Y., F. Xiu, Y. Wang, J. Zou, W. P. Beyermann, Y. Zhou, and K. L. Wang, 2011, "Coherent magnetic semiconductor nanodot arrays," *Nanoscale Res. Lett.* **6**, 134
- Wang, Y., J. Zou, Z. Zhao, X. Han, X. Zhou, and K.L. Wang, 2008, "Direct structural evidences of $Mn_{11}Ge_8$ and Mn_5Ge_2 clusters in $Ge_{0.96}Mn_{0.04}$ thin films," *Appl. Phys. Lett.* **92**, 101913
- Wei, S., W. Yan, Z. Sun, Q. Liu, W. Zhong, X. Zhang, H. Oyanagi, and Z. Wu, 2006, "Direct determination of Mn occupancies in $Ga_{1-x}Mn_xN$ dilute magnetic semiconductors by x-ray absorption near-edge structure spectroscopy," *Appl. Phys. Lett.* **89**, 121901
- Wellmann, P. J., J. M. Garcia, J.-L. Feng, and P. M. Petroff, 1997, "Formation of nanoscale ferromagnetic MnAs crystallites in low-temperature grown GaAs," *Appl. Phys. Lett.* **71**, 2532
- Wellmann, P. J., J. M. Garcia, J.-L. Feng, and P. M. Petroff, 1998, "Giant magnetoresistance in a low-temperature GaAs/MnAs nanoscale ferromagnet hybrid structure," *Appl. Phys. Lett.* **73**, 3291
- Weng, H., and J. Dong, 2005, "First-principles investigation of transition-metal-doped group-IV semiconductors: R_xY_{1-x} ($R = Cr, Mn, Fe; Y = Si, Ge$)," *Phys. Rev. B* **71**, 035201
- Williamson, G., and W. Hall, 1953, "X-ray line broadening from filed aluminium and wolfram," *Acta Metall.* **1**, 22
- Woloś, A., and M. Kamińska, 2008, "Magnetic impurities in semiconductors," in *Spintronics*, edited by T. Dietl, D. D. Awschalom, M. Kamińska, and H. Ohno (Elsevier, Amsterdam) p. 325
- Woloś, A., M. Piersa, G. Strzelecka, K. P. Korona, A. Hruban, and M. Kamińska, 2009, "Mn configuration in III-V semiconductors and its influence on electric transport and semiconductor magnetism," *Phys. Status Solidi C* **6**, 2769
- Woodbury, H. H., and W. W. Tyler, 1955, "Properties of germanium doped with manganese," *Phys. Rev.* **100**, 659
- Wróbel, J., T. Dietl, A. Lusakowski, G. Grabecki, K. Fronc, R. Hey, K. H. Ploog, and H. Shtrikman, 2004, "Spin filtering in a hybrid ferromagnetic-semiconductor microstructure," *Phys. Rev. Lett.* **93**, 246601
- Xiu, F., Y. Wang, J. Kim, A. Hong, J. Tang, A. P. Jacob, J. Zou, and K. L. Wang, 2010a, "Electric-field-controlled ferromagnetism in high-Curie-temperature $Mn_{0.05}Ge_{0.95}$ quantum dots," *Nature Mater.* **9**, 337
- Xiu, F., Y. Wang, X. Kou, P. Upadhyaya, Y. Zhou, J. Zou, and K. L. Wang, 2010b, "Synthesis of high-Curie-temperature $Fe_{0.02}Ge_{0.98}$ quantum dots," *JACS Comm.* **132**, 11425
- Yada, S., Pham Nam Hai, S. Sugahara, and M. Tanaka, 2011, "Structural and magnetic properties of $Ge_{1-x}Mn_x$ thin films grown on Ge (001) substrates," *J. Appl. Phys.* **110**, 073903
- Yamazaki, Y., T. Kataoka, V. R. Singh, A. Fujimori, F.-H. Chang, D.-J. Huang, H.-J. Lin, C. T. Chen, K. Ishikawa, K. Zhang, and S. Kuroda, 2011, "Effect of co-doping of donor and acceptor impurities in the ferromagnetic semiconductor $Zn_{1-x}Cr_xTe$ studied by soft x-ray magnetic circular dichroism," *J. Phys.: Condens. Matter* **23** (17), 176002

- Yang, X. L., Z. T. Chen, L. B. Zhao, W. X. Zhu, C. D. Wang, X. D. Pei, and G. Y. Zhang, 2008, "Structural, optical and magnetic properties of $\text{Ga}_{1-x}\text{Mn}_x\text{N}$ films grown by MOCVD," *J. Phys. D: Appl. Phys.* **41**, 245004
- Yao, Jia-Hsien, Hsiu-Hau Lin, Yun-Liang Soo, Tai-Sing Wu, Jai-Lin Tsai, Ming-Der Lan, and Tsung-Shune Chin, 2012, "Room-temperature anomalous Hall effect in amorphous Si-based magnetic semiconductor," *Appl. Phys. Lett.* **100** (9), 092404
- Ye, L. H., and A. J. Freeman, 2006, "Defect compensation, clustering, and magnetism in Cr-doped anatase TiO_2 ," *Phys. Rev. B* **73**, 081304(R)
- Ye, S., P. J. Klar, Th. Hartmann, W. Heimbrot, M. Lampalzer, S. Nau, T. Torunski, W. Stolz, T. Kurz, H.-A. Krug von Nidda, and A. Loidl, 2003, "Anisotropy of the magnetotransport in $(\text{Ga},\text{Mn})\text{As}/\text{MnAs}$ paramagnetic-ferromagnetic hybrid structures," *Appl. Phys. Lett.* **83**, 3927
- Yokoyama, M., T. Ogawa, A. M. Nazmul, and M. Tanaka, 2006, "Large magnetoresistance ($> 600\%$) of a $\text{GaAs}:\text{MnAs}$ granular thin film at room temperature," *J. Appl. Phys.* **99**, 08D502
- Yokoyama, M., H. Yamaguchi, T. Ogawa, and M. Tanaka, 2005, "Zinc-blende-type MnAs nanoclusters embedded in GaAs ," *J. Appl. Phys.* **97**, 10D317
- Yoon, I. T., T. W. Kang, and D. J. Kim, 2006, "Magnetic behavior of Mn_3GaN precipitates in ferromagnetic $\text{Ga}_{1-x}\text{Mn}_x\text{N}$ layers," *Mat. Sci. Eng. B* **134**, 49
- Yu, I.-S., M. Jamet, T. Devillers, A. Barski, P. Bayle-Guillemaud, C. Beigné, J. Rothman, V. Baltz, and J. Cibert, 2010, "Spinodal decomposition to control magnetotransport in (Ge,Mn) films," *Phys. Rev. B* **82**, 035308
- Yu, I.-S., M. Jamet, A. Marty, T. Devillers, A. Barski, C. Beigné, P. Bayle-Guillemaud, and J. Cibert, 2011, "Modeling magnetotransport in inhomogeneous (Ge,Mn) films," *J. Appl. Phys.* **109**, 123906
- Zajac, M., R. Doradziński, J. Gosk, J. Szczytko, M. Lefeld-Sosnowska, M. Kamińska, A. Twardowski, M. Palczewska, E. Grzanka, and W. Gębicki, 2001, "Magnetic and optical properties of GaMnN magnetic semiconductor," *Appl. Phys. Lett.* **78**, 1276
- Zajac, M., J. Gosk, E. Grzanka, M. Kamińska, A. Twardowski, B. Strojek, T. Szyszko, and S. Podsiadło, 2003, "Possible origin of ferromagnetism in $(\text{Ga},\text{Mn})\text{N}$," *J. Appl. Phys.* **93**, 4715
- Zajac, M., J. Gosk, M. Kamińska, A. Twardowski, T. Szyszko, and S. Podsiadło, 2001, "Paramagnetism and antiferromagnetic d-d coupling in GaMnN magnetic semiconductor," *Appl. Phys. Lett.* **79**, 2432
- Zeng, C., Z. Zhang, K. van Benthem, M. F. Chisholm, and H. H. Weitering, 2008, "Optimal doping control of magnetic semiconductors via subsurfactant epitaxy," *Phys. Rev. Lett.* **100**, 066101
- Zhao, Y. J., T. Shishidou, and A. J. Freeman, 2003, "Ruderman-Kittel-Kasuya-Yosida-like ferromagnetism in $\text{Mn}_x\text{Ge}_{1-x}$," *Phys. Rev. Lett.* **90**, 047204
- Zhao, Yu-Jun, and A. Zunger, 2005, "Zinc-blende half-metallic ferromagnets are rarely stabilized by coherent epitaxy," *Phys. Rev. B* **71**, 132403
- Zheng, S., W. Zhu, Y. F. Gao, G. M. Stocks, and Z. Zhang, 2010, "Kinetic Monte Carlo simulations of nanocolumn formation in two-component epitaxial growth," *Appl. Phys. Lett.* **96**, 071913
- Zhou, Shengqiang, 2014, "Defect-induced ferromagnetism in semiconductors: A controllable approach by particle irradiation," *Nucl. Instrum. Methods Phys. Res. B* **326** (0), 55
- Zhou, X. H., X. S. Chen, X. G. Guo, L. Z. Sun, Y. L. Sun, and W. Lu, 2004, "Ferromagnetism of 3d-impurities substituted in Ge," *J. Magn. Magn. Mat.* **284**, 253
- Zhu, Wenguang, Zhenyu Zhang, and E. Kaxiras, 2008, "Dopant-assisted concentration enhancement of substitutional Mn in Si and Ge," *Phys. Rev. Lett.* **100**, 027205
- Zunger, A., 1986, "Electronic structure of 3d transition-atom impurities in semiconductors," in *Solid State Physics*, Vol. 39, edited by F. Seitz and D. Turnbull (Academic Press, New York) p. 275